



Quantitative Measurements of Nitric Oxide Concentration in High-Pressure, Swirl-Stabilized Spray Flames

Clayton S. Cooper and Normand M. Laurendeau
Purdue University, West Lafayette, Indiana

The NASA STI Program Office . . . in Profile

Since its founding, NASA has been dedicated to the advancement of aeronautics and space science. The NASA Scientific and Technical Information (STI) Program Office plays a key part in helping NASA maintain this important role.

The NASA STI Program Office is operated by Langley Research Center, the Lead Center for NASA's scientific and technical information. The NASA STI Program Office provides access to the NASA STI Database, the largest collection of aeronautical and space science STI in the world. The Program Office is also NASA's institutional mechanism for disseminating the results of its research and development activities. These results are published by NASA in the NASA STI Report Series, which includes the following report types:

- **TECHNICAL PUBLICATION.** Reports of completed research or a major significant phase of research that present the results of NASA programs and include extensive data or theoretical analysis. Includes compilations of significant scientific and technical data and information deemed to be of continuing reference value. NASA's counterpart of peer-reviewed formal professional papers but has less stringent limitations on manuscript length and extent of graphic presentations.
- **TECHNICAL MEMORANDUM.** Scientific and technical findings that are preliminary or of specialized interest, e.g., quick release reports, working papers, and bibliographies that contain minimal annotation. Does not contain extensive analysis.
- **CONTRACTOR REPORT.** Scientific and technical findings by NASA-sponsored contractors and grantees.

- **CONFERENCE PUBLICATION.** Collected papers from scientific and technical conferences, symposia, seminars, or other meetings sponsored or cosponsored by NASA.
- **SPECIAL PUBLICATION.** Scientific, technical, or historical information from NASA programs, projects, and missions, often concerned with subjects having substantial public interest.
- **TECHNICAL TRANSLATION.** English-language translations of foreign scientific and technical material pertinent to NASA's mission.

Specialized services that complement the STI Program Office's diverse offerings include creating custom thesauri, building customized data bases, organizing and publishing research results . . . even providing videos.

For more information about the NASA STI Program Office, see the following:

- Access the NASA STI Program Home Page at <http://www.sti.nasa.gov>
- E-mail your question via the Internet to help@sti.nasa.gov
- Fax your question to the NASA Access Help Desk at (301) 621-0134
- Telephone the NASA Access Help Desk at (301) 621-0390
- Write to:
NASA Access Help Desk
NASA Center for AeroSpace Information
7121 Standard Drive
Hanover, MD 21076



Quantitative Measurements of Nitric Oxide Concentration in High-Pressure, Swirl-Stabilized Spray Flames

Clayton S. Cooper and Normand M. Laurendeau
Purdue University, West Lafayette, Indiana

Prepared under Contract NAS3-27720

National Aeronautics and
Space Administration

Glenn Research Center

Trade names or manufacturers' names are used in this report for identification only. This usage does not constitute an official endorsement, either expressed or implied, by the National Aeronautics and Space Administration.

Available from

NASA Center for Aerospace Information
7121 Standard Drive
Hanover, MD 21076
Price Code: A10

National Technical Information Service
5285 Port Royal Road
Springfield, VA 22100
Price Code: A10

TABLE OF CONTENTS

	Page
LIST OF TABLES	vii
LIST OF FIGURES	viii
LIST OF SYMBOLS	xv
ABSTRACT	xix
1. INTRODUCTION	1
2. BACKGROUND AND PREVIOUS ATMOSPHERIC MEASUREMENTS.....	6
2.1 Introduction	6
2.2 Background	6
2.3 Laser-Induced Fluorescence Methodology	9
2.3.1 Two-Level Model.....	10
2.3.2 Molecular Dynamic Model	18
2.3.3 Utilization of Laser-Induced Fluorescence	22
2.4 Experimental Apparatus	23
2.4.1 Optical System	23
2.4.2 LDI Burner	27
2.5 Experimental Approach at Atmospheric Pressure	29
2.5.1 Spectroscopic Considerations	29
2.5.2 Mie Scattering Profiles.....	30
2.5.3 Narrowband Excitation Scans	32
2.5.4 Narrowband Detection Scans	32
2.5.5 Oxygen Background.....	34
2.6 Results and Discussion.....	37
2.6.1 Point LSF Measurements	37
2.6.2 Point LIF Measurements	39
2.6.3 Point-Extrapolated PLIF Measurements	40
2.7 Improvements to Fluorescence Measurements	41
2.8 Conclusions	44

	Page
3. HIGH-PRESSURE EXPERIMENTAL APPARATUS.....	47
3.1 Optical System	47
3.2 High-Pressure Facility.....	56
3.3 Data-Acquisition System.....	59
4. DEVELOPMENT AND APPLICATION OF A QUANTITATIVE CALIBRATION SCHEME FOR 2-ATM LEAN DIRECT-INJECTION SPRAY FLAMES	62
4.1 Introduction	62
4.2 Background	62
4.3 Operating Conditions	66
4.4 Spectral Validation	67
4.4.1 Excitation / Detection Scheme	67
4.4.2 Mie Scattering Profiles.....	67
4.4.3 Excitation and Detection Scans.....	68
4.5 In-Situ Calibration Method	71
4.5.1 Theory	71
4.5.2 Calibration Slope Comparisons.....	76
4.5.3 Relative Calibration Measurements	78
4.5.4 Experimental Procedure	83
4.6 Results	85
4.7 Conclusions	87
5. QUANTITATIVE MEASUREMENTS OF NITRIC OXIDE IN HIGH- PRESSURE (2-5 ATM), SWIRL-STABILIZED SPRAY FLAMES VIA LASER-INDUCED FLUORESCENCE.....	89
5.1 Introduction	89
5.2 Operating Conditions	90
5.3 Spectral Validation	90
5.3.1 Mie Scattering Profiles	92
5.3.2 Excitation and Detection Scans.....	92
5.4 Calibration Slope Experiments	94
5.4.1 Calibration Slope Comparison	94
5.4.2 Relative Calibration Measurements.....	98
5.5 Results and Discussion.....	102
5.6 Conclusions	108

6. PARAMETRIC STUDY OF NO PRODUCTION VIA QUANTITATIVE LASER-INDUCED FLUORESCENCE IN HIGH- PRESSURE, SWIRL- STABILIZED SPRAY FLAMES	109
6.1 Introduction	109
6.2 Operating Conditions	109
6.3 Results and Discussion.....	110
6.4 Conclusions	117
7. PARAMETRIC STUDY OF NO PRODUCTION VIA QUANTITATIVE LASER-INDUCED FLUORESCENCE IN HIGH-PRESSURE, LEAN PREMIXED- PREVAPORIZED SPRAY FLAMES	120
7.1 Introduction	120
7.2 Operating Conditions	121
7.3 Spectral Validation.....	124
7.4 Calibration Comparison	124
7.5 Results and Discussion.....	126
7.6 Conclusions	135
8. COMPARISON OF LASER-INDUCED AND PLANAR LASER-INDUCED FLUORESCENCE MEASUREMENTS OF NITRIC OXIDE IN A HIGH- PRESSURE, SWIRL-STABILIZED, SPRAY FLAME.....	136
8.1 Introduction	136
8.2 Background	137
8.3 Operating Conditions	139
8.4 Laser-Induced Fluorescence Measurements	139
8.4.1 Mie Scattering Profiles.....	140
8.4.2 LIF Measurement Scheme	140
8.4.3 NO LIF Profiles.....	143
8.5 PLIF Measurements	145
8.5.1 PLIF Excitation Scan Comparison.....	145
8.5.2 Calibration Slope Comparison	146
8.5.3 PLIF Experimental Method.....	150
8.5.4 NO PLIF Profiles	151
8.6 Conclusions	153
9. CONCLUSIONS AND RECOMMENDATIONS FOR FUTURE WORK.....	154
9.1 Conclusions	154
9.2 Recommendation.....	155

LIST OF REFERENCES	157
--------------------------	-----

APPENDICES

Appendix A: Error Analysis.....	163
A.1 Propagation of Errors	163
A.2 LIF Measurements.....	165
Appendix B: Modeling Work.....	169
B.1 Equivalence Ratio Comparison	183
B.2 Preheat Comparison.....	183
B.3 Pressure Comparison	187
B.4 Additional Sandia Models	187
B.5 REC Modeling.....	189

LIST OF TABLES

Table	Page
5.1: Operating conditions for LDI flames of this study.	91
A.1: Typical error terms for LDI flame ($P=4.27$ atm, $\phi_p=1.0$, $T_{air}=375$, $h=40$ mm, $r=0$ mm).....	168
B.1: Heptane mechanism reactions.	170

LIST OF FIGURES

Figure	Page
1.1: Generic lean direct-injection burner layout.....	4
1.2: Generic lean premixed-prevaporized burner layout.....	5
2.1: Schematic of two-level model for LIF. The rate coefficients shown are stimulated absorption (W_{12}), stimulated emission (W_{21}), spontaneous emission (A_{21}), collisional quenching (Q_{21}), photoionization (W_{2i}), and predissociation (P).....	12
2.2: Theoretical plot of normalized upper level population vs. normalized laser irradiance based on Eq. (2.15)	15
2.3: Saturation plot demonstrating the transition from linear to saturation excitation regimes.	17
2.4: Schematic of molecular dynamic model for LIF. The upper and lower laser-coupled rovibronic levels are labeled u and l , respectively. Vibrational quantum numbers in the upper and lower electronic state are labeled as v' and v'' , respectively. Specific rotational levels in the excited and ground electronic state are indicated as j and k , respectively. The rate processes of concern and their respective rate coefficients are stimulated absorption (W_{lu}), stimulated emission (W_{ul}), spontaneous emission ($A_{j,k}$), electronic quenching ($Q_{j,k}$), vibrational relaxation ($V_{v'',v''}$), rotational relaxation ($R_{j,k}$), and photoionization (W_i)	20
2.5: Schematic diagram of the experimental apparatus: M: mirror, FS: filter stack, RP: Rochon prism, A: aperture, SL: spherical lens, SP: splitter plate, PD: photodiode, IR: image rotator, LA: linear array, RAP: right angle prism	25
2.6: Schematic of atmospheric LDI burner.	28
2.7: Mie scattering radial profiles for atmospheric LDI flame at four axial heights.	31

Figure	Page
2.8: Excitation scans in reference McKenna burner ($\phi = 0.8$, $C_2H_6/O_2/N_2/NO$) doped with 80 ppm NO and atmospheric LDI burner at $h = 5$ mm, $r = 3$ mm.....	33
2.9: Detection scans in the atmospheric LDI flame with on- and off-line excitation for validation of the background subtraction technique for Mie scattering..	35
2.10: Corrected, uncorrected, and background NO concentration measurements in premixed $CH_4/O_2/N_2$ flames ($\phi = 0.6$, $N_2/O_2 = 2.2$) at pressures from 1 to 14.6 atm (Thomsen <i>et. al</i> , 1997).....	36
2.11: Radial NO profiles obtained with (a) LSF technique, (b) single-point scaled LIF technique, and (c) single-point scaled PLIF technique in $\phi = 1.0$, atmospheric LDI flame at an axial height of 5-mm..	38
2.12: Mie scattering radial profiles in a 2-atm LDI flame when utilizing or not utilizing two dichroic beamsplitters (CVI LWP-0-R226-T235-237-PW-2037-UV)..	42
2.13: Transmission characteristics of UV filters for broadband detection: (a) scattering at 226 nm, (b) NO detection signal.....	45
3.1: Schematic diagram of the experimental apparatus: M: mirror, FS: filter stack, A: aperture, L: spherical lens, BS: splitter plate, PD: photodiode, BES: elevation assembly, LA: linear array, RAP: right angle, MC: monochromator, PMT: photomultiplier tube.	49
3.2: Photomultiplier tube housing and lens assembly	52
3.3: Linearity of photomultiplier tube (PMT).	53
3.4: Linearity of photodiode (PD).	54
3.5: Schematic diagram of the PLIF experimental apparatus: M: mirror, FS: filter stack, A: aperture, L: spherical lens, BS: splitter plate, PD: photodiode, BES: elevation assembly, LA: linear array, RAP: right angle prism, HPV: high-pressure vessel, HS: horizontal translation stage, VS: vertical translation stage.....	55
3.6: High-pressure vessel cutaway view.	56
3.7: High-pressure LDI burner schematic	58

Figure	Page
3.8: Data-acquisition system overview.	60
4.1: Mie scattering radial profiles for 2-atm LDI flame [$\dot{m}_{\text{fuel}} = 0.165 \text{ g/s}$, $\phi = 0.9$, $T_{\text{air preheat}} = 375 \text{ K}$] at five axial heights	69
4.2: Excitation scans at 2 atm in (a) McKenna burner ($\phi = 0.8$, 3.76 dilution ratio) doped with 40 ppm NO, (b) LDI burner at $h = 15 \text{ mm}$, $r = 0 \text{ mm}$ doped with $\sim 80 \text{ ppm}$ NO. The NO on-line $Q_2(26.5)$ and off-line excitation wavelengths are labeled.	70
4.3: Detection scans at 2 atm in McKenna burner ($\phi = 0.8$, 3.76 dilution ratio) doped with 40 ppm NO and LDI burner at $h = 15 \text{ mm}$, $r = 0 \text{ mm}$ doped with $\sim 80 \text{ ppm}$ NO.	72
4.4: Sample calibration curve for high-pressure LIF measurements of NO, illustrating the subtraction technique when utilizing an on-line and off-line calibration referenced to the same LIF background.	74
4.5: NO fluorescence calibrations at 2 atm taken (a) in the post-flame zone of a lean ($\phi = 0.8$, 3.76 dilution ratio) $\text{C}_2\text{H}_6/\text{O}_2/\text{N}_2/\text{NO}$ flame stabilized on a water-cooled McKenna burner and (b) along the centerline, 35-mm above a heptane-fueled ($\phi = 0.9$, 3.76 dilution ratio, 373 K preheat) LDI burner.	77
4.6: NO calibration slopes at 2 atm measured for centerline axial locations and normalized to that at the 35-mm axial height. All calibrations are corrected for transmission effects at the given axial height.	80
4.7: Equilibrium state relationships for temperature and the electronic quenching rate coefficient (Q_e) for 2-atm heptane combustion. Note the negligible variation of Q_e at lean mixture fractions.	81
4.8: Fluorescence signal state relationship at 2 atm for a fixed ppm level of NO normalized to that at 1700 K. A decrease in the fluorescence signal of 20% corresponds to a temperature rise from 1700 K ($\phi = 0.6$) to $\sim 2050 \text{ K}$ ($\phi = 0.8$).	82
4.9: Absolute NO (ppm) measurements in 2-atm LDI flame. Radial NO profiles have been corrected for absorption and calibrated at each axial height.	86

Figure	Page
5.1: Mie scattering radial profiles for LDI flames at 2.09 atm [$\dot{m}_{\text{fuel}} = 0.165$ g/s, $\phi_p = 0.9$, $T_{\text{air preheat}} = 375$ K] and at 4.27 atm [$\dot{m}_{\text{fuel}} = 0.36$ g/s, $\phi_p = 0.9$, $T_{\text{air preheat}} = 373$ K].....	93
5.2: Excitation scans in: (a) 2.09-atm McKenna burner ($\phi = 0.8$, 3.76 dilution ratio) doped with 40 ppm NO and 2.09-atm LDI burner at $h = 15$ mm, $r = 0$ mm doped with ~80 ppm NO; (b) 4.27-atm LDI burner at $h = 15$ mm, $r = 0$ mm doped with ~100 ppm NO. The NO on-line $Q_2(26.5)$ and off-line excitation wavelengths are labeled.....	95
5.3: Detection scans in: (a) 2.09-atm McKenna burner ($\phi = 0.8$, 3.76 dilution ratio) doped with 40 ppm NO and 2.09-atm LDI burner at $h = 15$ mm, $r = 0$ mm doped with ~80 ppm NO; (b) 4.27-atm LDI burner at $h = 15$ mm, $r = 0$ mm doped with ~100 ppm.	96
5.4: NO fluorescence calibrations taken in: (a) post-flame zone of a lean ($\phi = 0.8$, 3.76 dilution ratio) $\text{C}_2\text{H}_6/\text{O}_2/\text{N}_2/\text{NO}$ flame stabilized on a water-cooled McKenna burner and centerline 35-mm axial height of a heptane-fueled ($\phi_p = 0.9$, 3.76 dilution ratio, 373 K preheat) LDI flame at 2.09 atm; (b) post-flame zone of a lean ($\phi = 0.8$, 3.76 dilution ratio) $\text{CH}_4/\text{O}_2/\text{N}_2/\text{NO}$ flame stabilized on a water-cooled McKenna burner and centerline 35-mm axial height of a heptane-fueled ($\phi_p = 0.9$, 3.76 dilution ratio, 373 K preheat) LDI flame at 4.27 atm.	99
5.5: NO calibration slopes at centerline axial locations when normalized to that at the 35-mm axial height for 2.09-, 3.18-, 4.27-, and 5.35-atm LDI flames. All calibrations are corrected for transmission effects at the given axial height and pressure. The relative slopes indicate variations in the temperature and the electronic quenching rate coefficient along the axis.	100
5.6: NO concentration profiles for 2.09-, 3.18-, 4.27-, and 5.35-atm lean ($\phi_p = 0.9$, 3.76 dilution ratio, 373 K preheat) direct-injection, swirl-stabilized, spray flames. Accuracy bars are typically 25% at the 95% confidence level over this pressure range.	103
5.7: Cross-sectional NO concentration profiles for 2.09-, 3.18-, 4.27-, and 5.35-atm lean ($\phi_p = 0.9$, 3.76 dilution ratio, 373 K preheat) direct-injection, swirl-stabilized, spray flames. Note the uniformity of the NO profiles throughout the measured region for the 3.18-, 4.27-, and 5.35-atm cases.	104

Figure	Page
5.8: Absolute NO (ppm) concentration profiles at the 40-mm axial height as a function of operating pressure. Radial measurement profiles have been corrected for absorption and calibrated at the 40-mm height location. Typical accuracy bars at the 95% confidence level are shown at one point on each profile.....	105
5.9: EINO _x measurements taken at the 40-mm axial height. The predicted EINO _x based on a P ^{0.5} scaling is shown as the solid line. The actual scaling of this data set is P ^{0.74}	107
6.1: Photograph of LDI flame at 4.27 atm [$\dot{m}_{\text{fuel}} = 0.36$ g/s, $\phi_p = 0.9$, $T_{\text{air preheat}} = 375$ K].	111
6.2: Radial NO concentration profiles for lean ($\phi_p = 0.9$, $T_{\text{air preheat}} = 375$ K) direct-injection, swirl-stabilized, spray flame at 4.27 atm. Note the uniformity of the NO profiles throughout the measured region.....	112
6.3: NO measurements at the 40-mm axial height ($\dot{m}_{\text{fuel}} = 0.36$ g/s, $\phi_p = 0.9$, $P = 4.27$ atm) as a function of air preheat temperature.	113
6.4: NO measurements at the 40-mm axial height ($T_{\text{air preheat}} = 375$ K, $P = 4.27$ atm) as a function of stoichiometry with (1) constant fuel flow rate ($\dot{m}_{\text{fuel}} = 0.36$ g/s) and (2) constant air flow rate ($\dot{m}_{\text{air}} = 6.07$ g/s).....	115
6.5: NO (ppm) vs. ϕ_p^2 , demonstrating coupled dilution and residence time effects based on exit velocity for the 4.27-atm LDI flame. The excellent correlation suggests thermal NO production in near stoichiometric regions.	118
6.6: NO (ppm) scaling demonstrating coupled dilution and residence time effect based on exit velocity for 1-atm LDI flame. The original data of Cooper and Laurendeau 1998a) have been scaled to account for both dilution and residence time effects.....	119
7.1: Schematic of lean, premixed-prevaporized burner..	122
7.2: Photograph of LPP flame at 4.27 atm [$\phi = 0.75$, $T_{\text{air preheat}} = 475$ K]. Note that the oval window restricts the field of view.	123
7.3: (A) Excitation scan taken in 4.27-atm LPP burner at $h = 20$ mm, $r = 0$ mm. The NO on-line Q ₂ (26.5) and off-line excitation wavelengths are labeled. (B) Detection scan taken at same conditions.	125

Figure	Page
7.4: NO fluorescence calibrations taken in the post-flame zone of a lean ($\phi = 0.8$, 3.76 dilution ratio) $\text{CH}_4/\text{O}_2/\text{N}_2/\text{NO}$ flame stabilized on a sintered bronze burner and at the centerline 35-mm axial height of a heptane-fueled ($\phi = 0.75$, 3.76 dilution ratio, 475 K preheat) LPP flame at 4.27 atm.....	127
7.5: Radial NO concentration profiles for lean ($\phi = 0.75$, $T_{\text{air preheat}} = 475 \text{ K}$) direct-injection, swirl-stabilized, spray flame at 4.27 atm. Note the radial divergence of the profiles.	129
7.6: NO measurements at the 20-mm axial height ($T_{\text{air preheat}} = 475 \text{ K}$, $P = 4.27 \text{ atm}$) as a function of stoichiometry. The predicted thermal NO scaling is based on complete combustion, with that for residence time based on exit velocity.....	130
7.7: NO measurements at the 20-mm axial height ($\phi = 0.75$, $P = 4.27 \text{ atm}$) as a function of air preheat temperature. The predicted thermal NO scaling is based on complete combustion, with that for residence time scaled based on exit velocity.....	133
7.8: NO measurements at the 20-mm axial height ($T_{\text{air preheat}} = 475 \text{ K}$, $P = 4.27 \text{ atm}$) as a function of pressure. The predicted thermal NO is based on equilibrium considerations with a pressure exponent of 0.5.....	134
8.1: Mie scattering radial profiles for LDI flame at 4.27 atm [$\dot{m}_{\text{fuel}} = 0.36 \text{ g/s}$, $\phi_p = 0.9$, $T_{\text{air preheat}} = 375 \text{ K}$].	141
8.2: Absolute NO (ppm) measurements in 4.27-atm LDI flame [$\dot{m}_{\text{fuel}} = 0.36 \text{ g/s}$, $\phi_p = 0.9$, $T_{\text{air preheat}} = 375 \text{ K}$]. Radial NO profiles have been corrected for extinction and calibrated at each axial height.....	144
8.3: Excitation scans in 4.27-atm LDI flame at $h = 15 \text{ mm}$, $r = 0 \text{ mm}$ doped with $\sim 80 \text{ ppm}$ NO using narrowband LIF detection and broadband PLIF detection. The NO on-line $Q_2(26.5)$ and the off-line excitation wavelengths are labeled.	147
8.4: NO fluorescence calibrations taken in 4.27-atm LDI flame using narrowband LIF detection and broadband PLIF detection. Both calibration curves have been normalized to unity at the maximum on-line doping condition. Note the background shift for off-line PLIF excitation.	148

Figure	Page
8.5: Ratio of off-line to on-line calibration signal in 4.27-atm LDI flame for narrowband LIF detection and broadband PLIF detection. The LIF data demonstrate a ratio which is constant with doping level. The PLIF data demonstrate a decrease with increasing NO concentration, revealing a preferential excitement of interfering species by the off-line wavelength within the broadband detection window.	149
8.6: Comparison of the corrected PLIF measurements to the LIF measurements. The PLIF measurements fall within the accuracy bars of the LIF data, emphasizing the utility of the PLIF technique for LDI spray flames when a scaling point can be obtained from quantitative LIF data.	152
B.1: Perfectly-stirred reactor residence time plot.	182
B.2: Comparison of PSR predictions to measured equivalence ratio scaling in LDI flame.	184
B.3: Comparison of PSR predictions to measured ϕ_p^2 scaling in LDI flames.	185
B.4: Comparison of PSR predictions to measured scaling for air preheat temperature in LDI flames.	186
B.5: Comparison of PSR predictions to measured pressure scaling in LDI flames.	188
B.6: Cold-flow velocity vector plot of REC simulation.	190
B.7: Combusting-flow velocity vector plot of REC simulation.	191
B.8: Combusting-flow temperature contour plot of REC simulation.	192
B.9: Combusting-flow NO mass fraction contour plot of REC simulation.	193

LIST OF SYMBOLS

English Symbols

<u>Symbols</u>	<u>Description</u>	<u>Units</u>
$A_{21}, A_{j,k}$	Einstein A coefficient for spontaneous emission	s^{-1}
B_{12}	Einstein B coefficient for stimulated absorption	$m^3/J \cdot s^2$
B_{21}	Einstein B coefficient for stimulated emission	$m^3/J \cdot s^2$
c	Speed of light	m/s
D_e	Burner exit diameter	m
g	Rovibronic level degeneracy	--
$g(\nu)$	Absorption lineshape	s
G	Photomultiplier gain	V/W
G_ϕ	Axial flux of angular momentum	$kg \cdot m^2/s^2$
G_x	Axial flux of linear momentum	$kg \cdot m/s^2$
h	Planck constant	J · s
$I_\nu(\nu)$	Laser spectral irradiance	$W/m^2 \cdot s^{-1}$
I_ν°	Normalized laser spectral irradiance	$W/m^2 \cdot s^{-1}$
I_ν^{sat}	Saturation spectral irradiance	$W/m^2 \cdot s^{-1}$
$L(\nu)$	Laser spectral distribution function	--
LIF	Laser-induced fluorescence signal	V/V
m	Calibration slope	V/ppm
\dot{m}_a	Air mass flow rate	g/s

<u>Symbols</u>	<u>Description</u>	<u>Units</u>
\dot{m}_f	Fuel mass flow rate	g/s
M	Molecular weight	kg/kmol
N	Number density of rovibronic level	cm ⁻³
N_1°	Initial number density of lower laser-coupled level	cm ⁻³
$[NO]$	NO number density	cm ⁻³
$Q_{2l}, Q_{j,k}, Q_e$	Electronic quenching rate coefficient	s ⁻¹
$R_{j,k}, R_{nm}$	Rotational relaxation rate between specific levels	s ⁻¹
S	Signal	V
S	Swirl number	--
T	Temperature	K
V_c	Collection volume	cm ³
V_f	Fluorescence voltage measured by photomultiplier tube	V
$V_{v'',v''}$	Vibrational relaxation rate in the lower electronic state	s ⁻¹
W_{l2}, W_{lu}	Stimulated absorption rate coefficient	s ⁻¹
W_{2l}, W_{ul}	Stimulated emission rate coefficient	s ⁻¹
W_{2i}, W_i	Photoionization rate coefficient	s ⁻¹
x	Mole fraction	--
Z	Mixture fraction	--

Greek Symbols

<u>Symbols</u>	<u>Description</u>	<u>Units</u>
β	Efficiency of the collection optics	--
$\delta()$	Absolute uncertainty (95% confidence limit)	--
$\Delta\nu_L$	Laser spectral FWHM	s ⁻¹
ε_f	Fluorescence emission	W/cm ³ · sr
$\varepsilon()$	Relative uncertainty (95% confidence limit)	--

<u>Symbols</u>	<u>Description</u>	<u>Units</u>
$\varepsilon(m_p)$	Relative uncertainty in calibration slope	--
Γ	Dimensionless spectral overlap integral	--
ν_f	Frequency of fluorescence transition	s ⁻¹
$\bar{\nu}_f$	Mean frequency of fluorescence transition	s ⁻¹
ϕ	Equivalence ratio	--
τ	Transmission	--
Ω_c	Solid angle of the collection optics	sr

Subscripts

<u>Symbols</u>	<u>Description</u>	<u>Units</u>
absolute	Actual NO concentration	--
back	Background signal	--
cal	Referenced to calibration flame	--
global	Referenced to the entire flame	--
h	Referenced to a particular height within the flame	--
j,m,k .. 1,2	Specific rovibronic level	--
l	Lower laser-coupled rovibronic level	--
LDI	LDI flame	--
net	Net value	--
NO	NO-based value	--
NO ₂	NO ₂ -based value	--
off	Off-line wavelength	--
on	On-line wavelength	--
P	Referenced to products	--
ppm	ppm-based measurement	--
rel, relative	NO concentration relative to the calibration flame	--
soot	Soot-based measurement	--

<u>Symbols</u>	<u>Description</u>	<u>Units</u>
u	Upper laser-coupled rovibronic level	--
undoped	Measurement taken with no NO doping	--

Superscripts

<u>Symbols</u>	<u>Description</u>	<u>Units</u>
'	Refers to upper rovibronic level	--
"	Refers to lower rovibronic level	--

ABSTRACT

Lean direct-injection (LDI) spray flames offer the possibility of reducing NO_x emissions from gas turbines by rapid mixing of the liquid fuel and air so as to drive the flame structure toward partially-premixed conditions. We consider the technical approaches required to utilize laser-induced fluorescence methods for quantitatively measuring NO concentrations in high-pressure LDI spray flames. In the progression from atmospheric to high-pressure measurements, the LIF method requires a shift from the saturated to the linear regime of fluorescence measurements. As such, we discuss quantitative, spatially resolved laser-saturated fluorescence (LSF), linear laser-induced fluorescence (LIF), and planar laser-induced fluorescence (PLIF) measurements of NO concentration in LDI spray flames.

Spatially-resolved LIF measurements of NO concentration (ppm) are reported for preheated, LDI spray flames at pressures of 2-5 atm. The spray is produced by a hollow-cone, pressure-atomized nozzle supplied with liquid heptane. NO is excited via the $Q_2(26.5)$ transition of the $\gamma(0,0)$ band. Detection is performed in a 2-nm region centered on the $\gamma(0,1)$ band. A complete scheme is developed by which quantitative NO concentrations in high-pressure LDI spray flames can be measured by applying linear LIF. NO is doped into the reactants and convected through the flame with no apparent destruction, thus allowing an NO fluorescence calibration to be taken inside the flame environment. The in-situ calibration scheme is validated by comparisons to a reference flame. Quantitative NO profiles are presented and analyzed so as to better understand the operation of lean-direct injectors for gas turbine combustors. Moreover, parametric studies are provided for variations in pressure, air-preheat temperature, and equivalence ratio. Similar parametric studies are performed for lean, premixed-prevaporized flames to permit comparisons to those for LDI flames.

Finally, PLIF is expanded to high pressure in an effort to quantify the detected fluorescence image for LDI flames. Success is achieved by correcting the PLIF calibration via a single-point LIF measurement. This procedure removes the influence of any preferential background that occurs in the PLIF detection window. In general, both the LIF and PLIF measurements verify that the LDI strategy could be used to reduce NO_x emissions in future gas turbine combustors.

1. INTRODUCTION

The drive to engineer more efficient gas-turbine combustors, while producing pollutant levels below the strict limits set by government regulations, has resulted in a vast body of research to improve our understanding of these complex devices. Nevertheless, continuing advances in experimentation and computational modeling are necessary to integrate the many aspects of gas-turbine combustion, including turbulence-chemistry interactions (Gupta *et al.*, 1997; Gupta *et al.*, 1991), pollutant production (Polifke *et al.*, 1996), fuel patternation (Locke *et al.*, 1998), and temperature distribution (Ghaffarpour, 1993). Much of this research is ultimately aimed at reducing NO_x emissions. Of the numerous possibilities to approach NO_x reduction, the utilization of swirl-based geometries provides excellent potential. In general, swirl is imparted to the combustion air via annular guide vanes or by upstream tangential air injection (see Fig. 1.1). The effect of swirl is to create a toroidal recirculation zone which, for non-premixed combustion, promotes more efficient fuel/air mixing and provides flame stabilization. For premixed combustion, recirculation produces a region of hot combustion products that aids in flame anchoring at either an upstream or downstream stagnation point (Yegian and Cheng, 1998).

Laser-induced fluorescence (LIF) and its variations are the predominant optical technique utilized over the past decade to make minor-species concentration measurements in laboratory flames. Laser-based diagnostic techniques such as LIF have undergone extensive development and refinement, and have achieved an ability to produce quantitative measurements of minor species, such as nitric oxide, with accuracies of $\pm 20\%$ and detection limits approaching 1 part-per-million (Reisel *et al.*, 1993).

This research has been designed to advance the diagnostic capabilities of the LIF technique and to utilize these advancements in spray flames that simulate real gas-turbine

conditions. The lean direct-injection (LDI) geometry of Figure 1.1 was selected as the primary burner of interest. In this configuration, the spray is produced by a hollow-cone, pressure-atomized nozzle and injected into swirling air that exits the burner, thus mixing the fuel and air fast enough to achieve partially-premixed conditions. This flame geometry is characterized by a toroidal recirculation zone that serves as the primary stability mechanism. We have utilized this geometry at high pressures (2-5 atm) to develop both LIF and planar-LIF techniques capable of quantitative measurements of NO concentrations [NO]. Recognizing that a primary competitor to the LDI configuration is the lean, premixed-prevaporized (LPP) burner (Fig. 1.2), we have modified the LDI geometry so that the fuel is injected upstream of the exit, thus producing a premixed, swirling flame. Similar LIF work is performed in this configuration so as to make comparisons with the LDI measurements.

In Chapter 2, we review relevant literature and the technical approach required to utilize laser-induced fluorescence (LIF) methods for quantitatively measuring [NO] in atmospheric LDI spray flames. In the progression from atmospheric to high-pressure measurements, the LIF method requires a shift from the saturated to the linear regime of fluorescence measurements. As such, we discuss quantitative, spatially resolved laser-saturated fluorescence (LSF), linear laser-induced fluorescence (LIF), and planar laser-induced fluorescence (PLIF) measurements of NO concentration in atmospheric, LDI spray flames.

The experimental apparatus used in performing the high-pressure measurements is presented in Chapter 3, with descriptions of the LIF and PLIF facilities. Chapter 4 presents the first quantitative LIF measurements of NO concentration obtained in an LDI burner at high pressure (2 atm). The technique developed for these measurements is subsequently utilized to characterize the operation of LDI spray flames at pressures up to 5 atm.

Chapter 5 presents a comprehensive mapping of the LDI spray flame at high pressures. The degree of uniformity inside the recirculation zone is exemplified by the results of this work. Quantitative radial NO profiles are presented at 2.09, 3.18, 4.27, and 5.35 atm and analyzed so as to better understand the operation of lean-direct injectors for

gas turbine combustors. Downstream NO measurements in the LDI flames indicate an overall pressure scaling corresponding to $P^{0.74}$. Chapter 6 continues with a parametric study of the 4.27-atm flame by varying the air-preheat temperature and the equivalence ratio. A unique correlation relating NO to ϕ^2 is reported and discussed. Chapter 7 then repeats these parametric studies in a lean, premixed-prevaporized flame to provide a comparison to the LDI investigation.

Chapter 8 reports planar laser-induced fluorescence (PLIF) measurements of [NO] for the 4.27-atm LDI spray flame. The feasibility of using PLIF in lieu of LIF is assessed with respect to measuring NO concentrations in high-pressure LDI spray flames. Excitation scans and calibration comparisons are performed to assess the background contribution for PLIF detection. Quantitative radial NO profiles measured by LIF are presented and analyzed so as to correct the PLIF measurements to within the accuracy bars of the LIF measurements via a single-point scaling of the PLIF image. Overall conclusions and recommendations for the continuation of this work to higher pressures are made in Chapter 9.

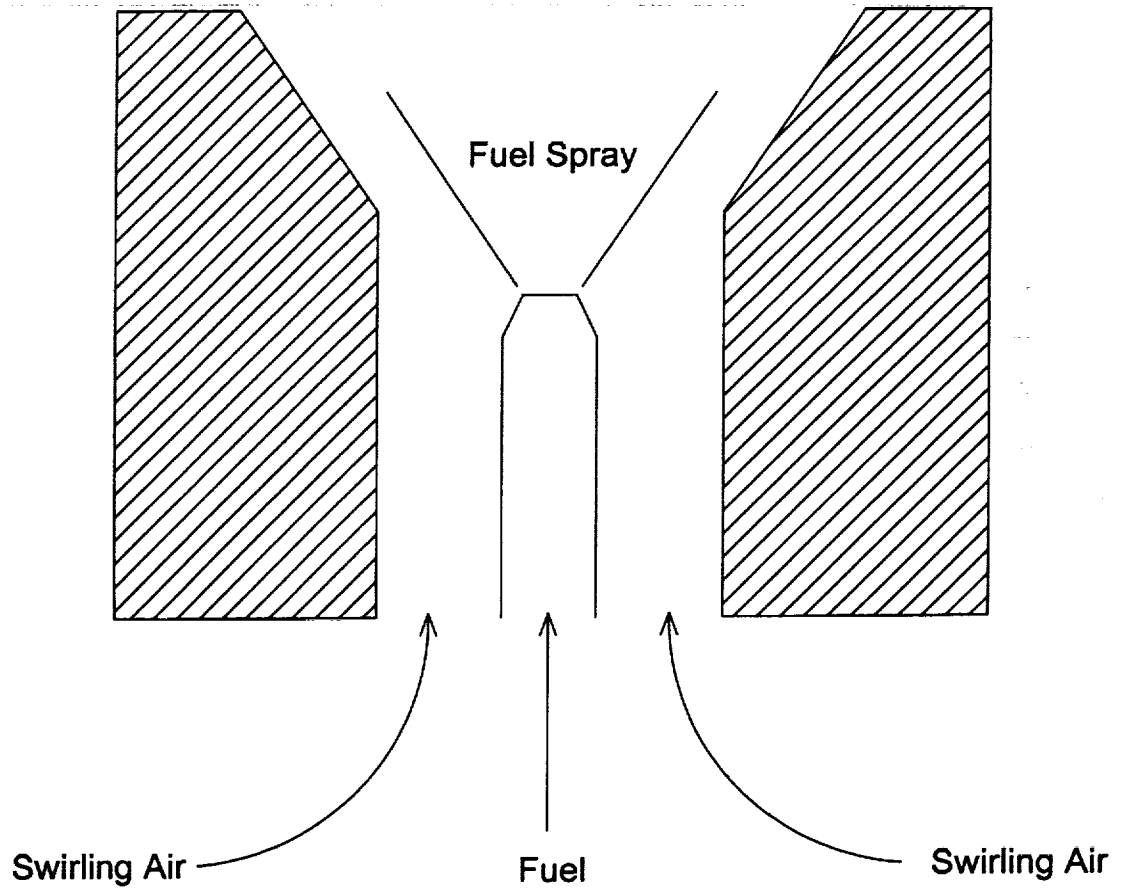


Figure 1.1: Generic lean direct-injection burner layout.

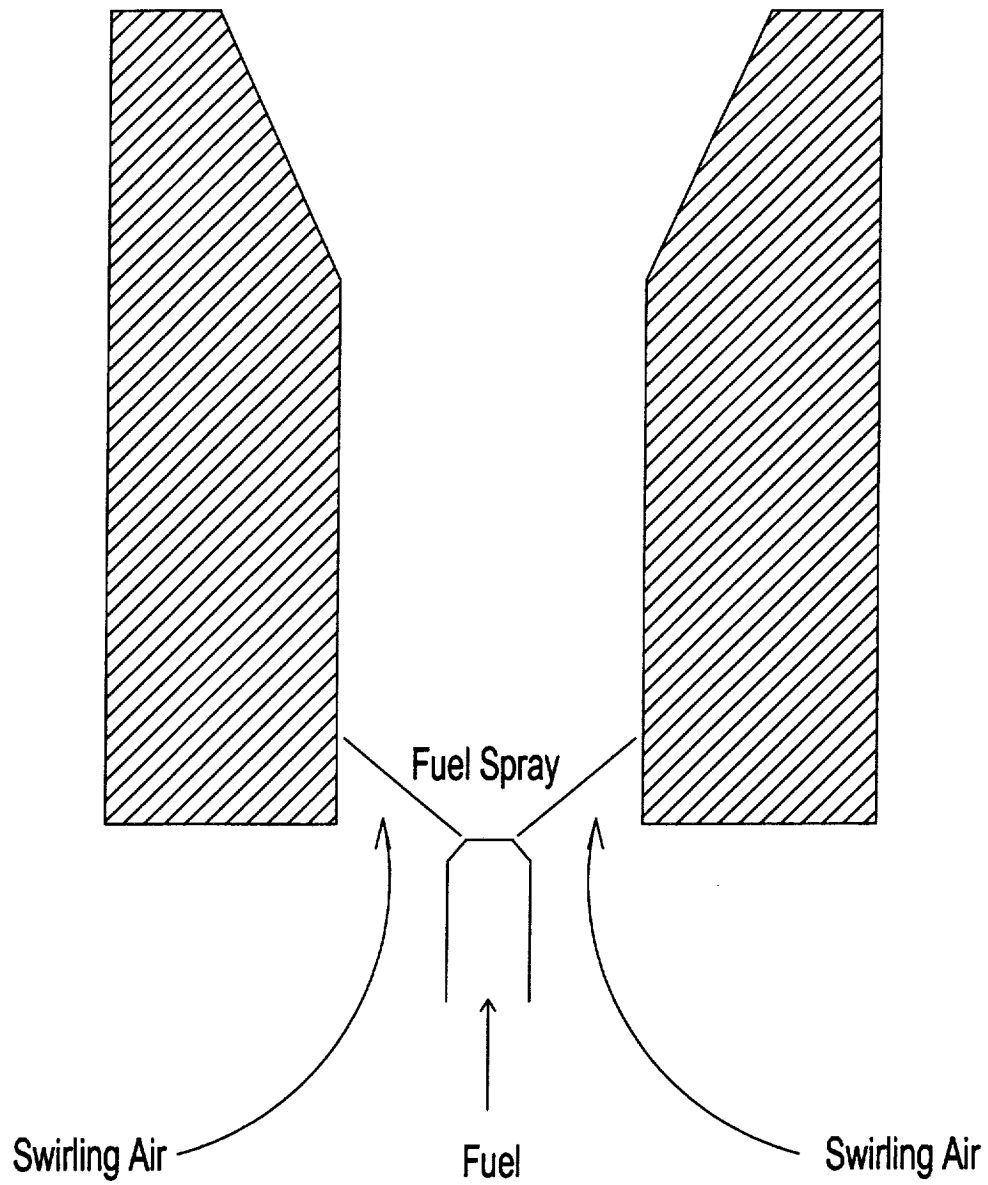


Figure 1.2: Generic lean premixed-prevaporized burner layout.

2. BACKGROUND AND PREVIOUS ATMOSPHERIC MEASUREMENTS

2.1 Introduction

The combustion diagnostics community has recently begun to focus its efforts toward practical combustion devices. One impetus behind this effort is the need to develop aeropropulsion gas turbine combustors with ultra-low NO_x emissions. For the past several years, the Flame Diagnostics Laboratory at Purdue University has been advancing optically non-intrusive techniques to measure concentrations of nitric oxide [NO] in lean direct-injection (LDI) spray flames. LDI flames offer the possibility of reducing NO_x emissions from gas turbines by rapid mixing of the liquid fuel and air so as to drive the flame structure toward partially premixed conditions. In this chapter, we review relevant literature and the technical approach required to utilize laser-induced fluorescence (LIF) methods for quantitatively measuring [NO] in atmospheric LDI spray flames. In the progression from atmospheric to high-pressure measurements, the LIF method requires a shift from the saturated to the linear regime of fluorescence measurements. As such, we discuss quantitative, spatially resolved laser-saturated fluorescence (LSF), linear laser-induced fluorescence (LIF), and planar laser-induced fluorescence (PLIF) measurements of NO concentration in atmospheric, LDI spray flames. In general, the results are comparable, although novel filtering techniques are required at higher flame pressures.

2.2 Background

With the onset of stringent NO_x emissions standards over the last few decades, the attention of the combustion diagnostics community has turned to quantitatively measuring NO concentrations in practical combustion devices. In particular, many

researchers have probed liquid-fueled spray flames to better understand the complex flowfields associated with this type of turbulent reactive flow. Structural experimentation has focused on velocity and temperature distributions so as to offer general insight and to aid in the development of numerical models for the flowfield. Lee and Chehroudi (1995), for example, investigated the structure of a swirling, hollow-cone spray flame similar to that occurring in the primary zone of a gas turbine combustor, though at atmospheric pressure. They proposed a mean spray structure based on measurements of the drop-size distribution and of the mean and rms values of the axial, radial, and tangential drop velocities. Similarly, Bulzan (1995) investigated a swirl-stabilized, pressure-atomized, liquid-spray flame by measuring both the gas- and liquid-phase velocity distributions, the drop-size distribution, and gas-phase temperature profiles.

Spray flames pose a particularly daunting challenge to diagnosticians who seek quantitative measurements of species concentrations. Inefficient atomization of the fuel can introduce very large Mie scattering interferences, particularly in the near-field spray region. Because of the large molecular weights of typical hydrocarbon fuels and fuel fragments, fluorescence from unburned hydrocarbons (UHC) and polycyclic aromatic hydrocarbons (PAH) often pose a challenge to selective detection of the spectral signature from those species of interest. Nevertheless, the most prominent optical method for *qualitatively* measuring species concentrations in spray flames has been planar laser-induced fluorescence (PLIF).

Allen *et al.* (1994) obtained qualitative PLIF images of OH concentration in a heptane-air spray flame burning over a pressure range of 0.1 to 0.8 MPa. They tested both solid and hollow-cone spray nozzles. In this work, the effect of interfering PAH fluorescence was assessed by using a spectrometer to spectrally separate the fluorescence into individual features. Hydroxyl excitation was achieved by employing the $P_1(8)$ transition at 285.67 nm. A laser-induced signal was discovered, exhibiting features at 350 nm, 400 nm, and 450 nm, but on a quasi-continuum background when operating at atmospheric pressure. The strength and spectral characteristics of this broad background were observed to be independent of excitation wavelength within a 5-nm region centered on the $P_1(8)$ transition, which indicates a broad absorbing species such as a heavy

hydrocarbon. As the pressure rose, the above spectral features became non-discernable and exhibited a P^2 increase in fluorescence strength.

In an extension of their 1994 work, Allen *et al.* (1995) performed similar [OH] imaging in ethanol flames and further assessed the effects of PAH interferences. With respect to NO measurements, Allen *et al.* (1995) proposed that excitation near 226 nm may produce more severe laser-attenuation and hence PAH fluorescence. To test this conjecture, Upshulte *et al.* (1996) obtained qualitative PLIF images of NO, O₂, and fuel vapor by employing excitation wavelengths of 226 nm and 308 nm. Measurements were made for ethanol fuel in the same high-pressure, spray-flame combustor used by Allen *et al.* (1994). As expected, a broad interference signal attributed to PAH was discovered and assigned to a nominal 5% of the NO signal at atmospheric pressure.

Locke *et al.* (1995) utilized PLIF with 282-nm excitation to image OH concentrations in a high-pressure (10-14 atm) combustor supplied with Jet-A fuel (0.59-0.83 kg/s) through lean direct-injection ($\phi=0.41-0.53$) with preheated air (811-866 K). Though this work only assessed the qualitative distribution of OH radicals in the reacting flow, the combustor was designed to simulate actual gas turbine conditions. The authors found that elastically scattered light and PAH fluorescence *were not evident* in the downstream regions of their direct injection combustor. This was a significant contribution to the combustion diagnostics community, as quantitative measurements at real-world conditions are an end goal of spray flame optical diagnostics, and the interferences mentioned are a severe limitation for many measurement environments.

While PLIF images offer significant information on the chosen flowfields, barriers to quantitative measurements have not been completely overcome by the current technology. Some of these barriers include (1) spatial variations in the electronic quenching rate coefficient, (2) interferences from other species owing to broadband detection, and (3) absorption of the laser sheet as it passes through the control volume. In an effort to make PLIF concentration images quantitative, Cooper *et al.* (1998) developed a procedure whereby qualitative PLIF images in spray flames can be scaled to a single laser-saturated fluorescence (LSF) measurement so as to make the images quantitative within the error bars of the more accurate LSF point data. The quantitative nature of the

LSF measurements arises from the fluorescence being nearly independent of both laser irradiance and the electronic quenching rate coefficient.

This chapter is concerned with the advancement of laser-induced fluorescence techniques for measuring NO in swirling, liquid-fueled spray flames incorporating a hollow-cone, pressure-atomized nozzle. The spray flame is based on the lean direct-injection (LDI) configuration, which is of current importance to gas turbine combustion. The end goal of this work is to develop a laser-induced fluorescence technique capable of measuring quantitative NO concentrations in LDI-based spray flames at high pressure. We begin by reviewing similar measurements at atmospheric pressure. We then use these results to suggest improvements for application to high-pressure spray flames, as pursued in later chapters.

2.3 Laser-Induced Fluorescence Methodology

Two distinct regimes exist by which to excite molecules via laser-induced fluorescence measurements (Laurendeau and Goldsmith, 1989). The first and most prominent technique is termed linear laser-induced fluorescence (typically referred to as LIF). In this regime the excited population and hence the fluorescence is directly proportional to the laser spectral irradiance and is inversely proportional to the electronic quenching rate coefficient. The limitation of this technique lies in its dependence upon the electronic quenching rate coefficient. Collisional quenching induces a non-radiative transition that directly reduces the excited-state population of the molecule and thus the fluorescence signal. LIF techniques generally require the transport of an NO fluorescence calibration from a reference flame into the flame of interest. However, this calibration procedure is acceptable only when both flames can be sufficiently modeled so as to estimate the electronic quenching rate coefficient, which depends on the local species composition, pressure, and temperature.

The second technique is termed laser-saturated fluorescence (LSF) and relies on pumping the population of the excited state toward the maximum population allowed by molecular dynamics. At this point, the excited population is essentially independent of

the laser power and the electronic quenching rate coefficient. This tactic allows the transport of an NO fluorescence calibration into flames that cannot be adequately modeled, such as the LDI flame used in this work. However, the large laser irradiances required can severely depopulate the ground rovibronic level so that repopulation by neighboring rotational levels through rotational energy transfer (RET) causes concern when attempting to model the molecular dynamic process. A simplified model that allows for RET population transfer is the balanced cross-rate model proposed by Lucht *et al.* (1980). In this model, the validity of the LSF technique rests on a balance between repopulation into the directly-excited ground rovibronic level and depopulation out of the directly-excited upper rovibronic level.

2.3.1 Two-Level Model

To introduce the dynamics associated with molecular LIF, it is instructive to consider a two-level model developed for many atomic species and a limited number of molecular species. Though not fully representative of molecular dynamics, the two-level approach will implicitly be assumed to model the molecular rovibronic levels in the ground and excited electronic states. A schematic of the rate processes involved in this model is illustrated in Figure 3.1.

Following the description of the two-level model detailed by Laurendeau and Goldsmith (1989), four assumptions are made:

1. The excitation beam is uniform and linearly polarized.
2. The entire population is assumed to be in level 1 prior to laser excitation, i.e. $N_1 + N_2 = N_1^*$.
3. The sampled fluorescence signal is measured at the temporal peak of the emissive pulse, for which the population in level 2 is at steady state.
4. The fluorescence signal consists of a single wavelength corresponding to the spontaneous emission from level 2 to level 1.

Based on the above assumptions, six rate processes are shown in Figure 2.1. These processes and their corresponding rate coefficients (s^{-1}) are: stimulated absorption (W_{12}),

stimulated emission (W_{21}), spontaneous emission (A_{21}), collisional quenching (Q_{21}), photoionization (W_{2i}), and predissociation (P). Photoionization and predissociation are shown for completeness and will be assumed negligible in the derivation that follows. Most excited states are not predissociative unless specifically chosen to be so, and photoionization can often be neglected for modest laser irradiances.

Considering the remaining four rate processes, rate equations for the upper and lower level populations can be written as

$$\frac{dN_1}{dt} = -N_1 W_{12} + N_2 (W_{21} + A_{21} + Q_{21}), \quad (2.1)$$

and

$$\frac{dN_2}{dt} = N_1 W_{12} - N_2 (W_{21} + A_{21} + Q_{21}). \quad (2.2)$$

Adding Eq. (2.1) and Eq. (2.2) yields

$$\frac{d(N_1 + N_2)}{dt} = 0, \quad (2.3)$$

which verifies assumption number two, namely that

$$N_1 + N_2 = N_1^0. \quad (2.4)$$

Before proceeding to solve for the upper population as a function of the initial population, we must expand the rate coefficient for stimulated absorption. Following Eckbreth (1996), we find that

$$W_{12} = \frac{B_{12}}{c} \int I_\nu(\nu) g(\nu) d\nu, \quad (2.5)$$

where B_{12} is the Einstein coefficient for stimulated absorption ($\text{m}^3/\text{J}\cdot\text{s}^2$), $I_\nu(\nu)$ is the laser spectral irradiance ($\text{W}/\text{m}^2\cdot\text{s}^{-1}$), and $g(\nu)$ is the absorption lineshape (s) which is defined so that

$$\int g(\nu) d\nu = 1. \quad (2.6)$$

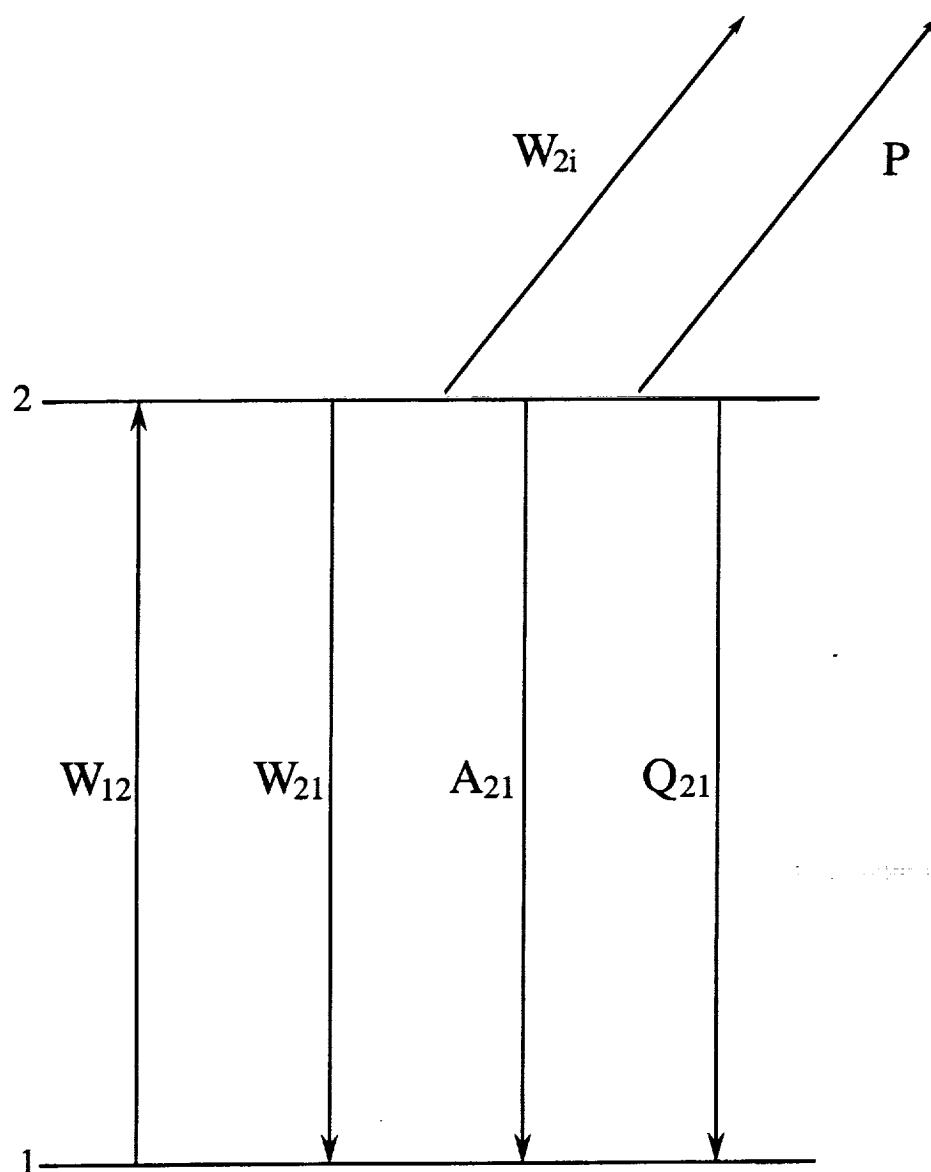


Figure 2.1: Schematic of two-level model for LIF. The rate coefficients shown are stimulated absorption (W_{12}), stimulated emission (W_{21}), spontaneous emission (A_{21}), collisional quenching (Q_{21}), photoionization (W_{2i}), and predissociation (P).

Thus, the excitation efficiency depends on the spectral overlap between the laser and absorption lineshape. Employing Partridge and Laurendeau's (1995) nomenclature, we define the laser spectral irradiance as

$$I_\nu(\nu) = I_\nu^* L(\nu), \quad (2.7)$$

where I_ν^* is the normalized laser spectral irradiance and $L(\nu)$ is the laser spectral distribution function which is normalized as

$$\int_{\nu} L(\nu) d\nu = \Delta\nu_L, \quad (2.8)$$

where $\Delta\nu_L$ is the laser spectral FWHM. The laser irradiance, I , is thus related to the laser spectral irradiance by

$$I = I_\nu^* \Delta\nu_L. \quad (2.9)$$

Using the above nomenclature, we find that the stimulated absorption coefficient becomes

$$W_{12} = \frac{B_{12}}{c} I_\nu^* \Gamma, \quad (2.10a)$$

where Γ is the dimensionless spectral overlap integral defined by

$$\Gamma = \int_{\nu} L(\nu) g(\nu) d\nu. \quad (2.11)$$

Similarly, for stimulated emission,

$$W_{21} = \frac{B_{21}}{c} I_\nu^* \Gamma, \quad (2.10b)$$

where the Einstein coefficients for stimulated absorption and emission are related to the degeneracies of the upper and lower levels (g_1 and g_2) by

$$g_1 B_{12} = g_2 B_{21}. \quad (2.12)$$

At the peak of the fluorescence pulse, for which the population in level 2 has reached steady state and $\dot{N}_2 = 0$, Eqs. (2.1) and (2.4) can be combined to yield

$$N_2 = N_1^* \frac{W_{12}}{W_{12} + W_{21}} \left[\frac{1}{1 + \frac{A_{21} + Q_{21}}{W_{12} + W_{21}}} \right]. \quad (2.13)$$

To more effectively relate the excited population to the laser power, we define

$$I_v^{sat} = \frac{A_{21} + Q_{21}}{B_{12} + B_{21}} c. \quad (2.14)$$

Employing Eq. (3.10), we can now manipulate Eq. (2.13) to yield

$$N_2 = N_1^o \frac{B_{12}}{B_{12} + B_{21}} \left[\frac{1}{1 + \frac{I_v^{sat}}{I_v^o \Gamma}} \right]. \quad (2.15)$$

At this point, we define two distinct regimes in which to make LIF measurements. The first regime requires that $I_v^o \Gamma \ll I_v^{sat}$, and is termed linear LIF owing to the linear dependence of the excited population on laser irradiance. The simplified expression from Eq. (2.15) is

$$N_2 = N_1^o \frac{B_{12}}{A_{21} + Q_{21}} \frac{I_v^o \Gamma}{c}. \quad (2.16)$$

Unfortunately, linear LIF depends on both the laser irradiance and the collisional quenching environment, which constitutes this method's limitations.

A second operating regime requires that $I_v^o \Gamma \gg I_v^{sat}$, which gives from Eq. (2.12)

$$N_2 = N_1^o \frac{g_2}{g_1 + g_2} \quad (2.17)$$

For this saturated LIF regime, the excited population is independent of both the laser irradiance and the collisional quenching rate coefficient, Q_{21} . This independence represents the advantage of laser-saturated fluorescence (LSF) over linear LIF. Often the collisional quenching environment is unknown and cannot be adequately modeled; therefore, linear LIF measurements would remain qualitative, whereas LSF measurements could be quantified in such environments. A theoretical plot of the normalized upper level population vs. normalized laser irradiance based on Eq. (2.15) is shown in Figure 2.2. Note the linear operating regime and the saturated operating regime. For comparison, an actual broadband fluorescence signal vs. laser irradiance curve (termed a "saturation curve") was measured in a lean ($\phi=0.8$), atmospheric, flat

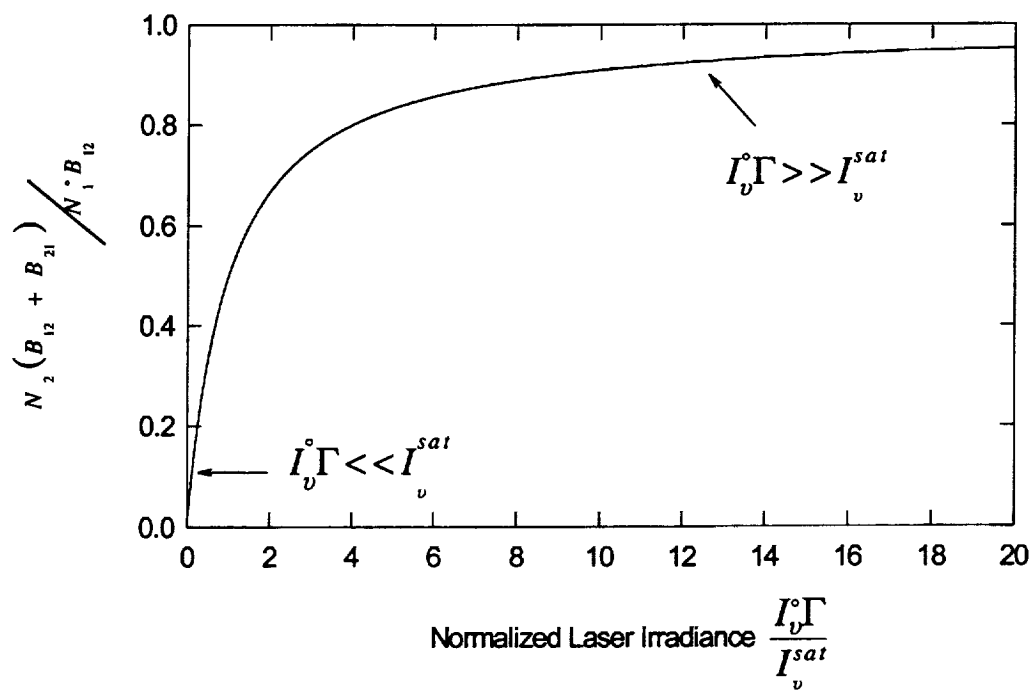


Figure 2.2: Theoretical plot of normalized upper level population vs. normalized laser irradiance based on Eq. (2.15).

$C_2H_6/O_2/N_2$ flame stabilized on a McKenna burner with a dilution ratio of 3.76 (see Fig. 2.3).

Returning to the nomenclature of Laurendeau and Goldsmith (1989), the fluorescence yield ϵ_f ($W/cm^3 \cdot sr$) is related to the population of the excited level via

$$\epsilon_f = \frac{h\nu_f A_{21}}{4\pi} N_2, \quad (2.18)$$

where ν_f (s^{-1}) represents the frequency at which the fluorescence occurs. For this two-level model, ν_f is equivalent to the excitation frequency. Molecular LIF often requires detection at a wavelength different from the excitation wavelength owing to Rayleigh and Mie scattering interferences. The fluorescence signal depends on both the collection optics and the detection scheme via

$$V_f = \beta G \Omega_c V_c \epsilon_f, \quad (2.19)$$

where V_f is the fluorescence voltage measured by the photomultiplier tube, β is the efficiency of the collection optics, G is the photomultiplier gain (V/W), Ω_c is the solid angle of the collection optics (sr), and V_c is the collection volume (cm^3). Utilizing Eqs. (2.18) and (2.19), and the expressions for N_2 via linear LIF or LSF in Eqs. (2.16) and (2.17), the resulting expressions for the measured fluorescence signal as a function of the initial population in the ground level are:

$$\text{LIF:} \quad V_f = (V_c N_1^*) \left[\frac{B_{12} I_\nu^* \Gamma}{(A_{21} + Q_{21})c} \right] (h\nu_f A_{21}) \left(\beta G \frac{\Omega_c}{4\pi} \right) \quad (2.20)$$

$$\text{LSF:} \quad V_f = (V_c N_1^*) \left[\frac{g_2}{g_1 + g_2} \right] (h\nu_f A_{21}) \left(\beta G \frac{\Omega_c}{4\pi} \right) \quad (2.21)$$

For either of the above expressions, the first set of parentheses represents the species population in the ground level available for excitation. The second set of parentheses represents the fraction of the ground level population excited to level two, while the third set represents the fluorescence emitted from the excited population. The fourth set represents the fraction of that fluorescence collected by the detection system.

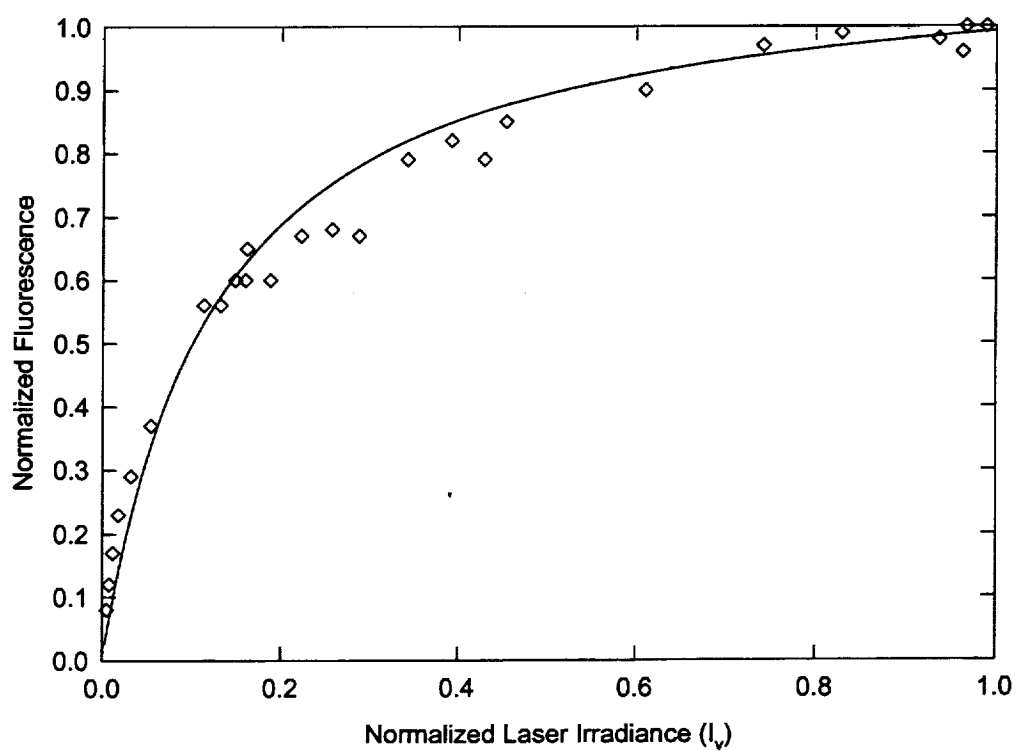


Figure 2.3 Saturation plot demonstrating the transition from linear to saturation excitation regimes.

2.3.2 Molecular Dynamic Model

The two-level model is an excellent tool to address the basic rate processes present in LIF dynamics. For most species of interest in combustion, however, the two-level model is not sufficiently accurate. Additional rate processes that must be accounted for in a complete molecular dynamics model include the depopulation of the directly excited level via rotational energy transfer (RET), vibrational energy transfer (VET), and photoionization. Another advantage of the molecular dynamic approach lies in its ability to model not one, but numerous rovibronic transitions from numerous excited levels. Carter *et al.* (1987) assessed the influence of these effects on the LIF dynamics of OH at high pressure, while Reisel *et al.* (1993) performed a similar analysis for NO at atmospheric pressure.

A schematic of the rate processes involved is illustrated in Figure 2.4. As shown, the upper and lower laser-coupled rovibronic levels are labeled u and l , respectively. Vibrational quantum numbers in the upper and lower electronic state are labeled v' and v'' , respectively. Specific rotational levels in the excited and ground electronic state are indicated as j and k , respectively. The rate processes of concern and their respective rate coefficients are stimulated absorption (W_{lu}), stimulated emission (W_{ul}), spontaneous emission ($A_{j,k}$), electronic quenching ($Q_{j,k}$), vibrational relaxation ($V_{v'',v''}$), rotational relaxation ($R_{j,k}$), and photoionization (W_i). For reasons to be discussed, vibrational relaxation is only considered in the ground electronic state. Electronic quenching, vibrational relaxation and rotational relaxation are similar in that these processes involve collisional transfer of energy with another molecule.

This molecular LIF model contains numerous paths for energy transfer not available in the two-level model. Once a molecule is excited into an upper rovibronic level, five paths are available for energy transfer. The first path is that of photoionization. The second path is that of spontaneous emission through all available rovibronic transitions to lower energy levels, labeled globally as $A_{0,0}$, $A_{0,1}$, $A_{0,2}$, and $A_{0,3}$ for transitions between the upper $v'=0$ state to the various vibrational levels in the ground electronic state. The third path, electronic quenching, involves collisional transfer of energy and subsequent reversion to the ground electronic state without emission of

radiation. The fourth and fifth paths, vibrational and rotational relaxation, also involve collisional transfer of energy, and tend to statistically populate the upper and lower rovibronic manifolds in a process termed “thermalization.” Thermalization of a manifold involves both vibrational and rotational relaxation paths which force the molecular population toward a statistical Boltzmann distribution based on the environmental conditions of the molecular species. Upward vibrational relaxation is much less likely on a statistical basis; hence, vibrational relaxation is not presented in the upper electronic state shown in Figure 2.4 since the $v'=0$ level is typically used for the excitation transition. Typical detection of NO fluorescence occurs in the $v''=1$ level of the ground electronic state, and vibrational relaxation is included here for completeness.

The cascade of fluorescence from the numerous excited rovibronic levels, which are coupled with the directly excited level u through rotational relaxation, permits detection of a vibrational band of fluorescence (Reisel *et al.*, 1993; Carter and Laurendeau, 1994), as opposed to a single transition as in the two-level model. This technique, termed broadband LIF, provides a much larger fluorescence signal, but can allow interferences from other species owing to its larger detection window. Photoionization of a molecule has the effect of depleting the excited rovibronic level and its contribution must be assessed for use in the molecular LIF model. Reisel *et al.* (1993) showed the photoionization rate to be comparable to the electronic quenching rate for saturated LIF studies of NO at atmospheric pressure. For linear LIF studies, however, photoionization need not be considered owing to the very low laser irradiance.

Following the procedure of the two-level model and the work detailed by Reisel *et al.* (1993), we begin by invoking the rate equations for the directly excited upper level and the rotationally coupled upper levels:

$$\frac{dN_u}{dt} = N_l W_{lu} - N_u \left\{ W_{ul} + W_i + \sum_k Q_{u,k} + \sum_k A_{u,k} \right\} - \sum_{j \neq u} N_u R_{u,j} + \sum_{j \neq u} N_j R_{j,u}, \quad (2.22)$$

and

$$\frac{dN_j}{dt} = \sum_{m \neq j} \{ N_m R_{m,j} - N_j R_{j,m} \} - N_j \left\{ \sum_k Q_{j,k} + \sum_k A_{j,k} \right\}. \quad (2.23)$$

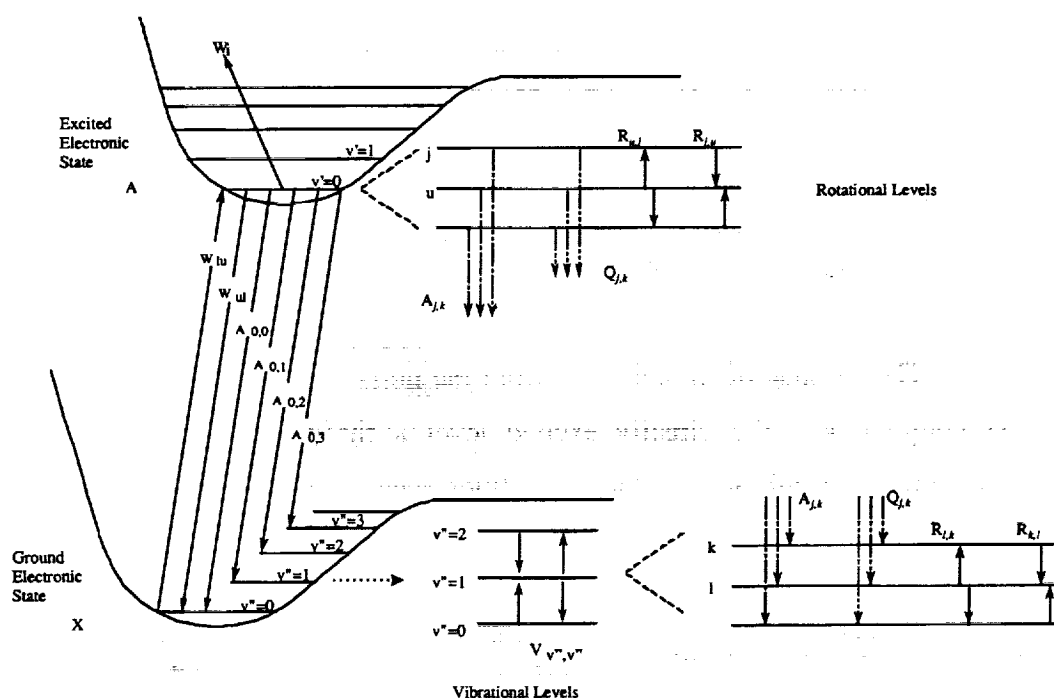


Figure 2.4: Schematic of molecular dynamic model for LIF. The upper and lower laser-coupled rovibronic levels are labeled u and l , respectively. Vibrational quantum numbers in the upper and lower electronic state are labeled as v' and v'' , respectively. Specific rotational levels in the excited and ground electronic state are indicated as j and k , respectively. The rate processes of concern and their respective rate coefficients are stimulated absorption (W_{lu}), stimulated emission (W_{ul}), spontaneous emission ($A_{j,k}$), electronic quenching ($Q_{j,k}$), vibrational relaxation ($V_{v'',v''}$), rotational relaxation ($R_{j,k}$), and photoionization (W_i).

To successfully make LIF measurements, the excited population in the upper rotational manifold, including the directly excited level and the rotationally coupled levels, must reach a steady-state distribution. We assume that the directly excited population, N_u , is approximately constant at the peak of the fluorescence pulse and that no significant depletion occurs in the laser-coupled levels. Since the rate coefficient for spontaneous emission is much smaller than that for electronic quenching, the influence of spontaneous emission can be neglected in Eq. (2.23). Solving the differential rate equation (2.23) then yields

$$N_j(t) = \frac{a(1 - e^{-bt})}{b}, \quad (2.24)$$

where the constants are defined as

$$a = \sum_{m \neq j} N_m R_{m,j} \quad (2.24a)$$

and

$$b = \sum_k Q_{j,k} + \sum_{m \neq j} R_{j,m}. \quad (2.24b)$$

Therefore, when $bt \geq 2.5$, $N_j(t)$ is within 10% of its steady-state population. The total rotational relaxation rate, $\sum_{m \neq j} R_{j,m}$, from a given level of NO at atmospheric flame conditions is on the order of 10^9 s^{-1} (Mallard *et al.*, 1982), which results in a response time for an individual rovibronic level on the order of 1 ns or less. Hence, during a typical 7-ns laser pulse, the entire upper rotational manifold should be approaching steady state.

Therefore, assuming steady state of the upper rotational manifold population at the peak of the emissive pulse, we derive the following expressions for the number density of the directly excited level and the rotationally coupled levels:

$$N_u = \frac{N_i W_{lu} + \sum_{j \neq u} N_j R_{j,u}}{W_{ul} + W_i + \sum_k Q_{u,k} + \sum_k A_{u,k} + \sum_{j \neq u} R_{u,j}}, \quad (2.25)$$

and

$$N_j = \frac{\sum_{m \neq j} N_m R_{m,j}}{\sum_k Q_{j,k} + \sum_k A_{j,k} + \sum_{m \neq j} R_{j,m}}. \quad (2.26)$$

For broadband LIF, the fluorescence from each of these transitions can be collected simultaneously. Through use of Eqs. (2.18) and (2.19), the overall broadband fluorescence signal will be

$$V_f = \beta G \left(\frac{\Omega_c}{4\pi} \right) (h \bar{\nu}_f V_c) \left\{ A_{u,k} N_u + \sum_{j \neq u} A_{j,k} N_j \right\}, \quad (2.27)$$

where $\bar{\nu}_f$ is the mean frequency (s^{-1}) of the fluorescence transition. Though the above derivation does not specifically address the influence of rotational energy transfer on either linear or saturated LIF, it does reveal the advantage of broadband LIF, namely more signal when compared to detection of a single transition.

2.3.3 Utilization of Laser-Induced Fluorescence

The atmospheric-pressure study presented here provides a step toward high-pressure measurements by assessing the advantages and disadvantages of the three common LIF-based techniques: laser-saturated fluorescence (LSF), linear laser-induced fluorescence (LIF), and planar laser-induced fluorescence (PLIF). The first two, LSF and LIF, are spatially and spectrally resolved *narrowband* measurements which utilize a monochromator to spectrally filter the fluorescence. The probe volume is defined by the projection of the limiting aperture in the detection optics onto the laser beam. The last technique, PLIF, is a spectrally *broadband* measurement which employs an ICCD camera with a filter set that typically has a wide spectral detection window and therefore cannot selectively detect the fluorescence of a single species. PLIF measurements capture a complete 2-D image of the fluorescence induced by the laser sheet as it transverses the flame. Pressure-broadening of the absorption transition will mandate the use of a linear technique at high pressure. As such, the atmospheric study was designed to determine the ability of the linear techniques to quantitatively measure NO concentration. In

addition, consideration must be given to spectral studies so as to avoid detection of rogue species. Such studies must assess both scattering and fluorescence interferences that are often present in the harsh environment of a spray flame.

2.4 Experimental Apparatus

2.4.1 Optical System

The requisite UV radiation for NO excitation was produced using a Quanta-Ray GCR-4 Nd:YAG laser, a PDL-3 dye laser, and a WEX-2C wavelength extender. The Nd:YAG laser incorporated an injection seeder (model 6300) to force a single longitudinal mode in the laser cavity, which produces a fundamental output vertically-polarized at 1064 nm. The Nd:YAG fundamental was then frequency doubled (532 nm) via angle-tuned, type II phase matching in a temperature-stabilized KD*P (KD_2PO_4) crystal housed in a harmonic generator (model HG-II). The resulting horizontally-polarized, 532-nm beam and concentric, vertically-polarized, 1064-nm beam were spatially separated via a dichroic harmonic separator (model DHS-2) by employing two dichroic mirrors centered at 532 nm. The ensuing vertically-polarized, Nd:YAG second harmonic was used to pump a tunable dye laser (model PDL-3). Pyrromethene 580 dye (Partridge and Laurendeau, 1994) was dissolved in 100% ethanol and employed in both the oscillator and amplifier stages with concentrations of 8.6×10^{-4} M and 1.2×10^{-4} M, respectively. The PDL oscillator grating drive was modified and interfaced to a 100-to-1 gear reducer and a 200 step-per-revolution stepper motor that provided a spectral resolution of 4.8×10^{-5} nm/step in the PDL fundamental (574 nm).

The vertically-polarized dye fundamental was then frequency doubled (287 nm) via angle-tuned, type I phase matching within a KD*P crystal housed in the CM-1 module of a WEX-2C wavelength extender. The residual vertically-polarized Nd:YAG fundamental from the HG-II harmonic generator was frequency mixed with the dye second harmonic via angle-tuned, type I phase matching within a KD*P crystal housed in the CM-2 module of the WEX-2C. This frequency mixing process yields an excitation

wavelength of ~ 226 nm. The excitation beam was spatially separated from the residual concentric beams (1064, 574, 287 nm) via a Pellin-Broca prism and exited the WEX-2C in a vertically-polarized state. In addition, a Fabry-Perot wavelength stabilization system operating at 572 nm was used to control PDL drift (Cooper and Laurendeau, 1997a).

The optical elements common to both the LSF and LIF experiments are shown schematically in Figure 2.5. The UV radiation exited the WEX-2C vertically polarized and was steered using dichroic mirror M1 (CVI model KRF-1037-0). The maximum beam energy at this point was ~ 7 mJ/pulse. A filter stack (FS1) was used as a gross attenuator, while a Rochon Prism (RP) was used for fine attenuation of the beam power. Apertures A1 and A2 were used to block scattering and reflections from optical surfaces. Additionally, aperture A2 limited the diameter of the laser input to the spherical lens, SL1, to ~ 6 mm. A 1000-mm focal length, fused-silica lens (Newport model SPX034), SL1, was used to focus the laser beam into the probe volume. Fused-silica splitter plates SP1 and SP2 were used to split off $\sim 10\%$ of the beam for power monitoring via photodiodes PD:A and PD:B. A fused-silica right angle prism (CVI model RAP-050-UV) was used to direct the beam over the burner. Aperture A3 was positioned prior to the burner and was used to eliminate forward scattering and off-axis focusing in the probe volume. For the LSF experiments, FS1 and RP were removed since attenuation of the beam power was not necessary.

A portion of the isotropic fluorescence emitted from the NO molecules in the probe volume was captured and collimated by a 50-mm diameter, 254-mm focal length, fused silica spherical lens (CVI model PLCX-50.8-130.8-UV) which is labeled SL2 in Figure 2.5. To raise the collimated beam vertically to the monochromator entrance slit height, we used an image rotator, IR, and a 76-mm diameter mirror, M2 (CVI model PAUV-PM-3050-C). The image rotator consisted of two mirrors identical to M2, which rotated the probe volume image so that it was aligned parallel to the vertical entrance slit of the monochromator. A second lens SL3, identical to SL2, was used to focus the fluorescence onto the monochromator entrance slit.

The above collection optics layout produced a magnification of unity and an f-number ($f/\#$) of $f/5.9$. The unity magnification resulted in a probe volume that is the

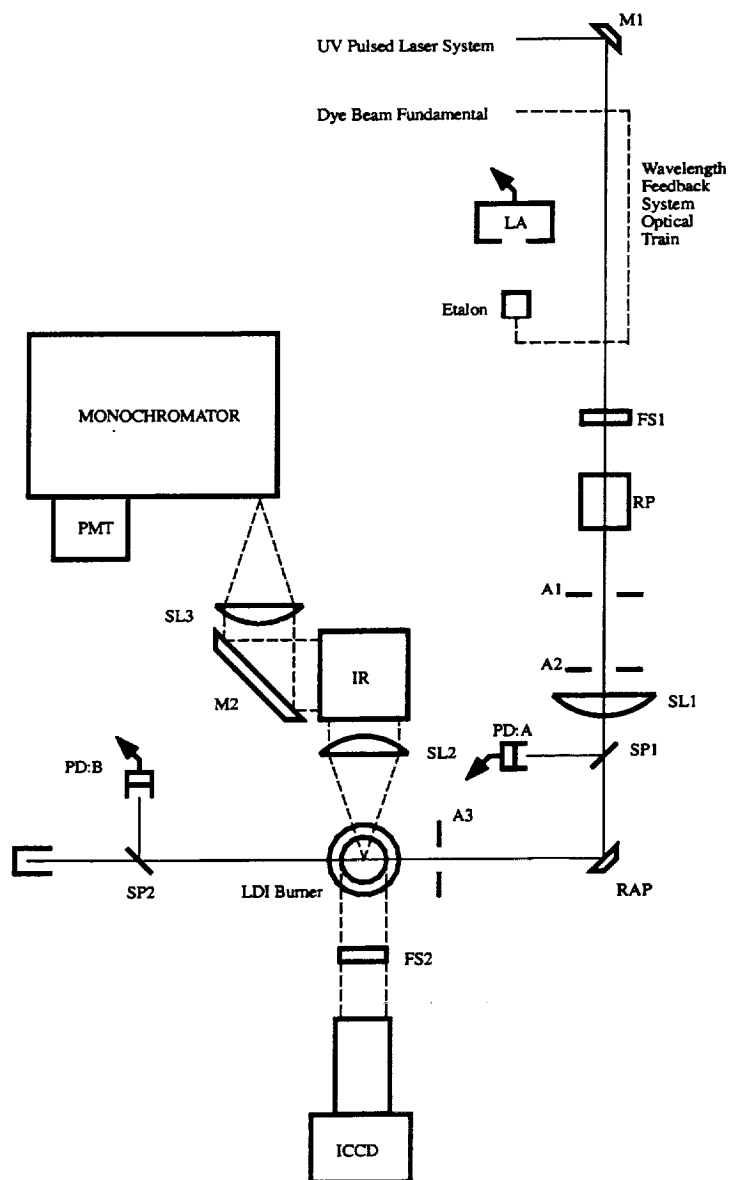


Figure 2.5: Schematic diagram of the experimental apparatus: M: mirror, FS: filter stack, RP: Rochon prism, A: aperture, SL: spherical lens, SP: splitter plate, PD: photodiode, IR: image rotator, LA: linear array, RAP: right angle prism.

projection of the monochromator entrance slit over the laser beam axis. To optimize both the throughput and the theoretical spectral resolution of the monochromator, the collection optics were configured such that the $f/\#$ closely matched that of the monochromator. The collection optics were limited to $f/5.9$, whereas the monochromator $f/\#$ was $f/6.0$.

The fluorescence from NO and other interfering species was spectrally filtered using a SPEX model 1700 $\frac{3}{4}$ -m monochromator. The entrance slit included a vertically positioned, stepped diaphragm (2, 5, and 10 mm tall) and three Hartmann diaphragm settings (1 mm tall) to limit the projected collection volume along the axis of the laser beam. A 110-mm \times 110-mm, 1200 groove/mm holographic grating with a 250-nm blaze angle was used in first order to provide a dispersion of 1.1 nm/mm. The monochromator grating drive incorporated a 50-to-1 gear reducer and a 200 step-per-revolution stepper motor to provide a minimum spectral resolution of $\sim 3 \times 10^{-4}$ nm/step.

The entrance slit settings were adjusted depending on the type of experiment performed. For the LSF experiments, the entrance slit was 68- μ m wide and 1-mm tall (Hartmann setting no. 2). This setting defined a cross-sectional area 68- μ m wide along the diameter of the laser beam and 1-mm long along the axis of the laser beam. For an ~ 240 - μ m beam waist, this slit setting spatially integrated only the center $\sim 26\%$ of the beam, thus avoiding linear fluorescence along the wings of the laser beam. However, the collection scheme was still sensitive to depth-of-field wing effects (Reisel *et al.*, 1993; Carter *et al.*, 1992). For the LIF experiments, the entrance slit width was opened to match the beam waist. In this manner, the entire spatial fluorescence was captured which ensured the inclusion of the linear wings, thus minimizing the focused portion along the centerline which could tend toward partial saturation.

The exit slit width was set to 1.818 mm, thus defining an integrated spectral region of ~ 2 nm FWHM in the LSF and LIF experiments. This setting was chosen based on extensive work by previous researchers (Reisel *et al.*, 1993; Partridge *et al.*, 1996). The detection sensor is a photomultiplier tube (Hamamatsu model R106UH-HA) wired for fast temporal response (Harris *et al.*, 1976).

For the PLIF experiments, a laser sheet, $\sim 550\text{ }\mu\text{m}$ wide by 18 mm tall, is generated via a cylindrical lens (Newport model SPX034) used in place of SL1, and passed through the probe volume for NO excitation. A Princeton Instruments model ICCD-576TC-RG proximity focused ICCD detector incorporating a 578×384 pixel, charge-coupled device (CCD) (Thomson model CSF 7883) with $23\text{-}\mu\text{m}$ square pixels was utilized for detection of the NO fluorescence. The fluorescence was focused on the ICCD detector by utilizing an aberration-corrected, five fused-silica element, UV-Micro-Nikkor, 105-mm focal-length $f/4.5$ lens (Nikon Corp., Melville, NY), such that each pixel corresponds to a $77\text{-}\mu\text{m}$ square in the image plane of the flame. A filter set (FS2) consisting of a wide-band interference filter (92-nm FWHM) spectrally centered at 250 nm (Acton model 250-W-2S), and coupled with 6 mm of a UG5 CG filter, was used to reduce the Mie scattering from the liquid droplets. This filter scheme was selected based on previous work (Partridge *et al.*, 1996) and provides an $\sim 70\text{-nm}$ FWHM spectral window with a peak transmission at 270 nm.

An ICCD thermoelectric cooler was used in conjunction with an external water chiller/circulator (Lauda model RMT-6, Brinkman Instruments) to reduce the temperature of the ICCD to -32°C . A pulse generator (Princeton Instruments model FG-100) was used to produce a gate of 30 ns to the ICCD. Operation of the ICCD and supporting hardware was effected by a detector/controller (Princeton Instruments model ST-130). The user interface to the ICCD system was provided by CSMA software (version 2.3A, Princeton Instruments), which was also used for all image analysis and reduction.

2.4.2 LDI burner

The burner utilized here is based on a lean-direct injection (LDI) design and typifies that used in the primary zone of advanced gas turbine combustors. The stainless steel LDI module ($16.5\text{ cm} \times 3.8\text{ cm}$ dia.) accommodates a fuel tube (6.4 mm dia.) that enters the module co-axially at the bottom (see Fig. 2.6). For operation at atmospheric pressure, a 60° helical swirler (22.9 mm dia.) is mounted at the top of the fuel delivery tube. The swirler itself is tapped to allow a Delavan 6-mm peanut nozzle (Flow# = 0.4)

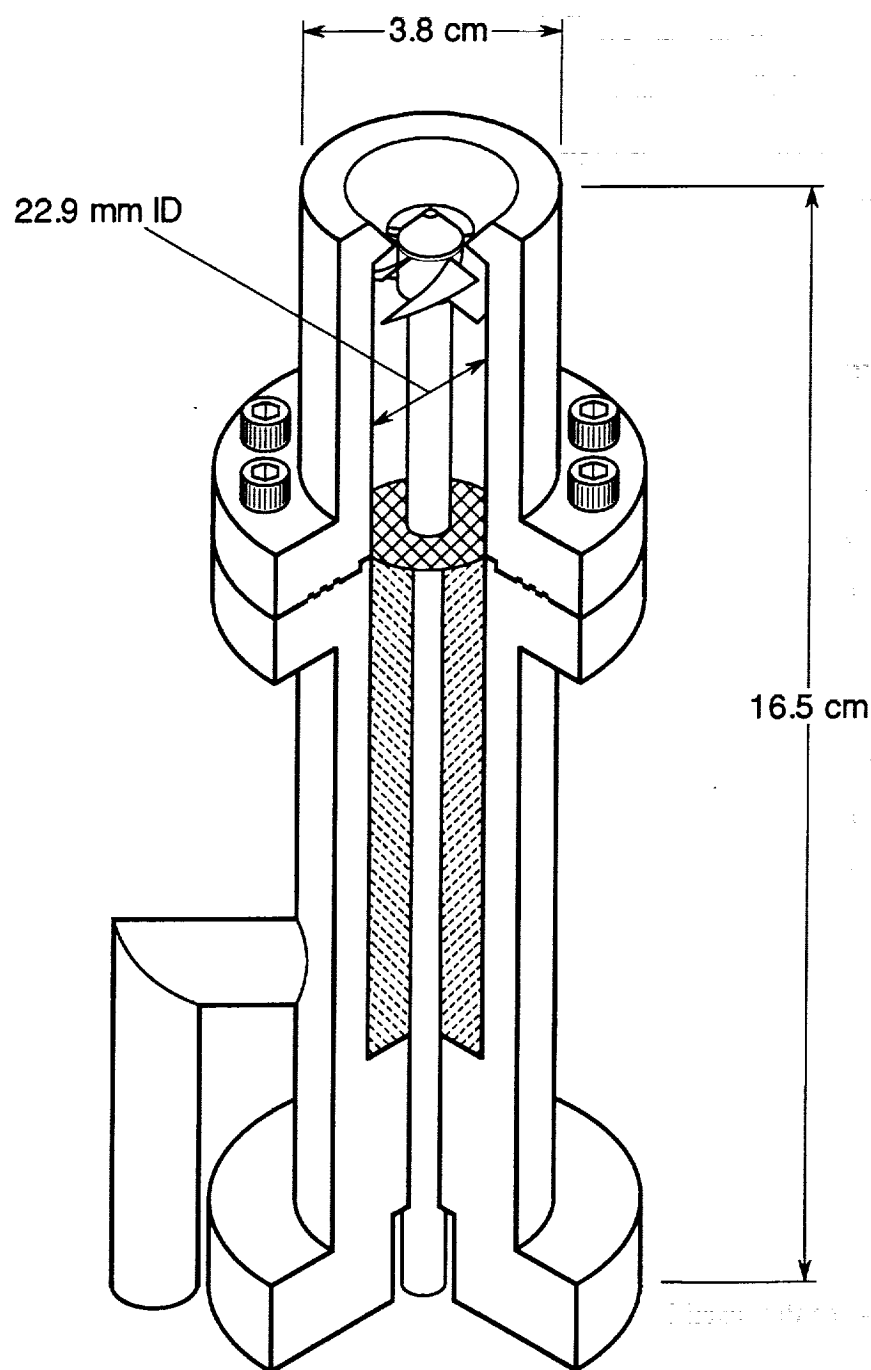


Figure 2.6: Schematic of atmospheric LDI burner.

with a 62° spray cone to be directly threaded into the swirler. The nozzle is positioned vertically relative to the converging/diverging orifice (12.7 mm dia. at 40°). The depth of the nozzle below this orifice is adjustable via a slide-through fitting located at the bottom of the module. The air is preheated to 475 K, delivered perpendicular to the module axis, and passed through packed glass beads (~ 1.5 mm dia.) that fill the module cavity (22.9 mm dia.). The glass beads ensure purely vertical flow of the air entering the air swirler.

The swirling motion of the air imparted by the helical vanes in this type of burner will affect the combustion efficiency, temperature distribution, and exhaust species concentrations (Jones and Wilhelmi, 1989). Rink and Lefebvre (1989) have performed a study of the effect of general spray characteristics on NO formation and have shown that NO_x emissions depend on inlet air temperature, combustion pressure, fuel H/C ratio, and atomization quality. The drop size, which affects combustion efficiency, depends strongly on the axial and radial flow velocities, but is apparently independent of the azimuthal velocity (McDonnell *et al.*, 1992).

For the work presented here, the LDI burner was operated at an overall equivalence ratio of unity, based on mass inputs to the burner. Since the flame is unconfined, entrained air will lower the effective equivalence ratio. This operating point was chosen for our initial atmospheric measurements to provide ample NO and thus enhanced fluorescence signals to the detection systems. At higher pressures, leaner overall equivalence ratios are considered, as detailed in Chapters 5 and 6.

2.5 Experimental Approach at Atmospheric Pressure

2.5.1 Spectroscopic Considerations

Previous work in our laboratory has shown considerable success when performing quantitative narrowband NO concentration measurements in a variety of flames (Reisel and Laurendeau, 1995; Thomsen *et al.*, 1997; Cooper and Laurendeau, 1997b). Typically, excitation of the $Q_2(26.5)$ line of the $\gamma(0,0)$ vibrational band of NO at 225.58 nm is followed by detection of the $\gamma(0,1)$ vibrational band with a 2-nm window centered

at 235.78 nm. This combination has been selected based on extensive interference and background investigations (Reisel *et al.*, 1993; Partridge *et al.*, 1996). To facilitate use of this excitation/detection scheme in a liquid droplet environment, we must consider the possible effects of Mie scattering interference, fuel and fuel-fragment fluorescence, and laser beam extinction. Fortunately, extinction in our LDI flame is minimal, with a maximum of 7% attenuation of the beam at the 2.5-mm axial height.

2.5.2 Mie Scattering Profiles

Dense droplet regions in spray flames often pose the greatest challenge to selectively detecting minor species. The large laser irradiances employed for the saturated-LIF technique exacerbate Mie-scattering breakthrough in monochromators since the NO signal saturates while that for Mie scattering remains linearly proportional to laser power. In our case, the narrowband detection window is shifted only ~10 nm from the excitation wavelength. Because of this small shift, the NO fluorescence is superimposed on a background largely comprised of Mie scattering from dense droplet regions. These locations also offer possible fluorescence from fuel, fuel fragments, and unburned hydrocarbons (UHC). In particular, when measuring NO fluorescence using a broadband PLIF system, fluorescence must be considered from polycyclic aromatic hydrocarbons (PAH). An effective means to locate those regions in spray flames that are densely packed with droplets is to measure scattering profiles. Scattered light at the incident laser wavelength is passed through neutral density filters and collected via the $\frac{3}{4}$ -m monochromator in a 2-nm window centered at ~226 nm. Figure 2.7 indicates the strong Mie scattering that occurs along the spray, especially at lower heights above the burner. As expected, very little interference is present along the centerline since the burner incorporates a hollow-cone spray nozzle.

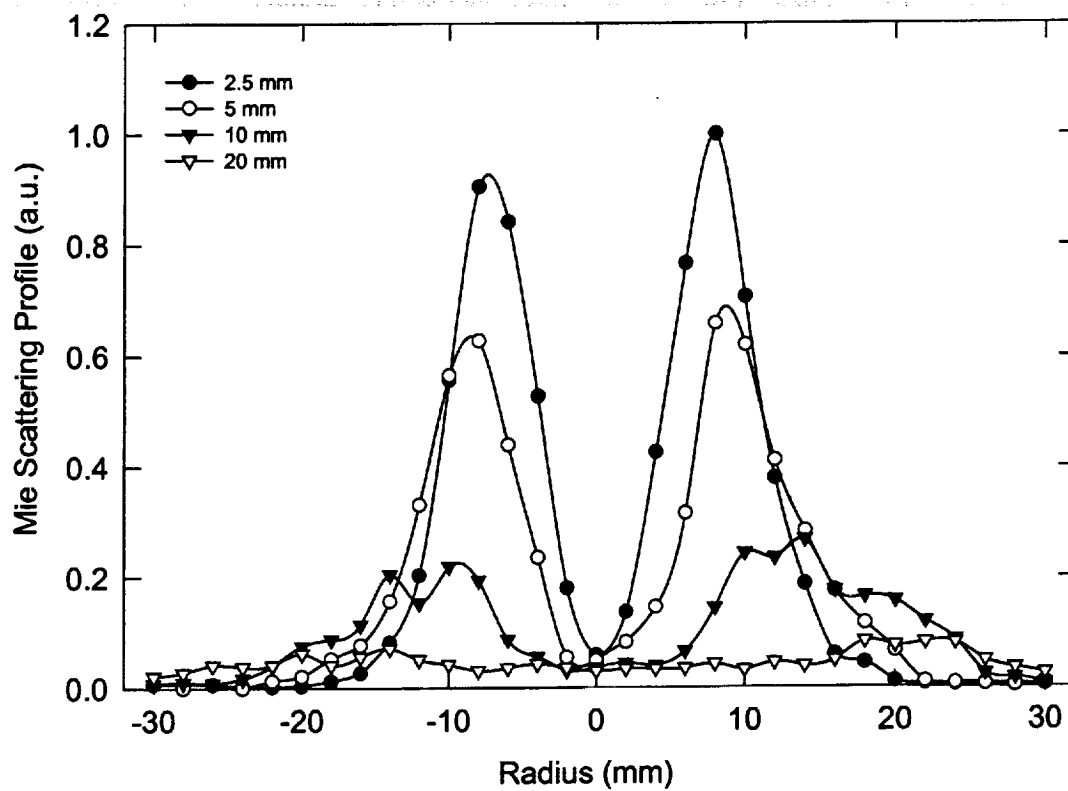


Figure 2.7: Mie scattering radial profiles for atmospheric LDI flame at four axial heights.

2.5.3 Narrowband Excitation Scans

Quantitative NO measurements in spray flames require a background correction procedure to account for Mie scattering and fluorescence interferences from other species. Previously, Allen *et al.* (1995) utilized an off-resonance/on-resonance excitation scheme to investigate fluorescence interferences in PLIF measurements of OH concentration. For our flames, an "off-line" excitation wavelength can be identified that offers little to no spectral signature from NO and other species in our detection window. As a comparative standard for spectral work within the LDI flame, an excitation scan was obtained in the post-flame region of a lean ($\phi=0.8$), atmospheric $C_2H_6/O_2/N_2/NO$ flame stabilized on a water-cooled McKenna burner (3.76 dilution ratio) with 80-ppm of doped NO (Fig. 2.8). In this excitation scan, detection occurs by using a fixed 2-nm window centered at 235.78 nm, i.e., within the $\gamma(0,1)$ band of NO. Similarly, an excitation scan taken at $h = 5$ mm, $r = 3$ mm in the LDI flame is shown and scaled to the reference signal level at the 225.58-nm excitation wavelength. Note the overall baseline offset caused by Mie scattering and the similarity of the spectra, indicating that other species such as unburned hydrocarbons and polycyclic aromatic hydrocarbons are apparently not observable within the 2-nm narrowband detection window. On this basis, the off-line location chosen to account for Mie scattering is labeled near 225.53 nm.

2.5.4 Narrowband Detection Scans

The next step in validating the off-line wavelength subtraction method requires that narrowband detection scans be performed with excitation provided at both the on-line resonant NO wavelength and the off-line non-resonant wavelength. These experiments assess possible NO and hydrocarbon excitations which might occur within the $\gamma(0,1)$ band of NO. To assess the actual excitation of NO occurring at the off-line wavelength, detection scans in the previously mentioned McKenna burner were obtained using the off-line location. The results showed ~5% excitation of the $\gamma(0,1)$ band of NO relative to the on-line excitation signal. Although this influence is undesirable, a 5% resonant signal can easily be accounted for in data processing.

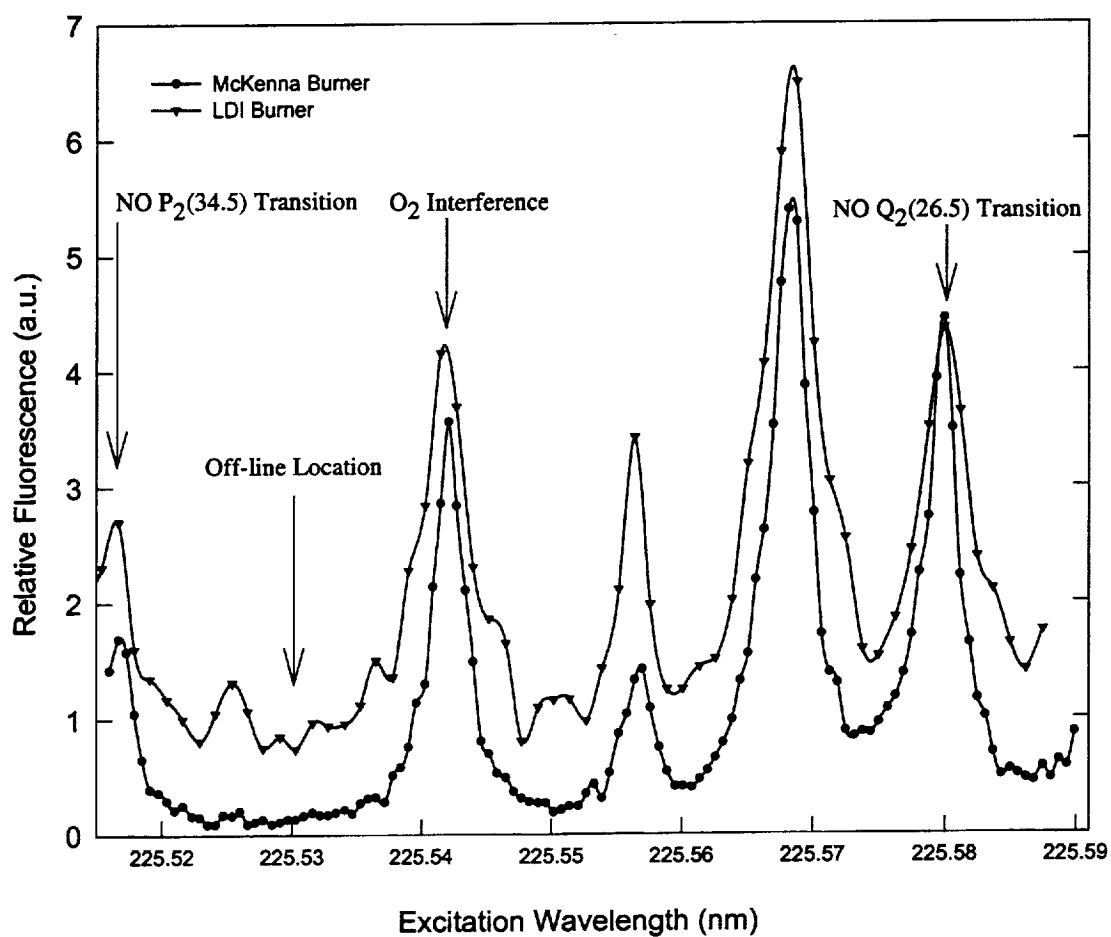


Figure 2.8: Excitation scans in reference McKenna burner ($\phi = 0.8$, $C_2H_6/O_2/N_2/NO$) doped with 80 ppm NO and atmospheric LDI burner at $h = 5$ mm, $r = 3$ mm.

To determine if the Mie scattering spectral wings within the $\gamma(0,1)$ band of NO can be effectively modeled via the chosen off-line excitation wavelength, spectrally broad and narrow detection scans were taken at various locations in the LDI flame with both on-line and off-line excitation. Figure 2.9a depicts a typical detection scan at an axial height of 10 mm and a radius of 12 mm. Figure 2.9b shows more detailed on- and off-line detection scans at the same location. In both cases, agreement between the on- and off-line signals is excellent away from the $\gamma(0,1)$ band of NO. It is still possible that interferences could exist from UHC and PAH fluorescence in fuel-rich regions of the spray flame. On the other hand, any fluorescence from large molecules such as UHCs or PAHs that might exist in fuel-rich regions would likely exhibit broad absorption and fluorescence signatures and thus the off-line excitation signal for these types of molecules would be comparable to that for on-line excitation.

2.5.5 Oxygen Background

Previous work by Partridge *et al.* (1996) and Thomsen *et al.* (1997) has shown that an off-line location chosen in the valley between the $P_2(34.5)$ transition of NO and the O_2 interference labeled in Figure 2.8 provides an effective representation of the broadband O_2 background at high pressure. In particular, Thomsen *et al.* (1997) demonstrated that this off-line location was transportable over a range of lean equivalence ratios and dilution ratios in premixed methane flames. The work reported here addresses the utility of this off-line excitation wavelength with respect to simulation of the Mie background within the NO $\gamma(0,1)$ band without exciting transitions from other species. The off-line location reported by Thomsen *et al.* (1997) is actually shifted to a slightly shorter wavelength than that chosen here. At atmospheric pressure, the spectral difference is negligible and causes no interference problems from major species. However, at higher pressures, the location chosen for this work would lie in the left wing of the O_2 interference shown in Figure 2.8 (Thomsen *et al.*, 1997). To emphasize the necessity of background subtraction for such interferences, Figure 2.10 depicts the increase in background interference with pressure in $CH_4/O_2/N_2$ flames ($\phi = 0.6$, $N_2/O_2 =$

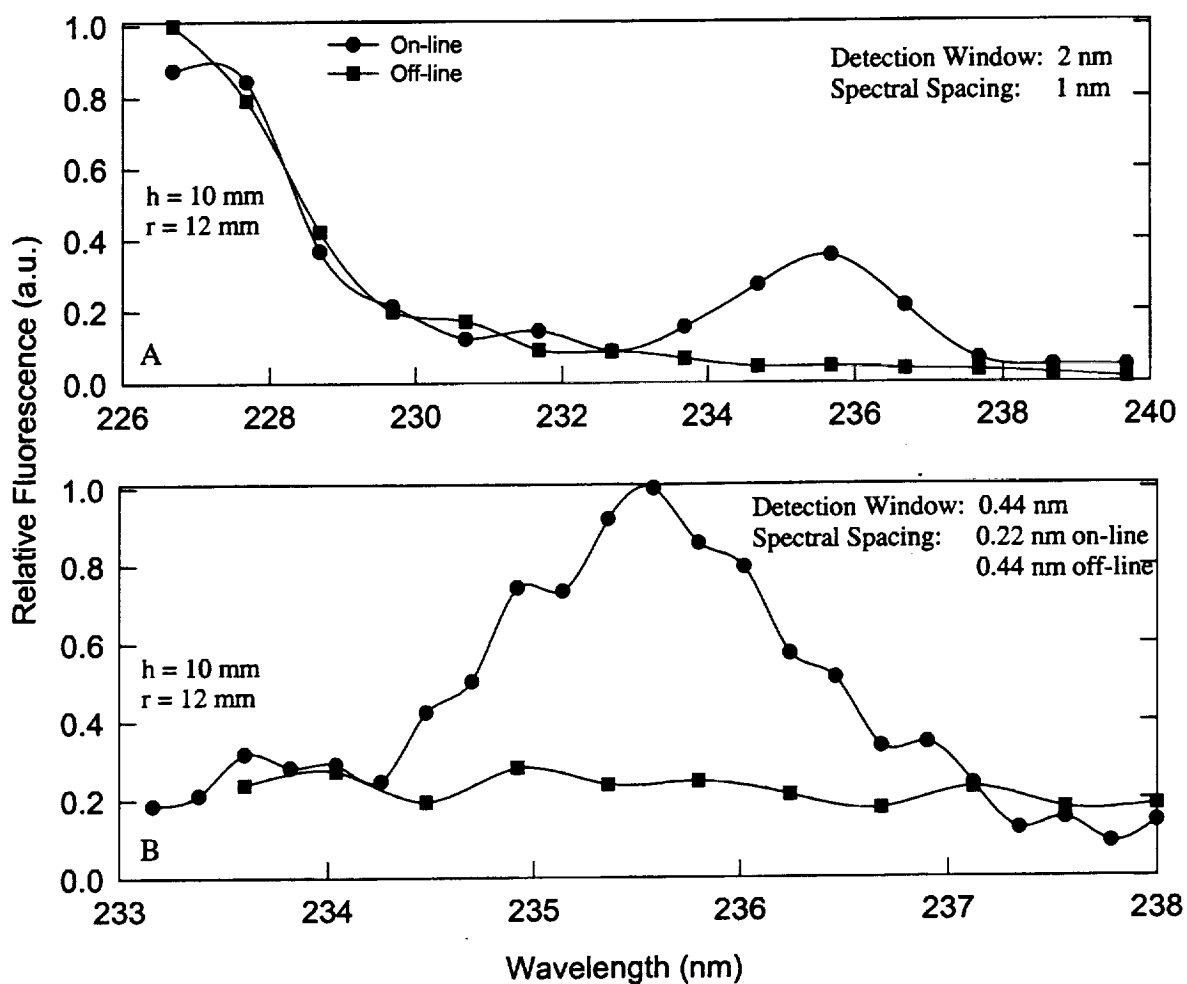


Figure 2.9: Detection scans in the atmospheric LDI flame with on- and off-line excitation for validation of the background subtraction technique for Mie scattering.

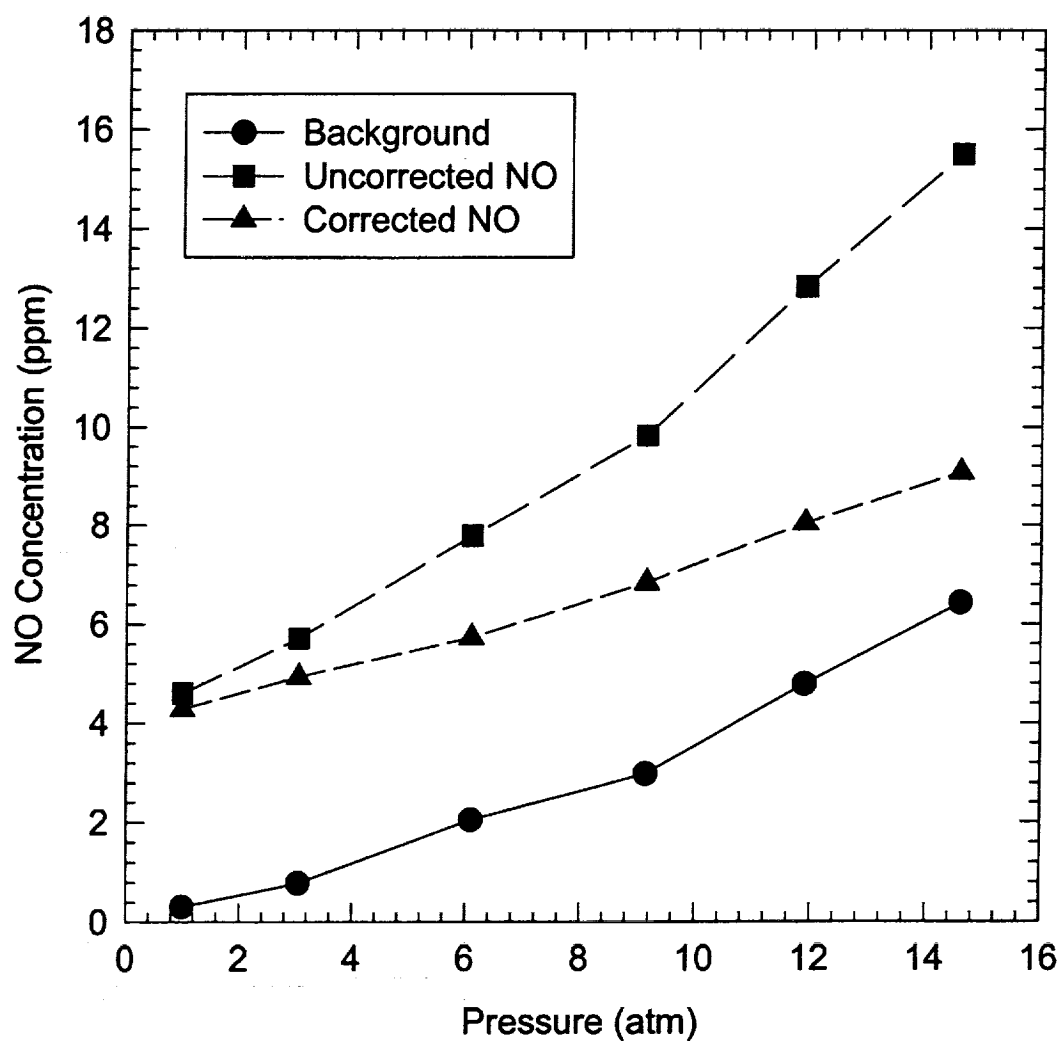


Figure 2.10: Corrected, uncorrected, and background NO concentration measurements in premixed $\text{CH}_4/\text{O}_2/\text{N}_2$ flames ($\phi = 0.6$, $\text{N}_2/\text{O}_2 = 2.2$) at pressures from 1 to 14.6 atm (Thomsen *et. al*, 1997).

2.2) stabilized on a water-cooled McKenna burner (Thomsen *et al.*, 1997). Both background-corrected and uncorrected measurements of NO concentrations are plotted as a function of pressure. In addition, the equivalent background “concentration” is included for reference. As can be seen, at atmospheric conditions, the corrected and uncorrected measurements are nearly identical and the background could essentially be ignored. However, at 14.6 atm, the background contribution is almost as large as the actual NO concentration. Hence, ignoring the O₂ or Mie background in high-pressure measurements would lead to a gross over determination of NO concentrations.

2.6 Results and Discussion

2.6.1 Point LSF Measurements

The NO number density profile determined via LSF at the 10 mm axial height for the LDI flame at $\phi = 1.0$ is shown in Figure 2.11a. While the entire flame has been previously mapped (Cooper and Laurendeau, 1998b), Figure 2.11a briefly demonstrates the utility of the LSF technique. Because LSF measurements are relatively independent of the electronic quenching rate coefficient, an NO calibration for the LDI measurements was transferred from that obtained in a suitable reference flame stabilized on a water-cooled McKenna burner (C₂H₆/O₂/N₂/NO, $\phi=0.8$, 3.76 dilution ratio). Accuracy bars are shown at 10-mm radial increments. Typical accuracies at the 95% confidence limit based on 600 on-line laser shots and 300 off-line laser shots for this operating condition ranged from $\pm 12\%$ to $\pm 30\%$, with the larger accuracy bars near the peak Mie scattering regions of the flame. The repeatability for these measurements is $\sim 15\%$. The symmetry of the NO profile arises from the intense recirculation of combustion products and air into the center of the flame (Lee and Chehroudi, 1995). While cross-sections of the spray exhibit a double-peaked profile (see Fig. 2.7), the internal recirculation zone characteristic of these highly swirling flames distributes the products of combustion almost symmetrically throughout the flame.

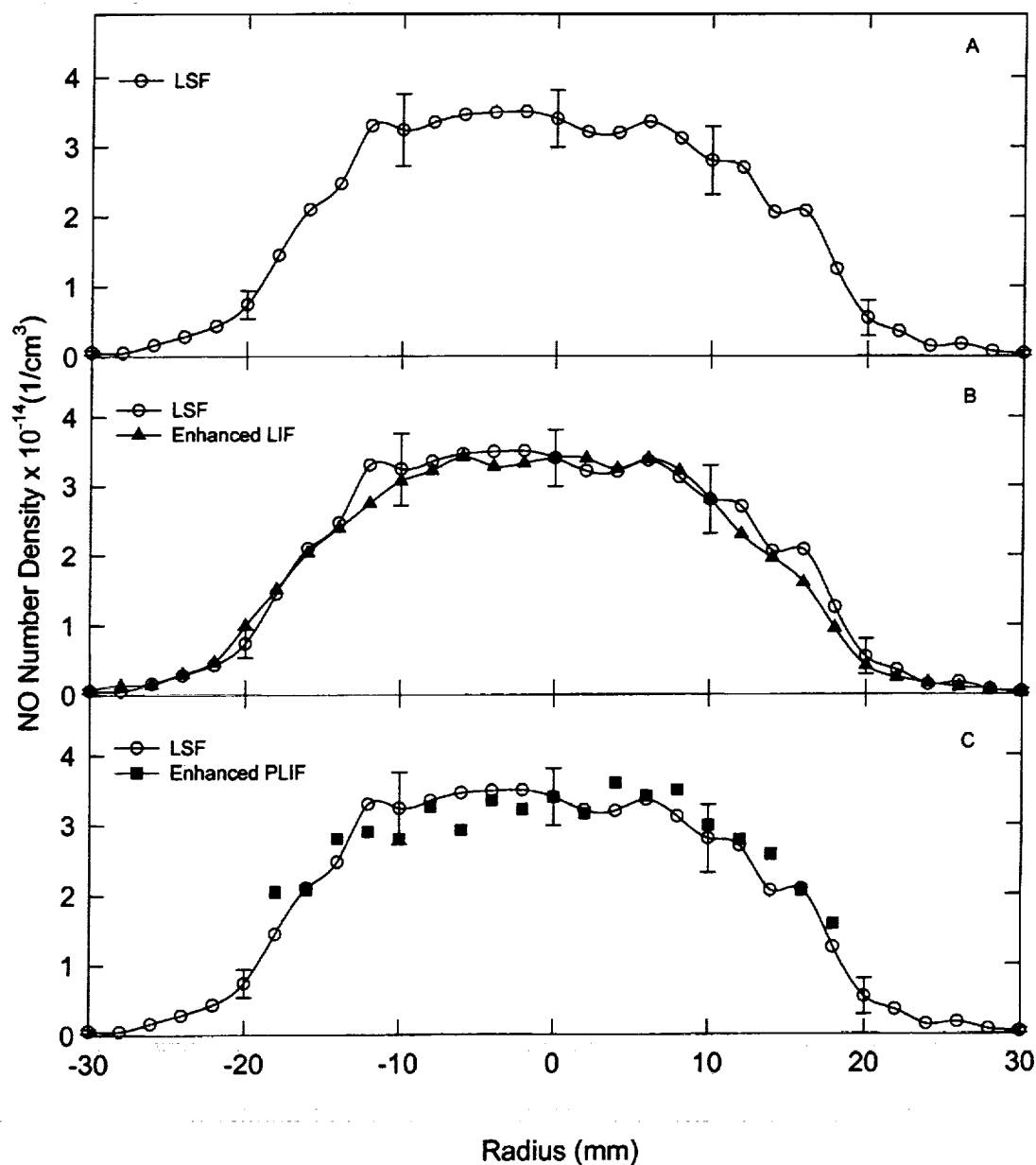


Figure 2.11: Radial NO profiles obtained with (a) LSF technique, (b) single-point scaled LIF technique, and (c) single-point scaled PLIF technique in $\phi = 1.0$, atmospheric LDI flame at an axial height of 5-mm.

2.6.2 Point LIF Measurements

Measurements of NO concentration were also obtained while operating in the linear fluorescence regime (LIF). As in the LSF measurements, a calibration was transferred from the reference flame; however, in this case, only semi-quantitative NO concentrations are possible. Since the calibration scales inversely with the electronic quenching rate coefficient, actual quantitative measurements would require scaling the LDI measurements using

$$[NO]_{LDI, absolute} = \left(\frac{Q_{e, LDI}}{Q_{e, cal}} \right) [NO]_{LDI, relative} \quad (2.28)$$

However, as the flame environment cannot be adequately modeled to estimate the electronic quenching rate coefficient, we require another method of quantifying the LIF measurements. The magnitude of the un-scaled LIF measurements was ~34% greater than that of the LSF measurements. Possible errors owing to the effects of RET dynamics on the LSF measurements are not sufficient to account for this deviation (Cooper *et al.*, 1998). We therefore invoked the more quantitative nature of the LSF measurements with respect to electronic quenching and presumed that they accurately represented NO concentrations in the LDI flame. Thus, we enhanced the qualitative nature of the LIF measurements by suitably scaling the LIF-based NO profiles. By presuming that the local quenching rate coefficient does not vary significantly within the LDI flame owing to intense recirculation, this experimentally-based correction can make use of a single point to scale the LIF profiles (Cooper *et al.*, 1998). The centerline point at the 10-mm axial height location was arbitrarily chosen to perform this scaling, and provided an LIF scaling factor of 0.75.

The results are illustrated in Figure 2.11b, with the accuracy bars of the LSF measurements shown. The accuracy bars for the LIF measurements are similar and generally range from $\pm 12\%$ to $\pm 25\%$. Though not displayed here, the LIF-based NO profiles for the entire flow field from 2.5 mm to 20 mm above the burner collapsed within the error bars of the LSF profiles (Cooper *et al.*, 1998). The excellent correlation between the LSF and LIF profiles implies that the local quenching rate coefficient in this

turbulent flame is essentially constant. The intense recirculation zone characteristic of highly swirling flames is responsible for the well-mixed nature of this LDI flame.

2.6.3 Point-Extrapolated PLIF Measurements

This uniformity of the electronic quenching rate coefficient permits us to consider PLIF as an additional tool by which to explore the NO concentration field. If the broadband fluorescence is not plagued by Mie scattering or laser-induced interferences, i.e., O₂, PAH, or UHC fluorescence, then the opportunity exists to obtain images of NO concentration. These images will be spatially correct owing to the uniform electronic quenching rate coefficient; however, they will remain qualitative without an accurate estimate of this quenching rate coefficient.

The procedure to convert PLIF images to NO concentrations is as follows (Cooper *et al.*, 1998). We utilized the on-line wavelength (225.58 nm) resonant with the Q₂(26.5) transition to excite NO molecules. An image was then recorded corresponding to the on-chip summation of 2400 fluorescence events. The laser was tuned next to the off-line wavelength (225.53 nm) and a similar image was recorded. The data are then processed to account for flame luminosity (subtraction), the distribution of energy in the laser sheet (normalization), and the scattering background (subtraction).

To directly compare the PLIF data with those obtained via LSF, 1-mm squares were averaged throughout the image and horizontal stripes were extracted corresponding to the radial profiles measured with LSF and LIF, in this case at $h = 10$ mm. Considering the nearly invariant electronic quenching rate coefficient in this flame, the PLIF data should accurately scale to within the accuracy bars of the more quantitative LSF measurements. We chose the centerline point at the 10-mm axial height to perform this scaling, which provided a PLIF scaling factor of 0.75, in agreement with the LIF measurements. The results are illustrated in Figure 2.11c. In general, excellent agreement is achieved between the PLIF and LSF measurements at atmospheric pressure. However, the excitation/detection scheme used for the PLIF measurements at 1 atm are not suitable at higher pressures owing to the larger background produced by preferential

excitement of molecular oxygen. Fortunately, an alternate procedure appropriate at higher pressures has been developed, as presented in Chapter 8.

2.7 Improvements to Fluorescence Measurements

The above PLIF measurements utilized broadband detection of the $\gamma(0,1)$, $\gamma(0,2)$ and $\gamma(0,3)$ vibronic bands at 236 nm, 246 nm, and 258 nm, respectively. The filter set for PLIF utilized a wide-band interference filter centered at 250 nm with a 92-nm FWHM and 6-mm of UG5 colored glass filters. This combination considerably attenuates the strong $\gamma(0,1)$ band positioned at 236 nm, but has heretofore been necessary to provide sufficient rejection of Rayleigh and Mie scattering relative to the fluorescence signal. Through the help of CVI Laser Corporation, we have identified a dichroic mirror capable of increasing the signal-to-background ratio (SBR) by a factor of four, thus permitting more accurate LIF-based measurements.

In this section, we compare the previous filter scheme with a CVI LWP-0-R226-T235-237-PW-2037-UV mirror. This product is a long-wave pass, dichroic beamsplitter designed to reject 226-nm radiation and transmit 235-nm to 237-nm radiation at zero angle of incidence. The additional NO bands at 246-nm and 258-nm are also transmitted owing to the long-wave-pass nature of the mirror. The manufacturer's spectral traces for the dichroic indicate a transmission of ~2% at 226 nm and ~80% at 236 nm, while the UG5 has a transmission of ~9% at 226 nm and ~35% at 236 nm (Melles Griot, CVI Laser Corp.). The 226-nm and 236-nm wavelengths are significant, as these spectral positions serve as the excitation and principal detection regions for the measurement of [NO]. Typical narrowband LSF experiments at atmospheric pressure employ 2 mm of UG5 to reject the Mie background. Based on the manufacturers' spectral traces, an improvement in the SBR by a factor of ~100 could be achieved by instead using two dichroic mirrors. This replacement would also yield a five-fold increase in the overall fluorescence transmission.

Figure 2.12 demonstrates the effectiveness of these filters in rejecting Mie scattering from droplets when performing narrowband measurements. Mie scattering

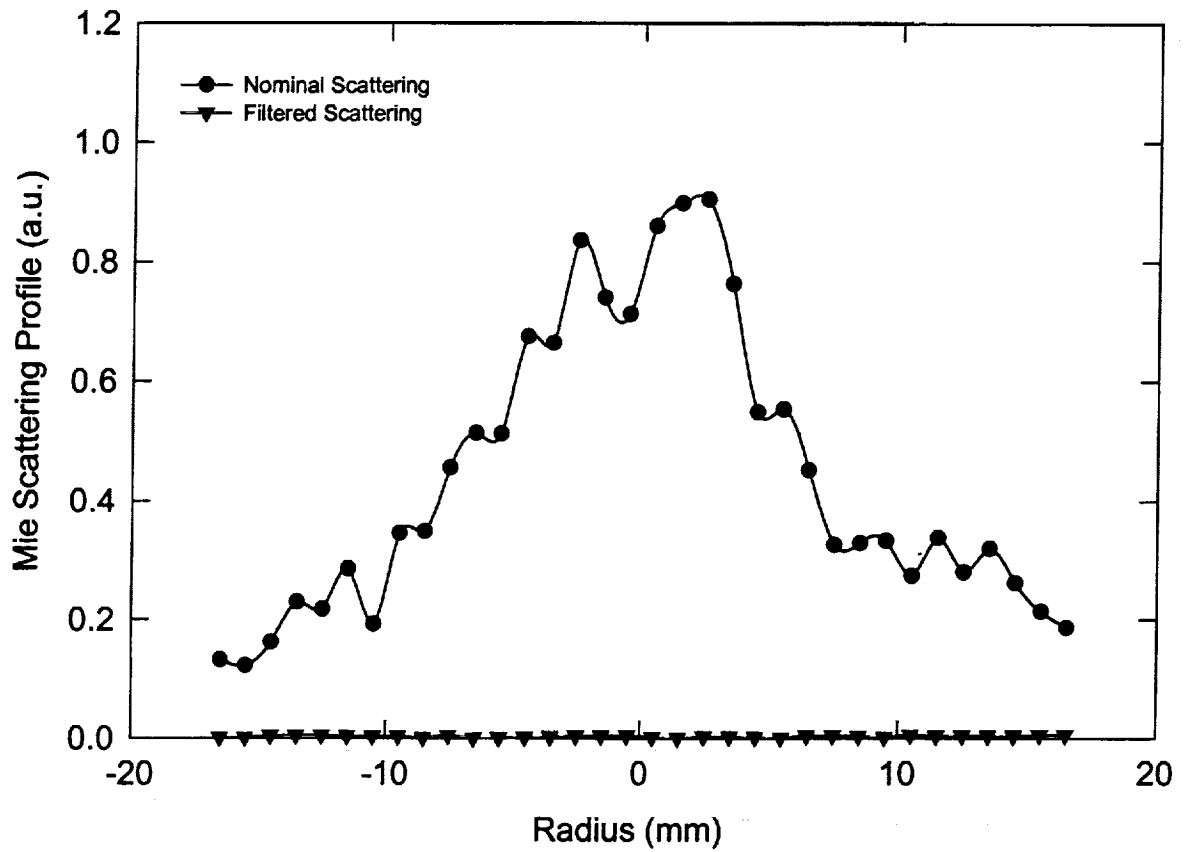


Figure 2.12: Mie scattering radial profiles in a 2-atm LDI flame when utilizing or not utilizing two dichroic beamsplitters (CVI LWP-0-R226-T235-237-PW-2037-UV).

profiles were taken in the usual manner in a 2-atm LDI spray flame and then compared to a repeat of the experiment when utilizing two of the dichroic mirrors. Recall that the Mie scattering profiles are measured by exciting and detecting at the same wavelength; thus the signal from such measurements is quite strong. Note the total rejection of the Mie-scattering signal upon insertion of the dichroic mirrors. This rejection should prove invaluable for both narrow- and broadband measurements at high pressure.

To assess the effectiveness of the different filters in rejecting 226-nm radiation, we captured 100 Rayleigh scattering events in room temperature air as a single image. A corresponding background image was subtracted from this initial image and the resulting image normalized by the laser power, as averaged over 100 laser pulses. From each final image, a representative region was averaged to determine the intensity of the scattering signal. A total of 6-mm of UG5 colored glass filter was tested and compared with a single dichroic mirror. The results of this test are displayed in Figure 2.13a, with the transmission characterized relative to zero mm UG5. We find that a single dichroic mirror rejects 226-nm radiation equivalent to 6-mm of UG5.

To compare the two filter schemes for PLIF measurements of NO, we performed detection experiments in the post-flame region of a $\text{C}_2\text{H}_6/\text{O}_2/\text{N}_2/\text{NO}$ premixed flame ($\phi = 0.8$) stabilized on a water-cooled McKenna burner and doped with 80 ppm of NO to enhance the fluorescence signal. Each image consisted of 1800 fluorescence events binned on chip and corrected for noise and laser power fluctuations. Recognizing that the image consists of NO and O_2 fluorescence, as well as contributions from Rayleigh scattering, it is difficult to isolate the portion of the signal arising solely from NO excitation. Nevertheless, any PLIF detection scheme will inherently sample these other signals and rely on a calibration to account for their presence in the spectra. Therefore, we have defined the total detected fluorescence signal here as the contribution from all fluorescing and scattering species. Similar to the 226-nm radiation, we calculate the transmission values and normalize these to the baseline case of zero mm of UG5. The results of this experiment are shown in Figure 2.13b. In this case, we find that one dichroic mirror transmits fluorescence equivalent to ~1 mm of UG5.

To characterize the filter we computed the signal-to-background ratio (SBR), defined here as the transmission of fluorescence divided by the transmission of the scattering at the excitation wavelength of 226 nm. These calculated values demonstrate that a single dichroic mirror delivers a factor of 3.5 increase in SBR as compared to that of 6-mm of UG5. This 350% increase in SBR is significant because traditional PLIF experiments in our laboratory for NO detection in undoped flames (<100 ppm) have generally displayed overall SBRs of ~2.5:1, which includes scattering and laser-induced fluorescence interferences. Hence, utilization of these dichroic mirrors represents an important advantage that will aid in improving the accuracy of PLIF images for NO species concentrations, especially at higher pressures.

2.8 Conclusions

We have reviewed the development of suitable laser-induced fluorescence techniques for measurements of NO concentration in LDI spray flames, including consideration of the numerous interferences possible in LIF work. These include Mie scattering, oxygen fluorescence, and fluorescence from hydrocarbon species. Quantitative LSF measurements have been presented of [NO] obtained in an LDI burner fueled with liquid heptane at atmospheric pressure. Linear LIF measurements of [NO], both narrowband linear LIF and broadband planar PLIF, require a scaling correction since a calibration cannot be effected via a reference flame. Because the electronic quenching rate coefficient is unknown for such complex turbulent flowfields, the LIF and PLIF profiles have been corrected for collisional effects based on single-point scaling with the more quantitative LSF data. The agreement between the saturated and scaled linear techniques is excellent, which provides an opportunity to use a similar procedure at higher pressures, i.e., single-point scaling to quantify linear fluorescence measurements.

A novel filter has been introduced that effectively rejects Mie scattering in LIF measurements of NO and significantly increases the signal-to-background ratio (SBR) for PLIF images. Employing a dichroic mirror manufactured by CVI Laser Corp., we have

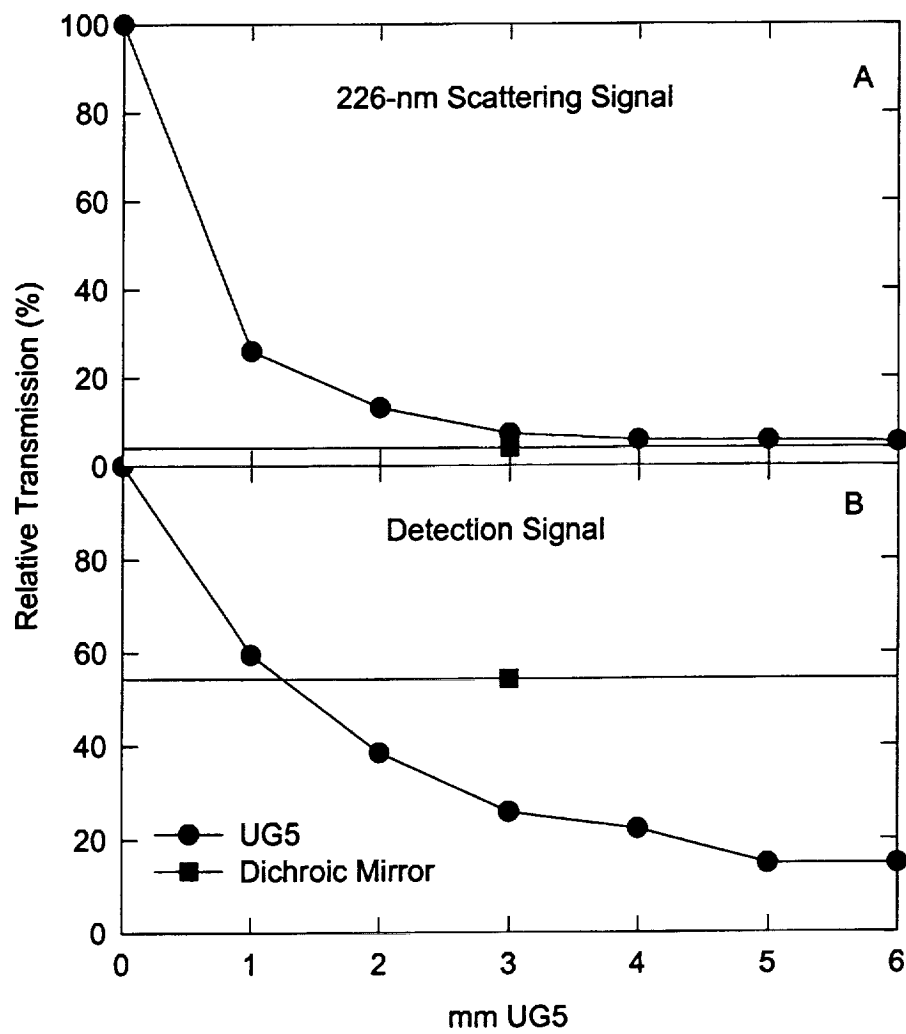


Figure 2.13: Transmission characteristics of UV filters for broadband detection: (a) scattering at 226 nm, (b) NO detection signal.

achieved a 350% increase in SBR for detection of NO in gaseous flames. This enhancement will prove invaluable for high-pressure PLIF images, for which Mie scattering from the droplets can overwhelm any NO fluorescence near the dense spray regions of the flame.

3. HIGH-PRESSURE EXPERIMENTAL APPARATUS

3.1 Optical System

The requisite UV radiation for NO excitation is produced using a Quanta-Ray GCR-3 Nd:YAG laser, a PDL-2 dye laser, and a WEX-1 wavelength extender. The Nd:YAG laser incorporated an intercavity etalon to force a single longitudinal mode in the laser cavity which produced a fundamental output vertically polarized at 1064 nm. The Nd:YAG fundamental was then frequency doubled (532 nm) via angle-tuned, type II phase matching in a temperature-stabilized KD*P (KD_2PO_4) crystal housed in the harmonic generator (model HG-II). The resulting horizontally polarized, 532-nm beam and concentric, vertically polarized, 1064-nm beam were spatially separated via a dichroic harmonic separator (model DHS-2) by employing two dichroic mirrors centered at 532 nm. The ensuing vertically-polarized, Nd:YAG second harmonic was used to pump a tunable dye laser (model PDL-2). Rhodamine 590 and Rhodamine 610 were used in 2.8:1 weight ratios for the PDL-2 oscillator stage, while a ratio of 1.62:1 was used in the amplifier stage.

The vertically-polarized dye fundamental was then frequency doubled (287 nm) via angle-tuned, type I phase matching within a KD*P crystal housed in the CM-1 module of a WEX-2C wavelength extender. The residual vertically-polarized Nd:YAG fundamental from the HG-II harmonic generator was frequency mixed with the dye second harmonic via angle-tuned, type I phase matching within a KD*P crystal housed in the CM-2 module of the WEX-1. The frequency mixing process yields an excitation wavelength of ~226 nm. The excitation beam was spatially separated from the residual concentric beams (1064, 574, 287 nm) via a Pellin-Broca prism and exited the WEX-2C in a vertically-polarized state. In addition, a Fabry-Perot wavelength stabilization system was used to control PDL drift (Cooper and Laurendeau, 1997). This system utilizes a

residual of the 574-nm radiation leaving the WEX-1 and distributes the energy through a Fabry-Perot etalon. A cross section of the resulting ring pattern is imaged on a linear array, (Hamamatsu N-MOS model# S3903-1024Q). The wavelength of the mixed UV beam can be correlated to the ring diameters and serves as an effective control for the dye laser.

The optical elements for the LIF experiments are shown schematically in Figure 3.1. The UV radiation exited the WEX-1 vertically polarized and was immediately passed through a fused-silica beam splitter plate (BS) to split off ~10% of the beam to trigger the data acquisition system via PD:Trig. The maximum beam energy at this point was ~2.5 mJ/pulse. Aperture A1, used to remove stray radiation exiting the WEX-1, was placed immediately in front of lens L1 (CVI model PLCX-25.4-772.6-UV), a 1500-mm focal length plano-convex UV lens. A beam elevating system, BES, was then used to elevate and steer the beam 90 degrees. The BES consisted of two right angle prisms (CVI model RAP-050-UV) located on independent horizontal and vertical translation stages. A filter wheel (Newport model FW-UV) was used to attenuate the beam energy for LIF experiments. PD:A monitored the laser energy via a beam splitter and a diverging lens L2. Lens L2 is a critical component that decreases the spatial sensitivity of the photodiode by distributing the radiative energy over a larger diameter on the surface of the opal diffuser located in the photodiode housing. Aperture A3 was used to block scattering and reflections from optical surfaces. Aperture A4 was positioned prior to the burner and was used to eliminate forward scattering and off-axis focusing in the probe volume. The beam was then focused into the high-pressure vessel (HPV) which was mounted on independent vertical (VS) and horizontal (HS) translation stages. For beam extinction experiments, a second photodiode (PD:B) was placed aft of the vessel in order to measure the beam energy steered via a right-angle prism (RAP) identical to those in the BES. The beam diameter at the focal position based on the 10%-90% cumulative energy distribution was 650 μm .

A portion of the isotropic fluorescence emitted from the NO molecules in the probe volume was captured and collimated by a 50.8-mm diameter, 309-mm focal length, fused silica spherical lens (CVI model PLCX-50.8-130.8-UV) which is labeled L3 in

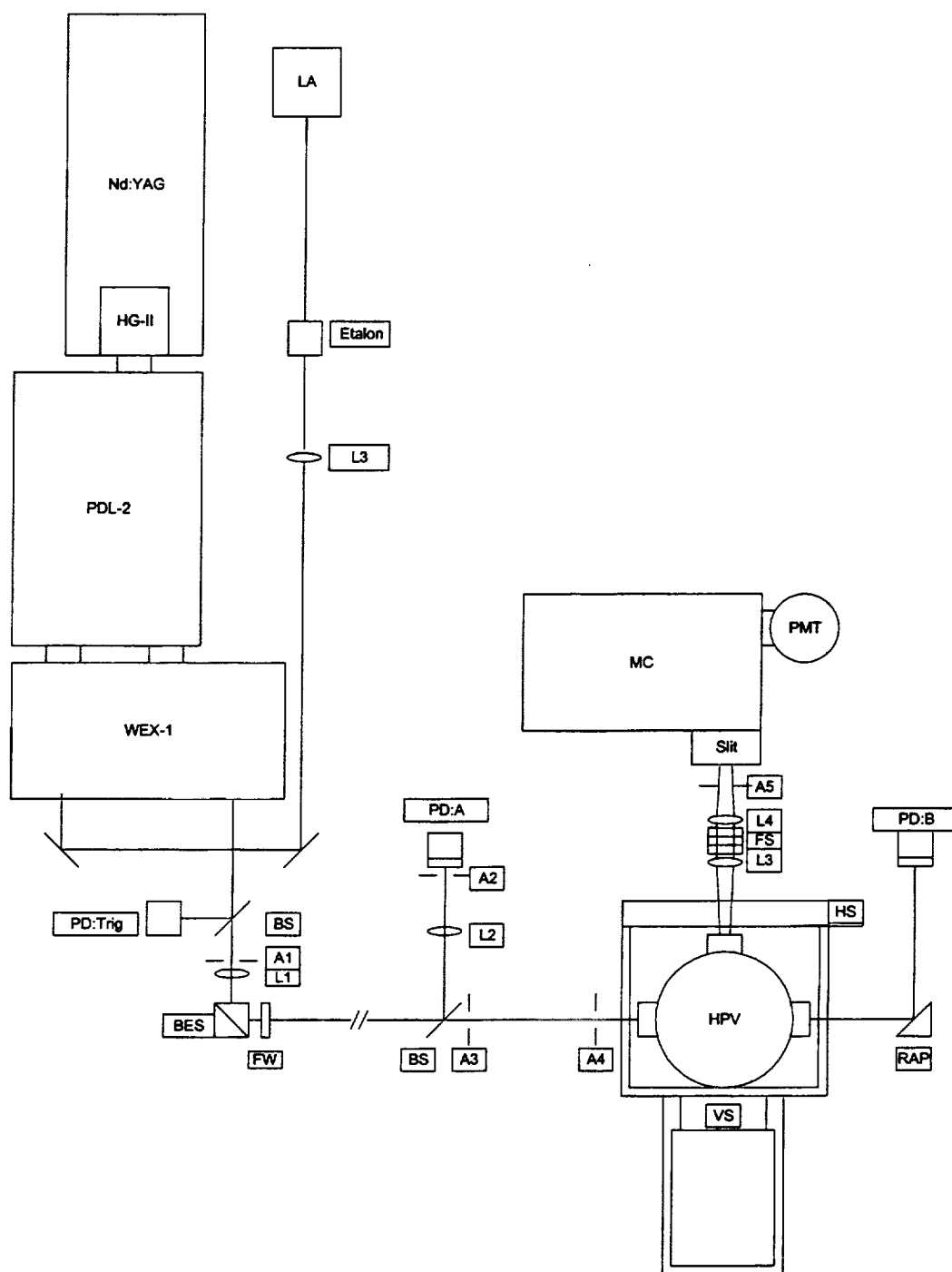


Figure 3.1: Schematic diagram of the experimental apparatus: M: mirror, FS: filter stack, A: aperture, L: spherical lens, BS: splitter plate, PD: photodiode, BES: elevation assembly, LA: linear array, RAP: right angle prism, MC: monochromator, PMT: photomultiplier tube, HPV: high-pressure vessel, HS: horizontal translation stage, VS: vertical translation stage.

Figure 3.1. The detection system is designed with a 1:1 magnification using identical lenses L3 and L4. A filter stack (FS) placed between the lenses incorporates two dichroic mirrors (CVI model LWP-0-R226-T235-237-PW-2037-UV) to filter out Rayleigh and Mie scattering. Additional neutral density filters were placed in FS as needed to ensure that the photomultiplier tube was not saturated during the measurements.

The above collection optics layout produced a magnification of unity and an f-number ($f/\#$) of $f/6.4$. The unity magnification resulted in a probe volume that is the projection of the monochromator entrance slit over the laser beam axis. However, only the slit projection along the beam length defines the probe dimensions. The beam diameter is smaller than the limiting slide aperture and thus it defines the height of the probe volume. To optimize both the throughput and the theoretical spectral resolution of the monochromator, the collection optics were configured such that the $f/\#$ closely matched that of the monochromator.

The $\frac{1}{2}$ -m monochromator (SPEX model 500M) was fitted with a photomultiplier tube (PMT) housing that contained a Hamamatsu R106UH-HA wired for fast temporal resolution (Harris *et al.*, 1976). A lens (CVI model PLCX-25.4-20.6-UV) was used to focus the diverging radiation from the exit slit of the monochromator to the full-width of the PMT window (see Fig 3.2). For the LIF experiments, the fluorescence signal was temporally integrated over 20 ns. The linearity of the PMT was measured over three orders of magnitude by referencing the PMT output voltage (current termination of 50 Ω) to known Rayleigh scattering signals. Figure 3.3 demonstrates the excellent linearity of the PMT and the dynamic range of 100:1.

For the LIF experiments, the entrance slit was 1-mm wide, thus defining a probe volume 650 μm along the diameter of the laser beam and 1-mm long along the axis of the laser beam. The exit slit width was set to define an integrated spectral region of ~ 2 nm FWHM. This setting was chosen based on extensive work by previous researchers (Reisel *et al.*, 1993; Partridge *et al.*, 1996).

Photodiodes PD:A and PD:B were used to measure the laser power and monitor shot-to-shot fluctuations. These detectors (Thorlabs DET 200) used PIN silicon photodiodes with high UV sensitivity mounted in circuits designed for high-speed light

detection. To minimize beam-positioning effects on the photodiode, an opal diffuser (Oriol model 48110) was placed ahead of the front photodiode surface. The linearity of the photodiode response was maintained with sufficient neutral-density and color-glass filters. The signals from the photodiodes were temporally integrated over a 20-ns gate. The linearity of the photodiodes was measured over three orders of magnitude by referencing the PMT output voltage (current termination of 50 Ω) to known Rayleigh scattering signals. Figure 3.4 demonstrates the excellent linearity of the PD and the dynamic range of 10:1.

For the PLIF experiments, a sheet of laser irradiance ~ 800 μm wide, is generated via a cylindrical lens and passed through the probe volume for NO excitation. The modified layout for the PLIF measurements is pictured in Figure 3.5. Mirror M1 (CVI model PAUV-PM-3050-C) is used to steer the fluorescence 90 degrees toward the PLIF camera. A Princeton Instruments model ICCD-576TC-RG proximity focused ICCD detector incorporating a 578×384 pixel, charge-coupled device (ICCD) (Thomson model CSF 7883) with 23- μm square pixels is utilized for detection of the NO fluorescence. The fluorescence is focused on the ICCD detector by utilizing an aberration-corrected, five fused-silica element, UV-Micro-Nikkor, 105-mm focal length f/4.5 lens (Nikon Corp., Melville, NY), such that each pixel corresponds to a 77 μm square in the image plane of the flame. A filter set (FS) consisting of a wide-band interference filter (92-nm FWHM) spectrally centered at 250 nm (Acton model 250-W-2S), and coupled with three dichroic mirrors (CVI model LWP-0-R226-T235-237-PW-2037-UV), is used to reduce the Mie scattering from the liquid droplets.

An ICCD thermoelectric cooler is used in conjunction with an external water chiller/circulator (Lauda model RMT-6, Brinkman Instruments) to reduce the temperature of the CCD to -32°C . A pulse generator (Princeton Instruments model FG-100) is used to produce a gate of 20 ns to the ICCD. Operation of the ICCD and supporting hardware is controlled by a detector-controller (Princeton Instruments model ST-130). The user interface to the ICCD system is provided by WinSPEC software, which is also used for all image analysis and reduction.

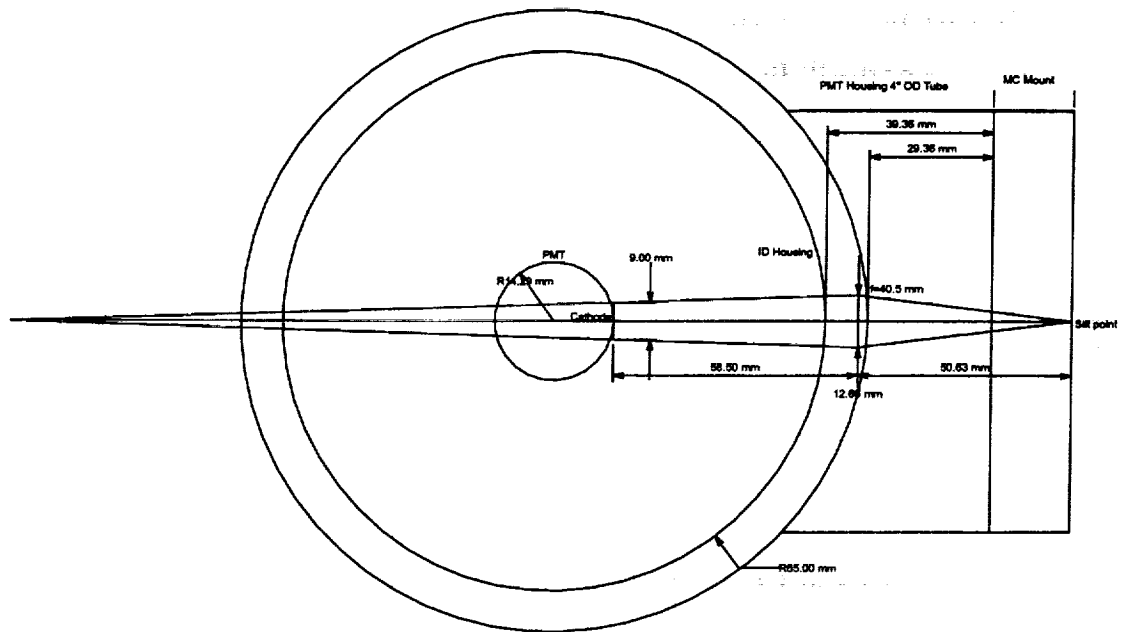


Figure 3.2: Photomultiplier tube housing and lens assembly.

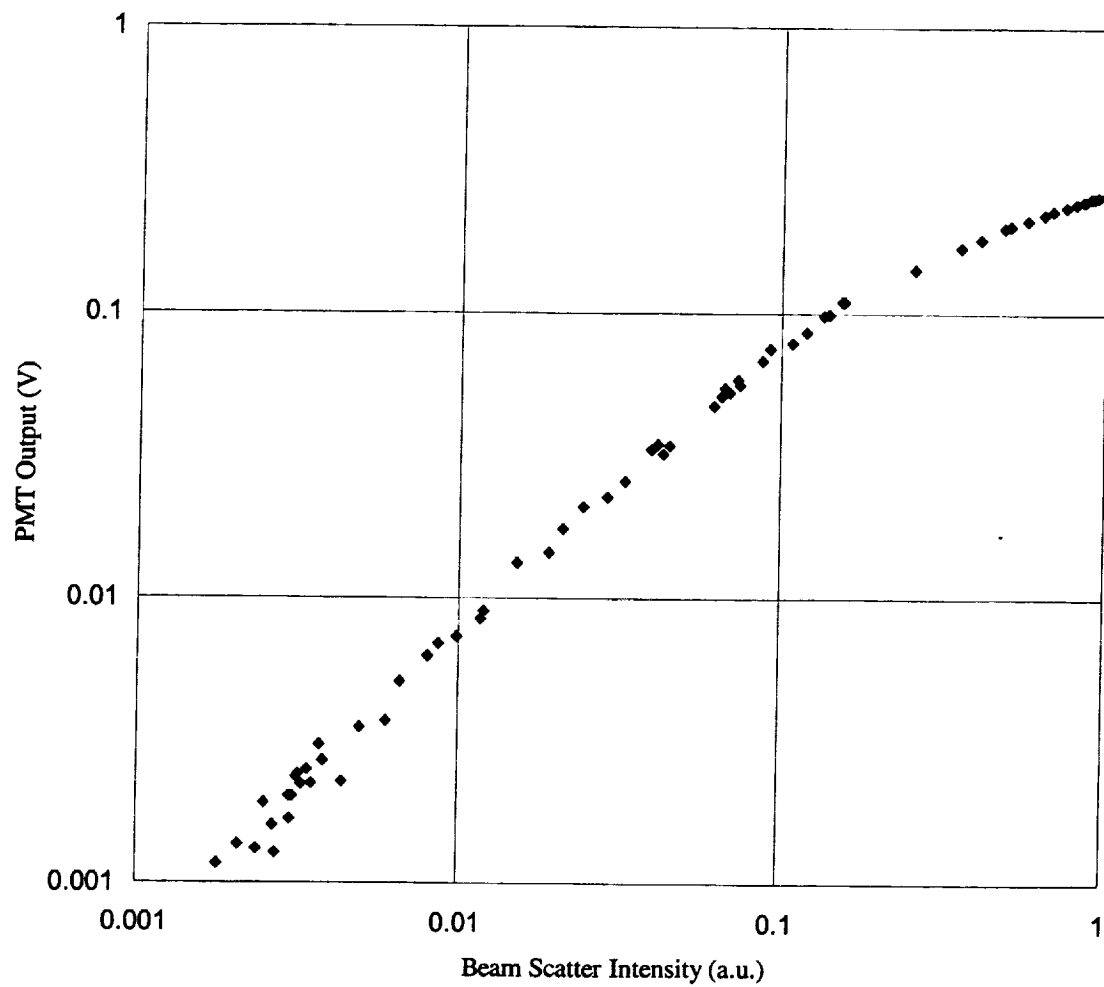


Figure 3.3: Linearity of photomultiplier tube (PMT).

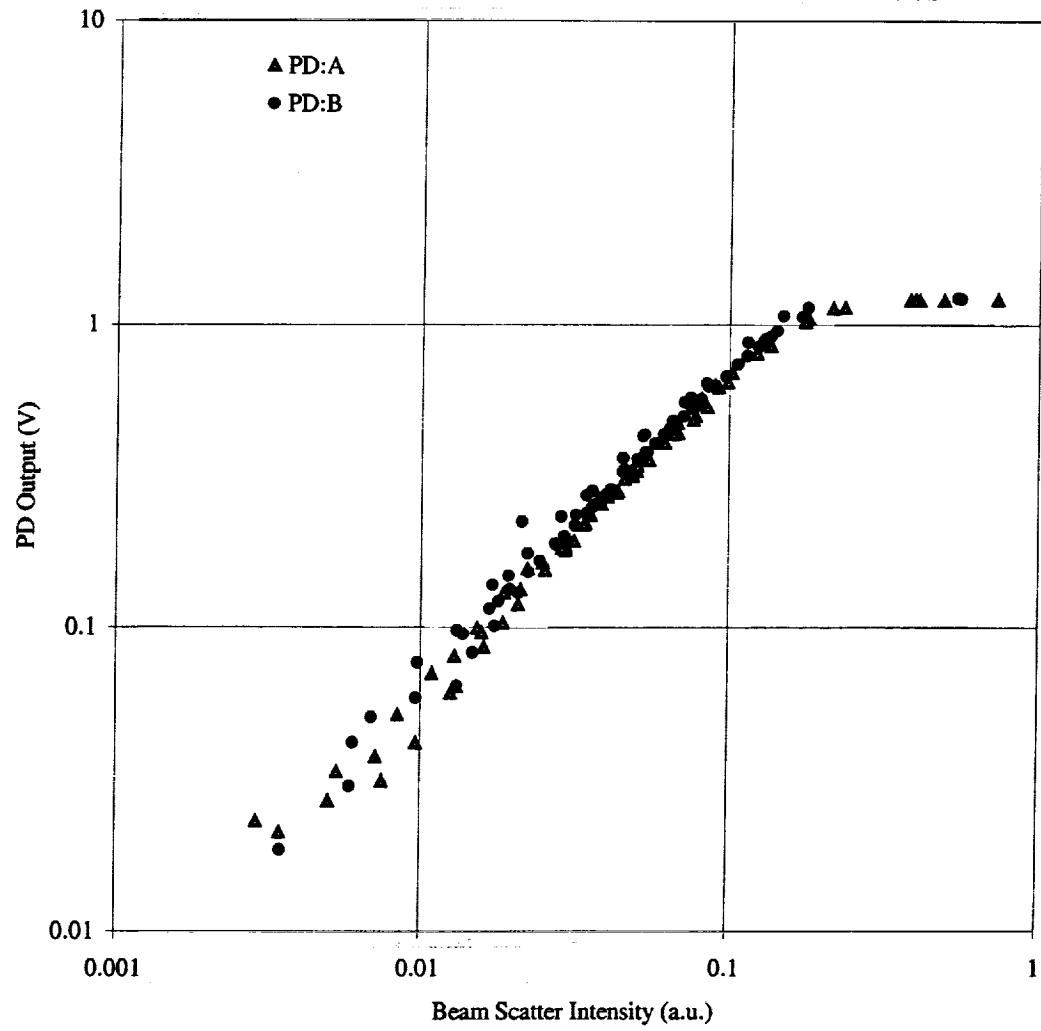


Figure 3.4: Linearity of photodiode (PD).

3.2 High-Pressure Facility

The high-pressure vessel (see Fig. 3.6) is custom-built (Parr Instrument Co.) and incorporates a water jacket and three UV fused-silica windows for transmission of the beam and ensuing fluorescence. The vessel is rated at 3.1 MPa internal pressure and 700 K internal wall temperature. The water jacket is a critical component that allows flame temperatures to be sustained inside the vessel. The burner utilized here was based on a lean direct-injection (LDI) design and typifies that used in the primary zone of advanced gas turbine combustors. The stainless steel LDI module (see Fig. 3.7) internal to the vessel (11.43 mm ID) accommodates a fuel tube (3.175 mm dia.) that enters the module outside of the vessel. A 60° helical swirler (11.43 mm dia.) was mounted at the top of the fuel delivery tube. The swirler itself was tapped to allow a macrolaminate Parker-Hannifan hollow-cone, pressure-atomized spray nozzle (OD = 5.3 mm) to be directly threaded into the swirler. The nozzle was positioned vertically relative to a converging/diverging orifice (10.16 mm dia. at 40°). The depth of the nozzle below this orifice (5.64 mm) was adjustable via copper washers located at the bottom of the module. Additionally, the orifice was mounted to the stem via a threaded channel and could be adjusted relative to the nozzle if needed. The main air was preheated in each experiment and delivered axially to the module axis. The co-flow air was introduced to the burner via three holes in the bottom flange. A cap assembly was fitted over the main stem which allowed the co-flow air to enter the flowfield via the central orifice shown in Figure 4.6. The purpose of the co-flow air was to aid in flame stabilization at low pressures since the outer recirculation zone of the flame hindered flame stability.

The fuel delivery system incorporated a four-gallon, stainless-steel pressure vessel rated at 5.3 MPa. The stored heptane was pressurized with nitrogen at 1.5 MPa and metered via a rotameter flow controller. The air was provided from a building compressor. The air flows for the main and co-flow passages were adjusted with metering valves and monitored with Hastings model HFM-230 fast-response thermal mass flow meters. Preheating was achieved with two in-line air heaters controlled with voltage regulators. The maximum preheat air temperature was limited by boiling within the fuel tube, which leads to vapor lock in the injector.

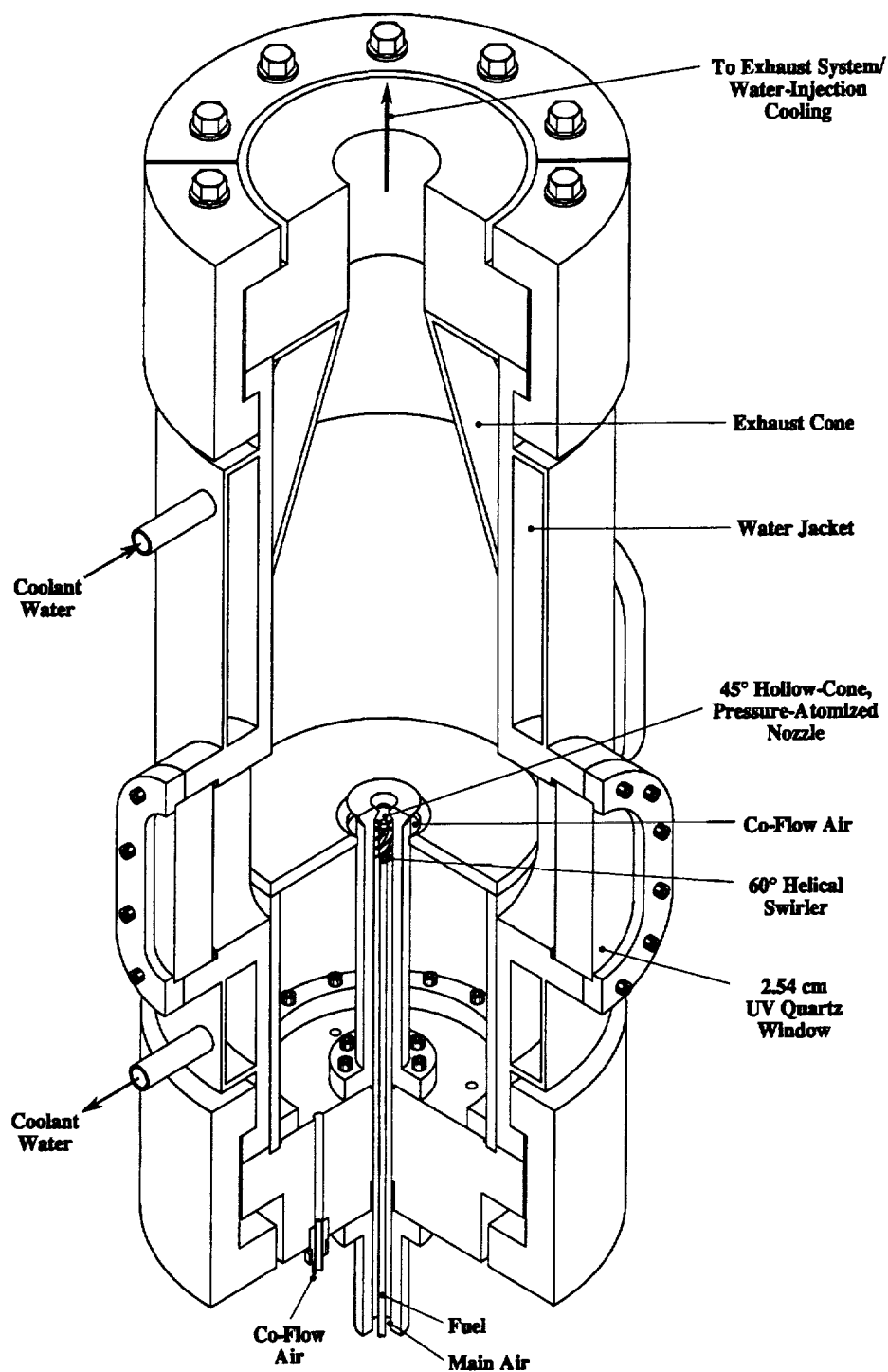


Figure 3.6: High-pressure vessel cutaway view.



Figure 3.7: High-pressure LDI burner schematic.

The small size of the vessel (22.2 cm OD, 15.2 cm ID) required a translation system capable of translating the full weight of the vessel both vertically and horizontally. The vertical translation stage (Daedal model 406014ET-MS-D2-L2-C4-M3-W1) is a modified single-axis series 406000ET linear table with an extended 16-inch carriage. The table has a travel of 101.6 mm, a positional accuracy of 89 μm , and a positional repeatability of $\pm 51 \mu\text{m}$. The modified table includes heavy-duty, angular-contact bearings to support a 135 kg axial load, a fail-safe electric brake, and optical limit/home switches for over-travel safety. A Parker model PDX-15-83-135 single-axis drive/indexer coupled with a 1.92 kg-cm² rotor inertia motor provides for vertical positioning of the burner relative to the detection system. A right-angle bracket is used to attach the stage to the optical table. An additional right-angle carriage is mounted to the faceplate of the vertical linear table to hold the horizontal stage.

The horizontal stage (Daedal standard model 315801AT-ES-D4-L2-C2-M1-E1) is an open-frame linear table with a travel of 200 mm, a positional accuracy of 40 μm , and a positional repeatability of $\pm 25 \mu\text{m}$. The table includes limit/home magnetic switches for over-travel safety. A Parker model PDX-13-57-102 single-axis drive/indexer coupled with a 0.309 kg-cm² rotor inertia motor provides for horizontal positioning of the burner relative to the detection system. Precise step control was achieved through an interface with LabVIEW software. The high-pressure vessel is mounted on the open-frame linear table via a base plate designed to secure the vessel and to allow for feed through of air and fuel lines through the optical table.

3.3 Data-Acquisition System

The data acquisition system designed for this work utilized two 486 desktop PCs and one 386 desktop PC (see Fig. 3.8). Two of the systems incorporated LabVIEW 3.0 based software interfaces to the control and monitoring systems labeled in Figure 3.8. A Stanford Research Systems NIM crate housing four SR250 gated integrators/boxcar averagers and an SR265 computer interface module served as the data sampling and

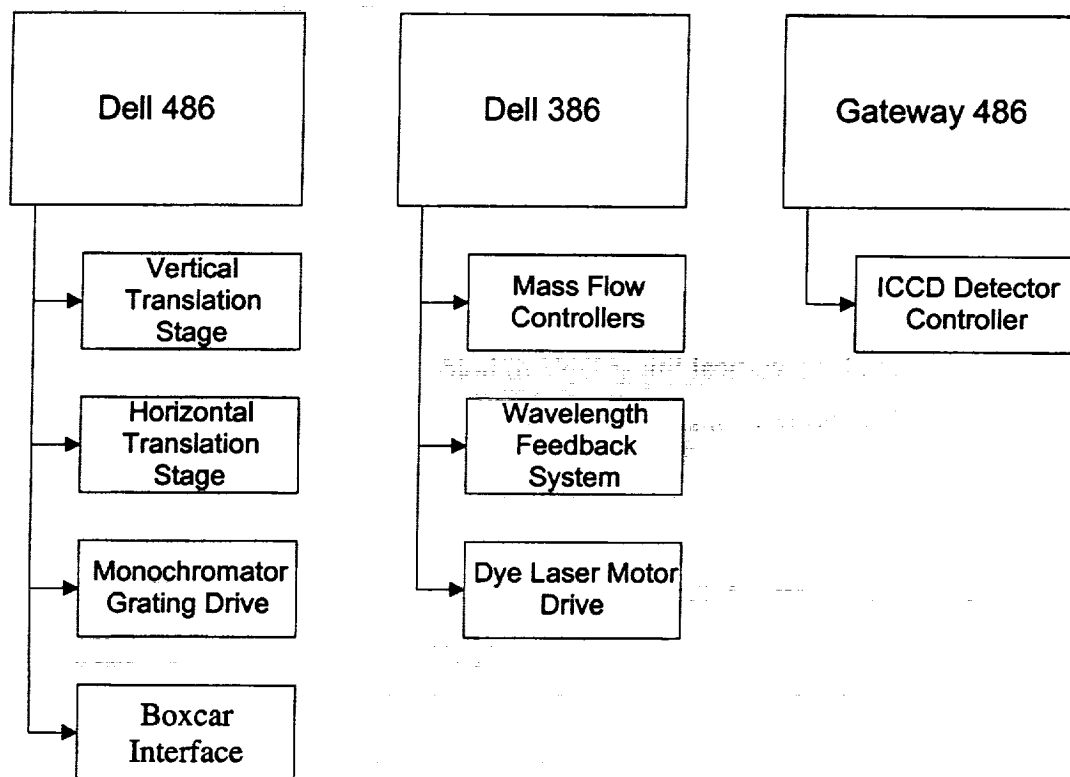


Figure 3.8: Data-acquisition system overview.

filtering system for the photodiodes and the photomultiplier tube in the LIF experiments. Only the photodiodes were sampled in the PLIF experiments. Each of the SR250 gated integrators/boxcar averagers provided gate position, width control, and signal amplification. The SR265 computer interface module allowed the sampled data from the above photo-electric channels to be transferred to the PC via a GPIB channel. The wavelength feedback system was monitored through an SCB-68 DAQ interface to sample the various channels from the linear array. Control of the burner translation stages and the PDL grating was achieved by serial interfaces to stepper motor drive systems. The monochromator grating drive was a stand alone module designed to receive pulses from the DAQ board and move the motor accordingly. The memory requirement for image acquisition mandated a stand-alone PC system for the ICCD detector-controller.

4. DEVELOPMENT AND APPLICATION OF A QUANTITATIVE CALIBRATION SCHEME FOR 2-ATM LEAN DIRECT-INJECTION SPRAY FLAMES

4.1 Introduction

In this chapter, we report spatially resolved laser-induced fluorescence (LIF) measurements of nitric oxide (NO) in a preheated, two-atmosphere, lean direct-injection (LDI) spray flame. The spray is produced by a hollow-cone, pressure-atomized nozzle supplied with liquid heptane. NO is excited via the $Q_2(26.5)$ transition of the $\gamma(0,0)$ band. Detection is performed in a 2-nm region centered on the $\gamma(0,1)$ band. A complete scheme is developed by which quantitative NO concentrations in high-pressure LDI spray flames can be measured by applying linear LIF. Standard excitation and detection scans are performed to assess possible interferences and to verify a non-resonant wavelength for subtracting the influence of oxygen interferences and Mie scattering in the NO detection window. NO is doped into the reactants and convected through the flame with no apparent destruction, thus allowing an NO fluorescence calibration to be taken inside the flame environment. The in-situ calibration scheme is validated by comparisons to a reference flame. Relative axial calibration slopes are utilized in order to obtain radial profiles of absolute NO concentrations. These quantitative NO profiles are presented and analyzed so as to better understand the operation of lean-direct injectors for gas turbine combustors.

4.2 Background

Much of the current research on gas-turbine combustors is ultimately aimed at reducing NO_x emissions. Of the numerous possibilities to approach NO_x reduction, the utilization of swirl-based geometries provides excellent potential. Swirl has been the

focus of numerous publications, each incorporating this approach in a unique manner. In general, swirl is imparted to the combustion air via annular guide vanes or by upstream tangential air injection. The effect of swirl is to create a toroidal recirculation zone which, for non-premixed combustion, promotes more efficient fuel/air mixing and provides flame stabilization. For premixed combustion, recirculation produces a region of hot combustion products that aids in flame anchoring at either an upstream or downstream stagnation point (Yegian and Cheng, 1998).

Though swirl provides numerous benefits to improve combustor design, a systematic understanding of how NO_x emissions are affected by specific properties of the recirculation zone remains elusive. Chen (1995) studied the effects of swirl number, overall equivalence ratio, Reynolds number based on primary air velocity, and residence time within the recirculation zone on NO_x emissions for nonpremixed hydrogen-air flames. The burner consisted of a fuel tube centered in a quarl that provided co-axial air with or without swirl. Annular co-flow was supplied about the quarl assembly at 2% of the primary air velocity to avoid possible wall effects associated with the enclosure used to measure NO_x emissions. Chen (1995) found that for a given primary Reynolds number and overall equivalence ratio ($\phi_0 = 0.5$), EINO_x remained essentially constant with increasing swirl number once the recirculation zone was established. Moreover, EINO_x decreased for a given swirl number as the Reynolds number increased past 10,000. EINO_x was also found to increase as ϕ_0 rose from 0.2 to 0.6 for $\text{Re} = 20,000$ -30,000 at a swirl number $S = 1.1$. Chen (1995) correlated this increase to the volume of the flame, which rose with increasing ϕ_0 . A time scale suitable for correlation of EINO_x was found to depend on the properties of the recirculation zone as opposed to the nozzle exit velocity. In particular, NO_x emissions decreased with a reduction in the residence time within the recirculation zone. Chen (1995) also concluded that the recirculation zone is generally shielded from the surrounding air and that the products of combustion do not mix with this air until they proceed downstream of the recirculation zone.

In a follow-on effort, Chen (1996) studied the influence of hydrocarbons on NO_x emissions by replacing the hydrogen with a 50% CH_4 -50% H_2 fuel mixture. Similar results were recorded with the exception that the emission level increased significantly

with rising swirl number. Chen (1996) attributed this observation to the increasing importance of prompt NO at higher swirl owing to the reduction in residence time available for the formation of thermal NO.

Cheng *et al.* (1998) studied unconfined methane jet flames with swirl imparted to the flow via a six-vane co-annular flow guide (45° or 55°) that provided swirl numbers of $S = 0.7$ or $S = 1.0$, respectively. Variations were considered in the ratio of momentum flux of the fuel to that of the swirling air. Methane was supplied with either an axial injector or an annular injector incorporating four holes inclined at 45° . Standard gas analyzers were used with a stainless steel sampling probe to measure the post-flame emission levels. Cheng *et al.* (1998) found that strong swirl, low momentum flux ratios, and annular fuel injection decidedly reduced NO_x emissions. In particular, annular injection produced less NO_x emissions when compared with axial injection owing to the straining of fuel into the shear layer. Strong swirl and low momentum flux ratios produced rapid mixing, thus increasing mixture homogeneity and shortening the characteristic time for NO_x formation. In comparison, CO emissions were found to increase with strong swirl and low momentum flux ratios and to decrease with annular fuel injection.

Shaffar and Samuelsen (1998) tested a similar burner incorporating radial injection of liquid fuel from eight holes into swirled air, which then passed through a venturi into the combustion zone. The premixedness of the mixture arose from the swirl and the flow time before combustion. Jet-A aviation fuel was tested with preheated combustion air at 1 and 5 atm, with NO_x emissions monitored at only 5 atm. The reported measurements of NO_x correlated with calculated flame temperatures, indicating that the NO_x was primarily thermal in origin. EINO_x values ranged from ~ 0.8 g/kg at an adiabatic flame temperature of ~ 1750 K to ~ 8.5 g/kg at ~ 2230 K.

Control of fuel and air mixing is a dominant factor in reducing NO_x formation, as this process determines the local radical pool, oxygen concentration, and flame temperature (Gupta, 1997). One important combustor design that often incorporates swirl is lean-premixed combustion. Although lean-premixed burners offer significant reduction of NO_x owing to lower flame temperatures, these burners often have drawbacks

associated with lean blow-off, acoustic instability, and increased size and weight. An alternate design incorporating swirl is that of lean direct-injection, which often employs a hollow-cone spray, thus effectively straining the injected fuel into the shear layer of the swirling air.

Alkabie *et al.* (1988) performed a study of flame stability, NO_x emissions, and combustion efficiency for propane and natural gas fired, lean direct-injection (LDI) combustors operating at atmospheric pressure. The burners employed a radial swirler design with fuel issuing from eight radial holes on a central fuel tube. The NO_x levels displayed a strong dependence on overall equivalence ratio, with a minimum NO_x level close to 10 ppm at $\phi_o = 0.3$ when corrected to 15% oxygen.

Hayashi (1995) compared the LDI-based configuration against a lean premixed-prevaporized (LPP) configuration, both burning kerosene and supplied with pre-heated air at atmospheric pressure in a confined combustion chamber. The direct-injection burner incorporated a co-rotational double swirler with a solid-cone fuel nozzle having a 60° nominal spray angle. The premixed burner was similar to the LDI burner, but with a mixing tube placed between the nozzle/swirler assembly and the combustion chamber. A strong dependence of NO_x emissions on overall equivalence ratio was reported for the LDI system, with levels of ~ 0.2 g/kg at $\phi_o = 0.6$ and ~ 4 g/kg at $\phi_o = 1.0$ for an inlet air temperature of 650 K. Hayashi (1995) also reported higher combustion efficiencies in the direct-injection mode and comparable NO_x emissions when the LDI burner was operated leaner than the LPP burner.

Cooper and Laurendeau (1998a) developed a saturated-LIF (LSF) technique capable of quantitative measurements of NO concentration in an atmospheric, unconfined, swirl-stabilized spray flame based on a lean direct-injection design. The burner incorporated a helical swirler with a central hollow-cone, pressure-atomized spray nozzle supplied with liquid heptane. A converging/diverging orifice was positioned immediately after the swirler/injector assembly. The diagnostic technique incorporated a subtraction method to remove Mie-scattering background from the NO fluorescence signal. Because of the inherently low sensitivity of LSF to variations in the electronic

quenching rate coefficient, a fluorescence calibration developed in a reference flame could be successfully transported to the LDI spray flame.

Cooper *et al.* (1998) continued the previous atmospheric work by comparing linear-LIF based techniques, both point-LIF and planar-LIF, to the LSF method. Because the linear techniques could not employ a transported calibration, the entire flow field was scaled by the ratio of a linear to a saturated fluorescence signal at a single point in the measurement field. This procedure produced an NO flow field for the linear measurements which fell entirely within the accuracy bars of the more quantitative LSF measurements. In this way, Cooper *et al.* (1998) demonstrated the feasibility of a potential calibration method for high-pressure LIF measurements of NO in spray flames. Here, we follow this work by detailing a successful calibration technique that promises quantitative measurements of NO at 1-10 atm.

4.3 Operating Conditions

The LDI burner is operated at a main equivalence ratio $\phi = 0.9$, with heptane fuel supplied to the nozzle at 0.165 g/s and air at 2.78 g/s. Though this condition does not fully model lean operation of the LDI module, it was chosen here to provide ample NO in the combustion products. An additional co-flow is added to aid in flame stabilization, which would provide an overall $\phi_o = 0.81$ if this air were completely entrained into the combustion products. The pressure is nominally reported at 2 atm, though the actual operating pressure was 2.09 atm. The main air is preheated to 375 K to assist in vaporization and mixing of the fuel. The nozzle is located 12 mm below the top of the burner. Because of intense mixing, the resulting flame is essentially non-sooting and blue.

4.4 Spectral Validation

4.4.1 Excitation/Detection Scheme

Our previous work addressed an excitation/detection scheme for use in atmospheric-pressure LDI flames (Cooper and Laurendeau, 1998a). Excitation of the $Q_2(26.5)$ line of the $\gamma(0,0)$ band of NO at 225.58 nm is followed by detection of the $\gamma(0,1)$ band with a 2-nm window centered at 235.78 nm. An off-line wavelength at ~225.53 nm is excited and monitored as a measure of the ubiquitous background for the NO fluorescence signals. This combination has been selected based on extensive interference and background investigations (Reisel *et al.*, 1993; Partridge *et al.*, 1996) and has shown considerable success in a variety of flames produced with gaseous and liquid fuels (Reisel and Laurendeau, 1995; Thomsen *et al.*, 1997; Cooper and Laurendeau, 1998b). The scheme has been particularly useful in high-pressure (1-15 atm) $\text{CH}_4/\text{O}_2/\text{N}_2$ flames (Thomsen *et al.*, 1997). For atmospheric sprays, the utility of this scheme lies in the subtraction of Mie-scattering interferences that break through the monochromator despite the ~10-nm separation between the excitation and detection wavelengths (Cooper and Laurendeau, 1998a). At higher pressures, such a scheme is critical to the detection of NO levels below 10 ppm owing to the background produced by the O_2 Schumann-Runge spectrum (Thomsen *et al.*, 1997).

4.4.2 Mie Scattering Profiles

To facilitate use of this excitation/detection scheme in a liquid droplet environment at higher pressures than those in the previous atmospheric work (Cooper and Laurendeau, 1998a), we must re-consider the possible effects of Mie scattering interference, fuel and fuel-fragment fluorescence, and laser beam extinction. We first assessed the influence of Mie scattering by measuring scattering profiles in order to locate regions of heavy droplet interference. Scattered light at the incident laser wavelength is passed through neutral density filters and collected via a 1/2-m monochromator in a 2-nm window centered at ~226 nm. Figure 4.1 indicates the strong

Mie scattering that occurs along the spray, especially at lower heights above the burner. The profiles are quite different from those measured in the previous atmospheric-pressure LDI work (Cooper and Laurendeau, 1998a). In particular, the previous LDI measurements resulted in axisymmetric double-peaked profiles that followed the typical spray sheath associated with strongly swirling spray flames (Lee and Chehroudi, 1995). However, the low flow rates required to stabilize the present 2-atm flame reduces the strength of the recirculation zone and the efficiency of the atomizer. Accordingly, the Mie scattering profiles demonstrate the symmetric features shown in Figure 4.2. Mie scattering profiles at higher pressures yield the more typical double-peaked structure as the strength of the recirculation zone increases and the atomization quality improves (see Chapter 5). In addition, as discussed in Chapter 3, two special CVI dichroic beamsplitters can be employed for NO detection to minimize any resulting interferences from Mie scattering (Cooper and Laurendeau, 1999a).

4.4.3 Excitation and Detection Scans

Excitation and detection scans were next performed to assess the level of potential interferences associated with possible unburned hydrocarbons. A reference $\text{C}_2\text{H}_6/\text{O}_2/\text{N}_2/\text{NO}$ flat flame ($\phi = 0.8$) stabilized on a water-cooled McKenna burner (3.76 dilution ratio) was utilized for comparison. The spectral signatures from NO and O_2 have been previously well characterized in such flames (Partridge *et al.*, 1996). Hence, a comparison of spectral scans taken in this standard flame with those obtained in the LDI case should aid in the identification of any interferences resulting from hydrocarbon fluorescence. Figure 4.2 illustrates two excitation scans: one taken in the flat flame with 40 ppm of NO doped into the flame to help define the $\gamma(0,1)$ band structure and one taken along the centerline at the 15-mm height in the LDI flame with ~80 ppm of NO doped into the flame. The excellent similarity indicates that other species such as unburned hydrocarbons and polycyclic aromatic hydrocarbons are apparently not excited within the 2-nm detection window. Moreover, the ratio of the on-line to off-line signals

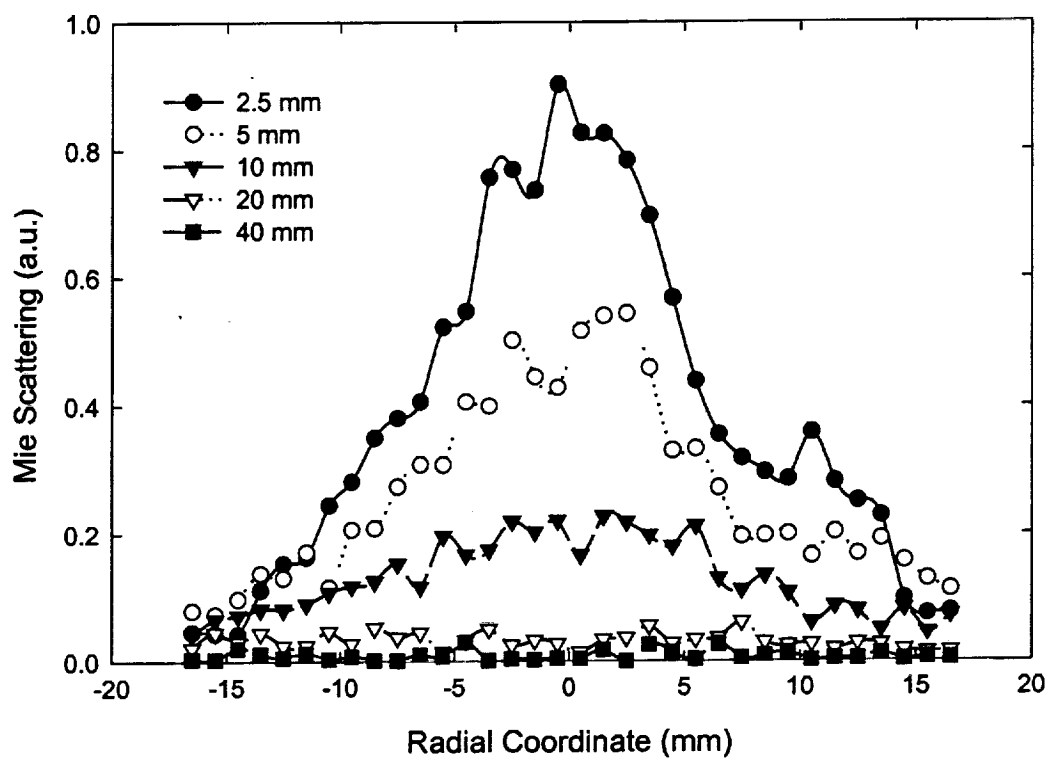


Figure 4.1: Mie scattering radial profiles for 2-atm LDI flame [$\dot{m}_{\text{fuel}} = 0.165 \text{ g/s}$, $\phi = 0.9$, $T_{\text{air preheat}} = 375 \text{ K}$] at five axial heights.

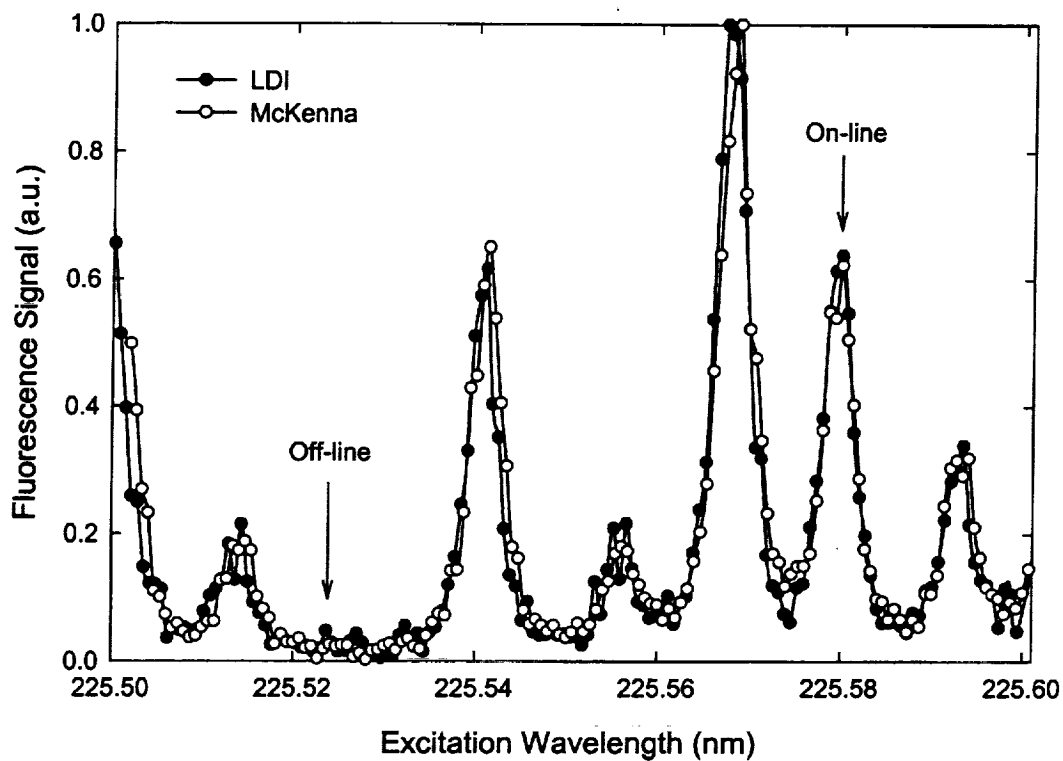


Figure 4.2: Excitation scans at 2 atm in (a) McKenna burner ($\phi = 0.8$, 3.76 dilution ratio) doped with 40 ppm NO, (b) LDI burner at $h = 15$ mm, $r = 0$ mm doped with ~ 80 ppm NO. The NO on-line $Q_2(26.5)$ and off-line excitation wavelengths are labeled.

demonstrates that the oxygen background and Mie scattering breakthrough are negligible for this particular combination of measurement location and operating condition.

A comparative detection scan for the LDI module was also obtained at this location ($h = 15$ mm, $r = 0$ mm). Figure 4.3 shows detection scans for the $\gamma(0,1)$ region with conditions identical to those in the above excitation scans except that the width of the detection window was reduced to 0.5 nm. Again, no unique features are present in Figure 4.4, indicating that the excitation/detection scheme used previously (Cooper and Laurendeau, 1998a) is appropriate for this 2-atm spray flame.

4.5 In-Situ Calibration Method

4.5.1 Theory

Having validated the excitation/detection scheme for this particular spray flame, it became necessary to devise a calibration method by which to quantify the fluorescence measurements. Previous atmospheric measurements (Cooper *et al.*, 1998a) utilized the laser-saturated fluorescence (LSF) methodology. Because of the low sensitivity of LSF to variations in the electronic quenching rate coefficient, a calibration obtained in a reference flame could be transported to the LDI flame so as to quantify the associated NO fluorescence measurements. A similar calibration technique for linear LIF was found to produce erroneous results when compared to saturated LIF. Specifically, the linear LIF-based measurements were 34% larger than the LSF-based measurements throughout the entire flame structure. This scaling results from the ratio of electronic quenching rate coefficients (Paul *et al.*, 1994) in the calibration and the LDI flame. To accurately transfer a calibration from one flame environment to another, the following scaling law must hold:

$$[NO]_{LDI, absolute} = \left(\frac{Q_{e, LDI}}{Q_{e, ref}} \right) [NO]_{LDI, relative} \quad (4.1)$$

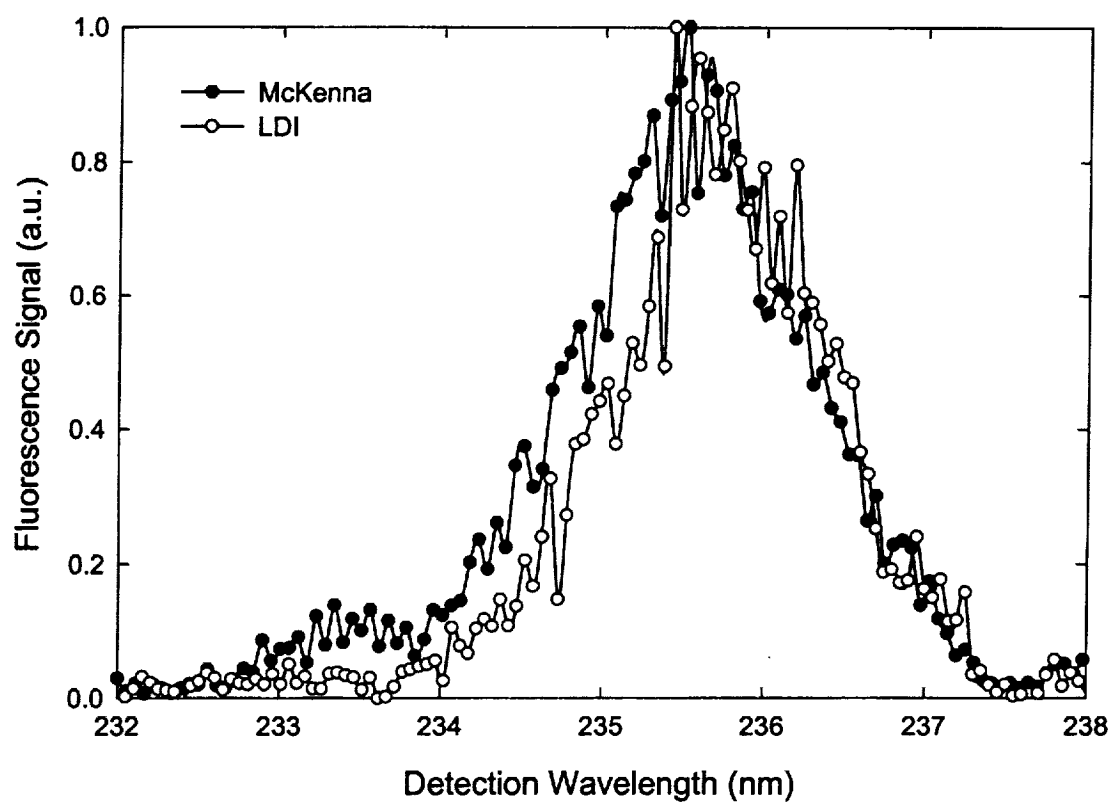


Figure 4.3: Detection scans at 2 atm in McKenna burner ($\phi = 0.8$, 3.76 dilution ratio) doped with 40 ppm NO and LDI burner at $h = 15$ mm, $r = 0$ mm doped with ~ 80 ppm NO.

In other words, the concentration measurements relative to the calibration obtained in the reference flame, $[NO]_{LDI,relative}$, must be scaled by the ratio of the electronic quenching rate coefficients in the LDI and reference flames. This procedure yields absolute concentration measurements, $[NO]_{LDI,absolute}$. While species profiles for a flat, premixed reference flame can be accurately predicted via PREMIX (Kee *et al.*, 1995), the LDI flame cannot be adequately modeled so as to provide the distribution of major species concentrations. Hence, an estimate cannot be determined for the required ratio of local electronic quenching rate coefficients.

The results from our atmospheric study demonstrate that the central region of the recirculation zone can provide a successful fluorescence calibration, barring any destruction of NO as it is transported from the reactants to this region (Cooper *et al.*, 1998). In a similar manner, the post-flame zone of a lean, flat flame stabilized on a reference McKenna burner is often used for fluorescence calibrations. A key consideration of any in-situ calibration method based on doped species is the potential destruction of that species. Doped NO in spray flames must be transported through the rich regions surrounding the liquid droplets, possibly promoting NO destruction. Moreover, the degree of local partial premixing and the local strain rate could play a large role in the destruction of NO. These issues are not readily modeled for the LDI flame, so that an experimental validation is required for any in-situ doping process.

Following Cooper and Laurendeau (1998a) and Thomsen *et al.* (1997), we utilized on- and off-line excitation to obtain calibration curves by varying the amount of NO doped into the flame. The off-line wavelength was chosen to have the same background signal as the on-line wavelength. As such, the intersection of the on-line and off-line calibration curves produces an offset signal corresponding to zero NO concentration that reflects the O₂ fluorescence and Mie scattering background common to both wavelengths, as demonstrated in Figure 4.4. Mathematically, the calibration process can be represented by the following development. First, the LIF signal (LIF_{on}) determined from the PMT and photodiode measurements during on-line excitation is

$$LIF_{on} = LIF_{back} + S_{on}, \quad (4.2)$$

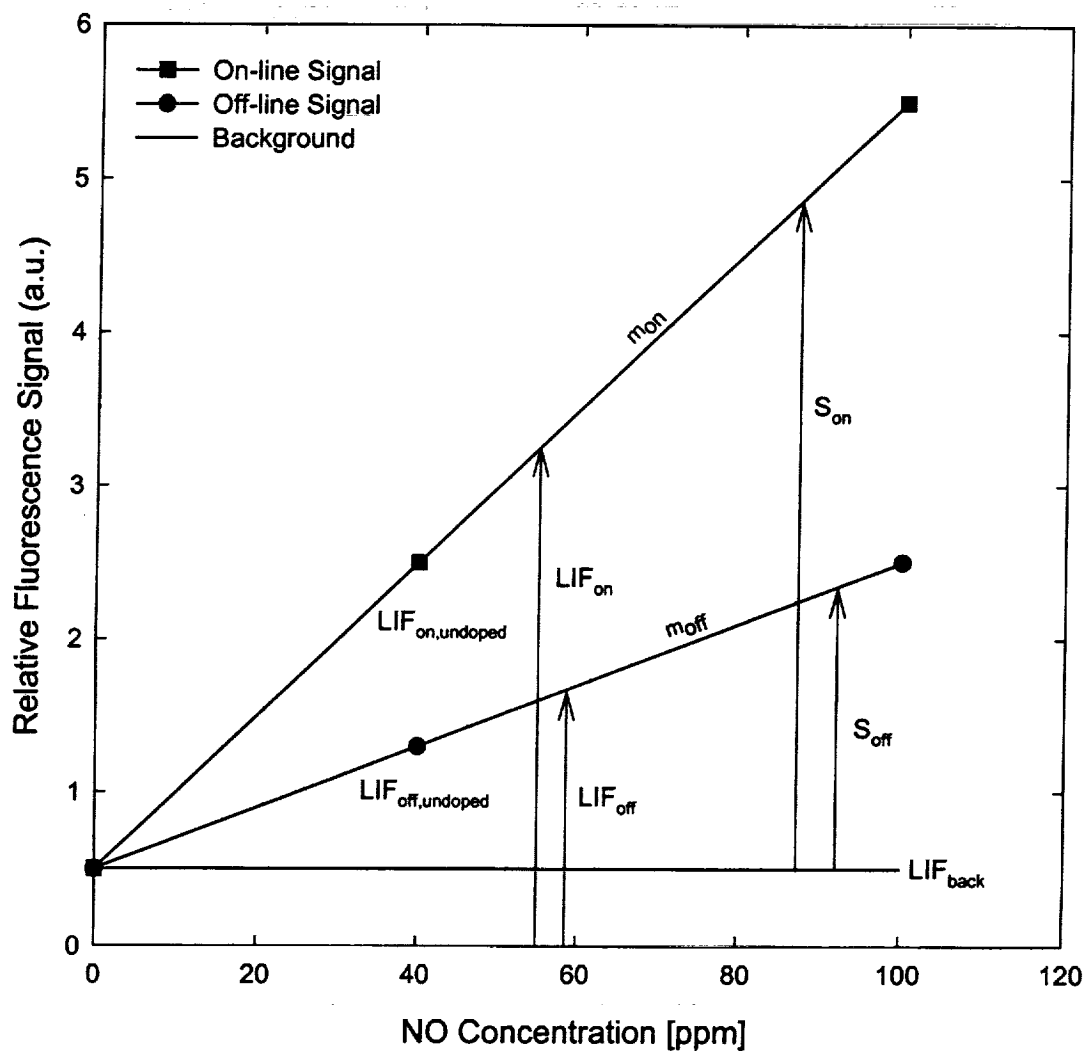


Figure 4.4: Sample calibration curve for high-pressure LIF measurements of NO, illustrating the subtraction technique when utilizing an on-line and off-line calibration referenced to the same LIF background.

where LIF_{back} represents the O_2 fluorescence and Mie scattering background and S_{on} is the actual NO linear fluorescence signal resulting from on-line excitation. Similarly, the off-line LIF signal (LIF_{off}) can be represented as

$$LIF_{off} = LIF_{back} + S_{off}, \quad (4.3)$$

where S_{off} is the NO fluorescence signal resulting from off-line excitation. An off-line NO fluorescence signal always occurs since it is impossible to completely avoid the partial excitation of an NO transition.

The on-line and off-line linear fluorescence signals are proportional to their respective calibration slopes, m_{on} and m_{off} :

$$S_{on} = m_{on}[NO], \quad (4.4)$$

$$S_{off} = m_{off}[NO]. \quad (4.5)$$

Subtracting Eq. (4.3) from Eq. (4.2), we obtain

$$LIF_{on} - LIF_{off} = S_{on} - S_{off}. \quad (4.6)$$

By defining the net calibration slope, m_{net} , as

$$m_{net} = m_{on} - m_{off}, \quad (4.7)$$

Eq. (4.6) can be reduced to

$$\frac{LIF_{on} - LIF_{off}}{m_{net}} = [NO]_{ppm,cal}. \quad (4.8)$$

The LIF signals for any undoped measurement pair, $LIF_{on,undoped}$ and $LIF_{off,undoped}$, can be quickly reduced to an [NO] concentration via Eq. (4.8). Since NO is doped into the flame as various ppm values, a measurement taken at the calibration location reduces to actual NO ppm. However, because of the existence of temperature gradients, the transfer of the calibration from one location to another in the spray flame would require accurate temperature measurements. The measurement of both on- and off-line LIF signals at every point in the flow is also critical to the success of this scheme owing to Mie scattering variations in spray flames. In particular, the above scheme is designed to account for any common background at the measurement location, whether from O_2 fluorescence or Mie scattering (Cooper and Laurendeau, 1998a). Consequently, as the

probe volume is displaced over the spray sheath, Mie scattering may provide an additional offset to the NO fluorescence signal.

4.5.2 Calibration Slope Comparison

To experimentally validate an in-situ doping method in the LDI burner, the flame was seeded with varying amounts of NO and the fluorescence was measured at these ppm levels. The measurement location was chosen to be along the centerline at a 35-mm axial height so as to avoid background interferences from O₂ fluorescence and Mie scattering. NO was seeded into the flow via a calibrated cylinder of 3000-ppm doped nitrogen. Oxygen was added accordingly to maintain a dilution ratio of 3.76, while the building air supplied to the burner was reduced to maintain the same total air flow rate. The local doped nitric oxide concentration was computed based on the product/reactant molar ratio, including the small amount of co-flow air used as diluent. The results of the calibration experiment were corrected for transmission of both the excitation beam and the ensuing fluorescence through the flame. A transmission of ~83% was measured at ~226 nm via photodiodes on either side of the flame. The same transmission was implicitly assumed for the resulting ~236-nm radiation. Subsequently, the LDI burner in the high-pressure vessel was replaced with a water-cooled McKenna burner. Calibration measurements were then performed in the post-flame region of a flat, lean ($\phi = 0.8$, 3.76 dilution ratio) C₂H₆/O₂/N₂/NO flame. Possible window soot deposited by the LDI flame during start-up was common to both burners and could be accounted for with respect to transmission losses at the end of the flat-flame experiment. Typical window soot transmission losses were less than 5%.

The two-atmosphere calibration experiments required excitation only at the on-line wavelength since the off-line wavelength gave negligible signal levels for both flames relative to that from resonant excitation (~3%). As noted previously, the probe volume location in the LDI flame was specifically chosen to avoid potential interferences, thus maximizing the signal that results from NO fluorescence for this comparison. The final calibrations are shown in Figure 4.5 with each data point

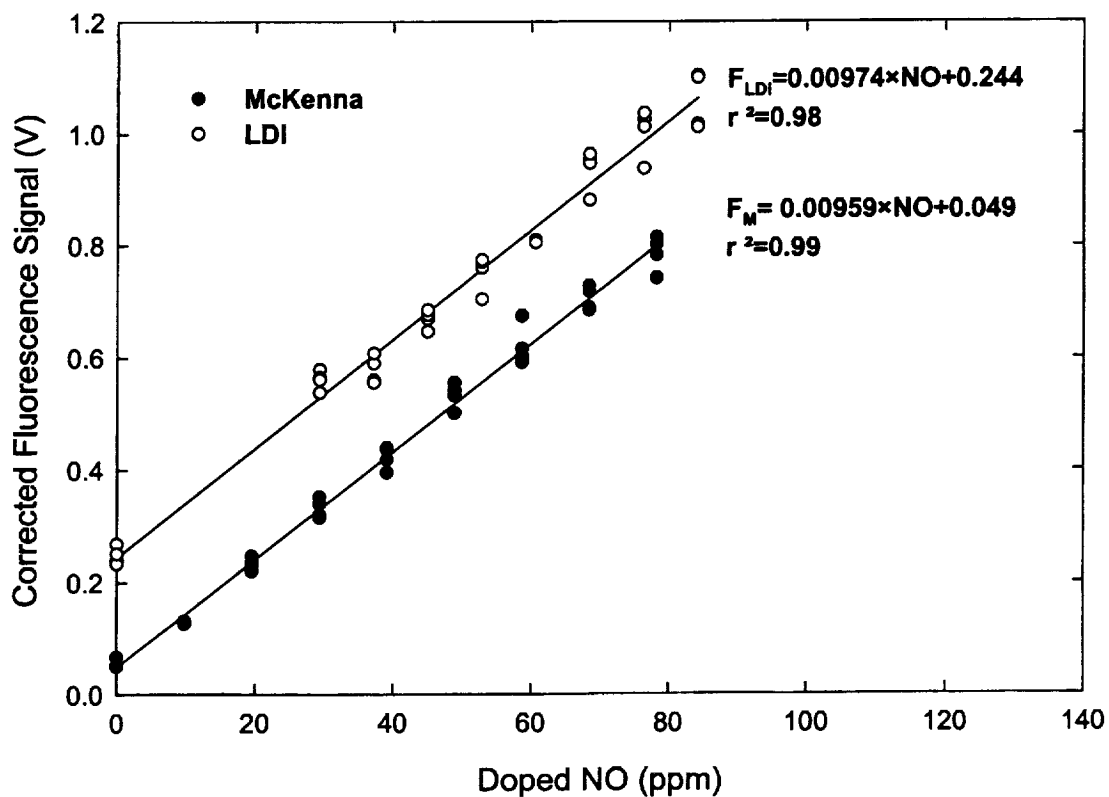


Figure 4.5: NO fluorescence calibrations at 2 atm taken (a) in the post-flame zone of a lean ($\phi = 0.8$, 3.76 dilution ratio) $C_2H_6/O_2/N_2/NO$ flame stabilized on a water-cooled McKenna burner and (b) along the centerline, 35-mm above a heptane-fueled ($\phi = 0.9$, 3.76 dilution ratio, 373 K preheat) LDI burner.

representing the average of 600 fluorescence events. The calibration slopes display excellent agreement, with the offsets indicating the relative NO ppm levels prior to doping. While the calibration slopes are essentially identical, it should be pointed out that the fluorescence signal is actually proportional to NO number density. Moreover, any variation in the quenching rate coefficient is inherently included in the measured slopes. Fortunately, quenching rate coefficients calculated from adiabatic flame temperatures and major species for these two flames agree to within 1% when assuming complete combustion (Paul *et al.*, 1994). Temperature measurements at the calibration location in the LDI flame via a robust type B thermocouple with a 775- μm bead diameter and with a conservative radiation correction of 200 K yields ~ 1700 K, which is similar to the temperature of 1715 K computed via PREMIX for the post-flame zone of the flat $\text{C}_2\text{H}_6/\text{O}_2/\text{N}_2/\text{NO}$ reference flame. All considerations aside, the similarity of the calibration slopes demonstrates that NO destruction is not a significant factor in the transport of doped NO to the central region of this LDI flame.

4.5.3 Relative Calibration Measurements

As indicated above, to enhance the accuracy of our NO measurements, we must consider the effects of both varying temperatures and electronic quenching rate coefficients throughout the measurement field. The presence of Mie-scattering signals in the central region (see Fig. 4.1) indicates that this particular 2-atm flame is not operating efficiently, likely producing considerable gradients in the axial temperature profile, even within the recirculation zone. To assess the change in calibration slope along the centerline axis, calibration slopes were measured at 2.5, 5, 10, 20, 35, and 40 mm above the burner. Each calibration slope was calculated as the difference between the on-line slope and the off-line slope, as backgrounds may change considerably owing to the presence of Mie scattering at lower elevations. These individual calibrations were corrected for beam and fluorescence extinction and are plotted in Figure 4.6 normalized to the slope at a height of 35-mm. Accuracy bars are typically $\pm 14\%$ at the 95% confidence limit and include a conservative 5% relative uncertainty in possible NO

destruction. For this procedure, we are assuming that NO is not destroyed sufficiently to negatively influence the resulting calibration.

The decrease in calibration slope with dropping axial height in Figure 4.6 can be interpreted as indicating an increase in temperature in the lower region of the LDI flame. Previous work at atmospheric pressure demonstrates that the electronic quenching rate coefficient (Q_e) in strongly swirling LDI spray flames is essentially uniform in the central region (Cooper and Laurendeau, 1998b). Figure 4.7 shows the negligible variation in Q_e for a 2-atm heptane flame based on equilibrium state relationships for the mole fractions of major species and temperature (Paul *et al.*, 1994). Though the temperature changes considerably, Q_e remains relatively uniform in the lean regions of the flame. The fluorescence signal is affected by both temperature and the electronic quenching rate coefficient, i.e.,

$$S_F \approx C \frac{x_{NO}}{T \cdot Q_e} \quad (4.9)$$

where x_{NO} is the mole fraction of NO, T is the temperature, and C is a constant based on optical parameters and the transition rate coefficients. On the basis of Eq. (4.9), it becomes beneficial to construct a state relationship for S_F via Figure 4.7, which indicates the relative change in fluorescence signal throughout the flame for a known ppm level of NO. In particular, Figure 4.8 plots the value of $1/T \cdot Q_e$ normalized to that at 1700 K (estimated temperature at 35-mm axial height for LDI flame) against the flame temperature for lean mixture fractions. By comparing the Mie-scattering profiles in Figure 4.1 to the calibration slopes in Figure 4.6, it appears that the decrease in calibration slope at lower axial heights is related to the presence of droplets in the lower centerline region of the flame. Specifically, the ~20% drop in calibration slope is consistent with an increase in temperature from 1700 K to ~2050 K, as demonstrated in Figure 4.8. This result is quite reasonable since the adiabatic flame temperature for $\phi = 1.0$ is above 2300 K and droplets are expected at lower elevations owing to the weak swirl discussed previously. We will therefore adopt the position that the calibration slopes depicted in Figure 4.6 represent the actual relative fluorescence calibrations at each axial height and are not the result of NO destruction.

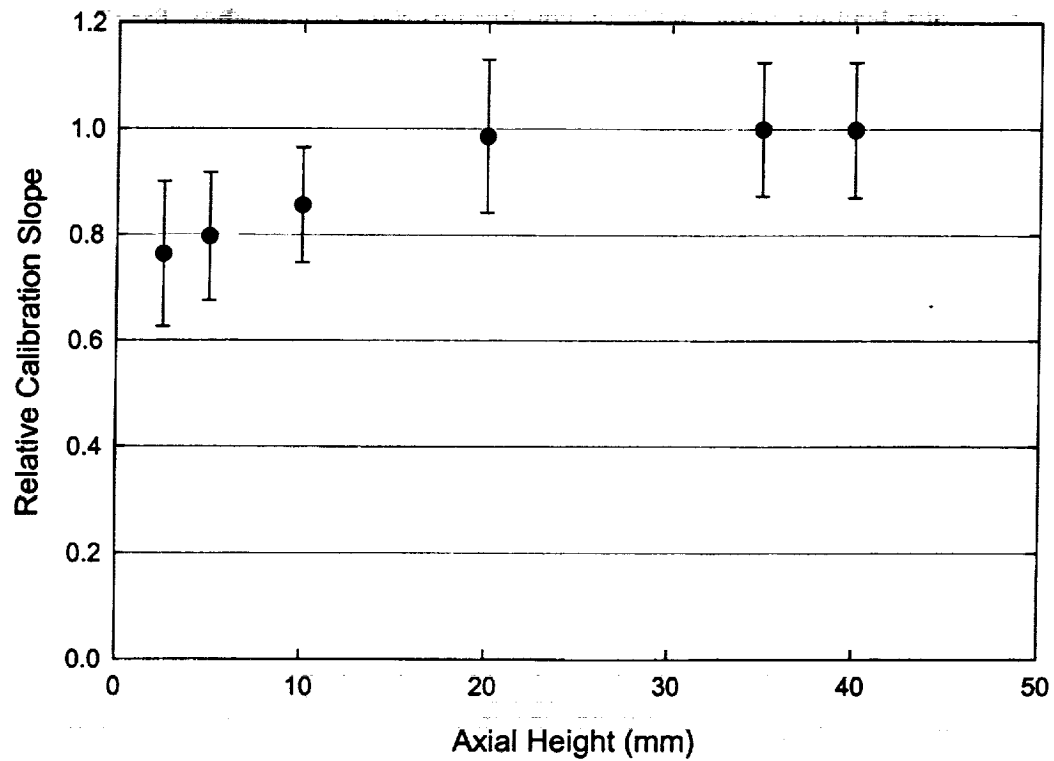


Figure 4.6: NO calibration slopes at 2 atm, measured for centerline axial locations and normalized to that at the 35-mm axial height. All calibrations are corrected for transmission effects at the given axial height.

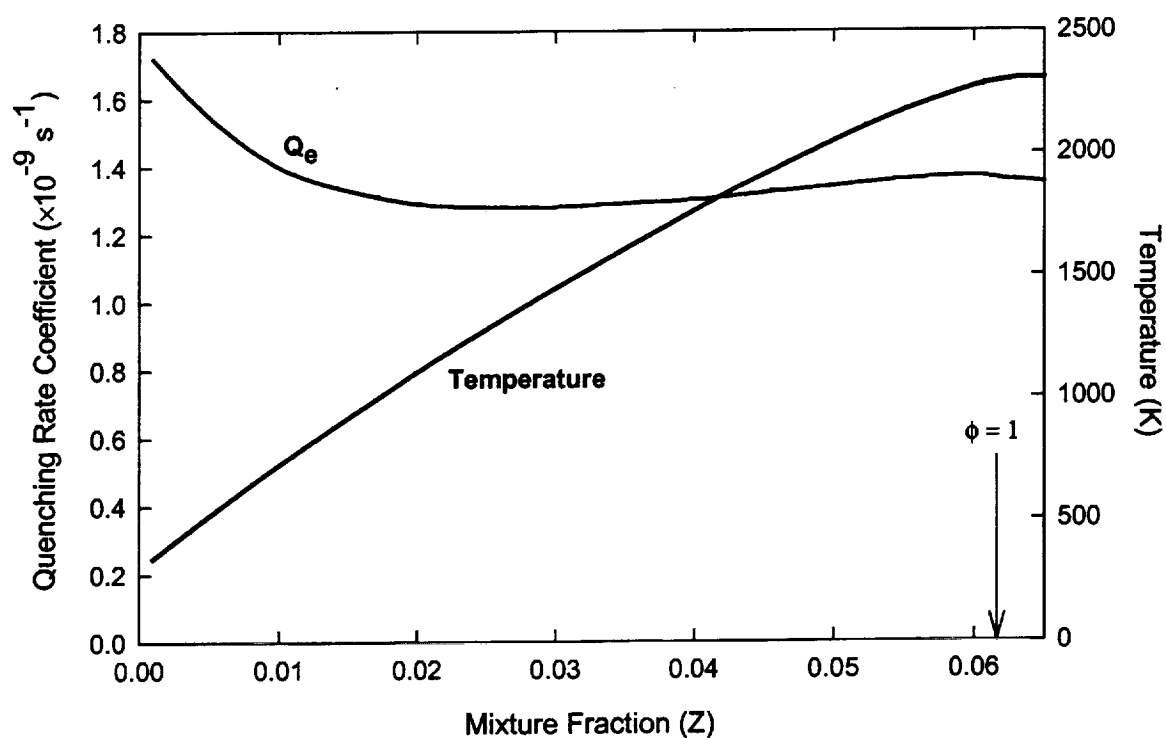


Figure 4.7: Equilibrium state relationships for temperature and the electronic quenching rate coefficient (Q_e) for 2-atm heptane combustion. Note the negligible variation of Q_e at lean mixture fractions.

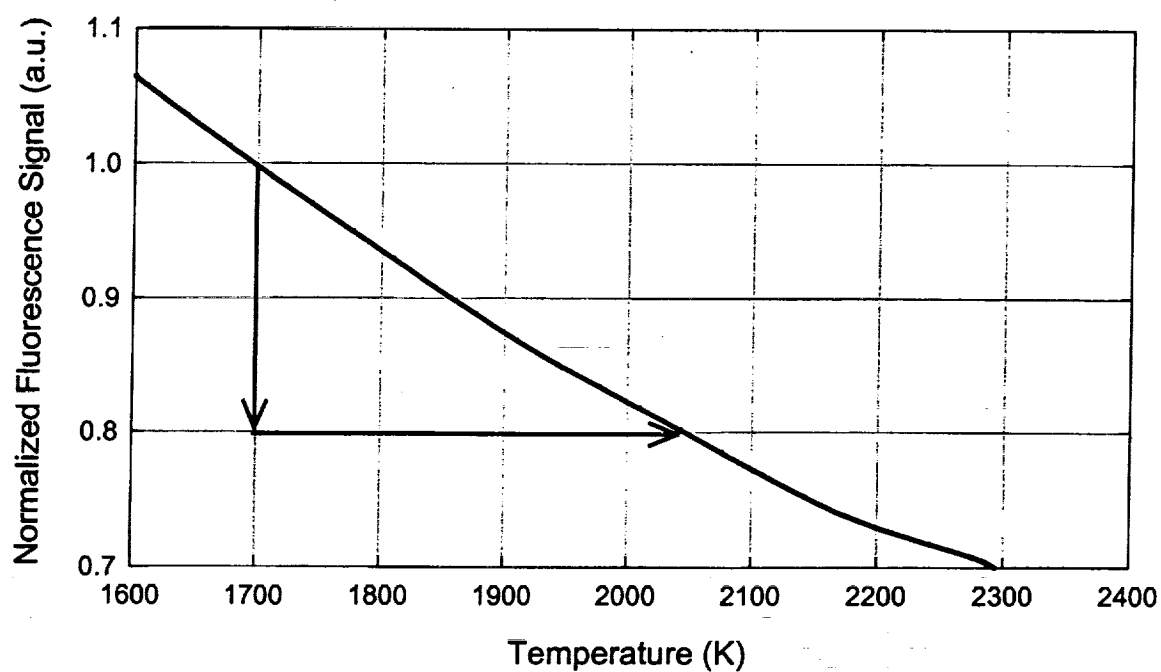


Figure 4.8: Fluorescence signal state relationship at 2 atm for a fixed ppm level of NO normalized to that at 1700 K. A decrease in the fluorescence signal of 20% corresponds to a temperature rise from 1700 K ($\phi = 0.6$) to ~2050 K ($\phi = 0.8$).

4.5.4 Experimental Procedure

To obtain NO profiles in the LDI spray flame, we employed the following experimental protocol. The quartz windows were cleaned at the start of the experiment to ensure minimal transmission losses owing to soot. Soot deposition occurred only during flame ignition when the flame was burned rich while the vessel was sealed and brought to the operating pressure. The LDI flame was stabilized in the pressure vessel for a period of one to two hours to allow the vessel to reach a steady temperature. During this period, the wavelength-feedback system was initialized, which required an excitation scan over the Q₂(26.5) transition. NO was then doped into the flame to obtain an NO fluorescence calibration at the 35-mm centerline height specific to the experimental measurements that day. The translation system was then employed to translate the entire high-pressure vessel relative to the probe volume. In this manner, fluorescence profiles along the major diameter were mapped utilizing both on-line and off-line excitation wavelengths at each point, thus accounting for variations in O₂ fluorescence and Mie scattering background throughout the flame.

Photodiodes placed at the optical entrance and exit of the vessel were utilized to measure laser-beam power ratios across the LDI flame and thus to calculate the global transmission (τ_{global}) at each axial height. This measurement represents beam extinction through the full diameter of the flame. The data reduction accounted for global extinction at each axial height by assuming equivalent absorption coefficients for both 226-nm and 236-nm radiation. The calculated τ_{global} was thus used to account for both beam extinction prior to reaching the probe volume and fluorescence trapping normal to the excitation beam. Power ratios were also measured through the entrance window to account for slight variations in soot deposition which could affect the transmission of the excitation beam. The effect of soot deposition on the window was thus calculated as a soot transmission (τ_{soot}) at each axial height. Recognizing that the flame is symmetric and that the photodiode used to measure the laser beam power is positioned prior to the vessel entrance window, the NO levels can be calculated via Eq. (8) as:

$$[NO]_{\text{ppm,rel}} = \frac{LIF_{\text{on,h}} - LIF_{\text{off,h}}}{m_{\text{net,cal}}} \cdot \frac{\tau_{\text{global,cal}} \cdot \tau_{\text{soot,cal}}}{\tau_{\text{global,h}} \cdot \tau_{\text{soot,h}}} \quad (4.10)$$

The LIF data designated $LIF_{on,h}$ and $LIF_{off,h}$ at a given height h are reduced to relative ppm values, $[NO]_{ppm,rel}$, by employing the 35-mm fluorescence calibration, $m_{net,cal}$. The term *relative* implies that the NO values are calculated relative to the fluorescence calibration at the temperature and electronic quenching rate coefficient corresponding to the 35-mm axial height location. The ratios of transmission values at the calibration height to those at the measurement height are necessary to correct the data, since the calibration slope $m_{net,cal}$ inherently includes the effects of losses at the calibration height. The resulting NO concentrations are thus expressed relative to the calibration point, to within any gradients in the electronic quenching rate coefficient throughout the measured region. As discussed previously, the electronic quenching rate coefficient is relatively constant in lean regions of the flame. Hence, if the temperature at the calibration point were accurately known, the NO profiles could be converted to absolute number density measurements.

On a separate day, the experiment was altered to measure the calibration slopes at the centerline of each axial height profiled (see Fig. 4.6). These calibration slopes require correction for extinction and soot transmission losses in a manner similar to the relative NO measurements. A final data reduction accounted for the ratio of the fluorescence calibration at a particular axial height to that at the 35-mm location, i.e.,

$$[NO]_{ppm,abs} = [NO]_{ppm,rel} \cdot \frac{m_{net,cal}}{\tau_{global,cal} \cdot \tau_{soot,cal}} \cdot \frac{\tau_{global,h} \cdot \tau_{soot,h}}{m_{net,h}} \quad (4.11)$$

In this manner, each radial profile was analyzed via a calibration specific to that axial height, thus providing a measure of the absolute NO ppm level, $[NO]_{ppm,abs}$. Notice also that the effect of global transmission and soot losses is now removed at a given axial height. Though these transmission values ultimately cancel in the final data reduction of Eqs. (4.10) and (4.11), experimental accuracy requires that these quantities be measured during each separate experiment owing to repeatability concerns.

Since each radial profile is referenced to the calibration taken at its centerline, the profiles become skewed as absorption reduces the transmission with increasing path length. Hence, those measurements taken past the centerline are preferentially lower,

whereas those taken prior to the centerline are preferentially higher. It should be emphasized, however, that the centerline measurement in each axial calibration is an absolute measurement, as all effects other than possible NO destruction are inherently included in the calibration, as previously discussed. To correct for the skewness of the NO profiles that resulted from absorption losses, the profiles were mirrored and averaged. A simple model was constructed to validate this correction technique for a range of absorption coefficient profiles and NO concentration profiles in an axisymmetric grid, recognizing that both the laser beam and NO fluorescence pass through different path lengths as a function of measurement position. The results indicate that this correction procedure is quite satisfactory owing to the centerline pivot point that the profiles are referenced to via the fluorescence calibration. The accuracy of the method increases as the NO concentration profiles and the absorption coefficient become more uniform throughout the flame.

4.6 Results

The resulting absolute NO profiles are displayed in Figure 4.9. Accuracy bars are indicated at each location and are typically $\pm 25\%$ at the 95% confidence limit. The repeatability of these measurements is $\sim 7\%$. The accuracy of previous LIF measurements in high-pressure gaseous flames typically ranges from 10% to 25% for pressures below 6 atm (Thomsen *et al.*, 1997). As for our previous atmospheric LDI flames, high swirl minimizes radial NO gradients at all axial heights. However, the maximum NO mole fraction decreases as the axial height rises, thus demonstrating the dilution of produced NO as the flame diverges. As indicated by Figure 4.6, a single calibration at $h = 35$ mm would be sufficient for quantitative measurements of NO at heights $h \geq 20$ mm in this LDI flame. Similarly, the same single-point calibration would provide NO concentrations accurate to within 20% at heights $h < 20$ mm.

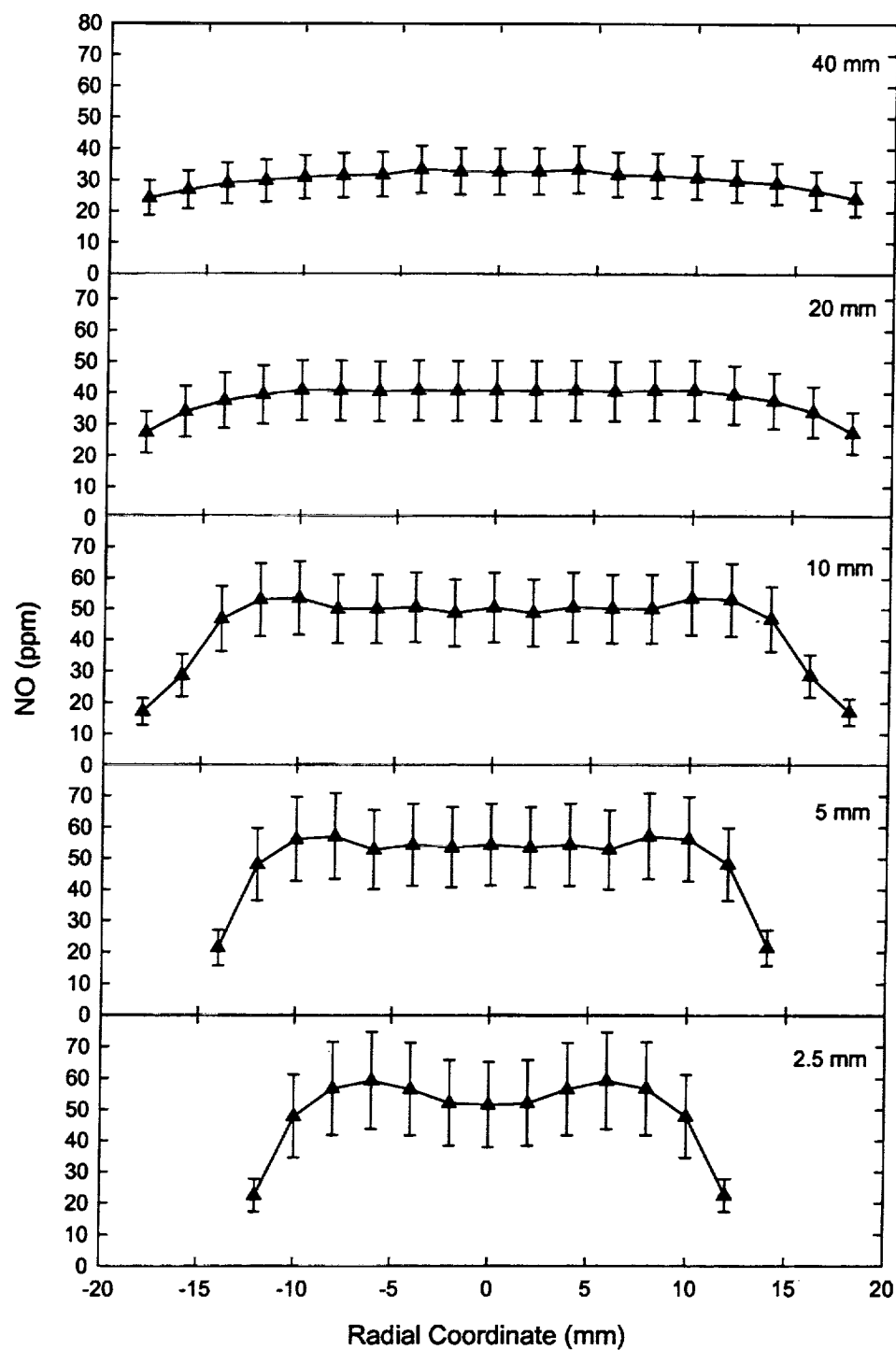


Figure 4.9: Absolute NO (ppm) measurements in 2-atm LDI flame. Radial NO profiles have been corrected for absorption and calibrated at each axial height.

If the calibrated measurement point at an axial height of 35 mm is taken to represent the emission level of this burner owing to its downstream location, then an $EINO_x$ value can be computed similar to that of Chen and Driscoll (1990), i.e.,

$$EINO_x = \frac{x_{NO} (ppm)}{1000} \cdot \frac{M_{NO_2}}{M_P} \cdot \frac{\dot{m}_f + \dot{m}_a}{\dot{m}_f}, \quad (4.12)$$

where M_{NO_2} and M_P represent the molecular weights of nitrogen dioxide and the products of combustion, while \dot{m}_f and \dot{m}_a represent the mass flow rates of fuel and air. The molecular weight of NO_2 is chosen to represent NO_x instead of NO . We assume for this calculation that the products result from complete combustion, which provides a good estimate of the product molecular weight owing to the overriding presence of nitrogen. Equation (10) yields an $EINO_x = 1.00$ g NO_x /kg fuel. Another method of measuring the emission level is based on 15% O_2 in the product stream. Following Turns (1996), the calibrated and corrected measurement would be 11 ppm. Assuming a pressure scaling of $P^{0.5}$ (Turns, 1996) and extrapolating the calibration point to 30 atm would yield an $EINO_x = 3.79$ g NO_x /kg fuel, which is below the aeropropulsion engine target of 5 g NO_x /kg fuel (Gupta, 1997). Though such exhaust values could be determined from sampling our exhaust stream, the ability to optically measure NO concentrations clearly provides the opportunity to better understand the production of NO within the flame.

4.7 Conclusions

Quantitative LIF measurements of NO concentration (ppm) have been obtained in an LDI burner fueled with liquid heptane operating at a pressure of 2 atm. The thrust of this chapter has been the development and validation of an in-situ calibration scheme by which to quantify NO fluorescence signals measured in high-pressure LDI spray flames. Through comparison of fluorescence calibrations taken in the spray flame and in a reference flame of known spectral characteristics at 2 atm, we have validated the use of a reactant doping method for such spray flames. Possible NO destruction did not present significant losses to the doped NO , thereby allowing a simple means by which to quantify

fluorescence measurements. Quantitative NO profiles were presented for the 2-atm LDI flame and were demonstrated to yield acceptable emission levels under current target goals for NO_x reduction.

5. QUANTITATIVE MEASUREMENTS OF NITRIC OXIDE IN HIGH-PRESSURE (2-5 ATM), SWIRL-STABILIZED SPRAY FLAMES VIA LASER-INDUCED FLUORESCENCE

5.1 Introduction

In this chapter, we present spatially resolved, linear laser-induced fluorescence measurements of nitric oxide (NO) in pre-heated, high-pressure (2.09 to 5.35 atm), lean direct-injection (LDI) spray flames. The spray is produced by a hollow-cone, pressure-atomized nozzle supplied with liquid heptane. NO is excited via the $Q_2(26.5)$ transition of the $\gamma(0,0)$ band. Detection is performed in a 2-nm region centered on the $\gamma(0,1)$ band. The goal of this chapter is the validation and application of a complete LIF scheme by which quantitative NO concentrations can be measured in high-pressure LDI spray flames. Standard excitation and detection scans are performed to assess possible interferences and to validate a non-resonant wavelength so as to subtract the influence of oxygen interferences in the NO detection window. NO is doped into the reactants and convected through the flame with no apparent destruction, thus allowing an NO fluorescence calibration to be taken inside the flame environment. The in-situ calibration scheme is validated by comparisons with reference flames at high pressure. Quantitative radial NO profiles are presented at 2.09, 3.18, 4.27, and 5.35 atm and analyzed so as to better understand the operation of lean-direct injectors for gas turbine combustors. Downstream NO measurements in the LDI flames indicate an overall pressure scaling corresponding to $P^{0.74}$.

5.2 Operating Conditions

The LDI burner is operated at a primary equivalence ratio $\phi_p = 0.9$, using heptane as the fuel. The flow rates for the study presented here are listed in Table 5.1. An additional air co-flow is added to aid in flame stabilization, which gives the tabulated overall ϕ_o if this air were completely entrained into the combustion products. The air is preheated to 373 K in all cases to assist in vaporization and mixing of the fuel. Because of the intense mixing, the flames are essentially non-sooting and blue, even at higher pressures.

5.3 Spectral Validation

Our previous work, as discussed in Chapters 2 and 4, addressed an excitation/detection scheme for use in LDI flames at 1-2 atm (Cooper and Laurendeau, 1998a; Cooper and Laurendeau, 1999b). Excitation of the $Q_2(26.5)$ line of the $\gamma(0,0)$ band of NO at 225.58 nm is followed by detection of the $\gamma(0,1)$ band with a 2-nm window centered at 235.78 nm. An off-line wavelength at ~ 225.53 nm is excited and monitored as a measure of the ubiquitous background for the NO fluorescence signals. This combination has been selected based on extensive interference and background investigations (Reisel *et al.*, 1993; Partridge *et al.*, 1996) and has shown considerable success in a variety of flames produced with gaseous and liquid fuels (Reisel and Laurendeau, 1995; Thomsen *et al.*, 1997; Cooper and Laurendeau, 1998b; Cooper and Laurendeau, 1999b). The scheme has been particularly useful in high-pressure (1-15 atm) $\text{CH}_4/\text{O}_2/\text{N}_2$ flames (Thomsen *et al.*, 1997). For LDI sprays, the utility of this scheme lies in the subtraction of Mie-scattering and O_2 interferences (Cooper and Laurendeau, 1998a; Cooper and Laurendeau, 1999b). At even higher pressures, such a scheme is critical to the detection of NO levels below 10 ppm owing to the background produced by the O_2 Schumann-Runge band (Thomsen *et al.*, 1997).

Table 5.1: Operating conditions for LDI flames of this study.

Nominal Pressure (atm)	Operating Pressure (atm)	Fuel Flow (g/s)	Primary Air Flow (g/s)	Secondary Air Flow (g/s)	ϕ_p	ϕ_b
2	2.09	0.17	2.78	0.30	0.90	0.81
3	3.18	0.26	4.40	0.38	0.90	0.83
4	4.27	0.36	6.07	0.32	0.90	0.85
5	5.35	0.49	8.32	0.32	0.90	0.87

5.3.1 Mie Scattering Profiles

The utility of our NO excitation/detection scheme in a liquid droplet environment at higher pressures requires that we re-consider the possible effects of Mie scattering interference, fuel and fuel-fragment fluorescence, and laser beam extinction. We assessed the influence of Mie scattering at 2 and 4 atm by measuring scattering profiles in order to locate regions of heavy droplet interference. Scattered light at the incident laser wavelength is passed through neutral density filters and collected via a 1/2-m monochromator in a 2-nm window centered at ~226 nm. Figure 5.1 depicts the Mie scattering profiles in both the 2- and 4-atm flames. As discussed in Chapter 4, the 2-atm profiles are quite different from those measured in the previous atmospheric LDI work (Cooper and Laurendeau, 1998a). In particular, the previous 1-atm LDI measurements resulted in axisymmetric double-peaked profiles that followed the spray sheath typically associated with strongly swirling spray flames (Lee and Chehroudi, 1995). However, the low flow rates required to stabilize the present 2-atm flame reduces the strength of the recirculation zone and the efficiency of the atomizer. Fortunately, as the operating pressure increases, the rising flow rate through the nozzle produces efficient atomization. The 4-atm Mie scattering profiles demonstrate this feature and compare favorably with the expected profiles based on our 1-atm study. As mentioned in Chapter 3, two special CVI dichroic beamsplitters are employed in NO detection to minimize any resulting interferences from Mie scattering, especially at lower heights above the LDI burner (Cooper and Laurendeau, 1999a)

5.3.2 Excitation and Detection Scans

Excitation and detection scans were next performed to assess the level of potential interferences associated with possible unburned hydrocarbons. A reference $\text{C}_2\text{H}_6/\text{O}_2/\text{N}_2/\text{NO}$ ($\phi = 0.8$) flat flame stabilized at 2.09 atm on a water-cooled McKenna burner (3.76 dilution ratio) was utilized for comparison. The spectral signatures from NO and O_2 have been previously well characterized in such flames (Partridge *et al.*, 1996). Hence, a comparison of spectral scans taken in this standard flame with those

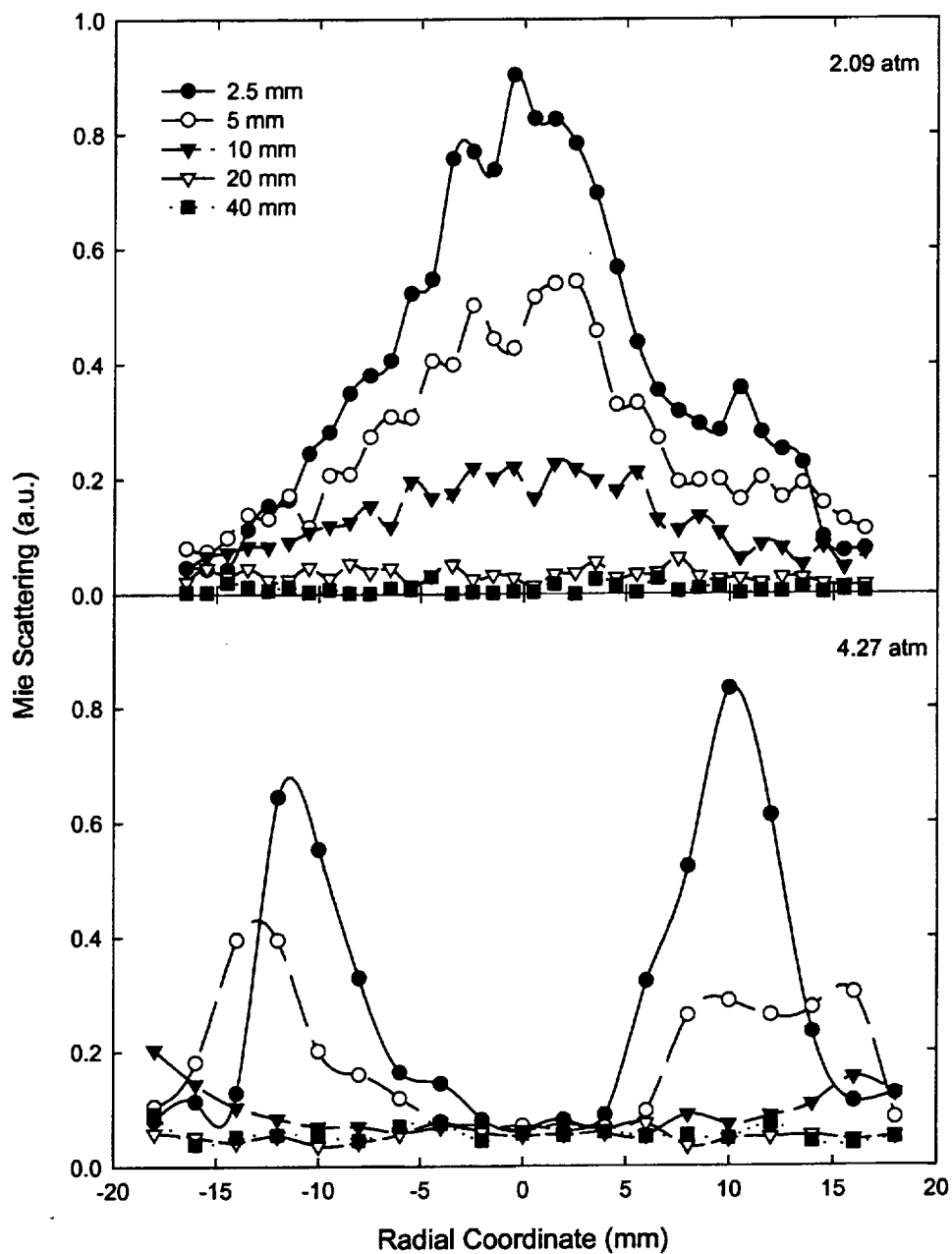


Figure 5.1: Mie scattering radial profiles for LDI flames at 2.09 atm [$\dot{m}_{\text{fuel}} = 0.165$ g/s, $\phi_p = 0.9$, $T_{\text{air preheat}} = 375$ K] and at 4.27 atm [$\dot{m}_{\text{fuel}} = 0.36$ g/s, $\phi_p = 0.9$, $T_{\text{air preheat}} = 373$ K].

obtained in the LDI case should aid in the identification of any interferences resulting from hydrocarbon fluorescence. Figure 5.2a illustrates two excitation scans: one taken in the flat flame with 40 ppm of NO doped into the flame to help define the $\gamma(0,1)$ band structure and one taken at the centerline 15-mm height in the 2.09-atm LDI flame with ~80 ppm of NO doped into the flame. Figure 5.2b illustrates an excitation scan taken at the centerline 15-mm height in the 4.27-atm LDI flame with ~100 ppm NO doped into the flame. The excellent similarity among these excitation scans indicates that other species such as unburned hydrocarbons and polycyclic aromatic hydrocarbons are apparently not monitored in the 2-nm detection window at these pressures. Moreover, the ratio of the on-line to off-line wavelengths demonstrates that the oxygen background and Mie scattering breakthrough are <10% of the on-line signal at this location in the LDI flames.

A comparative detection scan for the LDI module was also obtained at this same location ($h = 15$ mm, $r = 0$ mm). Figure 5.3 displays detection scans for the $\gamma(0,1)$ region with conditions identical to those in the above excitation scans except that the width of the detection window was reduced to 0.5 nm. Again, no unique features are present in Figure 5.3, indicating that the excitation/detection scheme used in Chapters 2 and 4 (Cooper and Laurendeau, 1998a; Cooper and Laurendeau, 1999b) is appropriate for these high-pressure spray flames.

5.4 Calibration Slope Experiments

5.4.1 Calibration Slope Comparison

A mathematical derivation of the background subtraction method utilized for this investigation is given in Chapter 4 (Cooper and Laurendeau, 1999b). In summary, on-line and off-line excitation wavelengths which have common interference backgrounds are used to isolate that portion of the detection signal attributable to NO

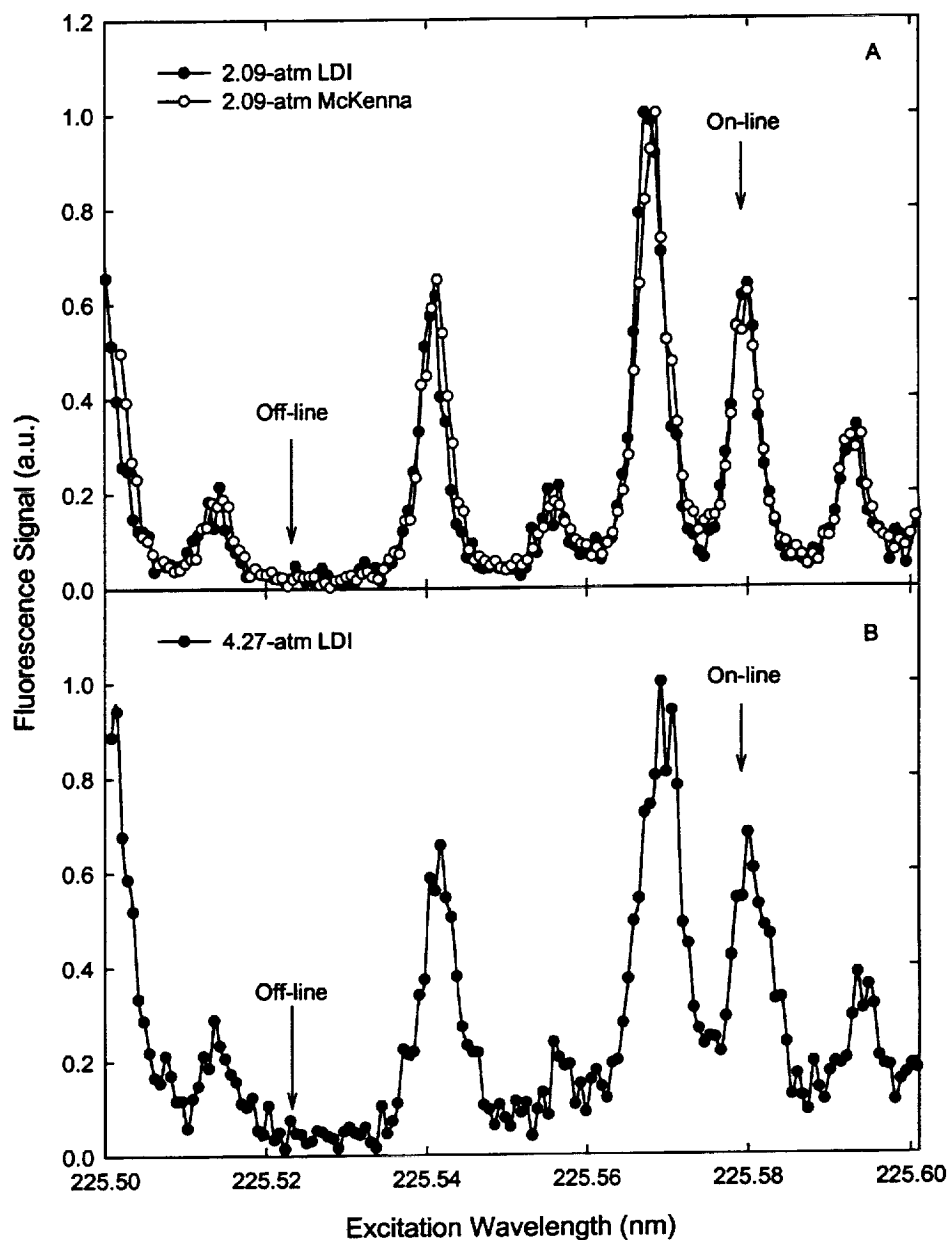


Figure 5.2: Excitation scans in: (a) 2.09-atm McKenna burner ($\phi = 0.8$, 3.76 dilution ratio) doped with 40 ppm NO and 2.09-atm LDI burner at $h = 15$ mm, $r = 0$ mm doped with ~ 80 ppm NO; (b) 4.27-atm LDI burner at $h = 15$ mm, $r = 0$ mm doped with ~ 100 ppm NO. The NO on-line $Q_2(26.5)$ and off-line excitation wavelengths are labeled.

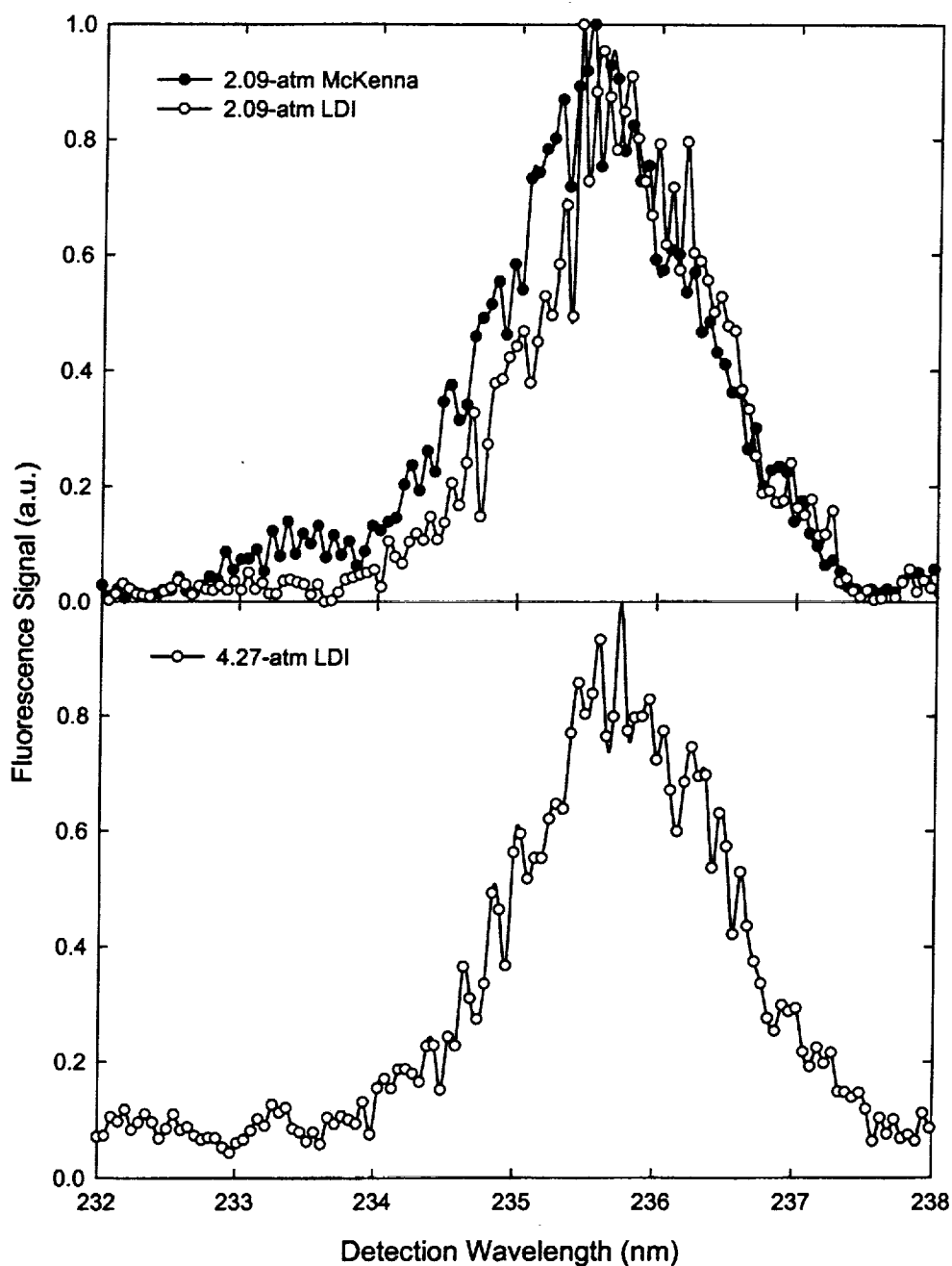


Figure 5.3: Detection scans in: (a) 2.09-atm McKenna burner ($\phi = 0.8$, 3.76 dilution ratio) doped with 40 ppm NO and 2.09-atm LDI burner at $h = 15$ mm, $r = 0$ mm doped with ~ 80 ppm NO; (b) 4.27-atm LDI burner at $h = 15$ mm, $r = 0$ mm doped with ~ 100 ppm.

fluorescence. The method also inherently removes O_2 fluorescence and Mie scattering interferences from the NO signal. On- and off-line measurements are required at each measurement location to account for variations in the background within different regions of the LDI flames.

To experimentally validate an in-situ doping method for the LDI burner, LDI flames at 2 and 4 atm were seeded with varying amounts of NO and the emissive signal was measured at these different ppm levels. The measurement location was chosen to be along the centerline at a 35-mm axial height so as to avoid background interferences from O_2 fluorescence and Mie scattering. NO was seeded into the flow via a calibrated cylinder of 3000-ppm doped nitrogen. In the 2-atm LDI flame, oxygen was added accordingly to maintain a dilution ratio of 3.76, while the building air supplied to the burner was reduced to maintain the same total air flow rate. The 4-atm flame required consecutive measurements with seeded nitrogen and with unseeded nitrogen, as the oxygen flow system was unable to match the required dilution ratio of 3.76. The results of the calibration experiments were corrected for transmission of both the excitation beam and the ensuing fluorescence through the flame. A transmission of ~83% in the 2-atm flame and ~68% in the 4-atm flame was measured at ~226 nm via photodiodes on either side of the flames. The same transmission was implicitly assumed for the resulting ~236-nm radiation. Subsequent to these individual experiments, the LDI burner in the high-pressure vessel was replaced with a water-cooled McKenna burner. Calibration measurements were then performed in the post-flame region of a flat, lean ($\phi = 0.8$, 3.76 dilution ratio) $C_2H_4/O_2/N_2/NO$ flame for the 2-atm case and of a flat, lean ($\phi = 0.8$, 3.76 dilution ratio) $CH_4/O_2/N_2/NO$ flame for the 4-atm case. Possible window soot deposited by the LDI flame during start-up could be accounted for by monitoring transmission losses at the end of the flat-flame experiment. Typical window soot transmission losses were less than 5%.

The 2-atm calibration experiments required calibration of only the on-line excitation wavelength since the off-line wavelength gave negligible signal levels relative to that at resonance (~3%). The 4-atm calibration included both on-line and off-line measurements, as the background signal was now larger (~10%). The results of these

comparative calibrations are shown in Figure 5.4. The calibration slopes at each pressure display excellent agreement, with the offsets indicating the relative NO ppm levels prior to doping. While the calibration slopes are essentially identical, it should be pointed out that the fluorescence signal is actual proportional to NO number density. Moreover, any variation in the quenching rate coefficient is inherently included in the measured slopes. Fortunately, quenching rate coefficients calculated from adiabatic flame temperatures and major species for both LDI flames agree to within 1% with those from their respective reference flames when assuming complete combustion (Paul *et al.*, 1994). Temperature measurements at the calibration location in the LDI flames as obtained via a robust type B thermocouple with a 775- μm bead diameter when using a 200 K radiation correction yield ~ 1700 K for the 2-atm flame and ~ 1830 K for the 4-atm flame. These temperatures are similar to those in the post-flame zone of the flat reference flames of 1715 K and 1782 K, respectively, as computed via PREMIX (Kee *et al.*, 1995). All considerations aside, the similarity of the calibration slopes at both pressures demonstrates that NO destruction is not a significant factor in the transport of doped NO to the central region of the LDI flames.

5.4.2 Relative Calibration Measurements

To enhance the accuracy of our NO measurements, we must consider the effects of both varying temperatures and electronic quenching rate coefficients throughout the measurement field. In particular, we measured calibration slopes along the centerline axis at 2.5, 5, 10, 20, 35, and 40 mm above the burner. Each calibration slope was calculated as the difference between the on-line slope and the off-line slope, as backgrounds may change considerably owing to the presence of Mie scattering at lower elevations. These individual calibrations were corrected for beam and fluorescence extinction and are plotted in Figure 5.5 after normalization to the slope at 35 mm. Accuracy bars are typically $\pm 16\%$ at the 95% confidence level and include a conservative 5% relative uncertainty in possible NO destruction. When employing this procedure, we

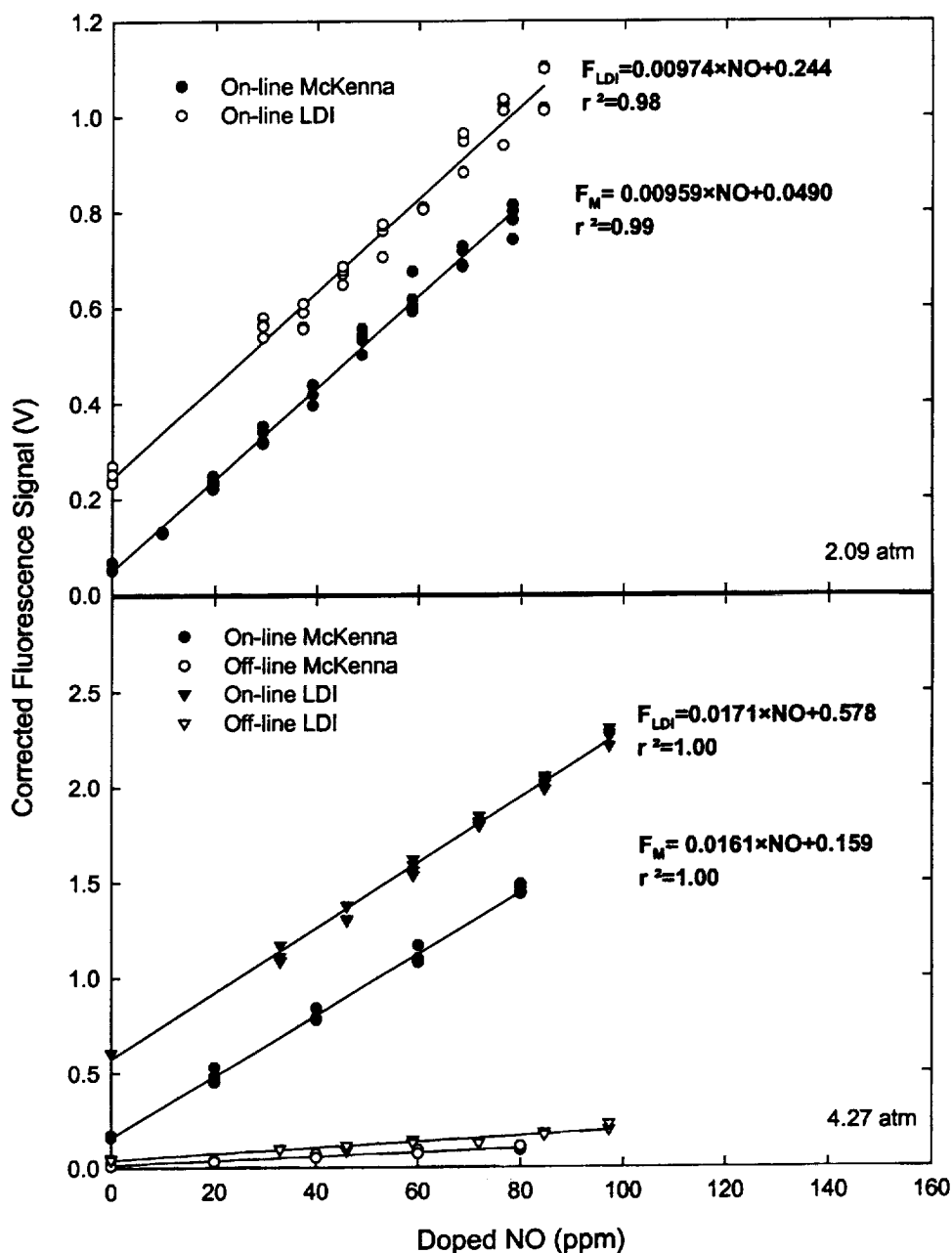


Figure 5.4: NO fluorescence calibrations taken in: (a) post-flame zone of a lean ($\phi = 0.8$, 3.76 dilution ratio) $C_2H_6/O_2/N_2/NO$ flame stabilized on a water-cooled McKenna burner and centerline 35-mm axial height of a heptane-fueled ($\phi_p = 0.9$, 3.76 dilution ratio, 373 K preheat) LDI flame at 2.09 atm; (b) post-flame zone of a lean ($\phi = 0.8$, 3.76 dilution ratio) $CH_4/O_2/N_2/NO$ flame stabilized on a water-cooled McKenna burner and centerline 35-mm axial height of a heptane-fueled ($\phi_p = 0.9$, 3.76 dilution ratio, 373 K preheat) LDI flame at 4.27 atm.

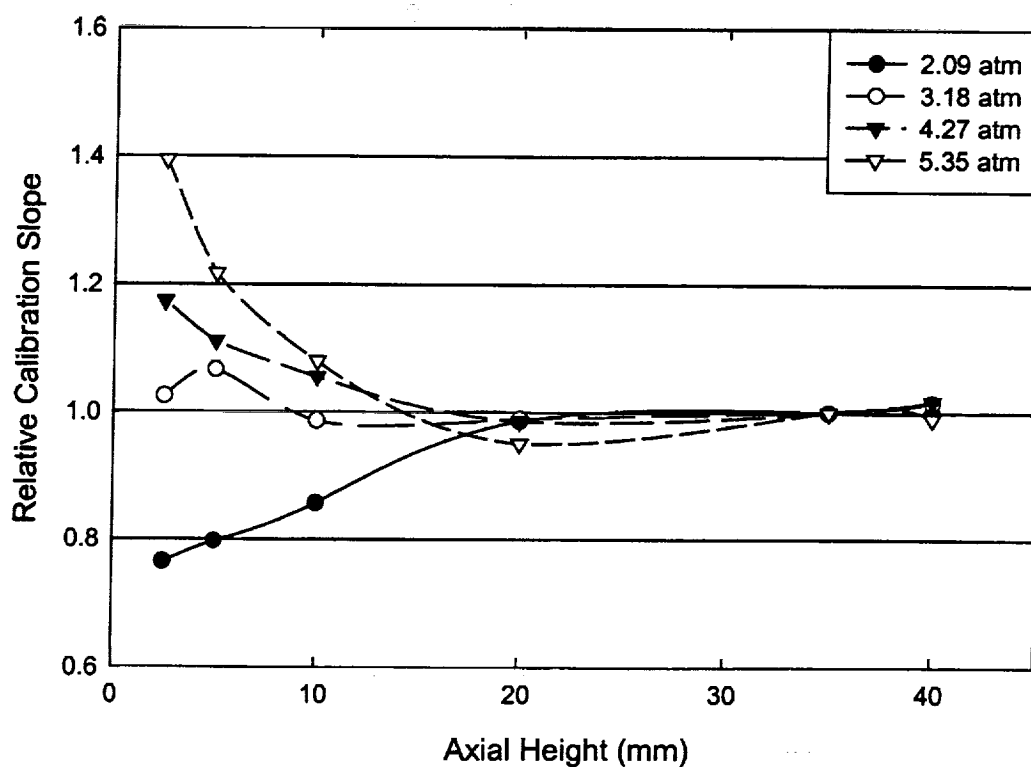


Figure 5.5: NO calibration slopes at centerline axial locations when normalized to that at the 35-mm axial height for 2.09-, 3.18-, 4.27-, and 5.35-atm LDI flames. All calibrations are corrected for transmission effects at the given axial height and pressure. The relative slopes indicate variations in the temperature and the electronic quenching rate coefficient along the axis.

are assuming that NO is not destroyed sufficiently to negatively influence the resulting calibration. The variation in calibration slope with axial height generally indicates the influence of temperature changes in the lower region of each LDI flame. Previous work at atmospheric pressure demonstrates that the electronic quenching rate coefficient (Q_e) is essentially uniform in the central region of strongly swirling LDI spray flames (Cooper and Laurendeau, 1998b). This feature can be readily demonstrated by constructing equilibrium state relationships for species and temperature (see Chapter 4) in the case of heptane combustion and computing Q_e values at lean mixture fractions. Though the temperature changes considerably, Q_e remains relatively uniform in the lean regions of the flame (Cooper and Laurendeau, 1999b).

The fluorescence signal for a fixed ppm-level of doped NO is related to temperature and the electronic quenching rate coefficient by

$$S_F \approx C \frac{x_{NO}}{T \cdot Q_e} \quad , \quad (5.1)$$

where x_{NO} is the NO mole fraction, T is the temperature, and C is a constant based on optical parameters and the transition rate coefficients. Since Q_e is essentially constant in LDI flames, the 20% drop in calibration slope for the 2-atm flame is consistent with an increase in temperature from 1700 K at 35 mm to ~2050 K at 5 mm above the LDI burner (Cooper and Laurendeau, 1999b). This result is quite reasonable since the adiabatic flame temperature for $\phi = 1.0$ is above 2300 K and droplets are expected at lower elevations (see Fig. 5.1). In a similar manner, the 4-atm flame may have a cooler region at lower elevations owing to changes in the recirculation zone position and strength with pressure. Specifically, an increase of the 4-atm calibration slope of ~20% would indicate a decrease in temperature from 1830 K to ~1560 K. This result is also reasonable since the Mie scattering profiles show little droplet scattering at lower elevations for the 4-atm case (see Fig. 5.1). We will therefore adopt the position that the calibration slopes depicted in Figure 5.5 represent the actual relative fluorescence calibrations at each axial height and are not the result of NO destruction.

5.5 Results and Discussion

The experimental procedure for obtaining NO profiles in the LDI spray flame is identical to that discussed in Section 4.5.4. Figure 5.6 demonstrates the corrected data whereby each radial profile is calibrated via the centerline fluorescence signal at a particular axial height and plotted as a function of pressure. A complete picture can now be presented that represents operation of the LDI burner over the 2- to 5-atm pressure range. Error bars are not shown here for clarity, but are typically $\pm 25\%$ at the 95% confidence limit (see Appendix A). The average repeatability for the profiles is within 7%, 5%, 12%, and 12% for the 2-, 3-, 4-, and 5-atm flames, respectively. In general, the profiles at each pressure demonstrate a uniformity of the NO mole fraction throughout the central region of these direct-injection flames. This feature can be attributed to the well-mixed nature of the internal recirculation zone for this swirl-based geometry (Alkabie and Andrews, 1989; Terasaki and Hayashi, 1996).

Figure 5.7 depicts the cumulative profiles at each pressure with a representative accuracy bar plotted at the centerline 40-mm location. The uniformity at each pressure can now be clearly seen for the 3- to 5-atm cases. For the 2-atm flame, the maximum NO mole fraction decreases as the axial height increases, likely demonstrating the dilution of produced NO as the flame diverges. Once efficient atomization of the fuel is achieved at $P \geq 3$ atm, the profiles converge to within the accuracy of the measurements. From Figure 5.6, the mole fraction of NO appears to vary only slightly with pressure at heights below 10 mm. However, past the 10-mm axial height, the combined effects of chemistry, temperature, and residence time yield increasing NO levels with rising pressure.

Figure 5.8 depicts the 40-mm height data and demonstrates a definitive increase in the NO level with pressure. Typical errors bars at the 95% confidence level are shown at a single point for each pressure to represent the accuracy of the radial profile. To determine the scaling of emissions with pressure and remove all errors except potential calibration errors, we chose to use a single point calibration at the 40-mm centerline height for each pressure. We calculate $EINO_x$ following Chen and Driscoll (1990), i.e.,

$$EINO_x = \frac{x_{NO} (ppm)}{1000} \cdot \frac{M_{NO_2}}{M_P} \cdot \frac{\dot{m}_f + \dot{m}_a}{\dot{m}_f}, \quad (5.2)$$

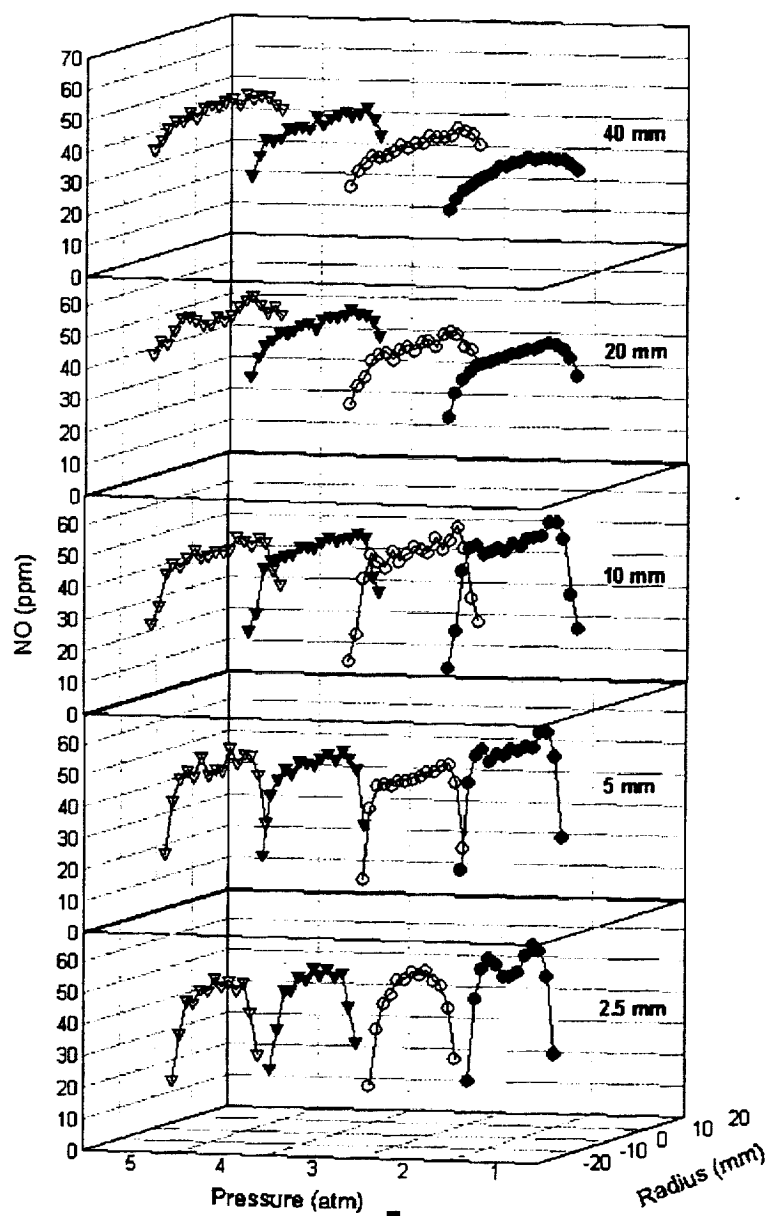


Figure 5.6: NO concentration profiles for 2.09-, 3.18-, 4.27-, and 5.35-atm lean ($\phi_p = 0.9$, 3.76 dilution ratio, 373 K preheat) direct-injection, swirl-stabilized, spray flames. Accuracy bars are typically 25% at the 95% confidence level over this pressure range.

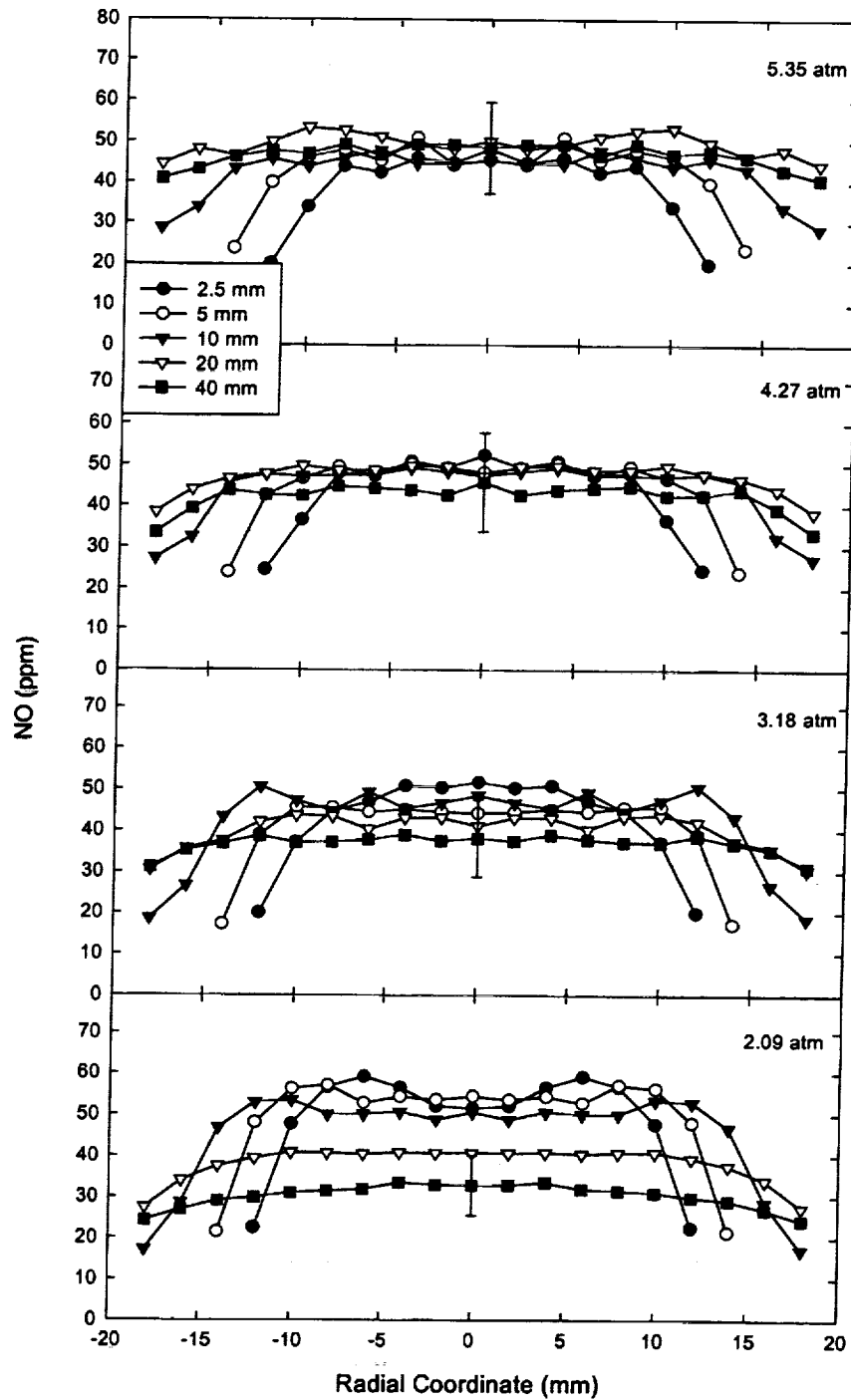


Figure 5.7: Cross-sectional NO concentration profiles for 2.09-, 3.18-, 4.27-, and 5.35-atm lean ($\phi_p = 0.9$, 3.76 dilution ratio, 373 K preheat) direct-injection, swirl-stabilized, spray flames. Note the uniformity of the NO profiles throughout the measured region for the 3.18-, 4.27-, and 5.35-atm cases.

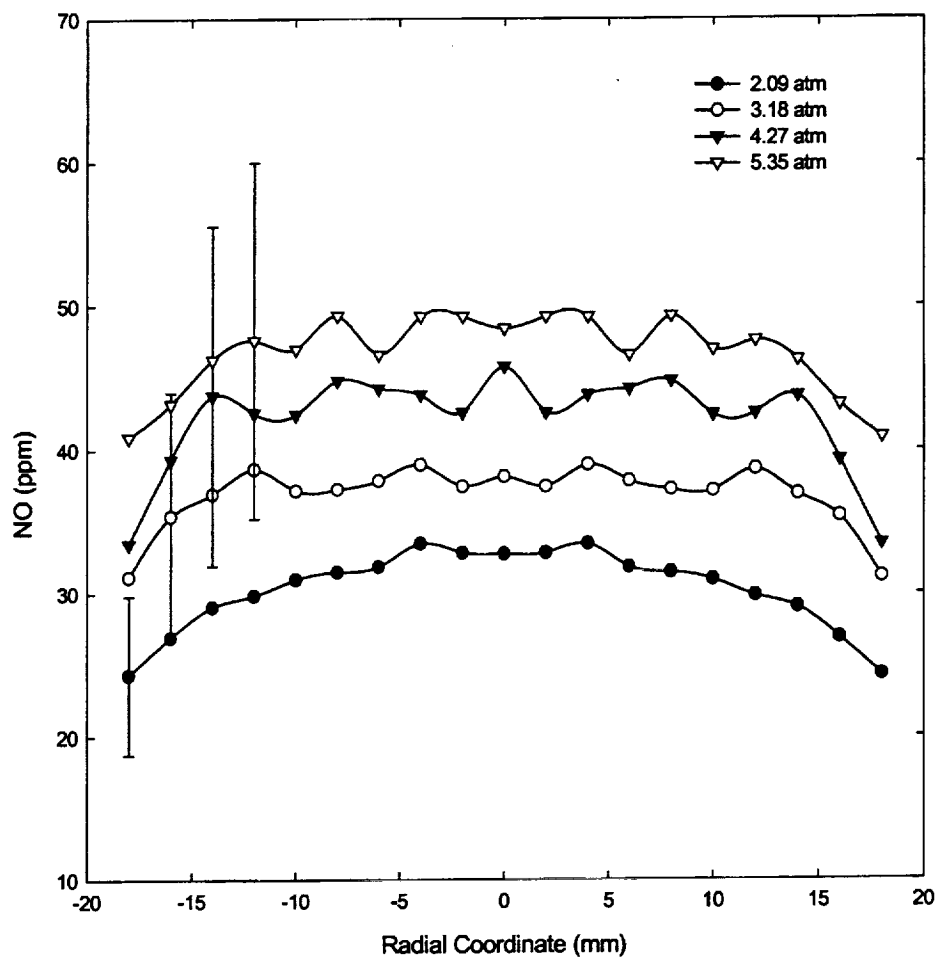


Figure 5.8: Absolute NO (ppm) concentration profiles at the 40-mm axial height as a function of operating pressure. Radial measurement profiles have been corrected for absorption and calibrated at the 40-mm height location. Typical accuracy bars at the 95% confidence level are shown at one point on each profile.

where M_{NO_2} and M_P represent the molecular weights of nitric oxide and the products of combustion, respectively, while \dot{m}_f and \dot{m}_a represent the mass flow rates of fuel and air, respectively. We assume for this calculation that the products are those for complete combustion, which should yield a good estimate of the product molecular weight owing to the presence of nitrogen. The $EINO_x$ results are plotted in Figure 5.9, along with a prediction for thermal NO based on a pressure exponent of 0.5 (Turns, 1996). From the data shown, the actual pressure-scaling coefficient is 0.74.

Correa (1992) notes that practical combustors employing turbulent diffusion flames have largely demonstrated a $P^{0.5}$ scaling. At temperatures greater than 1900 K, NO_x formation becomes predominately thermal in origin and is limited by the availability of oxygen atoms, whose concentration scales approximately as $P^{0.5}$ based on equilibrium considerations. However, the pressure exponent for NO_x formation is expected to increase as NO_x formation takes place primarily at near-stoichiometric interfaces owing to superequilibrium concentrations of oxygen atoms. For instance, Aigner *et al.* (1990) tested a partially-premixed injector and measured an NO_x scaling of $\sim P^{0.75}$. Correa (1992) indicates that the combustor of Aigner *et al.* (1990) was not operating in a well-stirred mode and thus exacerbated NO_x production.

It is difficult to determine the rationale for the observed pressure scaling in these LDI flames. Since the expected pressure exponent of 0.5 is based only on thermal NO production, it does not include the full effects of chemistry, turbulent mixing, burner geometry, and flame temperature scaling with pressure. For these experiments, the primary air mass flow was increased in a $\sim 1:1$ scaling with pressure so that the residence time based on exit velocity would not vary considerably. However, Chen (1995) points out that correlating NO formation to a time scale based on exit velocity is incorrect. A more appropriate measure would be the time scale associated with the recirculation zone, which requires velocity measurements within this region.

A more pertinent consideration is the temperature dependence of the forward reaction rate coefficient for the thermal NO mechanism (Turns, 1996):



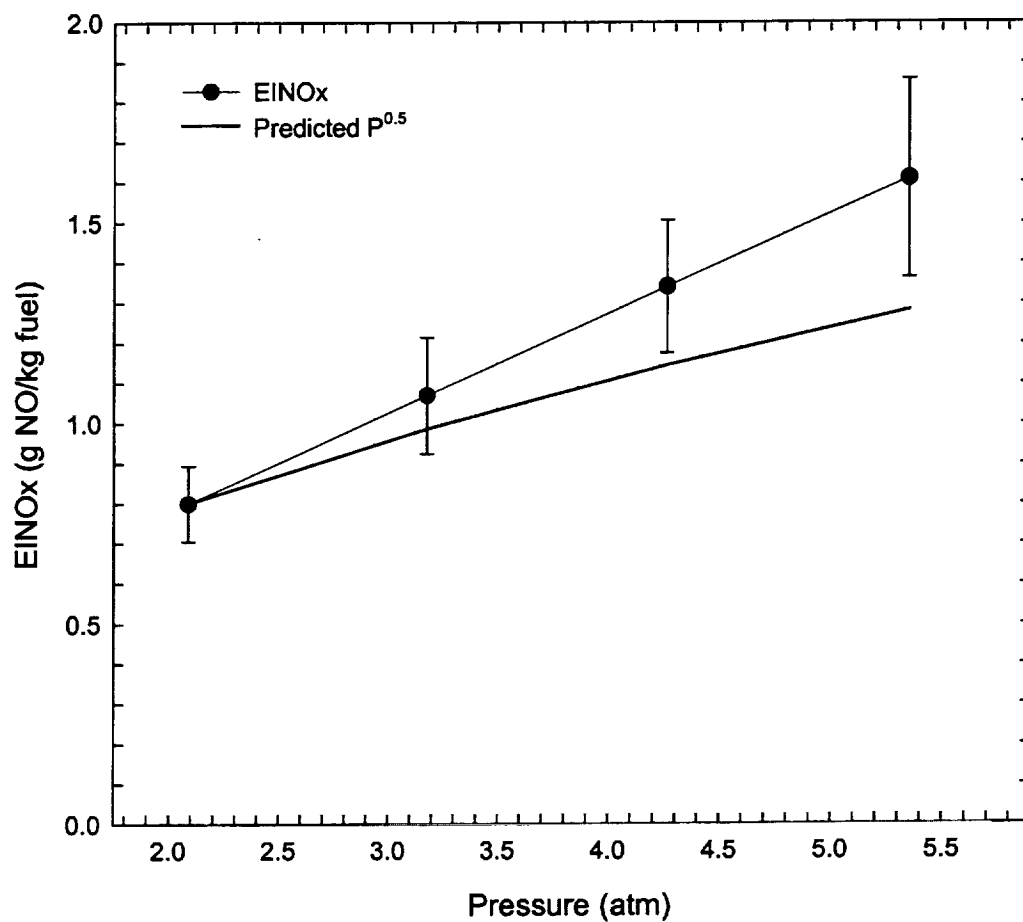


Figure 5.9: EINO_x measurements taken at the 40-mm axial height. The predicted EINO_x based on a $P^{0.5}$ scaling is shown as the solid line. The actual scaling of this data set is $P^{0.74}$.

$$k = 1.82 \cdot 10^{14} e^{\frac{-38370}{T(K)}} \text{ cm}^3/\text{gmol} \cdot \text{s} . \quad (5.4)$$

In the typical range of flame temperatures (1500 to 2000 K), the rate coefficient exponentially increases by two orders of magnitude. Recognizing that the flame temperature increases with pressure, and noting that stoichiometric interfaces are present in the LDI flame, it becomes feasible to attribute the observed $P^{0.74}$ scaling to an increase in flame temperature. However, as Correa (1992) points out, the $P^{0.5}$ scaling widely reported in combustion measurements may indicate a balance between the effect of higher temperatures at higher pressures and the effect of superequilibrium O-atom concentrations at lower pressures. Nevertheless, the results for our burner indicate that an extrapolation to 30 atm using the measured scaling would provide an $\text{EINO}_x = 5.75 \text{ g NO}_x/\text{kg fuel}$, which is only slightly above the aeropropulsion engine target of $5 \text{ g NO}_x/\text{kg fuel}$ (Gupta, 1997).

5.6 Conclusions

Quantitative LIF measurements of NO concentration (ppm) have been obtained in an LDI burner fueled with liquid heptane operating at pressures up to 5.35 atm. Through comparisons of fluorescence calibrations taken in LDI spray flames and in reference flames of known spectral characteristics, we have validated the use of a convenient reactant doping method. In particular, the results indicate insignificant destruction of doped NO, thereby allowing a simple means by which to quantify fluorescence measurements. Quantitative NO profiles were presented at operating pressures of 2.09, 3.18, 4.27, and 5.35 atm and were demonstrated to yield NO_x emissions close to target reduction levels. The NO profiles demonstrated a uniformity within the central recirculation region of the flame at pressures above 3 atm. The pressure scaling of the downstream measurements was found to be approximately $P^{0.74}$.

6. PARAMETRIC STUDY OF NO PRODUCTION VIA QUANTITATIVE LASER-INDUCED FLUORESCENCE IN HIGH-PRESSURE, SWIRL-STABILIZED SPRAY FLAMES

6.1 Introduction

In this chapter, we discuss the influence of equivalence ratio and air preheat temperature on nitric oxide (NO) concentrations in high-pressure, heptane spray flames. The burner is based on the lean direct-injection design and incorporates a pressure-atomized, hollow-cone spray nozzle. Helical vanes in the air passage coupled with a divergent exit and preheated air produce a strongly-swirling, clean, blue flame. NO concentration profiles are measured at 4.27 atm using laser-induced fluorescence (LIF) at five axial heights above the burner. The uniformity of NO throughout the central region of the flame demonstrates the well-mixed nature of the recirculation zone. Measurements are taken at the 40-mm centerline height to determine the effects of primary equivalence ratio ($\phi_p = 1.0$ to 0.8) and air preheat temperature ($T_{\text{air}} = 375$ K to 575 K). The results strongly suggest that NO formation occurs in near stoichiometric regions of the flame and is subsequently diluted with excess air. A residence time effect is evident and apparently scales as the mass flow rate of air relative to that for stoichiometric combustion, yielding a ϕ_p^2 scaling of the NO (ppm). Moreover, moderate increases in preheat temperature produce significant increases in NO (ppm) levels, suggesting thermal NO production.

6.2 Operating Conditions

The LDI burner is operated at 4.27 atm with a primary equivalence ratio $\phi_p = 0.90$. The primary equivalence ratio represents that calculated from the air and fuel

supplied through the main burner tube. Heptane fuel is supplied to the nozzle at 0.36 g/s and air at 6.07 g/s. An additional air co-flow is added to aid in flame stabilization, which yields an overall $\phi_o = 0.85$ if this air were completely entrained into the combustion process. The pressure was chosen based on scaling and stability issues for the flame.

A photograph of the LDI flame is shown in Figure 6.1. Note the non-sooting appearance and the symmetric nature of the flame. Usually, the air is preheated to 375 K to assist in vaporization and mixing of the fuel. Here, the preheat temperatures are varied from 375 K to 575 K. The equivalence ratios are varied from $\phi_p = 0.80$ to $\phi_p = 1.00$. NO measurements are obtained by employing the experimental protocol detailed in Chapter 4.

6.3 Results And Discussion

The NO (ppm) profiles for the 4.27-atm LDI flame are shown in Figure 6.2. Error bars are typically $\pm 25\%$ at the 95% confidence limit, with a repeatability for the profiles within 12%. Note the uniformity of the NO mole fraction throughout the central region of these direct-injection flames. This feature can be attributed to the well-mixed nature of the internal recirculation zone for swirl-based geometries (Alkabie and Andres, 1989; Terasaki and Hayashi, 1996), and has been noted in previous measurements of both atmospheric and high-pressure LDI spray flames (Cooper and Laurendeau, 1998a; Cooper and Laurendeau, 1999c).

The influence of air-preheat temperature on NO production is shown in Figure 6.3 for $\phi_p = 0.90$. All NO concentrations were measured at the 40-mm centerline height. A 92% increase in NO (ppm) is realized with only a 200 K increase in air-preheat temperature. This significant increase suggests thermal NO production owing to the strong correlation with preheat temperature. Moreover, if the residence time is inversely proportional to the burnt gas velocity, then the product of the forward rate coefficient and the residence time based on complete combustion at $\phi = 1.0$ would provide a 72% increase in the NO (ppm) level. Hence, the data support a stoichiometric combustion

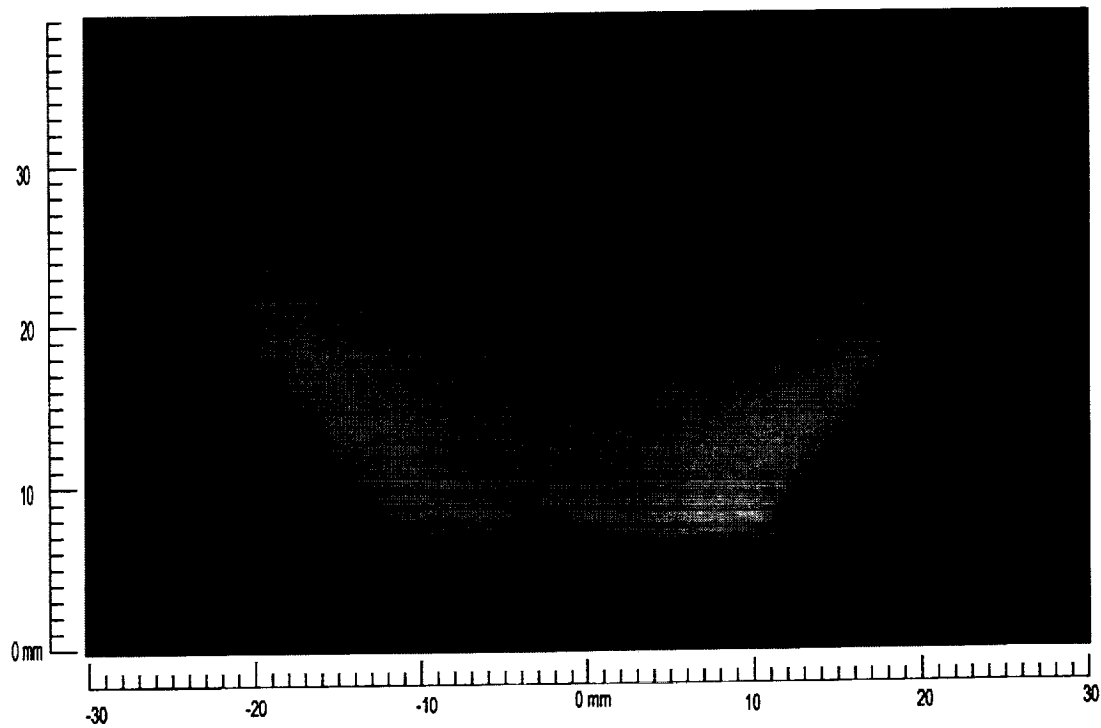


Figure 6.1: Photograph of LDI flame at 4.27 atm [$\dot{m}_{\text{fuel}} = 0.36$ g/s, $\phi_p = 0.9$, $T_{\text{air preheat}} = 375$ K].

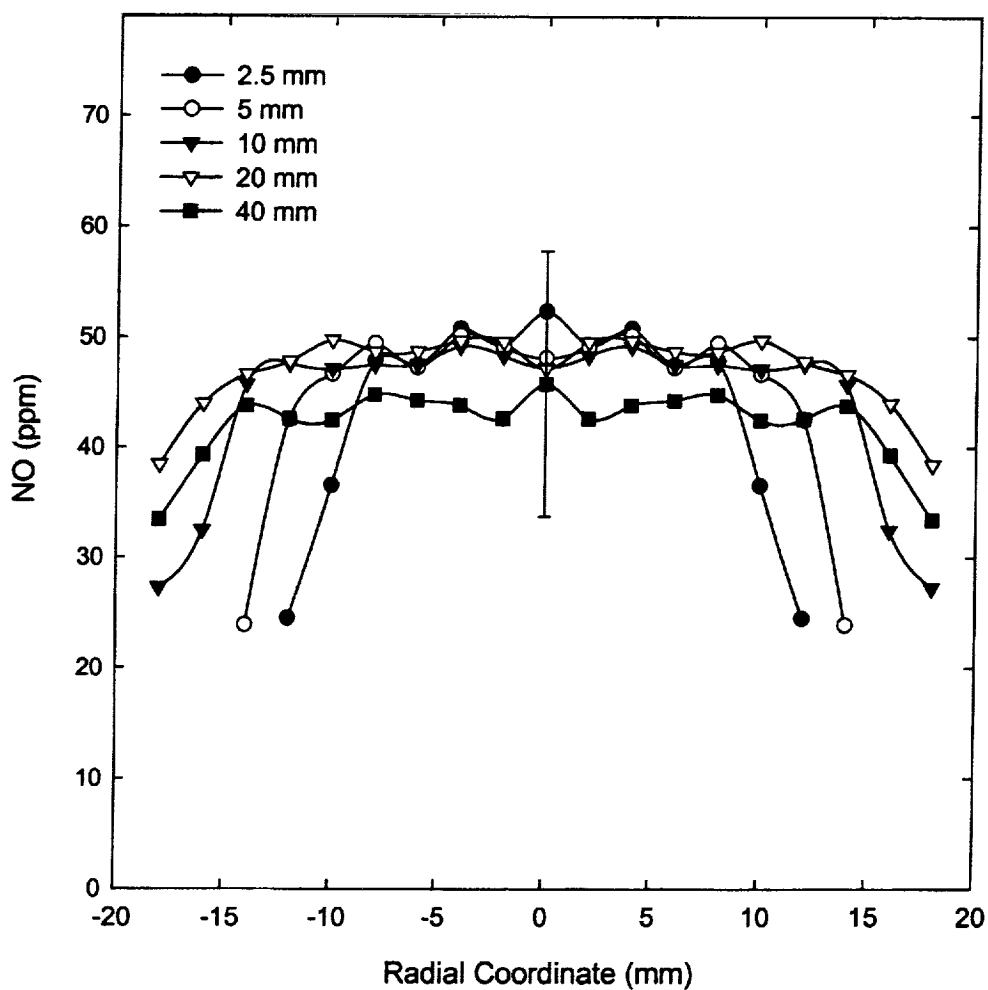


Figure 6.2: Radial NO concentration profiles for lean ($\phi_p = 0.9$, $T_{\text{air preheat}} = 375$ K) direct-injection, swirl-stabilized, spray flame at 4.27 atm. Note the uniformity of the NO profiles throughout the measured region.

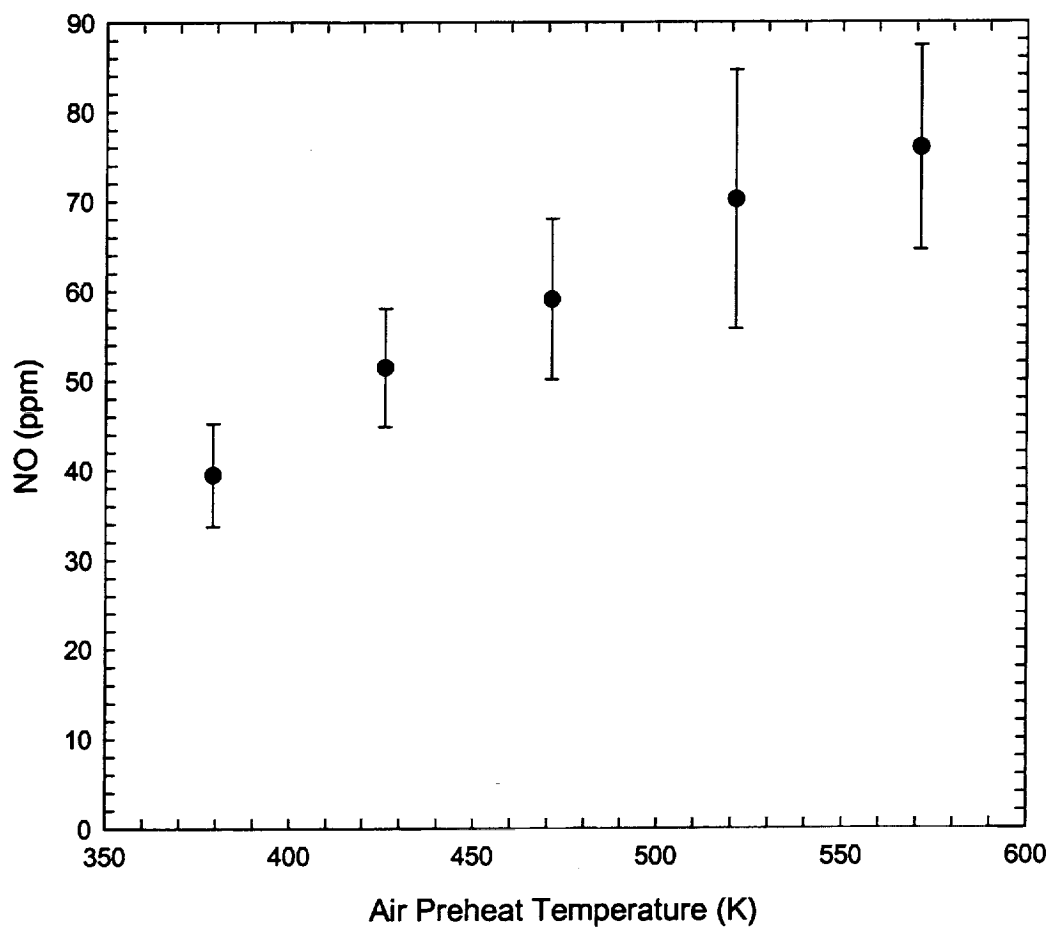


Figure 6.3: NO measurements at the 40-mm axial height ($\dot{m}_{\text{fuel}} = 0.36 \text{ g/s}$, $\phi_p = 0.9$, $P = 4.27 \text{ atm}$) as a function of air preheat temperature.

regime near the spray sheath owing to the strong correlation of NO (ppm) with air preheat temperature.

To determine the effect of stoichiometry, NO concentrations were measured at the 40-mm centerline height. Two methods were utilized to achieve the variation in equivalence ratio. First, the fuel flow rate was held constant at 0.36 g/s and the air flow rate was varied. In the second approach, the air flow rate was held constant at 6.07 g/s and the fuel flow rate was varied. The results are shown in Figure 6.4 and demonstrate a marked decrease in NO at leaner mixtures, namely a 45% decrease in NO (ppm) from $\phi_p = 1.0$ to $\phi_p = 0.8$. The data demonstrate a repeatability of 15% owing to a two-month lapse between data sets. The variation in recirculation zone temperature with stoichiometry can be determined experimentally by monitoring the variation in the NO calibration slope (Cooper and Laurendeau, 1999b). This procedure reveals an ~28% decrease in temperature from $\phi_p = 1.0$ to $\phi_p = 0.8$ at the 40-mm centerline height. This decrease in temperature would reduce the forward rate coefficient of the thermal NO formation reaction, i.e.,



$$k_f = 1.82 \cdot 10^{14} e^{\frac{-38370}{T(K)}} \text{ cm}^3/\text{gmol} \cdot \text{s} \quad (6.2)$$

by at least two orders of magnitude (Turns, 1996).

As the NO variation with stoichiometry does not demonstrate such a reduction, the primary location of NO most likely occurs in near-stoichiometric regions surrounding the spray sheath, consistent with our previous work at atmospheric pressure (Cooper and Laurendeau, 1998b). Dilution of the NO formed in the spray sheath by supplied excess air should give an ~20% decrease in the NO mole fraction at $\phi_p = 0.8$. The drop in recirculation zone temperature noted above could provide evidence of such cold-air dilution into the hot gas products from stoichiometric combustion. If a residence time is calculated based solely on the exit velocity of air relative to that at stoichiometric

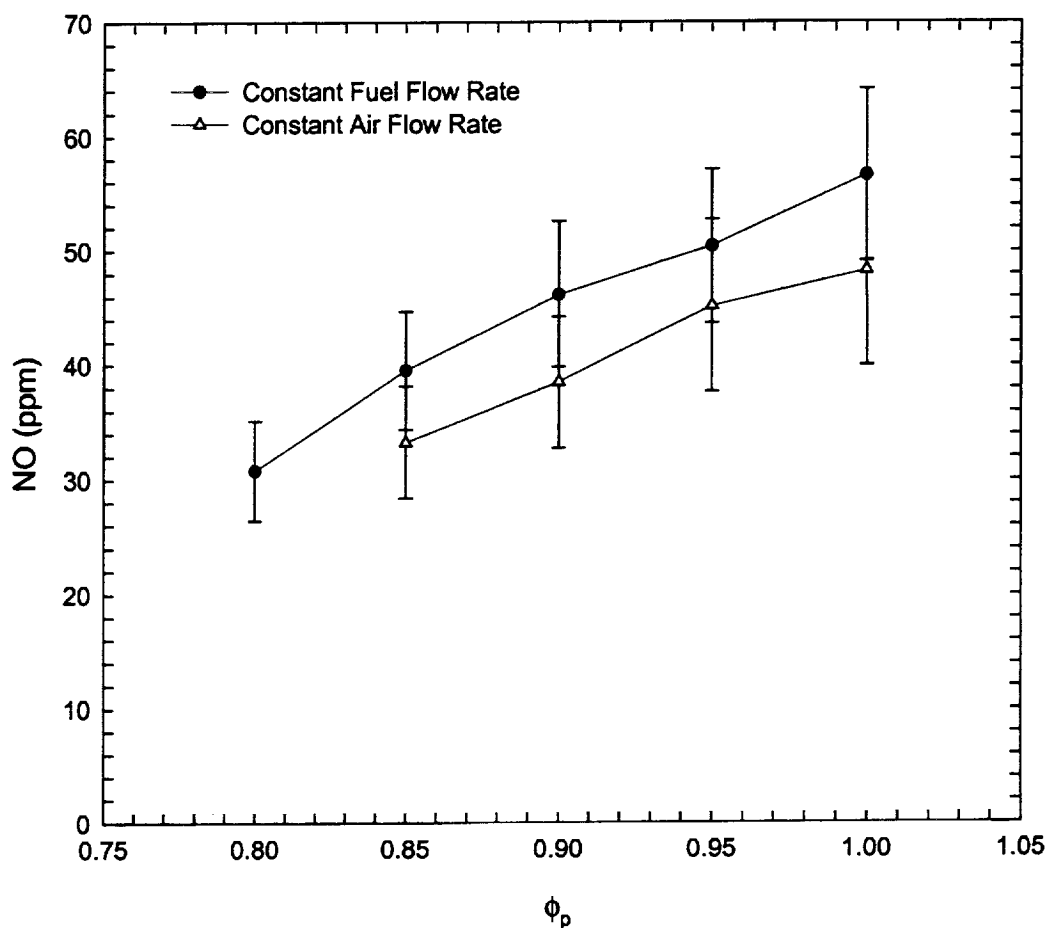


Figure 6.4: NO measurements at the 40-mm axial height ($T_{\text{air preheat}} = 375$ K, $P = 4.27$ atm) as a function of stoichiometry with (1) constant fuel flow rate ($\dot{m}_{\text{fuel}} = 0.36$ g/s) and (2) constant air flow rate ($\dot{m}_{\text{air}} = 6.07$ g/s).

conditions, the combined effect of dilution and residence time yields an approximate scaling for NO production of

$$NO \sim \phi_p^2. \quad (6.3)$$

A test of this hypothesis is displayed in Figure 6.5, where the NO concentration (ppm) has been normalized to that at $\phi_p = 1.0$. While this correlation does not prove the hypothesized scaling, it does lend credence to the effects of coupled dilution and residence time on thermal NO formed in near-stoichiometric regions. If the co-flowing air is considered to be completely entrained, then the scaling would be proportional to $\phi_p \phi_o$, thus basing the residence time on the stoichiometric supplied air and the dilution on the total air. On a normalized basis, the results would be almost identical to Figure 6.5.

Cooper and Laurendeau (1998b) previously assessed the variation of NO with stoichiometry in atmospheric, unconfined, LDI spray flames by computing the dilution arising from excess air. If the reported values are also scaled to reflect the coupled residence time and dilution effect of Eq. (6.3), the resulting correlation demonstrates identical behavior (see Fig. 6.6). In this case, the residence time is scaled with the primary equivalence ratio based on inputs to the burner, while the dilution is scaled with the overall equivalence ratio based on supplied and entrained excess air. Figure 6.6 lends strong evidence to coupled dilution and residence time effects on NO formed in near-stoichiometric regions. If NO were formed in non-stoichiometric regions, then chemical effects would hinder the collapse shown, i.e., the demonstrated collapse implies a steady-state formation rate integrated over time with the product subsequently diluted with excess air.

If our data are compared to those of previous researchers, it becomes apparent that this high-pressure LDI configuration is not achieving a significant level of premixedness. In particular, the NO data of Hayashi (1995) for direct-injection and lean-premixed prevaporized combustion of kerosene exhibit a much greater dependence on equivalence ratio in the range $\phi_p = 0.80$ to $\phi_p = 1.00$ for air preheat temperatures of 450-650 K.

The combined observations from our data suggest a residence time that scales linearly with either the fuel or air mass flow (relative to stoichiometric) and inversely

with the stoichiometric burnt gas temperature, i.e., the velocity of the stoichiometric products. Moreover, a dilution of the products of stoichiometric combustion seems apparent from the squared dependence of produced NO (ppm) on equivalence ratio. These observations are consistent with the results from a simple perfectly-stirred reactor model as discussed in Appendix B.

6.4 Conclusions

Quantitative LIF measurements of NO concentration have been obtained in high-pressure LDI flames for a range of equivalence ratios ($\phi_p=0.8-1.0$) and air-preheat temperatures (375-575 K). Parametric studies of these variables strongly suggest that NO formation occurs in near stoichiometric regions of the flame and is subsequently diluted with excess air. A residence time effect is evident and apparently scales as the mass flow rate of air relative to that for stoichiometric combustion, yielding a ϕ^2 scaling of the produced NO (ppm) with primary equivalence ratio. Moreover, moderate increases in preheat temperature produce significant increases in NO (ppm) levels, suggesting thermal NO production.

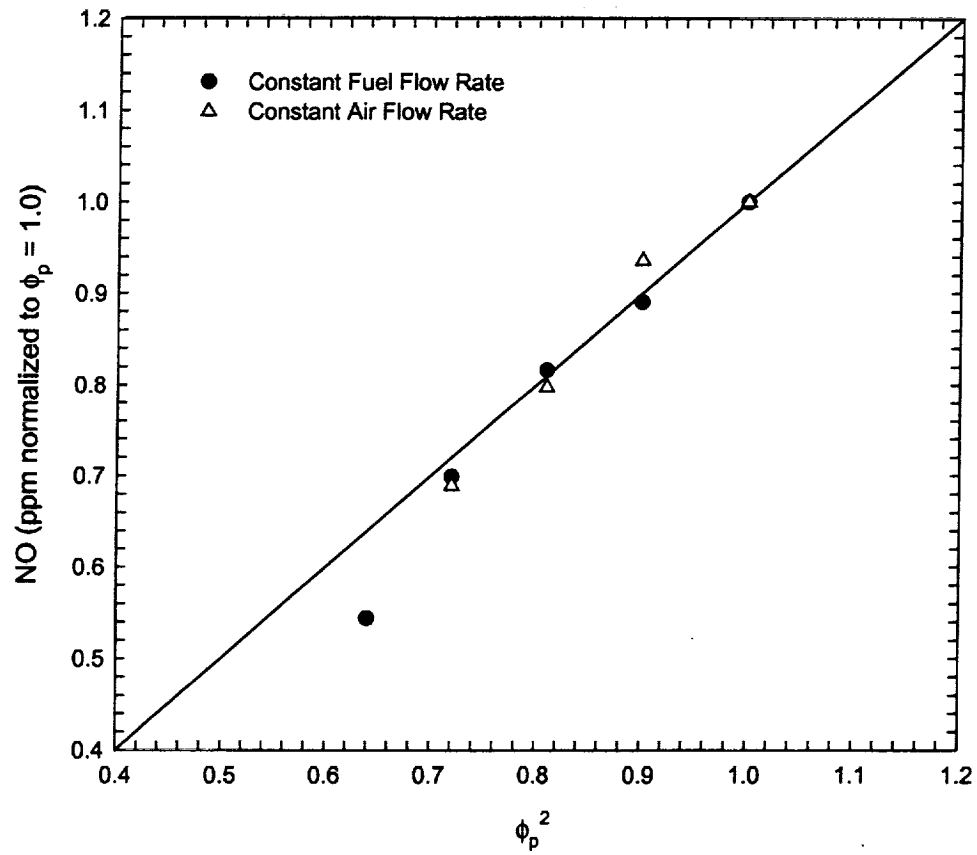


Figure 6.5: NO (ppm) vs. ϕ_p^2 , demonstrating coupled dilution and residence time effects based on exit velocity for the 4.27-atm LDI flame. The excellent correlation suggests thermal NO production in near stoichiometric regions.

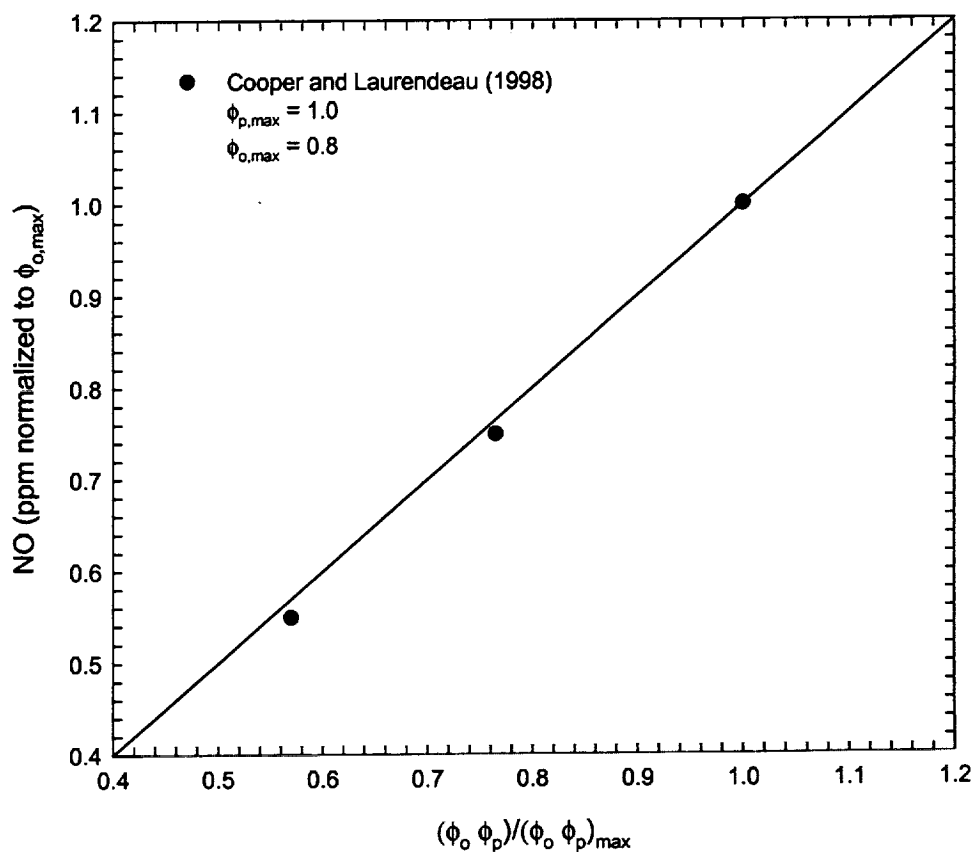


Figure 6.6: NO (ppm) scaling demonstrating coupled dilution and residence time effect based on exit velocity for 1-atm LDI flame. The original data of Cooper and Laurendeau (1998a) have been scaled to account for both dilution and residence time effects.

7. PARAMETRIC STUDY OF NO PRODUCTION VIA QUANTITATIVE LASER-INDUCED FLUORESCENCE IN HIGH-PRESSURE, LEAN PREMIXED-PREVAPORIZED SPRAY FLAMES

7.1 Introduction

In the push toward low NO_x technologies for aeroengines, one theme that stands out as a strong prospect for the future is the lean, premixed-prevaporized (LPP) combustor (Correa, 1992). Using this route, stoichiometric interfaces can be avoided, thus leading to reduced temperatures and suppression of the thermal route for NO_x formation. Another important benefit from LPP combustion is the reduced dependence on pressure. In fact, at sufficiently lean conditions for which the nitrous-oxide pathway dominates, little to no dependence on pressure can be realized (Correa, 1992).

The initial goal of this chapter was a direct comparison of LPP and LDI combustion by modifying the burner of Fig. 3.7 to include a premixing length. The nozzle was to be located at the beginning of this premixing length, with fuel injected into the swirling air generated by an upstream swirler. To achieve a swirl-stabilized flame, a second swirler would be positioned near the burner exit as in the LDI burner. In a similar manner, Hayashi (1995) compared LDI and LPP burners over a range of operating conditions. Unfortunately, the inner diameter of the burner and the expansion ratio at the exit of the burner ($\sim 13:1$) precluded attachment of a swirl-stabilized LPP flame with similar structural characteristics to the LDI flame. A compromise was thus made by replacing the burner with a new one having twice the inner diameter. Surprisingly, the flame did not stabilize in the same shape as the LDI flame (Fig. 6.1), but instead appeared to thermally attach to the inner rim of the exit swirler.

This lack of a direct comparison, however, should not restrict the utility of our results. A major thrust of this chapter is to demonstrate the compatibility of LIF

diagnostics to a range of spray flames. In particular, LIF has been shown to be a viable technique for NO detection in gaseous flames, both atmospheric and high-pressure (Reisel and Laurendeau, 1995; Thomsen *et al.*, 1997). Cooper and Laurendeau (1998a) demonstrated atmospheric LDI measurements, and later high-pressure LDI measurements (Cooper and Laurendeau, 1999b; Cooper and Laurendeau, 1999c). As the technology push seems ultimately directed toward LPP, it is important to validate the use of LIF in such environments. As will be shown, LIF is indeed successful as both a diagnostic technique and a tool by which important information can be obtained within high-pressure flames. In particular, the influences of equivalence ratio, air-preheat temperature, and pressure can be investigated, similar to that of Chapters 5 and 6 for the LDI flame.

7.2 Operating Conditions

A schematic of the LPP burner is shown in Figure 7.1. The burner is similar in design to the LDI burner; however, a premixing stem is located 41.7 cm below the burner exit. Fuel is injected at the entrance to this stem into preheated, swirling air generated by a 60° helical swirler. After passing through the premixer length, the gases are rotated by a second 60° helical swirler placed 1.16 cm below the exit orifice. The flame attaches to the inner ring of the helical swirler and forms a conical flame, as shown in Figure 7.2. The flame does not appear to undergo sufficient swirl to produce an internal recirculation zone. The LPP burner is nominally operated at 4.27 atm with an overall equivalence ratio $\phi = 0.75$. The equivalence ratio is that calculated from the air and fuel supplied through the main burner tube since no co-flow air is used. Heptane fuel is provided to the nozzle at 0.27 g/s. The nominal pressure was chosen to match that for the LDI work in Chapter 6. The air is nominally preheated to 475 K to assist in vaporization and mixing of the fuel; however, here the air preheat temperature was varied from 365 K to 480 K. Similarly, the equivalence ratio was varied from $\phi = 0.65$ to $\phi = 0.75$. These

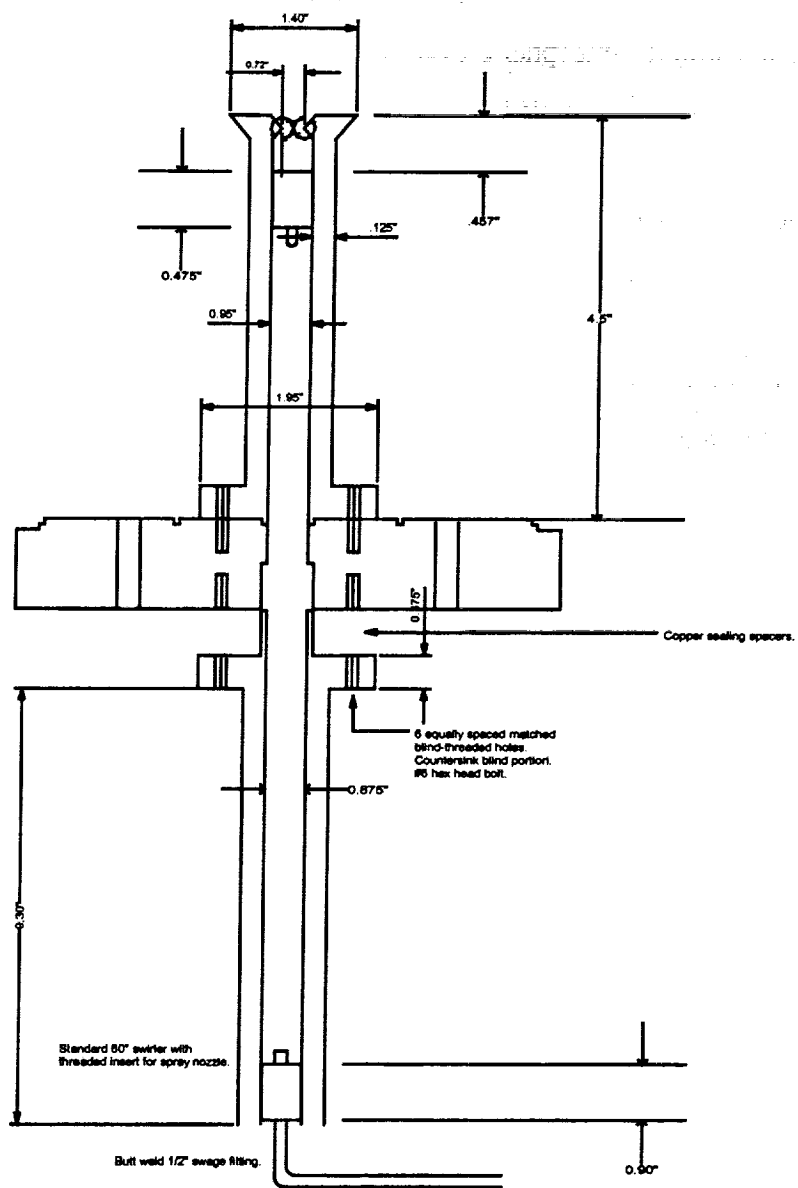


Figure 7.1: Schematic of lean, premixed-prevaporized burner.

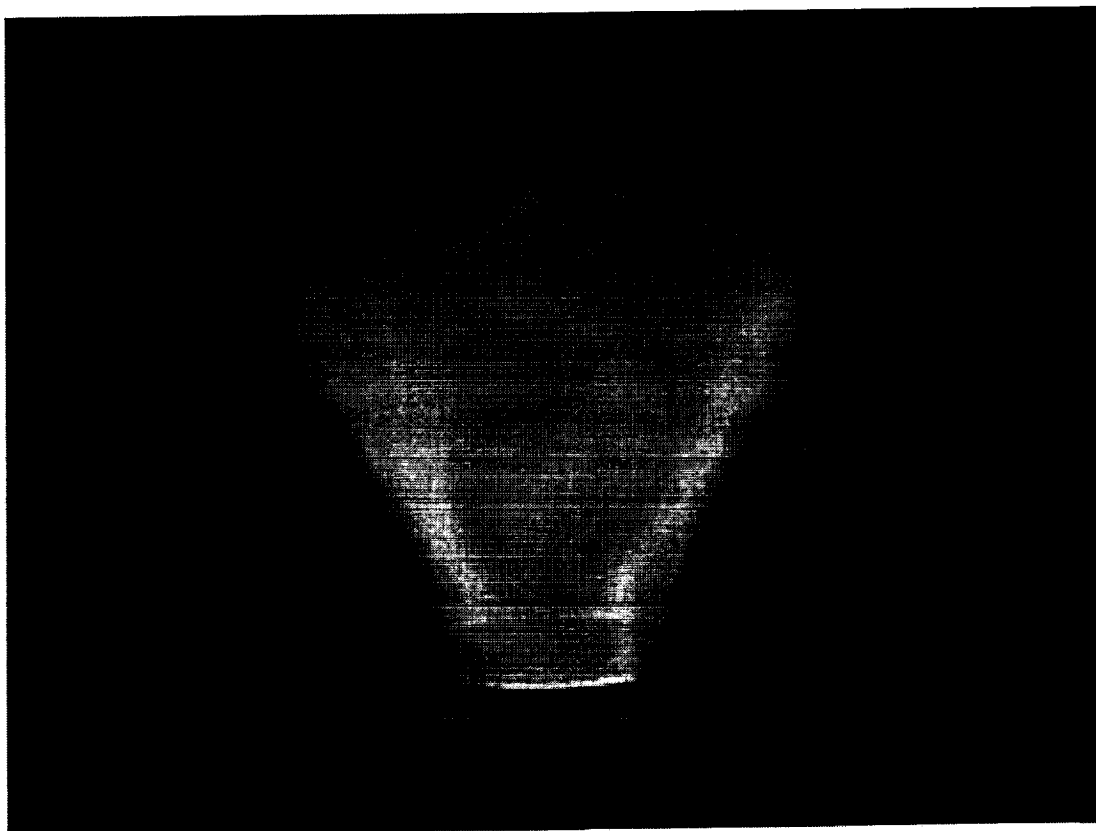


Figure 7.2: Photograph of LPP flame at 4.27 atm [$\phi = 0.75$, $T_{\text{air preheat}} = 475$ K]. Note that the oval window restricts the field of view.

boundaries define the stability limit for the flame shown in Figure 7.2. Lean blowoff occurs at $\phi \approx 0.63$. The flame stabilizes as a straight jet for $\phi > 0.77$, attached to the full periphery of the burner orifice. In a similar manner, preheat greater than 500 K forces transition to a straight jet. The conical flame was chosen based on stable, safe operation over a range of conditions. The straight jet transferred excessive heat to the burner assembly and prevented safe operation. The pressure effects on NO were studied over a range of 3.7 atm to 6.4 atm.

7.3 Spectral Validation

Our previous work addressed an excitation/detection scheme for use in atmospheric-pressure LDI flames (Cooper and Laurendeau, 1998a). Excitation of the $Q_2(26.5)$ line of the $\gamma(0,0)$ band of NO at 225.58 nm is followed by detection of the $\gamma(0,1)$ band with a 2-nm window centered at 235.78 nm. An off-line wavelength at ~ 225.53 nm is excited and monitored as a measure of the ubiquitous background for the NO fluorescence signals. Having validated this approach for use in the LDI flames of the previous chapters, we should expect the more benign environment of an LPP flame to also permit use of this scheme. Nevertheless, the scheme was validated with standard excitation and detection scans taken at the 20-mm centerline location in the LPP flame. As demonstrated in Figure 7.3, no unexpected interferences or anomalies are present in either the excitation or the detection spectra when referenced to those of Figures 5.2 and 5.3.

7.4 Calibration Comparison

To experimentally validate an in-situ doping method for the LPP burner, a 4.27-atm operating condition was selected and the flame was seeded with varying amounts of NO. The emissive signal was measured at these different ppm levels. The measurement location was arbitrarily chosen to be along the centerline at a 20-mm axial height. NO

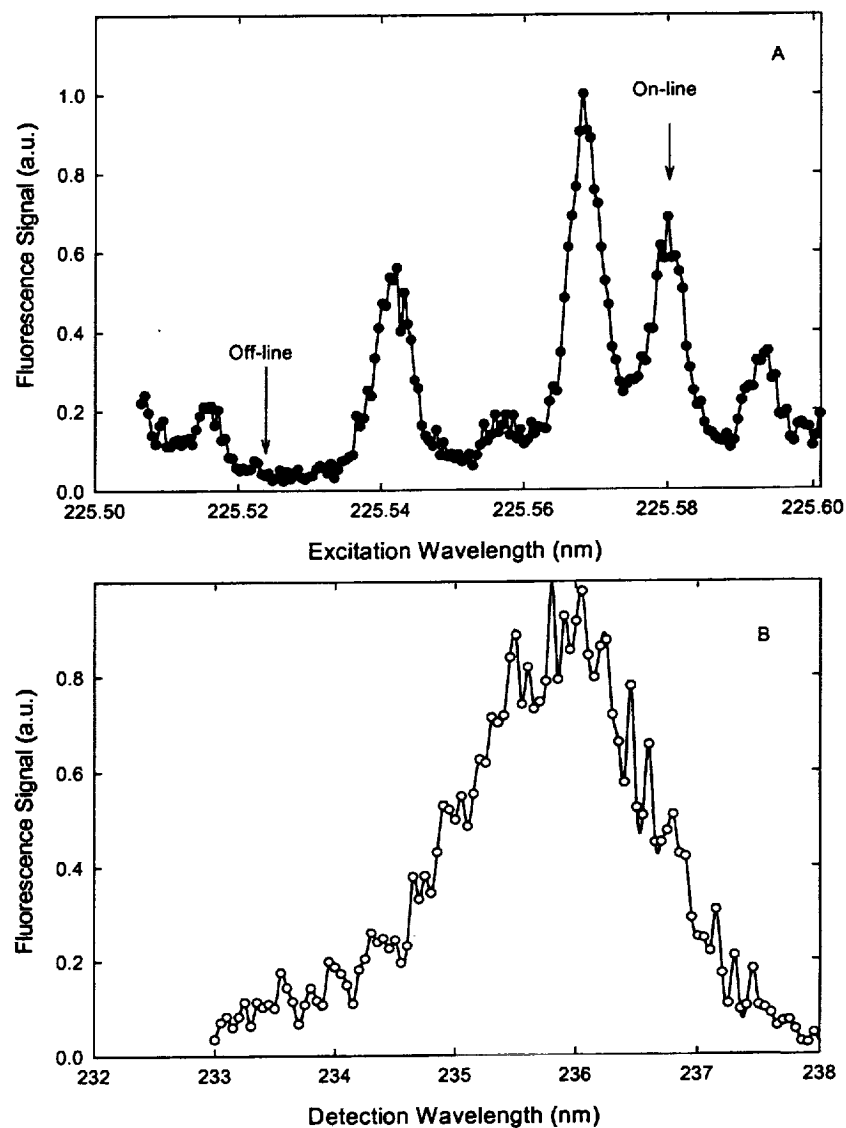


Figure 7.3: (A) Excitation scan taken in 4.27-atm LPP burner at $h = 20$ mm, $r = 0$ mm. The NO on-line $Q_2(26.5)$ and off-line excitation wavelengths are labeled. (B) Detection scan taken at same conditions.

was seeded into the flow via a calibrated cylinder of 3000-ppm doped nitrogen. Oxygen was added accordingly to maintain a dilution ratio of 3.76, while the building air supplied to the burner was reduced to maintain the same total air flow rate. A transmission of ~65% in the 4-atm flame was measured at ~226 nm via photodiodes on either side of the flame. The same transmission was implicitly assumed for the resulting ~236-nm radiation. Subsequent to these individual experiments, the LPP burner in the high-pressure vessel was replaced with a sintered bronze, flat-flame, burner. Calibration measurements were then performed in the post-flame region of a flat, lean ($\phi = 0.8$, 3.76 dilution ratio) $\text{CH}_4/\text{O}_2/\text{N}_2/\text{NO}$ flame. Possible window soot deposited by the LDI flame during start-up could be accounted for by monitoring transmission losses at the end of the flat-flame experiment. Typical window soot transmission losses were less than 6%.

The 4-atm calibration included both on-line and off-line measurements. The results of these comparative calibrations are shown in Figure 7.4. The calibration slopes display excellent agreement (<10% difference), with the offsets indicating the relative NO ppm levels prior to doping. While the calibration slopes are essentially identical, it should be pointed out that the fluorescence signal is actual proportional to NO number density. Moreover, any variation in the quenching rate coefficient is inherently included in the measured slopes. Fortunately, quenching rate coefficients calculated from adiabatic flame temperatures and major species for the LPP and flat flames agree to within 4% when assuming complete combustion (Paul *et al.*, 1994). The adiabatic flame temperatures for the LPP flame and the flat flame are 1979 K and 2000 K, respectively. Therefore, within the experimental accuracy of the calibration slopes (typically ~10%), we will adopt the position that destruction of NO is not a significant factor in the transport of doped NO to the central region of the LPP flame.

7.5 Results And Discussion

The experimental method for obtaining the NO profiles is similar to that discussed in Chapter 4, with the exception that relative calibrations are not utilized. Instead, the

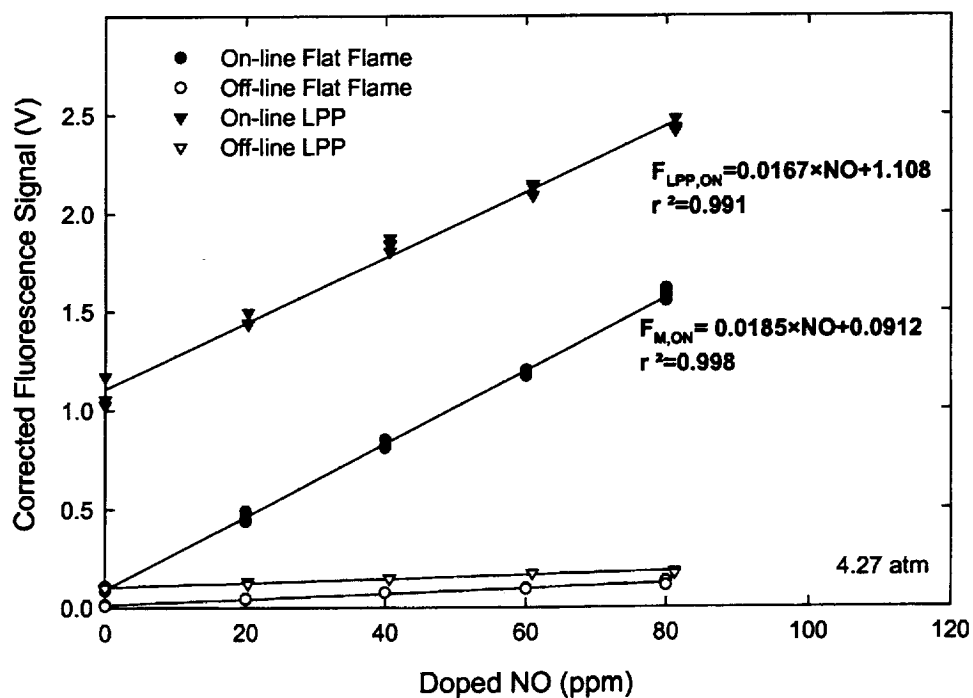


Figure 7.4: NO fluorescence calibrations taken in the post-flame zone of a lean ($\phi = 0.8$, 3.76 dilution ratio) $CH_4/O_2/N_2/NO$ flame stabilized on a sintered bronze burner and at the centerline 35-mm axial height of a heptane-fueled ($\phi = 0.75$, 3.76 dilution ratio, 475 K preheat) LPP flame at 4.27 atm.

radial profiles are calibrated to their specific centerline values immediately before measurement of each radial profile. This eliminates any error in the transmission calculations and in the transport of relative calibrations. The NO (ppm) profiles for the 4.27-atm LPP flame are shown in Figure 7.5, with each radial profile mirrored to reflect its symmetric nature. A representative accuracy bar is shown, with typical accuracies of $\pm 12\%$ at the 95% confidence limit. Note the radial divergence of the profiles as the flame spreads outward. Moreover, unlike the LDI flame, the LPP flame demonstrates continued production of NO up to a sufficient height within in the flame. This behavior suggest little, if any, recirculation of combustion products. The peak NO values are located at the 20-mm axial centerline position. Farther downstream, it appears that NO is radially distributed into a larger flame cross-section. This phenomenon could be a thermal effect, with a potentially hotter inner portion of the flame near the root and rapid heat loss as the flame diverges. The cooler downstream temperatures could freeze thermal NO production.

The influence of equivalence ratio demonstrates a pronounced effect on the formation of NO within this LPP flame. Figure 7.6 displays a factor of 10 increase in NO at the 20-mm centerline height as the equivalence ratio rises from 0.65 to 0.75. Since the adiabatic flame temperature would increase ~ 170 K owing to this change, thermal NO appears again to be the responsible mechanism. If we consider the forward reaction for thermal NO production,



$$k_f = 1.82 \cdot 10^{14} e^{\frac{-38370}{T(K)}} \text{ cm}^3/\text{gmol} \cdot \text{s}, \quad (7.2)$$

and assume equilibrium between O and O_2 ,



$$K_p = e^{\frac{-21215}{T(K)}}, \quad (7.4)$$

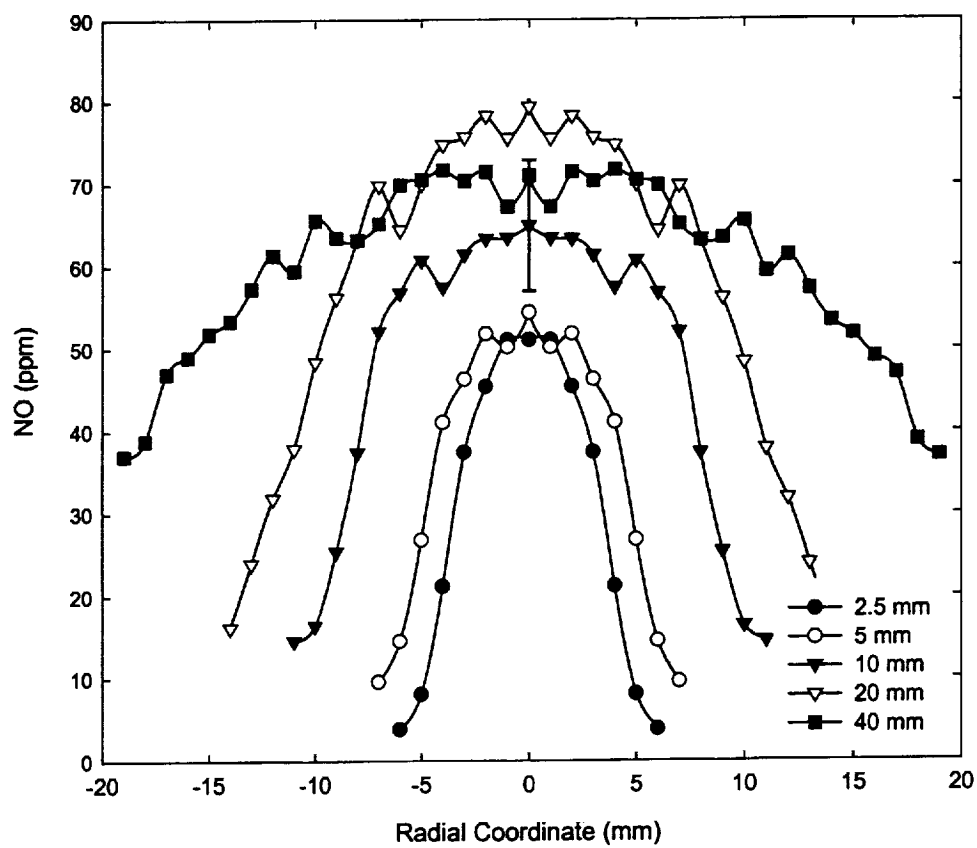


Figure 7.5: Radial NO concentration profiles for lean ($\phi = 0.75$, $T_{\text{air preheat}} = 475 \text{ K}$) direct-injection, swirl-stabilized, spray flame at 4.27 atm. Note the radial divergence of the profiles.

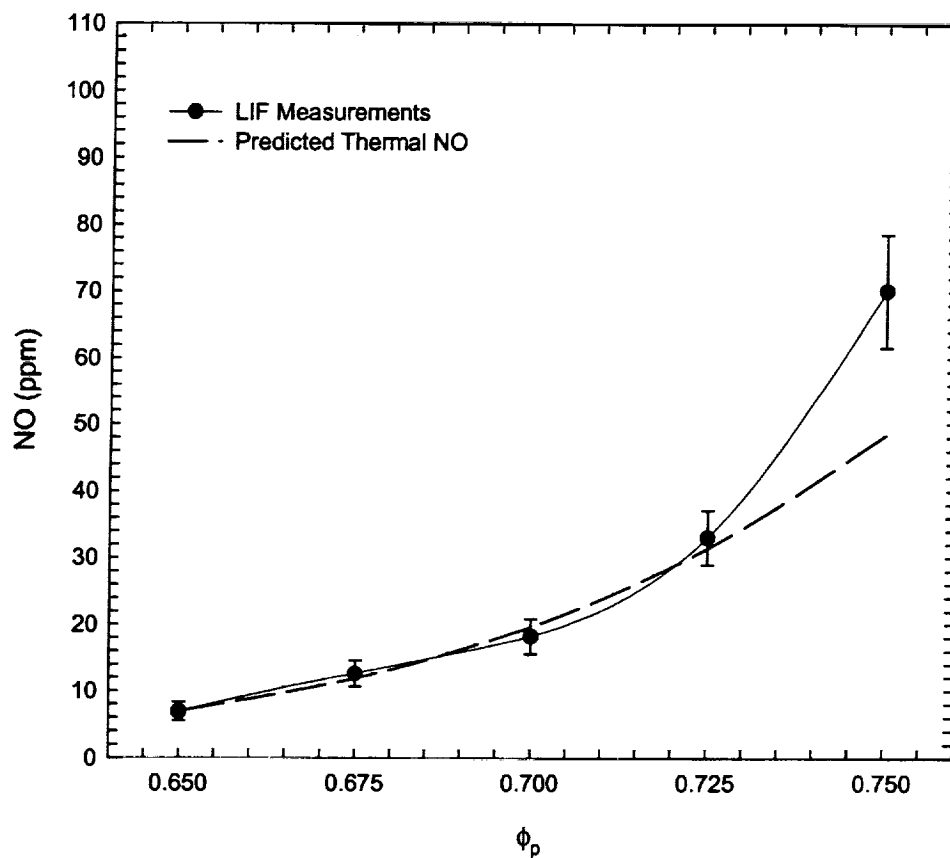


Figure 7.6: NO measurements at the 20-mm axial height ($T_{\text{air preheat}} = 475 \text{ K}$, $P = 4.27 \text{ atm}$) as a function of stoichiometry. The predicted thermal NO scaling is based on complete combustion, with that for residence time based on exit velocity.

then a simplified expression for the production of NO can be obtained, i.e.,

$$\frac{d[NO]}{dt} = 2k_f \left(\frac{K_p P^o}{R_u T} \right)^{1/2} [N_2][O_2]^{1/2}. \quad (7.5)$$

Recognizing that concentrations can be converted to mole fractions via

$$[N_2] = x_{N_2} \frac{P}{R_u T} \quad (7.6)$$

$$[O_2] = x_{O_2} \frac{P}{R_u T}, \quad (7.7)$$

the production of NO can be expressed on a mole-fraction basis as

$$\frac{dx_{NO}}{dt} = 2k_f \frac{(K_p P^o)^{1/2} P^{1/2}}{R_u T} (x_{N_2})(x_{O_2})^{1/2}. \quad (7.8)$$

Lastly, net NO production can be calculated by integrating Eq. (7.8) with respect to time to obtain

$$x_{NO} = \int_0^{\tau_{res}} \left(\frac{dx_{NO}}{dt} \right) dt. \quad (7.9)$$

Evaluation of Eq. (7.9) for premixed combustion at its adiabatic temperature and for a residence time that scales with the equivalence ratio based on changes in exit velocity reveals the dashed line of Figure 7.6, when normalized to the $\phi=0.65$ case. The comparison is excellent and confirms that NO production is predominantly thermal for this LPP flame.

The LPP data of Figure 7.6 demonstrate an exponential dependence on equivalence ratio. This exponential increase should be expected for premixed conditions since the adiabatic flame temperature varies linearly over this range of equivalence ratios and the forward rate coefficient for thermal NO depends exponentially on temperature. Recall that the LDI data of Chapter 6 demonstrated a ϕ_p^2 scaling near stoichiometric conditions. Though a direct comparison cannot be made owing to a difference in the range of equivalence ratios, the exponential trend noted in LPP flames suggests that the LDI flame is not burning in a completely premixed mode.

The influence of air-preheat temperature on NO production is shown in Figure 7.7 for $\phi = 0.75$. All NO concentrations were measured at the 20-mm centerline height. A 362% increase in NO (ppm) is realized with only a 100 K increase in air-preheat temperature. This significant increase strongly suggests thermal NO production. In particular, a 100 K increase in air preheat induces a 70 K increase in the adiabatic flame temperature. A simplified prediction based on the analysis of Eqs. (7.1) through (7.9), when normalized to the 365-K case, does not fully correlate with the data because of the slight change in flame geometry which likely affects the location of peak NO. At the highest preheat used here, the flame base is broadened and flame attachment is transitioning to the exit orifice lip as opposed to the swirler.

Lastly, it is important to determine the pressure scaling for NO. At temperatures greater than 1900 K, NO_x formation becomes predominately thermal in origin and is limited by the availability of oxygen atoms, whose concentration scales approximately as $P^{0.5}$ based on equilibrium considerations. Figure 7.8 displays the pressure scaling of the 20-mm axial centerline location for $\phi = 0.75$, 475-K air preheat LPP flames. The mass flow rates of air and fuel were scaled such that the residence time based on exit velocity would be unchanged with pressure. Note that the predicted scaling based on thermal NO, normalized to the $P = 3.7$ -atm case, correlates within the error bars of the data. The LDI data of Chapter 5 demonstrated a $P^{0.74}$ scaling, indicating that the LDI flame is not burning sufficiently premixed so as to avoid stoichiometric influences on the pressure scaling.

7.6 Conclusions

While direct comparisons with the LDI flame cannot be realized owing to the different flame structures (thermally attached vs. swirl-stabilized), the data reported in this chapter demonstrate that LIF measurements can be a valuable tool for the detection of NO in LPP flames. As with the LDI data of Chapter 6, trends representing the effects of important changes in operating parameters can be measured directly within high-pressure flames.

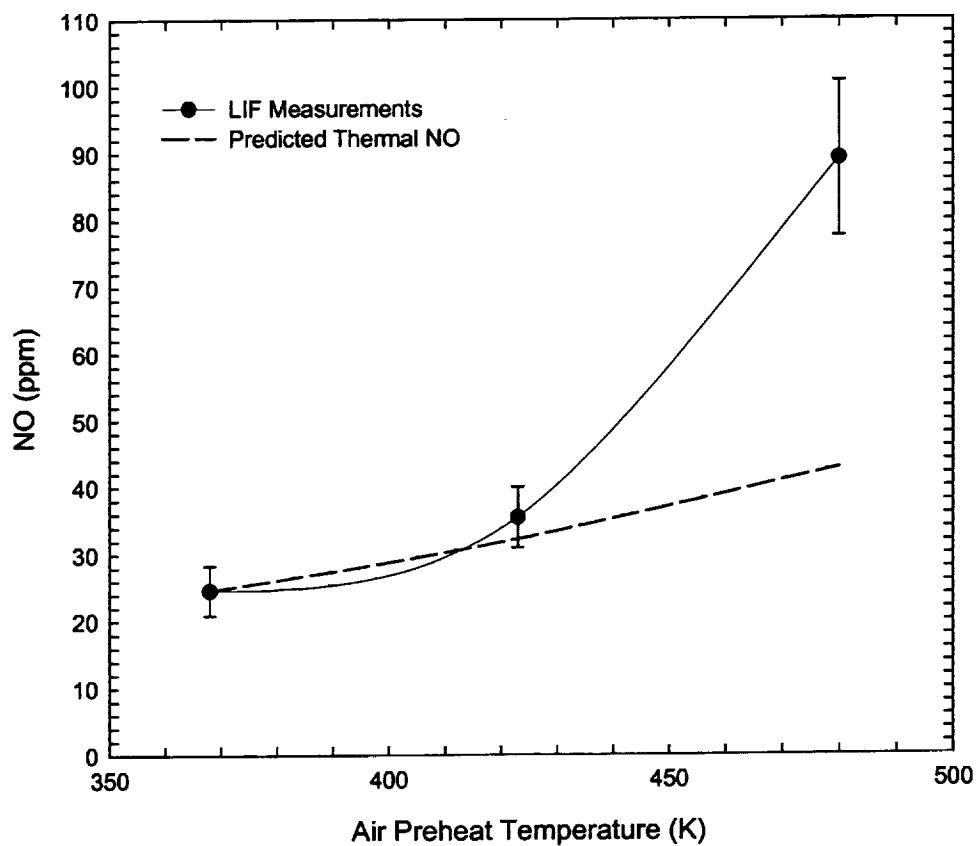


Figure 7.7: NO measurements at the 20-mm axial height ($\phi = 0.75$, $P = 4.27$ atm) as a function of air preheat temperature. The predicted thermal NO scaling is based on complete combustion, with that for residence time based on exit velocity.

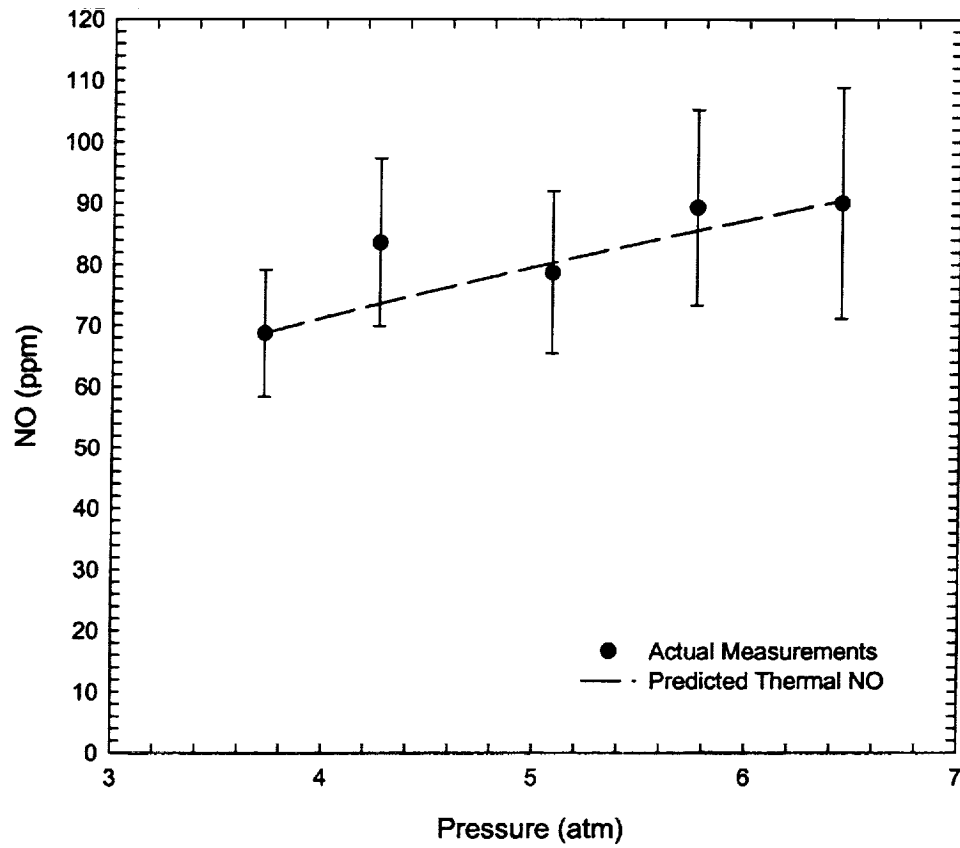


Figure 7.8: NO measurements at the 20-mm axial height ($T_{\text{air preheat}} = 475 \text{ K}$, $P = 4.27 \text{ atm}$) as a function of pressure. The predicted thermal NO is based on equilibrium considerations with a pressure exponent of 0.5.

Quantitative LIF measurements of NO concentration have been obtained in high-pressure LPP flames for a range of equivalence ratios ($\phi=0.65-0.75$), air-preheat temperatures (365-480 K), and pressures (3.7-6.4 atm). A simplified analysis of predicted thermal NO formation based on Eq. (7.9) offers comparisons to the measured data. In general, the qualitative trends demonstrate that thermal NO is the dominant mechanism for NO formation in these LPP flames.

8. COMPARISON OF LASER-INDUCED AND PLANAR LASER-INDUCED FLUORESCENCE MEASUREMENTS OF NITRIC OXIDE IN A HIGH-PRESSURE, SWIRL-STABILIZED, SPRAY FLAME

8.1 Introduction

In this chapter, we report spatially resolved linear laser-induced fluorescence (LIF) and planar laser-induced fluorescence (PLIF) measurements of nitric oxide (NO) in a pre-heated, high-pressure, lean direct-injection (LDI) spray flame. The feasibility of using PLIF in lieu of LIF is assessed with respect to measuring NO concentrations in an LDI spray flame at 4.27 atm. NO is excited via the resonant $Q_2(26.5)$ transition of the $\gamma(0,0)$ band while a non-resonant wavelength is employed to subtract background interferences. LIF detection is performed in a 2-nm region centered on the $\gamma(0,1)$ band. PLIF detection is performed in a 68-nm window that captures fluorescence from several vibrational bands. An in-situ NO doping scheme for fluorescence calibration is successfully employed to quantify the LIF signals. However, a similar calibration scheme for the reduction of PLIF images to quantitative field measurements is plagued by the laser-excited background. Excitation scans and calibration comparisons have been performed to assess the background contribution for PLIF detection. Quantitative radial NO profiles measured by LIF are presented and analyzed so as to correct the PLIF measurements to within the accuracy bars of the LIF measurements via a single-point scaling of the PLIF image.

8.2 Background

This investigation is concerned with the development of a quantitative, non-intrusive, scheme by which NO concentrations can be measured in high-pressure spray flames. Several researchers have utilized optical measurements of minor species in such flames. Allen *et al.* (1994) obtained qualitative [OH] images in heptane-air spray flames formed via both solid and hollow-cone nozzles and burned at pressures of 0.1-0.8 MPa.. Excitation of OH was achieved by employing the $P_1(8)$ transition at 285.67 nm. The effect of interfering PAH fluorescence was assessed by using a spectrometer to separate the fluorescence spectrum into individual features. A laser-induced signal exhibiting features at 350 nm, 400 nm, and 450 nm was found on a quasi-continuum background at lower pressures. The strength and spectral characteristics of this broad background were observed to be independent of excitation wavelength within a 5-nm region centered on the $P_1(8)$ transition, which indicated the presence of a broad absorbing species such as a large molecular weight hydrocarbon. As the pressure rose, the above spectral features became non-discernable and exhibited a P^2 increase in fluorescence strength.

In an extension of this work, Allen *et al.* (1995) performed similar [OH] imaging in ethanol flames and further assessed the effects of PAH interferences. While alluding to potential NO measurements, Allen *et al.* (1995) suggested that excitation near 226 nm may produce more severe laser attenuation and hence PAH fluorescence. To test this conjecture, Upshulte *et al.* (1996) obtained qualitative PLIF images of NO, O₂, and fuel vapor by employing excitation wavelengths of 226 nm and 308 nm. Measurements were made for ethanol fuel in the same high-pressure, spray-flame combustor used by Allen *et al.* (1995). As expected, a broad interference signal attributed to PAHs was discovered and assigned to a nominal 5% of the NO signal at atmospheric pressure.

Locke *et al.* (1995) utilized PLIF to image hydroxyl concentrations in a high-pressure (10-14 atm) combustor supplied with Jet-A fuel (0.59-0.83 kg/s) through lean direct-injection ($\phi = 0.41$ -0.53) with preheated air (811-866 K). Though this work only assessed the qualitative distribution of OH radicals in the reacting flow, the combustor was designed to simulate actual gas turbine conditions. The authors found that elastically scattered light and PAH fluorescence were not evident in the downstream regions of their

LDI-based combustor. This was a significant finding, as quantitative LIF measurements in harsh environments are an end goal of optical diagnostics in spray flames.

Cooper and Laurendeau (1998a) developed a saturated-LIF (LSF) technique capable of quantitative measurements of NO concentration in an atmospheric, unconfined, swirl-stabilized spray flame based on a lean direct-injection design. The burner incorporated a helical swirler with a central hollow-cone, pressure-atomized spray nozzle supplied with liquid heptane. A converging/diverging orifice was positioned immediately after the swirler/injector assembly. The diagnostic technique incorporated a subtraction method to remove Mie-scattering background from the NO fluorescence signal. Because of the inherently low sensitivity of LSF to variations in the electronic quenching rate coefficient, a fluorescence calibration developed in a reference flame could be successfully transported to the LDI spray flame.

Cooper *et al.* (1998) continued the previous work by comparing linear-LIF based techniques, both point-LIF and planar-LIF, to the LSF method. Because the linear techniques could not employ a transported calibration, the entire flow field was scaled by the ratio of a linear to a saturated fluorescence signal at a single point in the measurement field. This procedure produced an NO field that fell entirely within the accuracy bars of the more quantitative LSF measurements. In this way, Cooper *et al.* (1998) demonstrated the feasibility of a potential calibration method for high-pressure LIF measurements of NO in spray flames.

In a similar manner, Ravikrishna *et al.* (1999) quantified PLIF images of NO in partially-premixed ethane flames by scaling the entire image based on a single LSF point measurement. The authors chose the partially-premixed flame as a robust test case which included large gradients in temperature, species concentrations, and the electronic quenching rate coefficient. Despite using a single-point scaling method, over 90% of the PLIF measurements fell within the accuracy bars of the LSF data.

In this chapter, we assess the utility of planar laser-induced fluorescence for quantitative measurements of NO in the harsh environment of a high-pressure spray flame. In particular, broad-band PLIF measurements are compared to narrow-band LIF

measurements to evaluate the extent to which PLIF can be made quantitative despite strong interferences from hot O_2 and hydrocarbon intermediates (PAHs).

8.3 Operating Conditions

The LDI burner is operated at a pressure of 4.27 atm and a primary equivalence ratio $\phi_p = 0.9$ using liquid heptane metered at 0.36 g/s and air at 6.07 g/s. The air is preheated to 375 K to assist in vaporization and mixing of the fuel. Because of the intense mixing, the flame is essentially non-sooting and blue. An additional co-flow is introduced to aid in flame stabilization that reduces the overall equivalence ratio to 0.85, assuming complete entrainment into the combustion zone. This flame is identical to the nominal flame studied in Chapter 6, as pictured in Figure 6.1.

8.4 Laser-Induced Fluorescence Measurements

Our previous work developed an excitation/detection scheme for use in LDI flames at pressures of 1-5 atm (Cooper and Laurendeau, 1998a; Cooper and Laurendeau, 1999c). In particular, excitation of the $Q_2(26.5)$ line of the $\gamma(0,0)$ band of NO at 225.58 nm is followed by detection of the $\gamma(0,1)$ band with a 2-nm window centered at 235.78 nm. An off-line wavelength at ~ 225.53 nm is excited and monitored to determine any background for the NO fluorescence signal. At atmospheric pressure, the utility of this approach lies in subtraction of Mie-scattering interferences that break through the monochromator despite the ~ 10 -nm separation between the excitation and detection wavelengths. At higher pressures, this scheme is critical to the detection of NO levels below 10 ppm owing to the background produced by the O_2 Schumann-Runge spectrum.

Chapter 5 details linear LIF measurements for the LDI burner at pressures up to 5.35 atm (Cooper and Laurendeau, 1999b; Cooper and Laurendeau, 1999c). For these measurements, a calibration scheme was developed which allows in-situ doping of NO through the spray flame with no apparent destruction. The calibration slopes for the

spray flame were validated through comparisons with similar measurements in flames of known spectral and chemical characteristics.

8.4.1 Mie Scattering Profiles

The influence of Mie scattering at 4 atm was assessed by measuring scattering profiles so as to locate regions of heavy droplet interference. Scattered light at the incident laser wavelength is passed through neutral density filters and collected via a ½-m monochromator in a 2-nm window centered at ~226 nm. Figure 8.1 depicts the resulting Mie scattering profiles, plotted as arbitrary units and presented only to visualize the spray structure. These profiles compare favorably with the expected profiles based on our 1-atm study, namely axisymmetric double-peaked profiles that reveal the spray sheath typically associated with strongly swirling spray flames (Lee and Chehroudi, 1995).

8.4.2 LIF Measurement Scheme

Typical LIF measurements in harsh environments employ a calibration based on a well-characterized flame (Cooper and Laurendeau, 1998a; Cooper *et al.*, 1998). The accurate transfer of a calibration from one flame environment to another requires that

$$[NO]_{LDI, absolute} = \left(\frac{Q_{e, LDI}}{Q_{e, ref}} \right) [NO]_{LDI, relative}; \quad (8.1)$$

in other words, the concentration measurements relative to the calibration obtained in the reference flame, $[NO]_{LDI, relative}$, must be scaled by the ratio of the electronic quenching rate coefficients in the LDI and reference flames. This procedure yields absolute concentration measurements, $[NO]_{LDI, absolute}$. While species profiles for a flat, premixed reference flame can be accurately predicted via PREMIX (Kee *et al.*, 1985), the LDI flame cannot be adequately modeled so as to provide the distribution of major species concentrations. Consequently, an estimate cannot be determined for the required ratio of

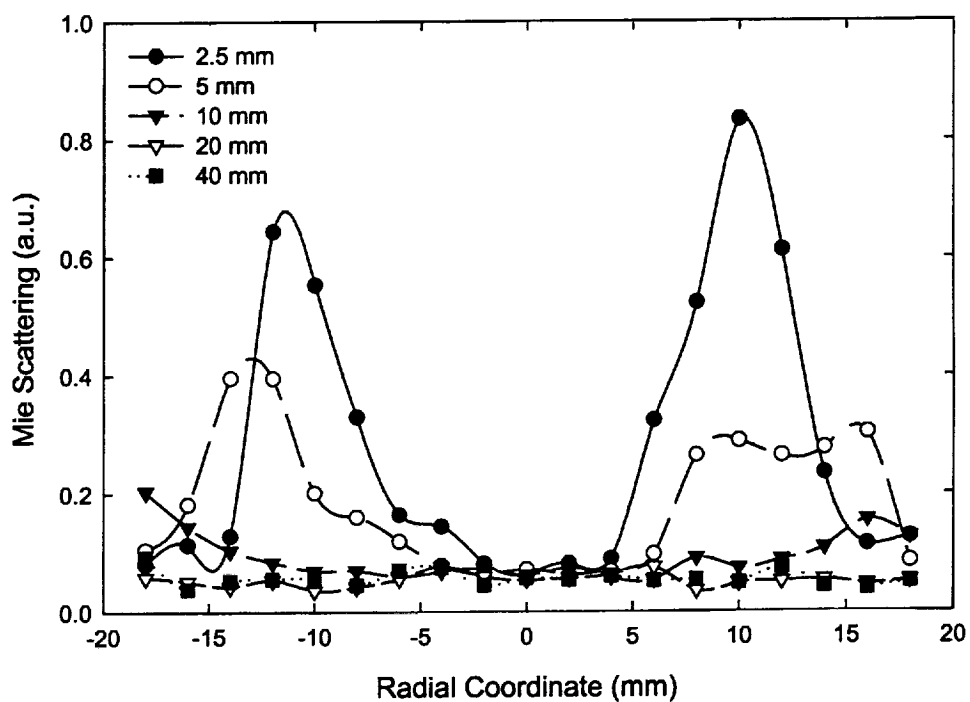


Figure 8.1: Mie scattering radial profiles for LDI flame at 4.27 atm [$\dot{m}_{\text{fuel}} = 0.36 \text{ g/s}$, $\phi_p = 0.9$, $T_{\text{air preheat}} = 375 \text{ K}$].

local electronic quenching rate coefficients, and thus an in-situ calibration method is required for LDI spray flames (Cooper and Laurendeau, 1999b; Cooper and Laurendeau, 1999c).

The results from our atmospheric study demonstrate that the central region of the recirculation zone can provide a successful fluorescence calibration, barring any destruction of NO as it is transported from the reactants to this region (Cooper *et al.*, 1998). Doped NO in spray flames must be transported through the rich regions surrounding the liquid droplets, possibly promoting NO destruction. Moreover, the degree of local partial premixing and the local strain rate could play a large role in the destruction of NO. These issues are not readily modeled for the LDI flame, so that an experimental validation is required for any in-situ doping process. In Chapter 4, we experimentally validated an in-situ doping method for the LDI burner, whereby the flame was seeded with varying levels of NO and the fluorescence signals at these levels were measured. The measurement location was chosen to be the centerline location at a 35-mm axial height so as to reduce background interferences. NO was seeded into the flow through 3000-ppm doped nitrogen. After this experiment, the high-pressure vessel was immediately modified to incorporate a flat-flame McKenna burner and placed back into the translation assembly. Calibration measurements were then performed in the post-flame region of a lean ($\phi = 0.8$, 3.76 dilution ratio) $\text{CH}_4/\text{O}_2/\text{N}_2/\text{NO}$ flame at the same pressure. This flame is well characterized and has been utilized previously for spectral and calibration comparisons (Thomsen *et al.*, 1997). As shown in Chapter 5, the excellent similarity of the calibration slopes demonstrates that NO destruction is not a significant factor in the transport of doped NO to the central region of LDI flames at pressures up to 5 atm (Cooper and Laurendeau, 1999b; Cooper and Laurendeau, 1999c). Further discussion of the experimental method employed to obtain NO profiles is included in Chapter 4.

8.4.3 NO LIF Profiles

Figure 8.2 demonstrates the corrected data whereby each radial profile is calibrated by the centerline fluorescence calibration at the particular axial height and plotted as a function of the radial coordinate. Accuracy bars are typically $\pm 25\%$ at the 95% confidence interval, with an average repeatability within 12%. In general, the NO profile at each axial height demonstrates a uniformity of the NO mole fraction throughout the central region of the LDI flame. In particular, note that the centerline value at each axial height is constant to within 15%. This can be attributed to the well-mixed nature of the internal recirculation zone for this geometry, as demonstrated by previous researchers (Alkabi and Andrews, 1989; Terasaki and Hayashi, 1996). In particular, Terasaki and Hayashi (1996) demonstrated fairly uniform radial temperatures within the recirculation zone in a similar swirl burner. Our measurements are focused on this homogeneously mixed recirculation zone and therefore are limited by radial temperature gradients near the shear layer. Careful examination of Figs. 8.1 and 8.2 demonstrates that our measurements are spatially located between the centerline and the spray sheath, thus avoiding radial temperature gradients.

Since each radial profile is referenced to the calibration taken at its centerline, the profiles ultimately become skewed as the laser transmission decreases with increasing path length. Hence, those measurements taken past the centerline are preferentially lower, whereas those taken prior to the centerline are preferentially higher. It should be emphasized, however, that the centerline measurement for each axial calibration is an absolute measurement, as all effects other than possible NO destruction are inherently included in the calibration. To correct for the skewness of the NO profiles that resulted from absorption losses, the profiles were mirrored and averaged. A simple model was constructed to validate this correction technique for a range of absorption coefficient profiles and NO concentration profiles in an axisymmetric flow, recognizing that both the laser beam and NO fluorescence pass through different path lengths as a function of measurement position. The results indicate that this correction procedure is quite satisfactory owing to the centerline pivot point that the profiles are referenced to via the

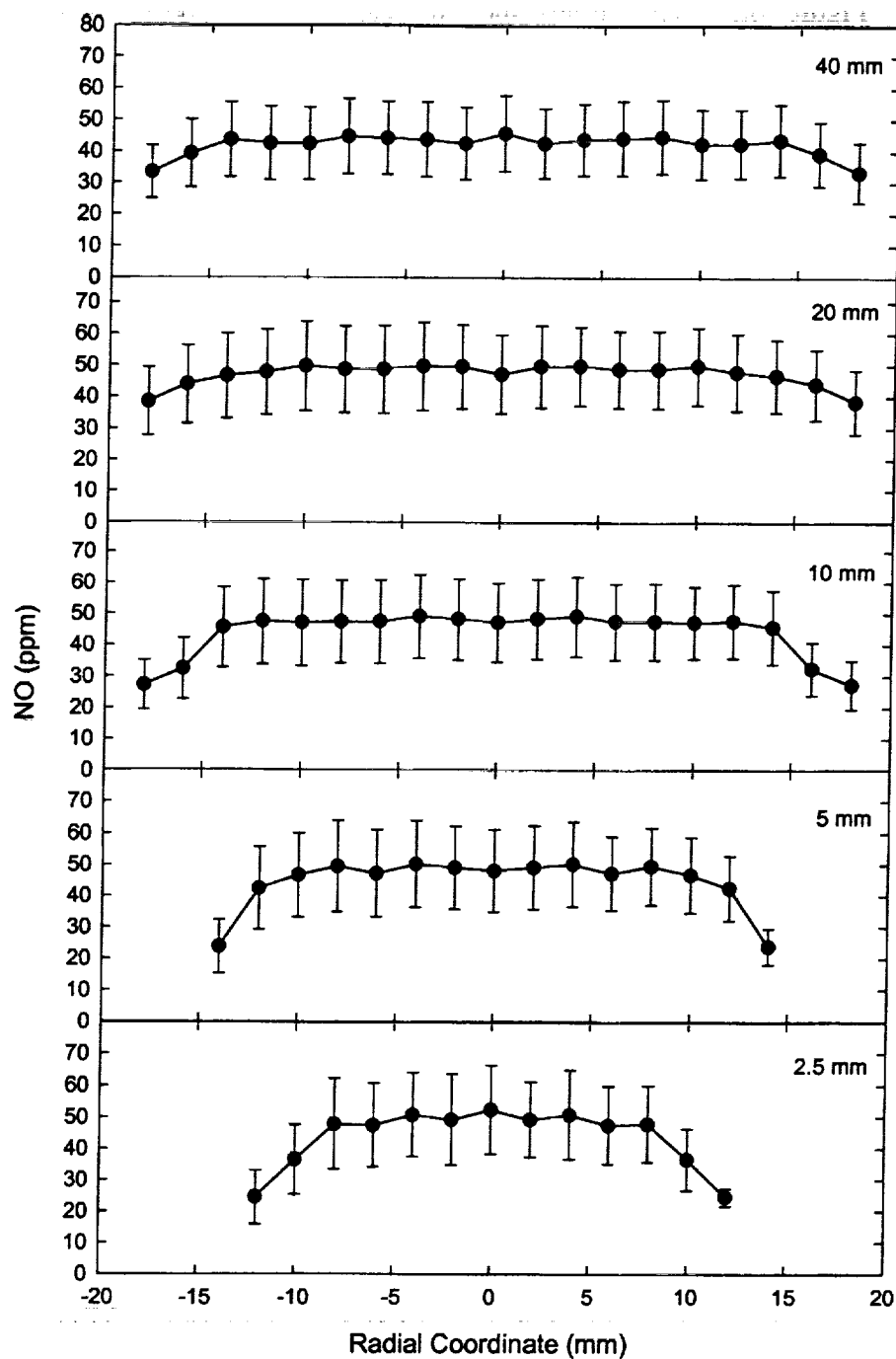


Figure 8.2: Absolute NO (ppm) measurements in 4.27-atm LDI flame [$\dot{m}_{\text{fuel}} = 0.36$ g/s, $\phi_p = 0.9$, $T_{\text{air preheat}} = 375$ K]. Radial NO profiles have been corrected for extinction and calibrated at each axial height.

fluorescence calibration. The accuracy of the method obviously increases as the NO concentration profiles and the extinction coefficient become more uniform across the flame.

8.5 PLIF Measurements

We have shown in Chapters 4 and 5 that the narrowband LIF technique yields excellent results despite the harsh environment of spray flames (Cooper and Laurendeau, 1999b; Cooper and Laurendeau, 1999c). This fact permits us to consider PLIF as an additional tool by which to explore the NO concentration field. If the detected fluorescence is not plagued by Mie scattering or laser-induced interferences, i.e., O₂, PAH, or UHC fluorescence, then the opportunity exists to make quantitative images of NO concentration. In particular, the subtraction technique must employ two excitation wavelengths having common backgrounds within the broadband spectral window for PLIF.

8.5.1 PLIF Excitation Scan Comparison

The narrowband detection window for LIF was chosen based on a common and small background at the two excitation wavelengths (Thomsen *et al.*, 1997). For the broadband detection window used in PLIF, off-line wavelength excitation should accurately mimic the Mie background; however, an accurate representation of any O₂ interferences cannot be guaranteed without further work. To experimentally assess the background in the PLIF detection window, an excitation image sequence was performed whereby the cumulative fluorescence from 1200 laser shots was summed on chip and normalized by the laser power. The laser excitation wavelength was shifted after each image so as to scan the spectral region of interest, namely 225.5 to 225.6 nm, thus encompassing the Q₂(26.5) transition of NO. A 1-mm × 1-mm region in each image at the centerline of the 15-mm axial height was averaged and compared with a similar scan at the same location when utilizing narrowband LIF. The results of this comparison are

shown in Figure 8.3, where the scans have been normalized to a maximum signal level of unity. The on-line excitation wavelength is labeled at the $Q_2(26.5)$ transition, while the off-line excitation wavelength used in the LIF measurements is labeled near 225.52 nm. The off-line wavelength demonstrates an increased PLIF signal level relative to that for LIF. Since the LIF spectrum has been well characterized (Thomsen *et al.*, 1997; Cooper and Laurendeau, 1999b; Cooper and Laurendeau, 1999c), we surmise that the off-line excitation wavelength likely excites an interference within the broadband detection window for PLIF that is not common to the on-line excitation wavelength.

8.5.2 Calibration Slope Comparison

To better characterize the increase in background when using a broadband detection window, calibration measurements were performed whereby NO was doped into the flame in a manner identical to that for previous LIF measurements (Cooper and Laurendeau, 1999b; Cooper and Laurendeau, 1999c). The NO doping gas contained 3000 ppm NO in N_2 which was metered to achieve levels of less than 100 ppm in the flame products. A 1-mm \times 1-mm square along the centerline in the well-mixed region was averaged and utilized to obtain a broadband calibration slope from the various doping levels. This region displays uniform narrowband calibration slopes which are independent of axial height owing to a lack of thermal gradients in the axial direction (Cooper and Laurendeau, 1999c). Hence, similar calibration slopes measured with narrowband LIF were taken at the same position in the flame for comparison. The two data sets, LIF and PLIF, were then normalized to unity at the maximum doping condition for on-line excitation. A comparison of the two calibration sets utilizing both on-line and off-line excitation is shown in Figure 8.4. While the on-line calibration slopes are very similar, the off-line calibration intercepts are quite different. The obvious shift validates the increased background observed in Figure 8.3. To further emphasize the preferential off-line excitation, the ratio of off-line to on-line signals is plotted in Figure 8.5. This ratio is very small for the LIF measurements owing to the essentially negligible common

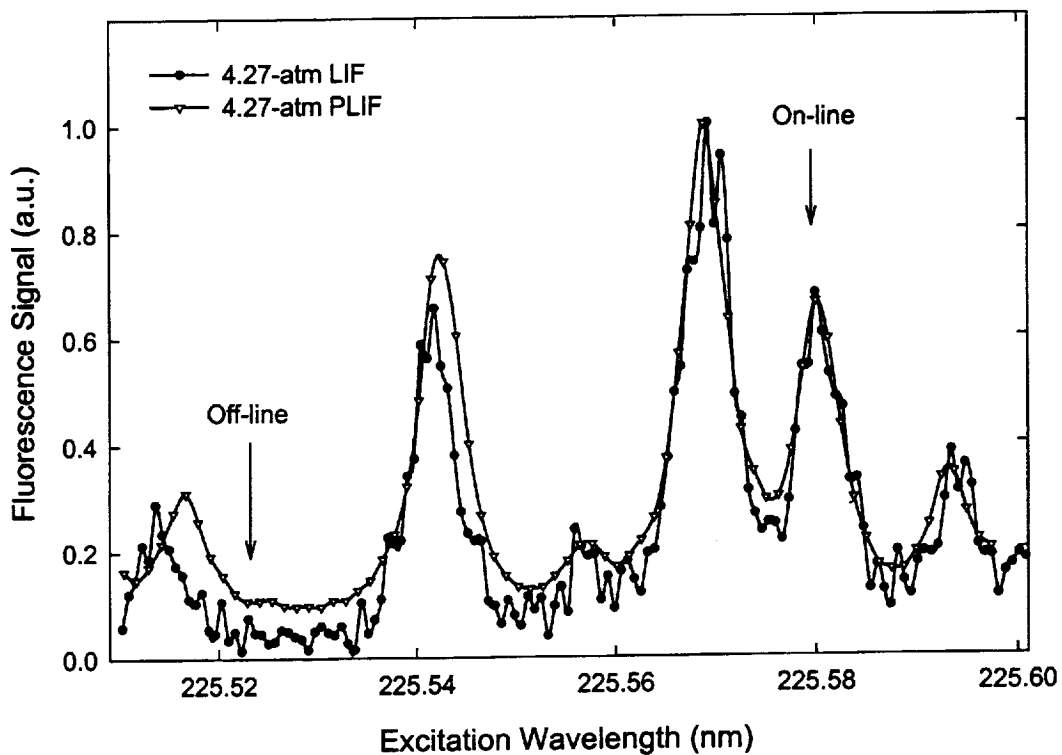


Figure 8.3: Excitation scans in 4.27-atm LDI flame at $h = 15$ mm, $r = 0$ mm doped with ~ 80 ppm NO using narrowband LIF detection and broadband PLIF detection. The NO on-line $Q_2(26.5)$ and the off-line excitation wavelengths are labeled.

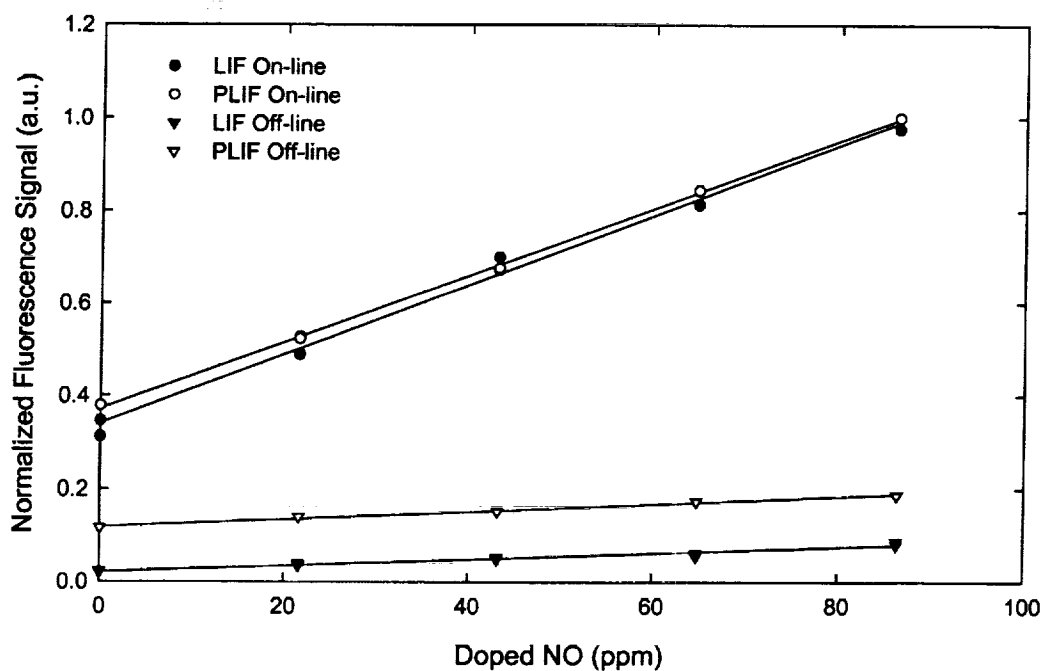


Figure 8.4: NO fluorescence calibrations taken in 4.27-atm LDI flame using narrowband LIF detection and broadband PLIF detection. Both calibration curves have been normalized to unity at the maximum on-line doping condition. Note the background shift for off-line PLIF excitation.

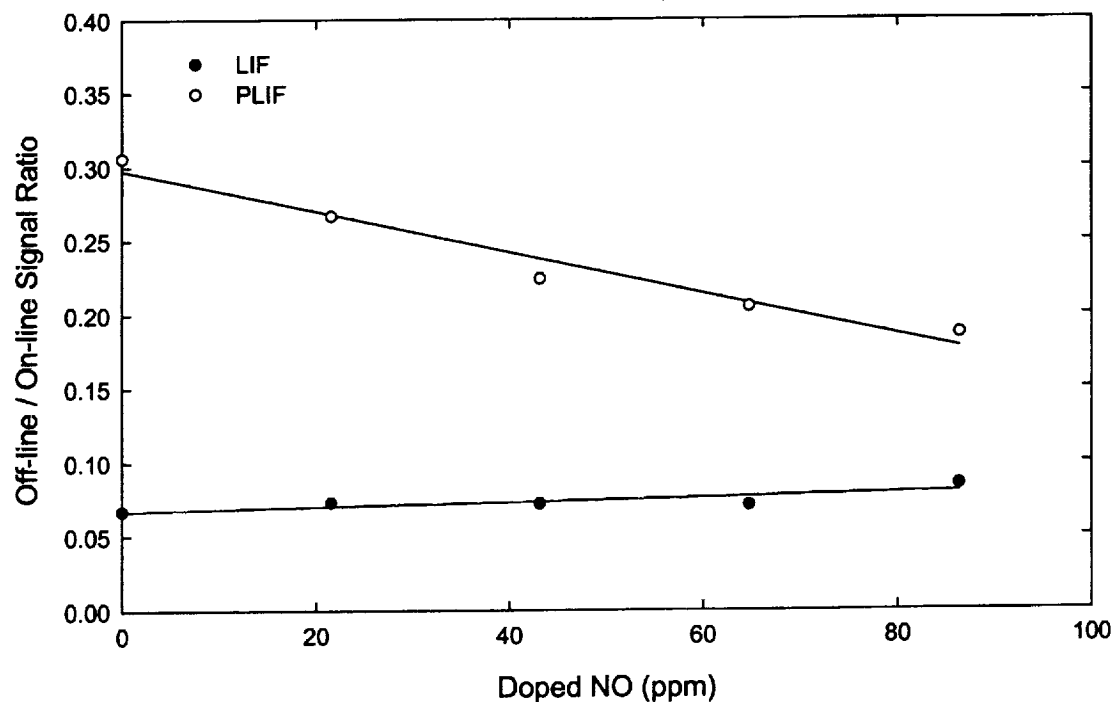


Figure 8.5: Ratio of off-line to on-line calibration signal in 4.27-atm LDI flame for narrowband LIF detection and broadband PLIF detection. The LIF data demonstrate a ratio which is constant with doping level. The PLIF data demonstrate a decrease with increasing NO concentration, revealing a preferential excitement of interfering species by the off-line wavelength within the broadband detection window.

background, whereas the ratio is much larger for PLIF measurements and demonstrates the expected result, i.e., as the level of doping rises, the ratio decreases owing to the increase in NO signal relative to the background.

To convert PLIF images to quantitative NO concentration measurements, Cooper *et al.* (1998) and Ravikrishna *et al.* (1999) utilized a single-point scaling technique to collapse the PLIF profiles to within the accuracy bars of more quantitative laser-saturated fluorescence (LSF) measurements. Cooper *et al.* (1998) were able to quantify time-average PLIF data since the electronic quenching rate coefficient was found to be essentially uniform in the central region of the LDI spray flame. Recognizing that the background is pressure dependent (Thomsen *et al.*, 1997), a complete spectral study would be required to identify an on-line/off-line scheme with a common background in the 68-nm detection window of the ICCD camera. As such an exhaustive study is not the focus of this work, we simply utilize a single-point scaling of the measurements to quantify the PLIF data.

8.5.3 PLIF Experimental Method

The procedure to convert a PLIF image to an NO concentration field is very similar to that for LIF. We utilized an on-line wavelength (225.58 nm) resonant with the $Q_2(26.5)$ transition of NO. NO was doped into the flame so as to achieve doped flow-field concentrations of 86, 65, 44, 22, and 0 ppm. For each doping condition, an image was recorded corresponding to the on-chip summation of 1200 laser shots. The laser was then tuned to an off-line wavelength (225.53 nm) and a similar image was recorded. The data were then processed as follows: (1) the flame luminosity was subtracted from the initial on- and off-line images by employing a similar image with no laser beam passing through the probe volume; (2) these on- and off-line images were normalized by the distribution of energy in the laser sheet via a 20-shot image which recorded Rayleigh scattering in air; and (3) the normalized off-line image was subtracted from the normalized on-line image. To directly compare the PLIF data with those obtained by LSF and LIF, 1-mm squares were averaged throughout the image and horizontal stripes

were extracted corresponding to $h = 5, 10$, and 20 mm. The slightly larger sampling volume of the PLIF measurements compared to that of the LIF measurements was chosen to increase the signal-to-noise ratio. A $1\text{-mm} \times 1\text{-mm}$ region along the centerline at each height was utilized to obtain a calibration slope from the five doping levels. In a manner identical to the LIF measurements, the radial profiles at each axial height ($5, 10$, and 20 mm) were then corrected with a fluorescence calibration specific to that height. To better compare the extracted PLIF data with the LIF data, the data sets for both measurements are not corrected for skewing with the mirror/average procedure.

8.5.4 NO PLIF Profiles

The PLIF measurements demonstrated qualitatively similar profiles, but were a nominal 16% smaller than the quantitative LIF measurements. This depression results from the increased background for the PLIF detection scheme, as discussed previously. Though a 16% discrepancy is not excessively large, more accurate data can be achieved by scaling the PLIF measurements using a ratio of the LIF/PLIF data at the centerline 10-mm axial height. The scale factor is ~ 1.19 . The result of such a scaling is pictured in Figure 8.6, with the PLIF data now collapsed to within the accuracy bars of the LIF data.

Several precautions must be noted in regard to the quantification of PLIF data. Since the background for the two excitation wavelengths is large and not common in the PLIF detection window, the off-line/on-line fluorescence signal depends on the doping level. Moreover, since we are using a subtraction procedure, the variation in this ratio throughout the flame would normally cause erroneous results and the PLIF data would not scale correctly with the LIF data. In addition, if the background itself shifts owing to changes in the concentrations of interfering species such as O_2 or owing to temperature gradients, then an effective collapse such as that demonstrated here would be difficult to achieve. However, Figure 8.2 demonstrates a very uniform NO concentration in the central region of the LDI spray flame. This uniformity in a minor species such as NO likely implies uniformity in the major species. The temperature variation within the 5-

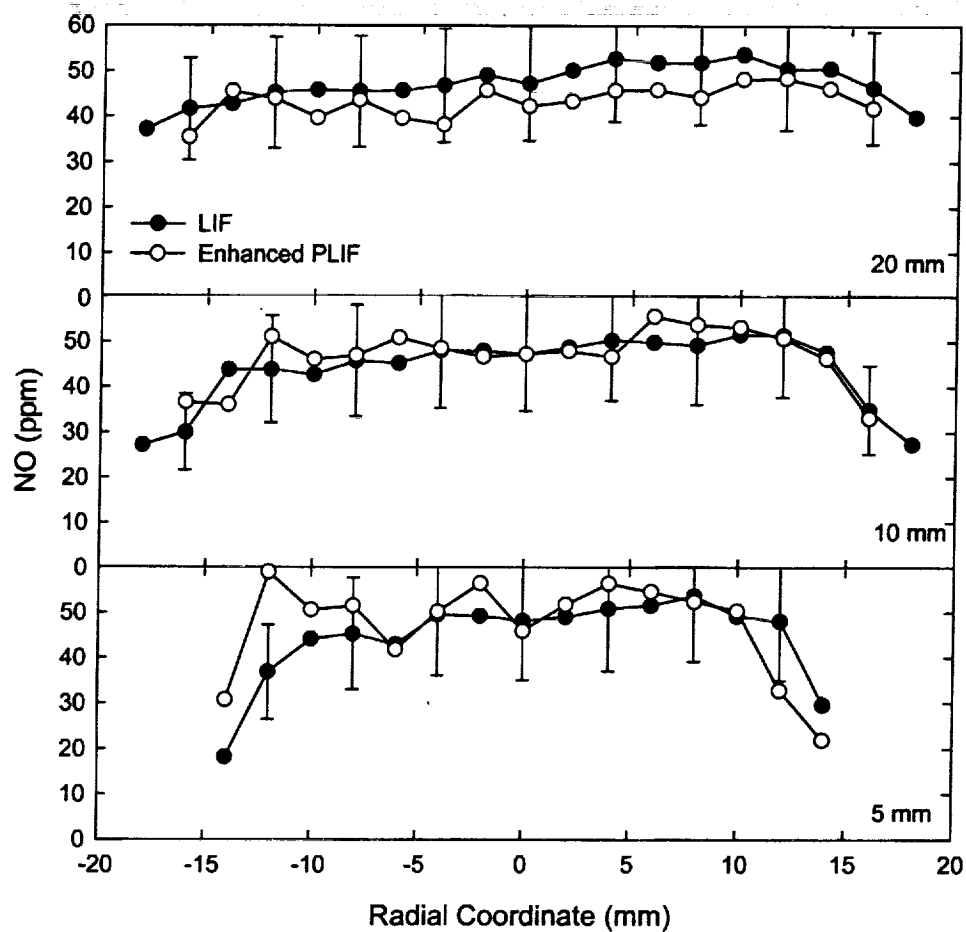


Figure 8.6: Comparison of the corrected PLIF measurements to the LIF measurements. The PLIF measurements fall within the accuracy bars of the LIF data, emphasizing the utility of the PLIF technique for LDI spray flames when a scaling point can be obtained from quantitative LIF data.

mm to 20-mm region along the central axis has been shown to be ~10% (Cooper and Laurendeau, 1999c). This uniformity in species concentrations and temperature leads to a constant off-line/on-line ratio that allows effective calibration. Hence, the LDI flame, with its recirculation zone, is uniquely suited to quantitative PLIF images, which thus permits this diagnostic tool to be used for the detection of NO.

8.6 Conclusions

Quantitative LIF measurements of NO concentration have been obtained in an LDI flame fueled with liquid heptane at 4.27 atm so as to assess the utility of PLIF as a diagnostic technique for high-pressure spray flames. The LIF profiles reveal a uniform distribution of NO (ppm) throughout the flame. Spectral studies for a PLIF detection scheme confirm that a broad detection window of 68 nm is plagued by fluorescence interferences from rogue species. Nevertheless, PLIF profiles can be quantified through a single-point scaling with the more quantitative LIF data owing to the unique attributes of the LDI flame.

The goal of this study was to develop a laser-induced fluorescence technique capable of measuring quantitative NO concentrations in 1-10 atm LDI-based spray flames. Considering the excellent profile comparisons between the two LIF-based techniques presented in this chapter, we conclude that qualitative PLIF measurements of [NO] at high pressure can be scaled in a similar fashion by using a single calibrated point so as to produce quantitative PLIF measurements of NO.

9. CONCLUSIONS AND RECOMMENDATIONS FOR FUTURE WORK

9.1 Conclusions

Quantitative LIF measurements of NO concentration (ppm) have been obtained in an LDI burner fueled with liquid heptane operating at pressures up to 5.35 atm. Spectral signals resulting from background interferences caused by Mie scattering and oxygen fluorescence are removed via an on-resonance/off-resonance subtraction routine. Through comparison of fluorescence calibrations taken in the LDI spray flame and in a reference flame of known spectral characteristics, we have validated the use of a convenient reactant doping method. In particular, the results indicate insignificant destruction of doped NO, thereby allowing a simple means by which to quantify fluorescence measurements. Quantitative NO profiles were presented at operating pressures of 2.09, 3.18, 4.27, and 5.35 atm and were demonstrated to yield NO_x emissions close to target reduction levels. The NO profiles demonstrated a uniformity within the central recirculation region of the flame at pressures above 3 atm. The pressure scaling of the downstream measurements was found to be approximately $P^{0.74}$.

NO concentrations have also been obtained in high-pressure LDI flames for a range of equivalence ratios ($\phi_p=0.8-1.0$) and air-preheat temperatures (375-575 K). Parametric studies of these variables strongly suggest that NO formation occurs in near stoichiometric regions of the flame and is subsequently diluted with excess air. A residence time effect is evident and apparently scales with the mass flow rate of air relative to that for stoichiometric combustion, yielding a ϕ^2 scaling of the produced NO (ppm) with primary equivalence ratio. Moreover, moderate increases in air-preheat temperature produce significant increases in NO (ppm) levels, suggesting thermal NO production.

Quantitative LIF measurements of NO concentration have been obtained for comparative purposes in high-pressure LPP flames for a range of equivalence ratios ($\phi=0.65-0.75$), air-preheat temperatures (365-480 K), and pressures (3.7-6.4 atm). Simplified analyses of predicted thermal NO formation have been compared to the measured data. The qualitative trends suggest that thermal NO is the dominant path for NO formation in these LPP flames.

The utility of PLIF as a diagnostic technique for high-pressure spray flames has been assessed by comparisons with LIF profiles of NO in a 4.27-atm LDI flame. Spectral studies for a PLIF detection scheme confirm that a broad detection window of 68 nm is plagued by fluorescence interferences from rogue species. Nevertheless, PLIF profiles can be quantified through a single-point scaling with the more quantitative LIF data owing to the unique attributes of the LDI flame.

9.2 Recommendations

The most significant addition to the NO data of this investigation would be the mapping of major species and temperature through the addition of a Raman scattering facility to compliment the existing LIF facility. The single contribution of NO concentrations, while valuable indeed, must be used alongside other information to understand the formation of pollutants within these spray flames. Another significant contribution would be the measurement of velocity fields that would better define the strength of the recirculation zone. Both additions would prove invaluable toward a complete understanding of this type of reacting flow.

Determination of the temperature throughout the flames is particularly important. Because of hardware limitations, a thermocouple cannot be traversed over the flame. A two-line LIF approach, either with NO or a seed species as the detected molecule, is a good possibility.

Another important contribution would be a diagnostic for the fuel vapor concentration. Several opportunities for fuel detection exist, including doping seed species into the flow or utilizing a "dirty" fuel that has significant hydrocarbon spectral

features. We have been pressed during this investigation to pursue such a diagnostic; however, sufficient time was unavailable, but such a study should be pursued in the future.

The next logical step is the introduction of a "dirty" fuel such as Jet-A into the LDI burner. The accurate modeling of real gas-turbine combustors is the ultimate goal, and to fully meet this goal, real fuels must be used. Heptane was chosen because it is non-sooting and very easy to work with. With the diagnostic now developed, the next immediate step would be to measure NO in flames supplied with industrial fuels.

Experimentally, the LDI burner eventually requires a new macrolaminate nozzle designed to provide larger mass flow rates of fuel without a large pressure drop, i.e. a larger flow number. To achieve the air flow rates needed to exceed ~6 atm within the vessel, a new building compressor and new ballast tanks will be required. Existing safety concerns limit the available building pressure to ~9 atm. Moreover, the ballast tanks, even when fully pressurized, cannot provide a steady continuous flow of air, i.e., compressor surge becomes a serious problem.

To monitor the flame front region, the spatial probe volume will have to be significantly decreased. Unfortunately, a reduction in probe volume forces a reduction in the signal-to-noise ratio and decreases the accuracy of the measurements. Currently, our photomultiplier tubes are shot limited, meaning that the largest contribution to our error lies in the inherent noise of the PMT. The introduction of a superior photomultiplier tube would greatly benefit further investigations.

During the course of this work, a unique way of preventing window condensation has been discovered for low heat-output flames, e.g., the McKenna burner. The use of infrared radiant heaters maintains the window surface at a sufficient temperature to avoid such problems, which can be a considerable nuisance in high-pressure work.

LIST OF REFERENCES

- Aigner, M., Mayer, A., Schiessel, P., and Strittmatter, W. (1990). "Second-generation Low-Emission Combustors for ABB Gas Turbines: Tests Under Full-Engine Conditions," *International Gas Turbine and Aeroengine Congress and Exposition*, Brussels, Belgium, ASME Paper No. 90-GT-308.
- Alkabie, H.S., Andrews, G.E. and Ahmad, N.T. (1988). "Lean Low NO_x Primary Zones using Radial Swirlers," ASME Paper No. 88-GT-245.
- Alkabie, H.S. and Andrews, G.E. (1989). "Ultra Low NO_x Emissions for Gas and Liquid Fuels using Radial Swirlers," ASME Paper No. 89-GT-322.
- Allen, M.G., McManus K.R., and Sonnenfroh, D.M. (1994). "PLIF Imaging Measurements in High-pressure Spray Flame Combustion," *AIAA Paper No. 94-2913*.
- Allen, M.G., McManus, K.R., Sonnenfroh, D.M. and Paul, P.H. (1995). "Planar Laser-Induced-Fluorescence Imaging Measurements of OH and Hydrocarbon Fuel Fragments in High-pressure Spray Flame Combustion," *Appl. Opt.* **34**, 6287-6300.
- Amin, E.M., Andrews, G.E., Pourkashnian, William, A., and Yetter, R.A. (1995). "A Computational Study of Pressure Effects on Pollutant Generation in Gas Turbine Combustors," ASME Paper No. 95-GT-304
- Beer, J.M. and Chigier, N.A. (1972). *Combustion Aerodynamics*, Applied Science Publishers, London.
- Bulzan, D. (1995). "Structure of a Swirl-Stabilized Combusting Spray," *J. Propul. Power* **11**, 1093-1102.
- Carter, C.D., Salmon, J.T., King, G.B., and Laurendeau, N.M. (1987). "Feasibility of Hydroxyl Concentration Measurements by Laser-saturated Fluorescence in High-Pressure Flames," *Appl. Opt.* **26**, 4551-4562.

- Carter, C.D., King, G.B., and Laurendeau, N.M. (1992). "Saturated Fluorescence Measurements of the Hydroxyl Radical in Laminar High-pressure $C_2H_6/O_2/N_2$ Flames," *Appl. Opt.* **31**, 1511-1522.
- Carter, C.D. and Laurendeau, N.M. (1994). "Wide- and Narrow-band Saturated Fluorescence Measurements of Hydroxyl Concentration in Premixed Flames from 1 bar to 10 bar," *Appl. Phys. B* **58**, 519-528.
- Chen, R.H. and Driscoll, J.F. (1990). "Nitric Oxide Levels of Jet Diffusion Flames: Effects of Coaxial Air and Other Mixing Parameters," *Twenty-Third Symposium (International) on Combustion*, The Combustion Institute, Pittsburgh, PA, 281-288.
- Chen, R.H. (1995). "Some Characteristics of NO_x Emission of Turbulent Nonpremixed Hydrogen-Air Flames Stabilized by Swirl-Generated Flow Recirculation," *Combust. Sci. & Tech.* **110**, 443-460.
- Chen, R.H. (1996). " NO_x and NO_2 Emission of Swirl-Stabilize Nonpremixed Flames of a H_2-CH_4 Mixture," *Combust. Sci. & Tech.* **120**, 321-333.
- Cheng, T.S. Chao, Y.C., Wu, D.C., Yuan, T., Lu, C.C., Cheng, C.K., and Chang, J.M. (1998). "Effects of Fuel-Air Mixing on Flame Structures and NO_x Emissions in Swirling Methane Jet Flames," *Twenty-Seventh Symposium (International) on Combustion*, The Combustion Institute, Pittsburgh, PA, 1229-1237.
- Cooper, C.S. and Laurendeau, N.M. (1997). "Effect of Pulsed Dye-Laser Wavelength Stabilization on Spectral Overlap in Atmospheric NO Fluorescence Studies," *Appl. Opt.* **36**, 5262-5265.
- Cooper, C.S. and Laurendeau, N.M. (1998a). "Quantitative Laser Saturated Fluorescence Measurements of Nitric Oxide in a Heptane Spray Flame," *Combust. Sci. and Tech.* **127**, 363-382.
- Cooper, C.S. and Laurendeau, N.M. (1998b). "Quantitative Laser-Saturated Fluorescence Measurements of Nitric Oxide in a Heptane-Fueled Lean Direct-Injection Spray Flame at Varying Global Equivalence Ratios," *Twenty-Seventh Symposium (International) on Combustion*, The Combustion Institute, Pittsburgh, PA, 1993-2000.
- Cooper, C.S. and Laurendeau, N.M. (1999a). "Laser-Induced Fluorescence Measurements in Lean Direct-Injection Spray Flames: Technique Development and Application," *Measurement Science and Technology*, in press.

- Cooper, C.S. and Laurendeau, N.M. (1999b). "In-Situ Calibration Technique for Laser-Induced Fluorescence Measurements of Nitric Oxide in High-Pressure, Direct-Injection, Swirling Spray Flames," Submitted for publication to *Combustion Science and Technology*.
- Cooper, C.S. and Laurendeau, N.M. (1999c). "Quantitative Measurements of Nitric Oxide in High-Pressure (2-5 atm), Swirl-Stabilized Spray Flames via Laser-Induced Fluorescence," Submitted for publication in *Combustion and Flame*.
- Cooper, C.S., Ravikrishna, R.V., and Laurendeau, N.M. (1998). "Comparisons of LSF, LIF, and PLIF Measurements of Nitric Oxide in a Lean Direct-Injection Spray Flame," *Appl. Opt.* **37**, 4823-4833.
- Correa, S.M. (1992). "A Review of NO_x Formation Under Gas-turbine Combustion Conditions," *Combust. Sci. and Technol.* **87**, 329-362.
- Eckbreth, A.C. (1996). *Laser Diagnostics for Combustion Temperature and Species*. Gordon and Breach Publishers, Amsterdam, Netherlands.
- Ghaffarpour, M. and Chehroudi, B. (1993). "Experiments on Spray Combustion in a Gas Turbine Model Combustor," *Combust. Sci. & Tech.* **92**, 173-200.
- Gupta, A.K., Ramavajjala, M.S., Chomiak, J., and Marchionna, N. (1991). "Burner Geometry Effects on Combustion and NO_x Emission Characteristics using a Variable Geometry Swirl Combustor," *J. Propulsion* **7**, 473-480.
- Gupta, A.K. (1997). "Gas Turbine Combustion: Prospects and Challenges," *Energy Convers. Mgmt.* **38**, 1311-1318.
- Gupta, A.K., Lewis, M.J., and Qi, S. (1997). "Effect of Swirl on Combustion Characteristics in Premixed Flames," *ASME Paper No. 97-GT-276*.
- Harris, J.M., Lytle, F.E., and McCain, T.C. (1976). "Squirrel-cage photomultiplier base design for measurements of nanosecond fluorescence decays," *Anal. Chem.* **48**, 2095-2098.
- Hayashi, S. (1995). "Compatibility between low-NO_x emissions and high-combustion efficiency by lean direct injection combustion," *ASME Paper No. 95-GT-276*.
- Held, Timothy. (2000). General Electric Aircraft Engines, Cincinnati, OH, *personal communication*.
- Jones, W.P. and Wilhelmi J. (1989). "Velocity, Temperature, and Composition Measurements in a Confined Swirl Driven Recirculating Flow," *Combust. Sci. and Technol.* **63**, 13-31.

- Kee, R.J., Grcar, J.F., Smooke, M.D., and Miller, J.A. (1985). "A FORTRAN Program for Modeling Steady Laminar One-dimensional Premixed Flames," *Sandia Report SAND85-8240*.
- Laurendeau, N.M. and Goldsmith, J.E.M. (1989). "Comparison of Hydroxyl Concentration Profiles using Five Laser-induced Fluorescence Methods in a Lean Subatmospheric $H_2/O_2/Ar$ Flame," *Combust. Sci. and Tech.* **63**, 139-152.
- Lee, K. and Chehroudi, B. (1995). "Structure of a Swirl-stabilized Spray Flame Relevant to Gas Turbines and Furnaces," *J. Propul. Power* **11**, 1110-1117.
- Locke, R.J., Hicks, Y.R., Anderson, R.C., Ockunzzi, K.A., and North, G.L. (1995). "Two-dimensional Imaging of OH in a Lean Burning High Pressure Combustor," *AIAA Paper No. 95-0173*.
- Locke, R.J., Hicks, Y.R., Anderson, R.C., and Zaller, M.M. (1998). "Optical Fuel Injector Patternation Measurements in Advanced Liquid-Fueled, High Pressure, Gas Turbine Combustors," *Combust. Sci. and Tech.* **138**, 297-311.
- Lucht, R.P., Sweeney, D.W., and Laurendeau, N.M. (1980). "Balanced Cross-rate Model for Saturated Molecular Fluorescence in Flames using a Nanosecond Pulse Length Laser," *Appl. Opt.* **19**, 3295-3300.
- Magi, V. (1987). "REC-87: A New 3-D Code for Flows, Sprays and Combustion in Reciprocating and Rotary Engines," *Mechanical and Aerospace Engineering Report No. 1793, Princeton University*.
- McDonnel, V.G., Adachi, M., and Samuelsen, G.S. (1992). "Structure of Reacting and Non-reacting Swirling Air-assisted Sprays," *Combust. Sci. and Tech.* **82**, 225-248.
- Partridge, W.P. (1996). "Experimental Assessment and Enhancement of Planar Laser-Induced Fluorescence Measurements of Nitric Oxide in an Inverse Diffusion Flame," Ph.D. Thesis, School of Mechanical Engineering, Purdue University, West Lafayette, IN.
- Partridge, W.P. and Laurendeau, N.M. (1994). "Performance of Pyrromethene 580 and 597 in a Commercial Nd:YAG-pumped Dye-laser System," *Optics Letters* **19**, 1630-1632.
- Partridge, W.P., Klassen, M.S. Jr., Thomsen, D.D., and Laurendeau, N.M. (1996). "Experimental Assessment of O_2 Interferences on Laser-induced Fluorescence Measurements of NO in High-pressure, Lean Premixed Flames by use of Narrowband and Broadband Detection," *Appl. Opt.* **34**, 4890-4904.

- Paul, P.H., Gray, J.A., Durant, J.L. Jr., and Thoman, J.W. (1994). "Collisional Quenching Corrections for Laser-induced Fluorescence Measurements of $\text{NO } A^2\Sigma^+$," *AIAA J.* **32**, 1670-1675.
- Polifke, W., Döbbeling, K., Sattelmayer, T., Nicol, D.G., and Malte, P.C. (1995). "A NO_x Prediction Scheme for Lean-Premixed Gas Turbine Combustion Based on Detailed Chemical Kinetics," *ASME Paper No. 95-GT-108*.
- Ravikrishna, R.V., Parttridge, W.P., and Laurendeau, N.M. (1999). "Quantification of Planar Laser-induced Fluorescence Measurements of Nitric Oxide in Laminar Partially Premixed Flames," *Combust. Sci. and Tech.* **144**, 79-92.
- Reisel, J.R. and Laurendeau, N.M. (1995). "Quantitative LIF Measurements and Modeling of Nitric Oxide in High Pressure $\text{C}_2\text{H}_4/\text{O}_2/\text{N}_2$ Flames," *Combust. and Flame* **101**, 141-152.
- Reisel, J.R., Carter, C.D., and Laurendeau, N.M. (1993). "Laser-saturated Fluorescence Measurements of Nitric Oxide in Laminar, Flat, $\text{C}_2\text{H}_6/\text{O}_2/\text{N}_2$ Flames at Atmospheric Pressure." *Combust. Sci. and Tech.* **91**, 271-295.
- Rink, K.K. and Lefebvre, A.H. (1989). "The Influences of Fuel Composition and Spray Characteristics on Nitric Oxide Formation," *Combust. Sci. and Tech.* **68**, 1-14.
- Shaffar, S.W. and Samuelson, G.S. (1998). "A Liquid-Fueled, Lean Burn, Gas Turbine Combustor Injector," *Combust. Sci. and Tech.* **139**, 41-57.
- Syred, N. and Beer, J.M. (1974). "Combustion in Swirling flows: a Review," *Combust. and Flame* **23**, 143-201.
- Taylor, J.T. (1982). *An Introduction to Error Analysis: the Study of Uncertainties in Physical Measurements*, University Science Books, California.
- Terasaki, T. and Hayashi, S. (1996). "The Effects of Fuel-Air Mixing on NO_x Formation in Non-premixed Swirl Burners," *Twenty-Sixth Symposium (International) on Combustion*, The Combustion Institute, Pittsburgh, PA, 2733-2739.
- Thomsen, D.D., Kuligowski, F.F., and Laurendeau, N.M. (1997). "Background Corrections for Laser-induced Fluorescence Measurements of NO in Lean, High-pressure, Premixed Methane Flames," *Appl. Opt.* **36**, 3244-3252.
- Turns, S.R. (1996). *An Introduction to Combustion*, McGraw-Hill, Inc., New York.
- Upschulte, B.L., Allen M.G., and McManus, K.R. (1996). "Fluorescence Imaging of NO and O_2 in a Spray Flame Combustor at Elevated Pressures," *Twenty-Sixth Symposium (International) on Combustion*, The Combustion Institute, Pittsburgh, PA, 2779-2786.

Upschulte, B.L., Sonnenfroh, D.M., Allen, M.G., and Miller, M.F. (1998). "In-Situ, Multi-Species Combustion Sensor Using a Multi-Section Diode Laser," AIAA Paper No. 98-0402.

Yegian, D.T. and Cheng, R.K. (1998). "Development of a Lean Premixed Low-swirl Burner for Low NO_x Practical Applications," *Combust. Sci. and Tech* **139**, 207-227.

Appendix A: Error Analysis

To sufficiently quantify LIF measurements of NO, an estimate of the inherent errors contained in the measurements must be made. These measurements must be analyzed to determine both the precision and accuracy of the experimental data. The precision is a measure of the repeatability of the measurements, whereas the accuracy is a measure of how close the data compare to the actual values of NO concentration in the flame and thus contains the precision plus any systematic errors.

Factors affecting the precision, and hence the repeatability of the measurements, include PMT shot noise and electronic data acquisition noise. The accuracy of the measurements largely depend on the calibration scheme. The accuracy of the doped concentrations and possible destruction of NO in the flame affect the accuracy of the calibrated NO measurements in the LDI flames.

In the following, the focus is on determination of the measurement accuracy, as opposed to the precision. All uncertainties are based on a 95% confidence level. Therefore, the uncertainty of a measured quantity is defined as twice the standard deviation of the mean. For a given measured variable y with standard deviation σ that has been sampled N times, the uncertainty δy is then

$$\delta y = \frac{2\sigma}{\sqrt{N}}. \quad (\text{A.1})$$

A.1 Propagation of Errors

The method of propagation of errors (Taylor, 1982) can be used to determine the accuracy of the data. For a given function $q(x, \dots, z)$, where x, \dots, z are independent, random, measured quantities with respective uncertainties $\delta x, \dots, \delta z$, the uncertainty of q is defined as

$$\delta q = \sqrt{\left(\frac{\partial q}{\partial x} \delta x\right)^2 + \dots + \left(\frac{\partial q}{\partial z} \delta z\right)^2}. \quad (\text{A.2})$$

Thus for a given function of the type

$$q = x + \dots + z, \quad (\text{A.3})$$

the resulting uncertainty in q is

$$\delta q = \sqrt{(\delta x)^2 + \dots + (\delta z)^2}. \quad (\text{A.4})$$

For a function of the type

$$q = x \times \dots \times z, \quad (\text{A.5})$$

the uncertainty in q is

$$\delta q = \sqrt{(z \cdot \delta x)^2 + \dots + (x \cdot \delta z)^2}. \quad (\text{A.6})$$

Equation (A.6) can be framed in the form of a relative uncertainty, $\varepsilon(q) = \delta q / q$, to yield

$$\varepsilon(q) = \sqrt{\varepsilon(x)^2 + \dots + \varepsilon(z)^2}. \quad (\text{A.7})$$

We have therefore defined the relational expressions for uncertainties in q for summation functions and product functions where the variables x and z are independent of each other.

In the case where x and z are not independent, the uncertainty δq for a function of the form of Eq. (A.3) is

$$\delta q = \delta x + \dots + \delta z, \quad (\text{A.8})$$

whereas for a function of the form of Eq. (A.5) the relative uncertainty is

$$\varepsilon(q) = \varepsilon(x) + \dots + \varepsilon(z). \quad (\text{A.9})$$

A.2 LIF Measurements

As detailed in Chapter 4, the relative NO signal referenced to the 35-mm height is

$$[NO]_{ppm,rel} = \frac{LIF_{on,h} - LIF_{off,h}}{m_{net,cal}} \cdot \frac{\tau_{global,cal} \cdot \tau_{soot,cal}}{\tau_{global,h} \cdot \tau_{soot,h}} \quad (A.10)$$

Each value in the above equation has its own uncertainty as outlined below. The LIF signals, both online and offline, are represented generically as

$$LIF = \frac{V_{PMT} - V_{b,PMT}}{V_{PD} - V_{b,PD}} \quad (A.11)$$

As with any measured voltage, the electronic background, V_b , must be subtracted from the measured voltage, V , to yield the actual dynamic voltage. Accounting for the uncertainty in each of the above values yields

$$\varepsilon_{LIF} = \sqrt{\left[\frac{\sqrt{\delta V_{PMT}^2 + \delta V_{b,PMT}^2}}{V_{PMT} - V_{b,PMT}} \right]^2 + \left[\frac{\sqrt{\delta V_{PD}^2 + \delta V_{b,PD}^2}}{V_{PD} - V_{b,PD}} \right]^2} \quad (A.12)$$

The net uncertainty in the $LIF_{on,h} - LIF_{off,h}$ term is then

$$\delta_{LIF_{on,h} - LIF_{off,h}} = \sqrt{(\varepsilon_{LIF,on} \cdot LIF_{on})^2 + (\varepsilon_{LIF,off} \cdot LIF_{off})^2} \quad (A.13)$$

For this work, the extinction of fluorescence and laser irradiance through the flame must be taken into account, as well as soot transmission variations on the window. A similar procedure to account for the uncertainties in the transmission terms, both for the global and soot terms follows, recognizing that each transmission ratio is comprised of measured photodiode signals located before (PD,A) and after the flame (PD, B):

$$\frac{\tau_{cal}}{\tau_h} = \frac{\left[\frac{V_{PD,B} - V_{b,PD,B}}{V_{PD,A} - V_{b,PD,A}} \right]_{cal}}{\left[\frac{V_{PD,B} - V_{b,PD,B}}{V_{PD,A} - V_{b,PD,A}} \right]_h} \quad (A.14)$$

The measured NO signal in the LDI flame must be converted to a concentration via the differential doping calibration discussed in Chapter 4. We choose twice the standard error in the calibration slope, m , based on a least-squares fit of the data to be the relative uncertainty in the precision of the measured slope $\varepsilon(m_p)$. The subscript p has been used to denote precision. Additionally, the accuracy of the measured slope will be affected by the independent uncertainty of the NO concentration in the calibration gas, $\varepsilon(NO_b)$, and the dependent error associated with destruction of doped NO as it passes through the flamefront, $\varepsilon(NO_d)$. The relative uncertainty of the calibration gas concentration has been previously measured as $\sim 3\%$, whereas the relative uncertainty owing to NO destruction has been conservatively estimated as $\sim 5\%$ (Thomsen, 1997). Therefore, the relative uncertainty in the accuracy of the calibration slope is

$$\varepsilon(m_a) = \sqrt{\varepsilon(NO_b)^2 + \varepsilon(m_p)^2 + \varepsilon(NO_d)^2}, \quad (A.15)$$

where the subscript a has been used to denote the accuracy.

Finally, the total relative uncertainty in the measured $[NO]_{ppm,rel}$ for the LDI flame is a function of the individual uncertainties of each term. Recognizing that the uncertainties in transmission effects and LIF signals are dependent terms, that the calibration slope uncertainty in these equations is an independent term, and including a factor which accounts for the variation in fluorescence owing to Boltzman and electronic quenching rate effects, the total relative uncertainty is:

$$\varepsilon([NO]_{ppm,rel}) = \sqrt{\varepsilon_{LIF,on-LIF,off}^2 + \varepsilon(m_a)^2 + \varepsilon_\tau + \varepsilon(T,Q)} \quad (A.16)$$

The term ε_τ represent the relative uncertainty of the combined transmission effect in (A.10), namely

$$\varepsilon_\tau = \varepsilon \left(\frac{\tau_{global,cal} \cdot \tau_{soot,cal}}{\tau_{global,h} \cdot \tau_{soot,h}} \right). \quad (A.17)$$

The relative uncertainty in the $\varepsilon(T,Q)$ term has been conservatively estimated as 5%. Continuing in this same vein, the total relative uncertainty in the absolute NO concentration, $[NO]_{ppm,abs}$, can be calculated from Equation (4.11), repeated below:

$$[NO]_{ppm,abs} = [NO]_{ppm,rel} \cdot \frac{m_{net,cal}}{\tau_{global,cal} \cdot \tau_{soot,cal}} \cdot \frac{\tau_{global,h} \cdot \tau_{soot,h}}{m_{net,h}}. \quad (A.18)$$

The above error analysis, more appropriately termed an “accuracy analysis,” was used to determine the accuracy of the LIF measurements. Aside from the listed uncertainties given in the above derivation, all remaining uncertainties depend on the actual measured data.

As a simple example of this type of error analysis, Table A.1 demonstrates typical values at $h=40$ mm, $r=0$ mm for the 4.27-atm, $\phi_p=1.0$, $T_{air}=375$ LDI flame utilizing a calibration taken at that point. For this case, the ε_τ and $\varepsilon(T,Q)$ terms are not required since the calibration is taken at the same location and at the same time.

For the LIF measurements in this thesis, the typical relative uncertainty was $\pm 25\%$. No attempt was made to determine the accuracy of the PLIF measurements; however, based on previous work by Partridge (1996) in gaseous flames, the relative uncertainty can be estimated to be greater than $\pm 28\%$.

Table A.1 Typical error terms for LDI flame ($P=4.27$ atm, $\phi_p=1.0$, $T_{\text{air}}=375$ K, $h=40$ mm, $r=0$ mm).

Notation	Term	Value
<i>On-line</i>	$V_{PMT} - V_{b, PMT}$	2.260
<i>On-line</i>	δV_{PMT}	0.141
<i>On-line</i>	$\delta V_{b, PMT}$	0.00759
<i>On-line</i>	$V_{PD} - V_{b, PD}$	3.977
<i>On-line</i>	δV_{PD}	0.0394
<i>On-line</i>	$\delta V_{b, PD}$	0.000163
<i>Off-line</i>	$V_{PMT} - V_{b, PMT}$	0.183
<i>Off-line</i>	δV_{PMT}	0.0769
<i>Off-line</i>	$\delta V_{b, PMT}$	0.00300
<i>Off-line</i>	$V_{PD} - V_{b, PD}$	3.648
<i>Off-line</i>	δV_{PD}	0.0595
<i>Off-line</i>	$\delta V_{b, PD}$	0.000231
<i>On-line</i>	LIF_{on}	0.568
<i>On-line</i>	$\delta_{LIF_{on}}$	0.0358
<i>Off-line</i>	LIF_{off}	0.0502
<i>Off-line</i>	$\delta_{LIF_{off}}$	0.0211
<i>Net</i>	$LIF_{on,h} - LIF_{off,h}$	0.518
<i>Net</i>	$\delta_{LIF_{on,h} - LIF_{off,h}}$	0.0416
<i>Net</i>	m	0.00950
<i>Net</i>	$\varepsilon(NO_b)$	0.03
<i>Net</i>	$\varepsilon(m_p)$	0.0478
<i>Net</i>	$\varepsilon(NO_d)$	0.05
<i>Net</i>	$\varepsilon(m_d)$	0.106
<i>Net</i>	NO (ppm)	54.541
<i>Net</i>	ε_{NO}	0.133
<i>Net</i>	δ_{NO}	7.268

Appendix B: Modeling Work

Though the LDI flames utilized in this research are complex, we attempted to validate the measured trends through several computational models. One such method employed the SANDIA Perfectly-Stirred Reactor (PSR) Code, a subset of the AURORA code released by Reaction Design, and a heptane kinetic mechanism coupled with NO chemistry (Held, 2000). Table B.1 lists the reactions in the mechanism, along with their rate coefficients. A stoichiometric mixture was used with the residence time altered to reflect that supplied to the LDI burner at a given primary equivalence ratio. Dilution of the mixture was accomplished by scaling the stoichiometric products with the same equivalence ratio, thus accounting for the excess air that appears to dilute the products based on the discussion of Chapter 6. In this comparison, the equivalence ratio is analogous to the residence time in the reactor. A lower equivalence ratio means a lower residence time and more dilution by excess air. In addition, the PSR was modeled at a constant temperature based on adiabatic combustion, thus resembling the stoichiometric spray sheath suggested in Chapter 6. Taking the reference case to be at 4-atm, $\phi_p=0.9$, the PSR code residence time for this condition was chosen to yield the same net NO production (~46 ppm). The plot of temperature and NO (ppm) shown in Figure B.1 demonstrates the typical behavior of perfectly-stirred reactors. The range of residence times utilized in this study is noted and will be discussed shortly.

Table B.1: Heptane mechanism reactions.

(k = A T**b exp(-E/RT))			A(mole-cm-sec-K)	b	E (cal/mole)
1.	H+O2<=>O+OH		1.92E+14	.0	16439.0
2.	O+H2<=>H+OH		5.08E+04	2.7	6290.0
3.	H2+OH<=>H2O+H		2.16E+08	1.5	3430.0
4.	O+H2O<=>OH+OH		2.97E+06	2.0	13400.0
5.	H2+M<=>H+H+M		4.58E+19	-1.4	104380.0
	H2	Enhanced by	2.500E+00		
	H2O	Enhanced by	1.200E+01		
	CO	Enhanced by	1.900E+00		
	CO2	Enhanced by	3.800E+00		
	AR	Enhanced by	0.000E+00		
6.	H2+AR<=>H+H+AR		5.84E+18	-1.1	104380.0
7.	O+O+M<=>O2+M		6.17E+15	-.5	.0
	H2	Enhanced by	2.500E+00		
	H2O	Enhanced by	1.200E+01		
	AR	Enhanced by	0.000E+00		
	CO	Enhanced by	1.900E+00		
	CO2	Enhanced by	3.800E+00		
8.	O+O+AR<=>O2+AR		1.89E+13	.0	-1788.0
9.	O+H+M<=>OH+M		4.71E+18	-1.0	.0
	H2	Enhanced by	2.500E+00		
	H2O	Enhanced by	1.200E+01		
	AR	Enhanced by	7.500E-01		
	CO	Enhanced by	1.900E+00		
	CO2	Enhanced by	3.800E+00		
10.	H+OH+M<=>H2O+M		2.21E+22	-2.0	.0
	H2	Enhanced by	2.500E+00		
	H2O	Enhanced by	6.300E+00		
	AR	Enhanced by	3.800E-01		
	CO	Enhanced by	1.900E+00		
	CO2	Enhanced by	3.800E+00		
11.	H+O2(+M)<=>HO2(+M)		4.52E+13	.0	.0
	Low pressure limit:	.67000E+20	-.14200E+01	.00000E+00	
	H2	Enhanced by	2.500E+00		
	H2O	Enhanced by	1.200E+01		
	AR	Enhanced by	0.000E+00		
	CO	Enhanced by	1.900E+00		
	CO2	Enhanced by	3.800E+00		
12.	H+O2(+AR)<=>HO2(+AR)		4.52E+13	.0	.0
	Low pressure limit:	.61670E+18	-.80000E+00	.00000E+00	
	TROE centering:	.50000E+00	.10000E-29	.10000E+31	

13. HO2+H<=>H2+O2	6.63E+13	.0	2130.0
Declared duplicate reaction...			
14. HO2+H<=>H2+O2	3.00E+15	.0	12000.0
Declared duplicate reaction...			
15. HO2+H<=>OH+OH	1.69E+14	.0	874.0
16. HO2+O<=>O2+OH	1.81E+13	.0	-397.0
17. HO2+OH<=>H2O+O2	1.90E+16	-1.0	.0
18. HO2+HO2<=>H2O2+O2	4.20E+14	.0	11982.0
Declared duplicate reaction...			
19. HO2+HO2<=>H2O2+O2	1.30E+11	.0	-1629.3
Declared duplicate reaction...			
20. H2O2(+M)<=>OH+OH(+M)	2.95E+14	.0	48430.0
Low pressure limit: .12020E+18 .00000E+00 .45500E+05			
TROE centering: .50000E+00 .10000E+31 .10000E-29			
H2 Enhanced by 2.500E+00			
H2O Enhanced by 1.200E+01			
CO Enhanced by 1.900E+00			
CO2 Enhanced by 3.800E+00			
AR Enhanced by 0.000E+00			
21. H2O2(+AR)<=>OH+OH(+AR)	2.95E+14	.0	48430.0
Low pressure limit: .19040E+17 .00000E+00 .43000E+05			
TROE centering: .50000E+00 .10000E+31 .10000E-29			
22. H2O2+H<=>H2O+OH	1.00E+13	.0	3590.0
23. H2O2+H<=>HO2+H2	4.82E+13	.0	7950.0
24. H2O2+O<=>OH+HO2	9.55E+06	2.0	3970.0
25. H2O2+OH<=>HO2+H2O	1.00E+12	.0	.0
Declared duplicate reaction...			
26. H2O2+OH<=>HO2+H2O	5.80E+14	.0	9557.0
Declared duplicate reaction...			
27. CO+O+M<=>CO2+M	2.51E+13	.0	-4540.0
H2 Enhanced by 2.500E+00			
H2O Enhanced by 1.200E+01			
AR Enhanced by 8.700E-01			
CO Enhanced by 1.900E+00			
CO2 Enhanced by 3.800E+00			
28. CO+O2<=>CO2+O	2.53E+12	.0	47700.0
29. CO+OH<=>CO2+H	1.50E+07	1.3	-765.0
30. CO+HO2<=>CO2+OH	6.02E+13	.0	23000.0
31. HCO+M<=>H+CO+M	1.86E+17	-1.0	17000.0
H2 Enhanced by 2.500E+00			
H2O Enhanced by 1.200E+01			
CO Enhanced by 1.900E+00			
CO2 Enhanced by 3.800E+00			
32. HCO+O2<=>CO+HO2	7.58E+12	.0	410.0

33. HCO+H<=>CO+H2	7.23E+13	.0	.0
34. HCO+O<=>CO+OH	3.02E+13	.0	.0
35. HCO+OH<=>CO+H2O	3.02E+13	.0	.0
36. HCO+O<=>CO2+H	3.00E+13	.0	.0
37. HCO+HO2<=>CO2+OH+H	3.00E+13	.0	.0
38. HCO+CH3<=>CO+CH4	1.20E+14	.0	.0
39. HCO+HCO<=>CH2O+CO	1.80E+13	.0	.0
40. HCO+HCO<=>H2+CO+CO	3.00E+12	.0	.0
41. CH2O+M<=>HCO+H+M	4.00E+23	-1.7	91470.0
42. CH2O+M<=>CO+H2+M	8.25E+15	.0	69540.0
43. CH2O+H<=>HCO+H2	1.14E+08	1.7	1834.0
44. CH2O+O<=>HCO+OH	1.81E+13	.0	3080.0
45. CH2O+OH<=>HCO+H2O	4.80E+09	1.2	-447.0
46. CH2O+O2<=>HCO+HO2	2.00E+13	.0	39000.0
47. CH2O+HO2<=>HCO+H2O2	1.50E+13	.0	15200.0
48. CH2O+CH3<=>HCO+CH4	5.54E+03	2.8	5862.0
49. CH3O+M<=>CH2O+H+M	8.30E+17	-1.2	15500.0
50. CH3O+H<=>CH2O+H2	2.00E+13	.0	.0
51. CH3O+O<=>CH2O+OH	6.00E+12	.0	.0
52. CH3O+OH<=>CH2O+H2O	1.80E+13	.0	.0
53. CH3O+O2<=>CH2O+HO2	9.03E+13	.0	11980.0
Declared duplicate reaction...			
54. CH3O+O2<=>CH2O+HO2	2.20E+10	.0	1748.0
Declared duplicate reaction...			
55. CH3O+HO2<=>CH2O+H2O2	3.00E+11	.0	.0
56. CH3O+CO<=>CH3+CO2	1.60E+13	.0	11800.0
57. CH+O2<=>HCO+O	1.00E+13	.0	.0
58. CH2+H<=>CH+H2	9.64E+13	.0	.0
59. CH2+O<=>CO+H+H	1.05E+13	.0	.0
60. CH2+O<=>CO+H2	1.05E+13	.0	.0
61. CH2+O2<=>CO+OH+H	1.13E+13	.0	.0
62. CH2+O2<=>CO+H2O	4.82E+12	.0	.0
63. CH3+OH<=>CH2+H2O	1.50E+13	.0	5000.0
64. CH3+O<=>CH2O+H	8.43E+13	.0	.0
65. CH3+O2<=>CH3O+O	1.99E+18	-1.6	29230.0
66. CH3+HO2<=>CH3O+OH	2.00E+13	.0	1076.0
67. CH3+CH3(+M)<=>C2H6(+M)	9.03E+16	-1.2	654.0
Low pressure limit: .31800E+42 -.70300E+01 .27620E+04			
TROE centering: .61900E+00 .73200E+02 .11800E+04			
68. CH4(+M)<=>CH3+H(+M)	3.70E+15	.0	103800.0
Low pressure limit: .72100E+31 -.34900E+01 .10590E+06			
69. CH4+H<=>CH3+H2	5.47E+07	2.0	11210.0
70. CH4+O<=>CH3+OH	6.93E+08	1.6	8484.0
71. CH4+OH<=>CH3+H2O	5.72E+06	2.0	2639.0
72. CH4+O2<=>CH3+HO2	4.00E+13	.0	56910.0

73. $\text{CH}_4 + \text{HO}_2 \rightleftharpoons \text{CH}_3 + \text{H}_2\text{O}_2$	1.81E+11	.0	18580.0
74. $\text{CH}_3 + \text{CH}_3 \rightleftharpoons \text{C}_2\text{H}_4 + \text{H}_2$	1.00E+16	.0	32005.0
75. $\text{CH}_3 + \text{CH}_3 \rightleftharpoons \text{C}_2\text{H}_5 + \text{H}$	8.00E+15	.0	26512.0
76. $\text{C}_2\text{H} + \text{O} \rightleftharpoons \text{CO} + \text{CH}$	1.81E+13	.0	.0
77. $\text{C}_2\text{H} + \text{O}_2 \rightleftharpoons \text{HCCO} + \text{O}$	6.02E+11	.0	.0
78. $\text{C}_2\text{H} + \text{O}_2 \rightleftharpoons \text{CO} + \text{HCO}$	2.41E+12	.0	.0
79. $\text{HCCO} + \text{H} \rightleftharpoons \text{CH}_2 + \text{CO}$	3.00E+13	.0	.0
80. $\text{HCCO} + \text{O} \rightleftharpoons \text{H} + \text{CO} + \text{CO}$	1.20E+12	.0	.0
81. $\text{HCCO} + \text{O}_2 \rightleftharpoons \text{CO} + \text{CO} + \text{OH}$	1.46E+12	.0	2500.0
82. $\text{C}_2\text{H}_2 + \text{M} \rightleftharpoons \text{C}_2\text{H} + \text{H} + \text{M}$	7.46E+30	-3.7	127100.0
83. $\text{C}_2\text{H}_2 + \text{H} \rightleftharpoons \text{C}_2\text{H} + \text{H}_2$	6.02E+13	.0	22250.0
84. $\text{C}_2\text{H}_2 + \text{O} \rightleftharpoons \text{CH}_2 + \text{CO}$	1.75E+13	.0	3179.0
85. $\text{C}_2\text{H}_2 + \text{O} \rightleftharpoons \text{HCCO} + \text{H}$	3.56E+04	2.7	1391.0
86. $\text{C}_2\text{H}_2 + \text{OH} \rightleftharpoons \text{C}_2\text{H} + \text{H}_2\text{O}$	3.38E+07	2.0	14000.0
87. $\text{C}_2\text{H}_2 + \text{O}_2 \rightleftharpoons \text{C}_2\text{H} + \text{HO}_2$	1.20E+13	.0	74510.0
88. $\text{C}_2\text{H}_3(+\text{M}) \rightleftharpoons \text{C}_2\text{H}_2 + \text{H}(+\text{M})$	1.26E+32	-5.9	46800.0
Low pressure limit: .41700E+42 -.74900E+01 .45500E+05			
89. $\text{C}_2\text{H}_3 + \text{H} \rightleftharpoons \text{C}_2\text{H}_2 + \text{H}_2$	3.00E+13	.0	.0
90. $\text{C}_2\text{H}_3 + \text{O} \rightleftharpoons \text{CH}_2\text{CO} + \text{H}$	9.60E+13	.0	.0
91. $\text{C}_2\text{H}_3 + \text{OH} \rightleftharpoons \text{C}_2\text{H}_2 + \text{H}_2\text{O}$	3.00E+13	.0	.0
92. $\text{C}_2\text{H}_3 + \text{OH} \rightleftharpoons \text{CH}_3\text{HCO}$	3.00E+13	.0	.0
93. $\text{C}_2\text{H}_3 + \text{O}_2 \rightleftharpoons \text{CH}_2\text{O} + \text{HCO}$	4.48E+26	-4.5	5480.0
Declared duplicate reaction...			
94. $\text{C}_2\text{H}_3 + \text{O}_2 \rightleftharpoons \text{CH}_2\text{O} + \text{HCO}$	1.05E+38	-8.2	7030.0
Declared duplicate reaction...			
95. $\text{C}_2\text{H}_3 + \text{O}_2 \rightleftharpoons \text{C}_2\text{H}_2 + \text{HO}_2$	5.10E+21	-3.2	5660.0
96. $\text{C}_2\text{H}_3 + \text{O}_2 \rightleftharpoons 2\text{HCO} + \text{H}$	3.27E+23	-3.9	5010.0
97. $\text{C}_2\text{H}_3 + \text{HO}_2 \rightleftharpoons \text{CH}_2\text{CO} + \text{OH} + \text{H}$	3.00E+13	.0	.0
98. $\text{C}_2\text{H}_3 + \text{CH}_3 \rightleftharpoons \text{C}_2\text{H}_2 + \text{CH}_4$	3.90E+11	.0	.0
99. $\text{C}_2\text{H}_3 + \text{C}_2\text{H}_3 \rightleftharpoons \text{C}_2\text{H}_4 + \text{C}_2\text{H}_2$	9.60E+11	.0	.0
100. $\text{C}_2\text{H}_4(+\text{M}) \rightleftharpoons \text{C}_2\text{H}_2 + \text{H}_2(+\text{M})$	7.94E+12	.4	88760.0
Low pressure limit: .61000E+07 .28800E+01 .67200E+05			
101. $\text{H} + \text{C}_2\text{H}_3(+\text{M}) \rightleftharpoons \text{C}_2\text{H}_4(+\text{M})$	6.08E+12	.3	280.0
Low pressure limit: .14000E+31 -.38600E+01 .33200E+04			
TROE centering: .78200E+00 .20750E+03 .26630E+04 .60950E+04			
H2	Enhanced by	2.000E+00	
H2O	Enhanced by	6.000E+00	
CH4	Enhanced by	2.000E+00	
CO	Enhanced by	1.500E+00	
CO2	Enhanced by	2.000E+00	
C2H6	Enhanced by	3.000E+00	
AR	Enhanced by	7.000E-01	
102. $\text{C}_2\text{H}_4 + \text{H} \rightleftharpoons \text{C}_2\text{H}_3 + \text{H}_2$	1.32E+06	2.5	12240.0
103. $\text{C}_2\text{H}_4 + \text{O} \rightleftharpoons \text{CH}_3 + \text{HCO}$	1.32E+08	1.6	427.2
104. $\text{C}_2\text{H}_4 + \text{OH} \rightleftharpoons \text{C}_2\text{H}_3 + \text{H}_2\text{O}$	2.02E+13	.0	5955.0

105. $C_2H_4 + O_2 \rightleftharpoons C_2H_3 + HO_2$	4.22E+13	.0	57600.0
106. $C_2H_4 + CH_3 \rightleftharpoons C_2H_3 + CH_4$	6.62E+00	3.7	9500.0
107. $C_2H_5(+M) \rightleftharpoons C_2H_4 + H(+M)$	4.90E+09	1.2	37200.0
Low pressure limit: .51000E+65 -.13960E+02 .60100E+05			
108. $C_2H_5 + O \rightleftharpoons CH_3HCO + H$	9.60E+14	.0	.0
109. $C_2H_5 + OH \rightleftharpoons C_2H_4 + H_2O$	2.40E+13	.0	.0
110. $C_2H_5 + OH \rightleftharpoons CH_3 + H + CH_2O$	2.40E+13	.0	.0
111. $C_2H_5 + O_2 \rightleftharpoons C_2H_4 + HO_2$	8.43E+11	.0	3874.0
112. $C_2H_5 + HO_2 \rightleftharpoons CH_3 + CH_2O + OH$	2.40E+13	.0	.0
113. $C_2H_5 + HO_2 \rightleftharpoons C_2H_4 + H_2O_2$	3.00E+11	.0	.0
114. $C_2H_5 + C_2H_5 \rightleftharpoons C_2H_4 + C_2H_6$	1.40E+12	.0	.0
115. $C_2H_6 \rightleftharpoons C_2H_5 + H$	2.08E+38	-7.1	106500.0
116. $C_2H_6 + H \rightleftharpoons C_2H_5 + H_2$	5.42E+02	3.5	5166.0
117. $C_2H_6 + O \rightleftharpoons C_2H_5 + OH$	1.20E+12	.6	7311.0
118. $C_2H_6 + OH \rightleftharpoons C_2H_5 + H_2O$	5.13E+06	2.1	854.4
119. $C_2H_6 + O_2 \rightleftharpoons C_2H_5 + HO_2$	4.00E+13	.0	50900.0
120. $C_2H_6 + HO_2 \rightleftharpoons C_2H_5 + H_2O_2$	2.94E+11	.0	14940.0
121. $C_2H_6 + CH_3 \rightleftharpoons C_2H_5 + CH_4$	5.48E-01	4.0	8284.0
122. $C_2H_6 + C_2H_3 \rightleftharpoons C_2H_5 + C_2H_4$	6.00E+02	3.3	10500.0
123. $CH_2CO + M \rightleftharpoons CH_2 + CO + M$	3.60E+15	.0	59270.0
124. $CH_2CO + H \rightleftharpoons CH_3 + CO$	7.00E+12	.0	3000.0
125. $CH_2CO + O \rightleftharpoons HCO + HCO$	2.00E+13	.0	2294.0
126. $CH_2CO + OH \rightleftharpoons CH_2O + HCO$	1.00E+13	.0	.0
127. $CH_3CO(+M) \rightleftharpoons CH_3 + CO(+M)$	1.20E+22	-3.0	18800.0
Low pressure limit: .87300E+43 -.86200E+01 .22400E+05			
128. $CH_3CO + H \rightleftharpoons CH_3 + HCO$	9.60E+13	.0	.0
129. $CH_3CO + O \rightleftharpoons CH_3 + CO_2$	9.60E+12	.0	.0
130. $CH_3CO + OH \rightleftharpoons CH_2CO + H_2O$	1.20E+13	.0	.0
131. $CH_3CO + OH \rightleftharpoons CH_3 + CO + OH$	3.00E+13	.0	.0
132. $CH_3CO + HO_2 \rightleftharpoons CH_3 + CO_2 + OH$	3.00E+13	.0	.0
133. $CH_3HCO \rightleftharpoons CH_3 + HCO$	7.08E+15	.0	81760.0
134. $CH_3HCO + H \rightleftharpoons CH_3CO + H_2$	4.00E+13	.0	4207.0
135. $CH_3HCO + O \rightleftharpoons CH_3CO + OH$	5.00E+12	.0	1793.0
136. $CH_3HCO + OH \rightleftharpoons CH_3CO + H_2O$	1.00E+13	.0	.0
137. $CH_3HCO + O_2 \rightleftharpoons CH_3CO + HO_2$	2.00E+13	.5	42200.0
138. $CH_3HCO + HO_2 \rightleftharpoons CH_3CO + H_2O_2$	1.70E+12	.0	10700.0
139. $CH_3HCO + CH_3 \rightleftharpoons CH_3CO + CH_4$	1.74E+12	.0	8440.0
140. $C_3H_3 + O \rightleftharpoons CH_2O + C_2H$	2.00E+13	.0	.0
141. $C_3H_3 + O_2 \rightleftharpoons CH_2CO + HCO$	3.01E+10	.0	2870.0
142. $C_3H_3 + CH_3 \rightleftharpoons C_2H_5 + C_2H$	1.00E+13	.0	37500.0
143. $C_3H_3 + CH_3 \rightleftharpoons C_4H_6$	5.00E+12	.0	.0
144. $2C_3H_3 \rightleftharpoons C_6H_6$	3.00E+11	.0	.0
145. $2C_3H_3 \rightleftharpoons 3C_2H_2$	5.00E+11	.0	.0
146. $C_3H_3 + C_3H_4 \rightleftharpoons C_6H_6 + H$	2.20E+11	.0	2000.0
147. $C_3H_4 + M \rightleftharpoons C_3H_3 + H + M$	1.00E+17	.0	70000.0

H2	Enhanced by	2.500E+00			
H2O	Enhanced by	1.200E+01			
CO	Enhanced by	1.900E+00			
CO2	Enhanced by	3.800E+00			
CH4	Enhanced by	1.200E+01			
148. C3H4+H<=>C3H3+H2		1.00E+12	.0	1500.0	
149. C3H4+O<=>CH2O+C2H2		3.00E-03	4.6	-4243.0	
150. C3H4+O<=>CO+C2H4		9.00E-03	4.6	-4243.0	
151. C3H4+OH<=>C3H3+H2O		1.45E+13	.0	4170.0	
152. C3H4+OH<=>CH2CO+CH3		3.12E+12	.0	-397.0	
153. C3H4+O2<=>C3H3+HO2		4.00E+13	.0	61500.0	
154. C3H4+HO2<=>CH2CO+CH2+OH		4.00E+12	.0	19000.0	
155. C3H4+CH3<=>C3H3+CH4		2.00E+12	.0	7700.0	
156. C4H6<=>C2H2+C2H3+H		1.58E+16	.0	110000.0	
157. C4H6<=>C2H3+C2H3		1.80E+13	.0	85000.0	
158. C4H6+H<=>C2H3+C2H4		5.00E+11	.0	.0	
159. C4H6+H<=>H2+C2H2+C2H3		6.30E+10	.7	6000.0	
160. C4H6+OH<=>H2O+C2H2+C2H3		8.38E+12	.0	-930.0	
161. C4H6+CH3<=>CH4+C2H2+C2H3		7.00E+13	.0	18500.0	
162. C3H5<=>C3H4+H		1.50E+11	.8	59810.0	
163. C3H5+H<=>C3H4+H2		1.80E+13	.0	.0	
164. C3H5+O<=>C2H3HCO+H		6.02E+13	.0	.0	
165. C3H5+OH<=>C3H4+H2O		6.02E+12	.0	.0	
166. C3H5+O2<=>C3H4+HO2		1.33E+07	.0	.0	
167. C3H5+HO2<=>C2H3+CH2O+OH		6.72E+11	.0	.0	
168. C3H5+CH3<=>C3H4+CH4		3.00E+12	-.3	-262.0	
169. C3H5+C2H3<=>C3H6+C2H2		4.80E+12	.0	.0	
170. C3H5+C2H3<=>C3H4+C2H4		2.40E+12	.0	.0	
171. C3H5+C2H5<=>C3H6+C2H4		2.60E+12	.0	-131.0	
172. C3H5+C2H5<=>C3H4+C2H6		9.60E+11	.0	-131.0	
173. C3H6<=>C2H3+CH3		1.10E+21	-1.2	97710.0	
174. C3H6<=>C3H5+H		2.50E+15	.0	87580.0	
175. C3H6+H<=>C3H5+H2		1.73E+05	2.5	2490.0	
176. C3H6+H<=>C2H4+CH3		1.33E+13	.0	3261.0	
177. C3H6+O<=>CH2CO+CH3+H		7.70E+07	1.7	633.7	
178. C3H6+O<=>C2H5+HCO		3.43E+07	1.7	-192.8	
179. C3H6+O<=>C3H5+OH		1.75E+11	.7	5883.0	
180. C3H6+OH<=>C3H5+H2O		3.12E+06	2.0	-298.0	
181. C3H6+O2<=>C3H5+HO2		6.02E+13	.0	47600.0	
182. C3H6+HO2<=>C3H5+H2O2		9.64E+03	2.6	13900.0	
183. C3H6+CH3<=>C3H5+CH4		2.22E+00	3.5	5675.0	
184. C2H3HCO+H<=>C2H3+CO+H2		4.00E+09	1.2	2400.0	
185. C2H3HCO+O<=>C2H3+CO+OH		6.00E+12	.0	1900.0	
186. C2H3HCO+OH<=>C2H3+CO+H2O		8.00E+12	.0	.0	
187. C4H8<=>C3H5+CH3		1.00E+16	.0	73000.0	

188. $C_4H_8 + H \rightleftharpoons H_2 + C_4H_6 + H$	1.15E+05	2.5	2490.0
189. $C_4H_8 + O \rightleftharpoons OH + C_4H_6 + H$	1.32E+14	.0	5190.0
190. $C_4H_8 + OH \rightleftharpoons H_2O + C_4H_6 + H$	2.25E+13	.0	2217.0
191. $C_4H_8 + CH_3 \rightleftharpoons CH_4 + C_4H_6 + H$	2.50E+11	.0	8318.0
192. $C_5H_{10} \rightleftharpoons C_3H_5 + C_2H_5$	1.00E+16	.0	71340.0
193. $C_5H_{10} \rightleftharpoons C_3H_6 + C_2H_4$	3.16E+12	.0	57040.0
194. $C_5H_{10} + H \rightleftharpoons H_2 + C_4H_6 + CH_3$	1.15E+05	2.5	2490.0
195. $C_5H_{10} + O \rightleftharpoons OH + C_4H_6 + CH_3$	1.32E+14	.0	5190.0
196. $C_5H_{10} + OH \rightleftharpoons H_2O + C_4H_6 + CH_3$	2.25E+13	.0	2217.0
197. $C_5H_{10} + CH_3 \rightleftharpoons CH_4 + C_4H_6 + CH_3$	2.50E+11	.0	8318.0
198. $C_6H_{12} \rightleftharpoons 2C_3H_6$	3.98E+12	.0	57430.0
199. $C_6H_{12} \rightleftharpoons C_3H_5 + C_2H_4 + CH_3$	7.94E+15	.0	70740.0
200. $C_6H_{12} + H \rightleftharpoons C_3H_6 + C_2H_4 + CH_3$	7.23E+12	.0	1302.0
201. $C_6H_{12} + H \rightleftharpoons 2C_2H_4 + C_2H_5$	7.23E+12	.0	1302.0
202. $C_6H_{12} + H \rightleftharpoons H_2 + C_4H_6 + C_2H_5$	1.15E+05	2.5	2490.0
203. $C_6H_{12} + O \rightleftharpoons OH + C_4H_6 + C_2H_5$	1.32E+14	.0	5190.0
204. $C_6H_{12} + OH \rightleftharpoons H_2O + C_4H_6 + C_2H_5$	2.25E+13	.0	2217.0
205. $C_6H_{12} + CH_3 \rightleftharpoons CH_4 + C_4H_6 + C_2H_5$	2.50E+11	.0	8318.0
206. $C_3H_5 + HCO \rightleftharpoons C_3H_6 + CO$	6.00E+13	.0	.0
207. $C_3H_5 + CH_2O \rightleftharpoons C_3H_6 + HCO$	1.45E+08	1.8	18180.0
208. $C_3H_5 + C_2H_6 \rightleftharpoons C_3H_6 + C_2H_5$	2.35E+02	3.3	19830.0
209. $C_3H_6 + C_2H_3 \rightleftharpoons C_3H_5 + C_2H_4$	2.22E+00	3.5	4679.0
210. $2C_3H_5 \rightleftharpoons C_3H_4 + C_3H_6$	8.43E+10	.0	-263.0
211. $2C_3H_5 \rightleftharpoons C_6H_{10}$	1.02E+13	.0	-263.0
212. $C_4H_8 + H \rightleftharpoons C_2H_4 + C_2H_5$	7.23E+12	.0	1302.0
213. $C_4H_8 + H \rightleftharpoons C_3H_6 + CH_3$	7.23E+12	.0	1302.0
214. $C_5H_{10} + H \rightleftharpoons 2C_2H_4 + CH_3$	7.23E+12	.0	1302.0
215. $C_5H_{10} + H \rightleftharpoons C_3H_6 + C_2H_5$	7.23E+12	.0	1302.0
216. $PC_4H_9 \rightleftharpoons C_2H_5 + C_2H_4$	2.50E+13	.0	28800.0
217. $PC_4H_9 \rightleftharpoons H + C_4H_8$	1.30E+13	.0	39000.0
218. $NC_3H_7 \rightleftharpoons CH_3 + C_2H_4$	9.60E+13	.0	31070.0
219. $NC_3H_7 \rightleftharpoons H + C_3H_6$	1.25E+14	.0	37045.0
220. $C_7H_{16} \rightleftharpoons H + AC_7H_{15}$	1.80E+16	.0	100600.0
221. $C_7H_{16} \rightleftharpoons H + BC_7H_{15}$	1.20E+16	.0	98090.0
222. $C_7H_{16} \rightleftharpoons H + XC_7H_{15}$	1.20E+16	.0	98090.0
223. $C_7H_{16} \rightleftharpoons H + DC_7H_{15}$	6.00E+15	.0	98090.0
224. $C_7H_{16} \rightleftharpoons CH_3 + AC_6H_{13}$	4.00E+17	.0	87300.0
225. $C_7H_{16} \rightleftharpoons C_2H_5 + AC_5H_{11}$	4.00E+17	.0	85400.0
226. $C_7H_{16} \rightleftharpoons NC_3H_7 + PC_4H_9$	2.00E+17	.0	84900.0
227. $C_7H_{16} + H \rightleftharpoons H_2 + AC_7H_{15}$	1.32E+14	.0	9370.0
228. $C_7H_{16} + OH \rightleftharpoons H_2O + AC_7H_{15}$	1.74E+07	1.8	974.0
229. $C_7H_{16} + CH_3 \rightleftharpoons CH_4 + AC_7H_{15}$	5.01E+11	.0	13600.0
230. $C_7H_{16} + O \rightleftharpoons AC_7H_{15} + OH$	2.88E+06	2.4	5505.0
231. $C_7H_{16} + H \rightleftharpoons BC_7H_{15} + H_2$	1.96E+14	.0	7959.0
232. $C_7H_{16} + OH \rightleftharpoons H_2O + BC_7H_{15}$	3.80E+06	2.0	-596.0

233. C7H16+O<=>BC7H15+OH	2.77E+05	2.6	1910.0
234. C7H16+CH3<=>CH4+BC7H15	4.27E+11	.0	10500.0
235. C7H16+C3H5<=>C3H6+BC7H15	1.57E+02	3.3	18160.0
236. C7H16+H<=>XC7H15+H2	1.57E+14	.0	7959.0
237. C7H16+O<=>XC7H15+OH	2.21E+05	2.6	1910.0
238. C7H16+OH<=>XC7H15+H2O	4.37E+06	2.0	-1312.0
239. C7H16+CH3<=>XC7H15+CH4	3.42E+11	.0	10500.0
240. C7H16+C3H5<=>C3H6+XC7H15	1.57E+02	3.3	18160.0
241. C7H16+H<=>DC7H15+H2	9.80E+13	.0	7959.0
242. C7H16+O<=>DC7H15+OH	1.38E+05	2.6	1910.0
243. C7H16+OH<=>DC7H15+H2O	4.37E+06	2.0	-1312.0
244. C7H16+CH3<=>DC7H15+CH4	2.14E+11	.0	10500.0
245. C7H16+C3H5<=>C3H6+DC7H15	7.83E+01	3.3	18160.0
246. AC7H15<=>C2H4+AC5H11	2.50E+13	.0	28800.0
247. BC7H15<=>C3H6+PC4H9	1.60E+13	.0	28300.0
248. XC7H15<=>C4H8+NC3H7	1.50E+13	.0	29100.0
249. XC7H15<=>C6H12+CH3	2.40E+13	.0	33000.0
250. DC7H15<=>C5H10+C2H5	1.08E+13	.0	28000.0
251. AC7H15<=>BC7H15	2.00E+11	.0	11100.0
252. AC7H15<=>XC7H15	2.00E+11	.0	18100.0
253. AC7H15<=>DC7H15	2.00E+11	.0	20000.0
254. BC7H15<=>XC7H15	2.00E+11	.0	20000.0
Reverse Arrhenius coefficients:	2.00E+11	.0	20000.0
255. AC5H11<=>NC3H7+C2H4	2.50E+13	.0	28800.0
256. AC6H13<=>PC4H9+C2H4	2.50E+13	.0	28800.0
257. N+NO<=>N2+O	3.50E+13	.0	330.0
258. N+O2<=>NO+O	2.65E+12	.0	6400.0
259. N+OH<=>NO+H	7.33E+13	.0	1120.0
260. N2O+O<=>N2+O2	1.40E+12	.0	10810.0
261. N2O+O<=>2NO	2.90E+13	.0	23150.0
262. N2O+H<=>N2+OH	4.40E+14	.0	18880.0
263. N2O+OH<=>N2+HO2	2.00E+12	.0	21060.0
264. N2O(+M)<=>N2+O(+M)	1.30E+11	.0	59620.0
Low pressure limit:	.62000E+15	.00000E+00	.56100E+05
H2	Enhanced by	2.000E+00	
H2O	Enhanced by	6.000E+00	
CH4	Enhanced by	2.000E+00	
CO	Enhanced by	1.500E+00	
CO2	Enhanced by	2.000E+00	
C2H6	Enhanced by	3.000E+00	
AR	Enhanced by	7.000E-01	
265. HO2+NO<=>NO2+OH	2.11E+12	.0	-480.0
266. NO+O+M<=>NO2+M	1.06E+20	-1.4	.0
H2	Enhanced by	2.000E+00	
H2O	Enhanced by	6.000E+00	

CH4	Enhanced by	2.000E+00		
CO	Enhanced by	1.500E+00		
CO2	Enhanced by	2.000E+00		
C2H6	Enhanced by	3.000E+00		
AR	Enhanced by	7.000E-01		
267. NO2+O<=>NO+O2		3.90E+12	.0	-240.0
268. NO2+H<=>NO+OH		1.32E+14	.0	360.0
269. NH+O<=>NO+H		5.00E+13	.0	.0
270. NH+H<=>N+H2		3.20E+13	.0	330.0
271. NH+OH<=>HNO+H		2.00E+13	.0	.0
272. NH+OH<=>N+H2O		2.00E+09	1.2	.0
273. NH+O2<=>HNO+O		4.61E+05	2.0	6500.0
274. NH+O2<=>NO+OH		1.28E+06	1.5	100.0
275. NH+N<=>N2+H		1.50E+13	.0	.0
276. NH+H2O<=>HNO+H2		2.00E+13	.0	13850.0
277. NH+NO<=>N2+OH		2.16E+13	-.2	.0
278. NH+NO<=>N2O+H		4.16E+14	-.5	.0
279. NH2+O<=>OH+NH		7.00E+12	.0	.0
280. NH2+O<=>H+HNO		4.60E+13	.0	.0
281. NH2+H<=>NH+H2		4.00E+13	.0	3650.0
282. NH2+OH<=>NH+H2O		9.00E+07	1.5	-460.0
283. NNH<=>N2+H		3.30E+08	.0	.0
284. NNH+M<=>N2+H+M		1.30E+14	-.1	4980.0
H2	Enhanced by	2.000E+00		
H2O	Enhanced by	6.000E+00		
CH4	Enhanced by	2.000E+00		
CO	Enhanced by	1.500E+00		
CO2	Enhanced by	2.000E+00		
C2H6	Enhanced by	3.000E+00		
AR	Enhanced by	7.000E-01		
285. NNH+O2<=>HO2+N2		5.00E+12	.0	.0
286. NNH+O<=>OH+N2		2.50E+13	.0	.0
287. NNH+O<=>NH+NO		7.00E+13	.0	.0
288. NNH+H<=>H2+N2		5.00E+13	.0	.0
289. NNH+OH<=>H2O+N2		2.00E+13	.0	.0
290. NNH+CH3<=>CH4+N2		2.50E+13	.0	.0
291. H+NO+M<=>HNO+M		8.95E+19	-1.3	740.0
H2	Enhanced by	2.000E+00		
H2O	Enhanced by	6.000E+00		
CH4	Enhanced by	2.000E+00		
CO	Enhanced by	1.500E+00		
CO2	Enhanced by	2.000E+00		
C2H6	Enhanced by	3.000E+00		
AR	Enhanced by	7.000E-01		
292. HNO+O<=>NO+OH		2.50E+13	.0	.0

293.	$\text{HNO} + \text{H} \rightleftharpoons \text{H}_2 + \text{NO}$	4.50E+11	.7	660.0
294.	$\text{HNO} + \text{OH} \rightleftharpoons \text{NO} + \text{H}_2\text{O}$	1.30E+07	1.9	-950.0
295.	$\text{HNO} + \text{O}_2 \rightleftharpoons \text{HO}_2 + \text{NO}$	1.00E+13	.0	13000.0
296.	$\text{CN} + \text{O} \rightleftharpoons \text{CO} + \text{N}$	7.70E+13	.0	.0
297.	$\text{CN} + \text{OH} \rightleftharpoons \text{NCO} + \text{H}$	4.00E+13	.0	.0
298.	$\text{CN} + \text{H}_2\text{O} \rightleftharpoons \text{HCN} + \text{OH}$	8.00E+12	.0	7460.0
299.	$\text{CN} + \text{O}_2 \rightleftharpoons \text{NCO} + \text{O}$	6.14E+12	.0	-440.0
300.	$\text{CN} + \text{H}_2 \rightleftharpoons \text{HCN} + \text{H}$	2.10E+13	.0	4710.0
301.	$\text{NCO} + \text{O} \rightleftharpoons \text{NO} + \text{CO}$	2.35E+13	.0	.0
302.	$\text{NCO} + \text{H} \rightleftharpoons \text{NH} + \text{CO}$	5.40E+13	.0	.0
303.	$\text{NCO} + \text{OH} \rightleftharpoons \text{NO} + \text{H} + \text{CO}$	2.50E+12	.0	.0
304.	$\text{NCO} + \text{N} \rightleftharpoons \text{N}_2 + \text{CO}$	2.00E+13	.0	.0
305.	$\text{NCO} + \text{O}_2 \rightleftharpoons \text{NO} + \text{CO}_2$	2.00E+12	.0	20000.0
306.	$\text{NCO} + \text{M} \rightleftharpoons \text{N} + \text{CO} + \text{M}$	8.80E+16	-.5	48000.0
	H2	Enhanced by	2.000E+00	
	H2O	Enhanced by	6.000E+00	
	CH4	Enhanced by	2.000E+00	
	CO	Enhanced by	1.500E+00	
	CO2	Enhanced by	2.000E+00	
	C2H6	Enhanced by	3.000E+00	
	AR	Enhanced by	7.000E-01	
307.	$\text{NCO} + \text{NO} \rightleftharpoons \text{N}_2\text{O} + \text{CO}$	2.85E+17	-1.5	740.0
308.	$\text{NCO} + \text{NO} \rightleftharpoons \text{N}_2 + \text{CO}_2$	5.70E+18	-2.0	800.0
309.	$\text{HCN} + \text{M} \rightleftharpoons \text{H} + \text{CN} + \text{M}$	1.04E+29	-3.3	126600.0
	H2	Enhanced by	2.000E+00	
	H2O	Enhanced by	6.000E+00	
	CH4	Enhanced by	2.000E+00	
	CO	Enhanced by	1.500E+00	
	CO2	Enhanced by	2.000E+00	
	C2H6	Enhanced by	3.000E+00	
	AR	Enhanced by	7.000E-01	
310.	$\text{HCN} + \text{O} \rightleftharpoons \text{NCO} + \text{H}$	1.11E+04	2.6	4980.0
311.	$\text{HCN} + \text{O} \rightleftharpoons \text{NH} + \text{CO}$	2.77E+03	2.6	4980.0
312.	$\text{HCN} + \text{O} \rightleftharpoons \text{CN} + \text{OH}$	2.13E+09	1.6	26600.0
313.	$\text{HCN} + \text{OH} \rightleftharpoons \text{HOCN} + \text{H}$	1.10E+06	2.0	13370.0
314.	$\text{HCN} + \text{OH} \rightleftharpoons \text{HNCO} + \text{H}$	4.40E+03	2.3	6400.0
315.	$\text{HCN} + \text{OH} \rightleftharpoons \text{NH}_2 + \text{CO}$	1.60E+02	2.6	9000.0
316.	$\text{H} + \text{HCN} + \text{M} \rightleftharpoons \text{H}_2\text{CN} + \text{M}$	1.40E+26	-3.4	1900.0
	H2	Enhanced by	2.000E+00	
	H2O	Enhanced by	6.000E+00	
	CH4	Enhanced by	2.000E+00	
	CO	Enhanced by	1.500E+00	
	CO2	Enhanced by	2.000E+00	
	C2H6	Enhanced by	3.000E+00	
	AR	Enhanced by	7.000E-01	

317. $\text{H}_2\text{CN} + \text{N} \rightleftharpoons \text{N}_2 + \text{CH}_2$	6.00E+13	.0	400.0
318. $\text{CH} + \text{N}_2 \rightleftharpoons \text{HCN} + \text{N}$	2.86E+08	1.1	20400.0
319. $\text{CH} + \text{N}_2(+\text{M}) \rightleftharpoons \text{HCNN}(+\text{M})$	3.10E+12	.1	.0
Low pressure limit:	.13000E+26	-.31600E+01	.74000E+03
TROE centering:	.66700E+00	.23500E+03	.21170E+04 .45360E+04
H2	Enhanced by	2.000E+00	
H2O	Enhanced by	6.000E+00	
CH4	Enhanced by	2.000E+00	
CO	Enhanced by	1.500E+00	
CO2	Enhanced by	2.000E+00	
C2H6	Enhanced by	3.000E+00	
AR	Enhanced by	7.000E-01	
320. $\text{CH}_2 + \text{N}_2 \rightleftharpoons \text{HCN} + \text{NH}$	1.00E+13	.0	74000.0
321. $\text{CH}_2(\text{S}) + \text{N}_2 \rightleftharpoons \text{NH} + \text{HCN}$	1.00E+11	.0	65000.0
322. $\text{CH} + \text{NO} \rightleftharpoons \text{HCN} + \text{O}$	5.00E+13	.0	.0
323. $\text{CH} + \text{NO} \rightleftharpoons \text{H} + \text{NCO}$	2.00E+13	.0	.0
324. $\text{CH} + \text{NO} \rightleftharpoons \text{N} + \text{HCO}$	3.00E+13	.0	.0
325. $\text{CH}_2 + \text{NO} \rightleftharpoons \text{H} + \text{HNCO}$	3.10E+17	-1.4	1270.0
326. $\text{CH}_2 + \text{NO} \rightleftharpoons \text{OH} + \text{HCN}$	2.90E+14	-.7	760.0
327. $\text{CH}_2 + \text{NO} \rightleftharpoons \text{H} + \text{HCNO}$	3.80E+13	-.4	580.0
328. $\text{CH}_2(\text{S}) + \text{NO} \rightleftharpoons \text{H} + \text{HNCO}$	3.10E+17	-1.4	1270.0
329. $\text{CH}_2(\text{S}) + \text{NO} \rightleftharpoons \text{OH} + \text{HCN}$	2.90E+14	-.7	760.0
330. $\text{CH}_2(\text{S}) + \text{NO} \rightleftharpoons \text{H} + \text{HCNO}$	3.80E+13	-.4	580.0
331. $\text{CH}_3 + \text{NO} \rightleftharpoons \text{HCN} + \text{H}_2\text{O}$	9.60E+13	.0	28800.0
332. $\text{CH}_3 + \text{NO} \rightleftharpoons \text{H}_2\text{CN} + \text{OH}$	1.00E+12	.0	21750.0
333. $\text{HCNN} + \text{O} \rightleftharpoons \text{CO} + \text{H} + \text{N}_2$	2.20E+13	.0	.0
334. $\text{HCNN} + \text{O} \rightleftharpoons \text{HCN} + \text{NO}$	2.00E+12	.0	.0
335. $\text{HCNN} + \text{O}_2 \rightleftharpoons \text{O} + \text{HCO} + \text{N}_2$	1.20E+13	.0	.0
336. $\text{HCNN} + \text{OH} \rightleftharpoons \text{H} + \text{HCO} + \text{N}_2$	1.20E+13	.0	.0
337. $\text{HCNN} + \text{H} \rightleftharpoons \text{CH}_2 + \text{N}_2$	1.00E+14	.0	.0
338. $\text{HNCO} + \text{O} \rightleftharpoons \text{NH} + \text{CO}_2$	9.80E+07	1.4	8500.0
339. $\text{HNCO} + \text{O} \rightleftharpoons \text{HNO} + \text{CO}$	1.50E+08	1.6	44000.0
340. $\text{HNCO} + \text{O} \rightleftharpoons \text{NCO} + \text{OH}$	2.20E+06	2.1	11400.0
341. $\text{HNCO} + \text{H} \rightleftharpoons \text{NH}_2 + \text{CO}$	2.25E+07	1.7	3800.0
342. $\text{HNCO} + \text{H} \rightleftharpoons \text{H}_2 + \text{NCO}$	1.05E+05	2.5	13300.0
343. $\text{HNCO} + \text{OH} \rightleftharpoons \text{NCO} + \text{H}_2\text{O}$	4.65E+12	.0	6850.0
344. $\text{HNCO} + \text{OH} \rightleftharpoons \text{NH}_2 + \text{CO}_2$	1.55E+12	.0	6850.0
345. $\text{HNCO} + \text{M} \rightleftharpoons \text{NH} + \text{CO} + \text{M}$	1.18E+16	.0	84720.0
H2	Enhanced by	2.000E+00	
H2O	Enhanced by	6.000E+00	
CH4	Enhanced by	2.000E+00	
CO	Enhanced by	1.500E+00	
CO2	Enhanced by	2.000E+00	
C2H6	Enhanced by	3.000E+00	
AR	Enhanced by	7.000E-01	

346. $\text{HCNO} + \text{H} \rightleftharpoons \text{H} + \text{HNCO}$	2.10E+15	-.7	2850.0
347. $\text{HCNO} + \text{H} \rightleftharpoons \text{OH} + \text{HCN}$	2.70E+11	.2	2120.0
348. $\text{HCNO} + \text{H} \rightleftharpoons \text{NH}_2 + \text{CO}$	1.70E+14	-.8	2890.0
349. $\text{HOCN} + \text{H} \rightleftharpoons \text{H} + \text{HNCO}$	2.00E+07	2.0	2000.0
350. $\text{CH}_3 + \text{N} \rightleftharpoons \text{H}_2\text{CN} + \text{H}$	6.10E+14	-.3	290.0
351. $\text{CH}_3 + \text{N} \rightleftharpoons \text{HCN} + \text{H}_2$	3.70E+12	.1	-90.0
352. $\text{NH}_3 + \text{H} \rightleftharpoons \text{NH}_2 + \text{H}_2$	5.40E+05	2.4	9915.0
353. $\text{NH}_3 + \text{OH} \rightleftharpoons \text{NH}_2 + \text{H}_2\text{O}$	5.00E+07	1.6	955.0
354. $\text{NH}_3 + \text{O} \rightleftharpoons \text{NH}_2 + \text{OH}$	9.40E+06	1.9	6460.0

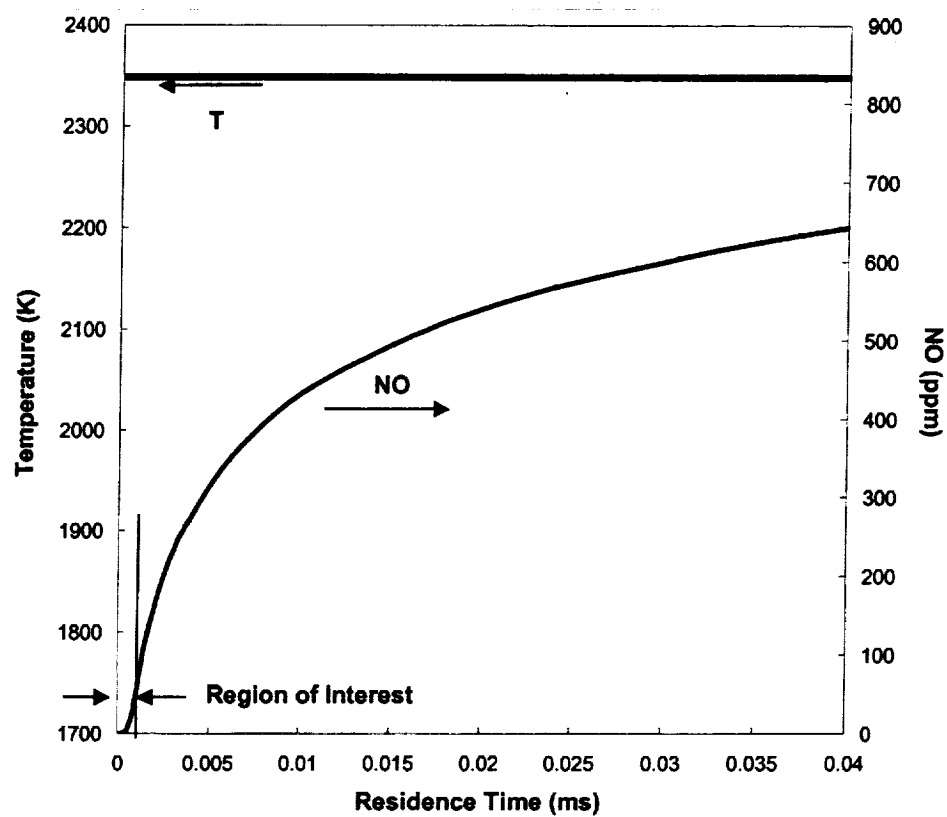


Figure B.1: Perfectly-stirred reactor residence time plot.

B.1 Equivalence Ratio Comparison

As noted in the previous discussion, the residence time for a stoichiometric mixture was scaled to reflect the primary equivalence ratio supplied to the LDI burner. The NO is then scaled by the same equivalence ratio to dilute the stoichiometric products with excess air. As Figure B.2 demonstrates, a remarkable comparison is achieved. Note that the reference condition of $\phi_p=0.9$ is the normalization point for the residence time, thus matching the NO (ppm) level at this stoichiometry. To better compare with the ϕ^2 scaling demonstrated in Chapter 6, Figure B.3 depicts the correlation achieved when the residence time (analogous to the equivalence ratio) is squared and the results compared to the actual data. The PSR adequately predicts the scaling of NO over this range of equivalence ratios. Unfortunately, the residence times associated with this correlation are on the order of 1 μ s, which is an unrealistic time scale for the LDI flame. A realistic time scale, based on the exit velocity and combustion temperature would be ~ 0.1 ms. We recognize this limitation and do not wish to overemphasize the correlations found in this appendix.

B.2 Preheat Comparison

To model the LDI preheat conditions, the adiabatic temperatures for the varying preheat temperatures were calculated and substituted into the constant temperature PSR code. The residence time was chosen based on the nominal 375-K air preheat, 4-atm, $\phi_p=0.9$ case, as above. The results are shown in Figure B.4. The shift in NO between the curves results only from the repeatability of the LDI measurements. In this data set, the $\phi_p=0.9$ NO level was ~ 39 ppm as opposed to ~ 46 ppm. Again, we see exceptional qualitative and quantitative comparisons.

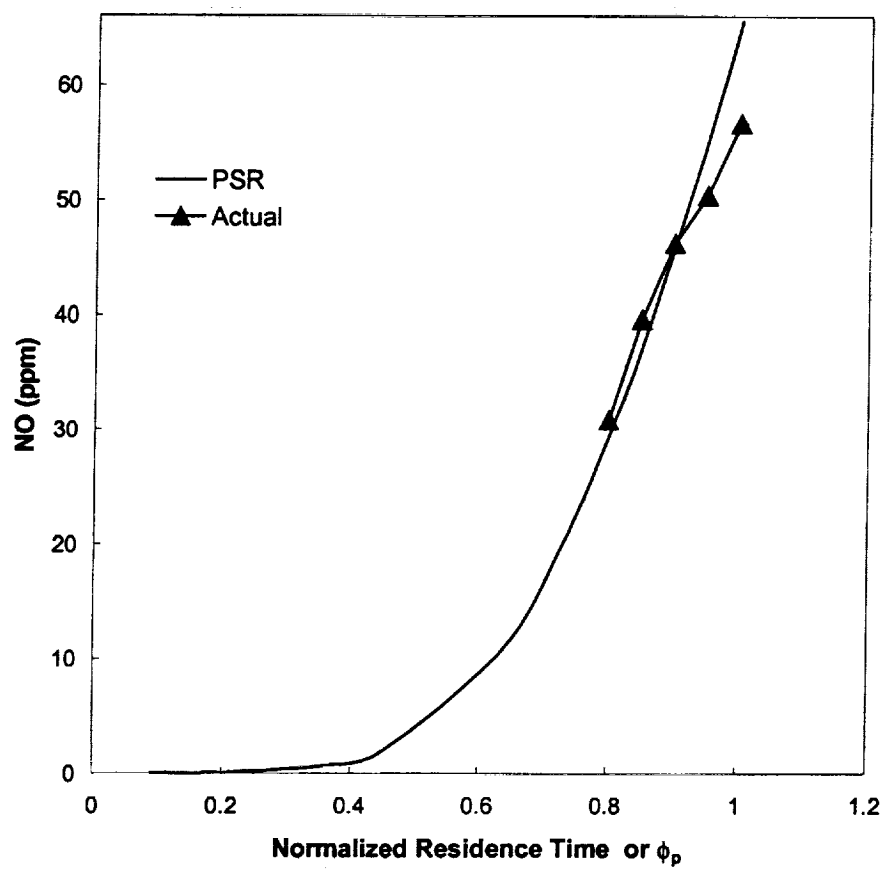


Figure B.2: Comparison of PSR predictions to measured equivalence ratio scaling in LDI flame.

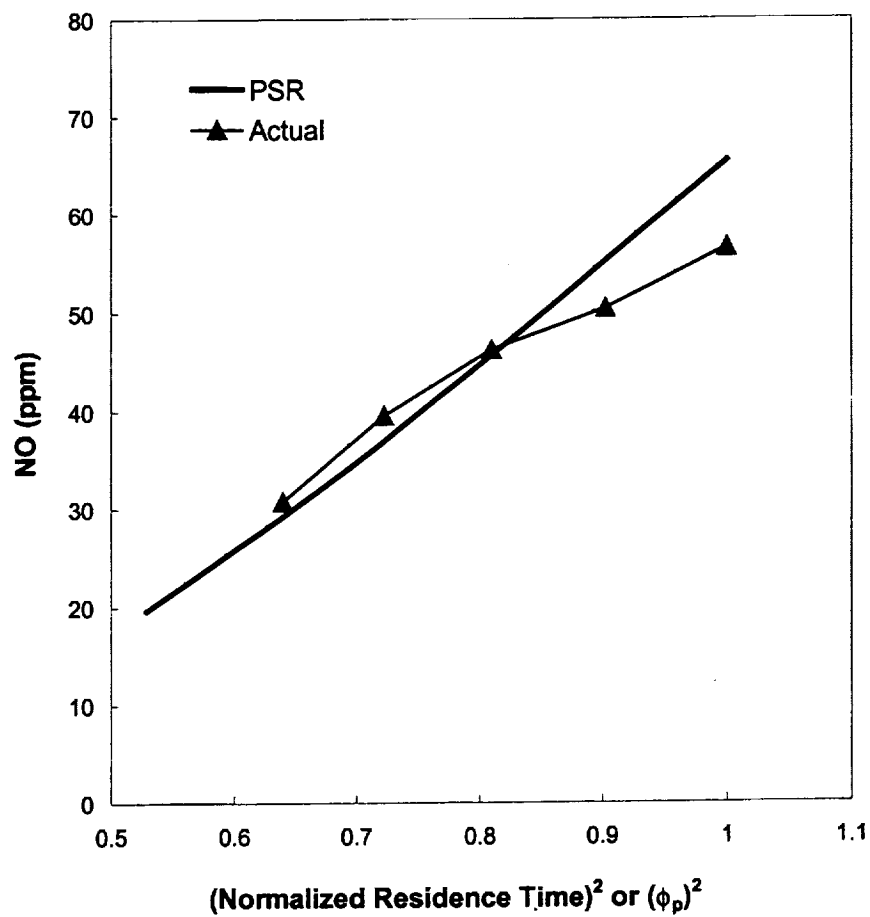


Figure B.3: Comparison of PSR predictions to measured ϕ_p^2 scaling in LDI flames.

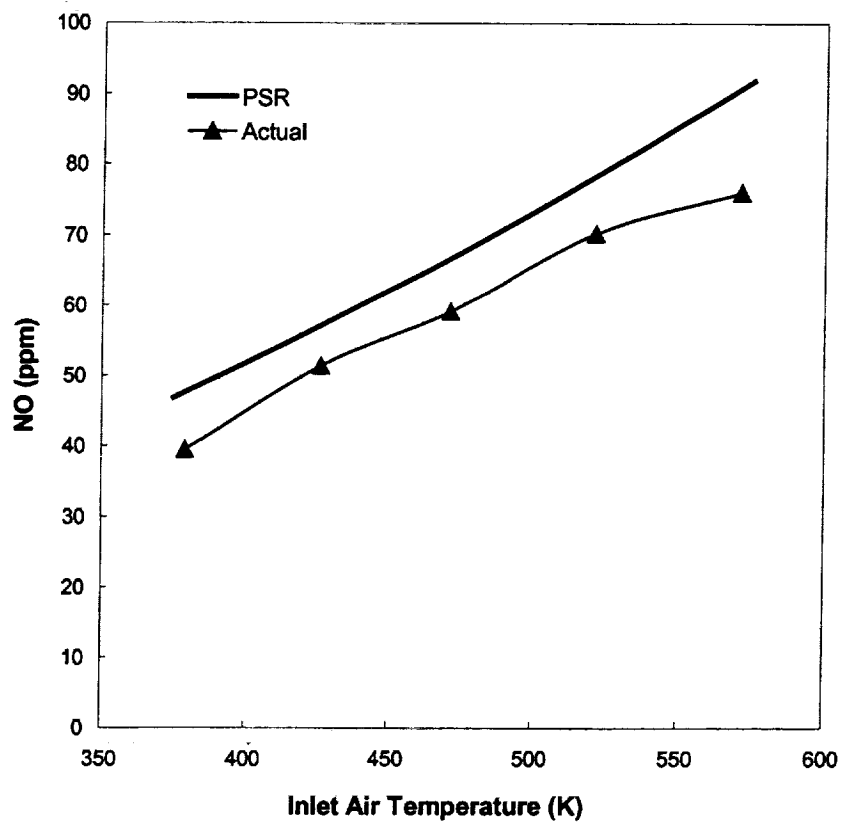


Figure B.4: Comparison of PSR predictions to measured scaling for air preheat temperature in LDI flames.

B.3 Pressure Comparison

A last comparison is that of the pressure scaling measured in the LDI flames. To perform this comparison, the adiabatic flame temperatures were calculated at the different pressures, and the residence times were scaled based on the flow scaling with pressure actually used in the experiments. These values were used in the constant temperature PSR code and the results are shown in Figure B.5. The PSR model does not accurately represent the measured trend for the LDI burner. Nevertheless, the qualitative trend is consistent in that the NO level increases with pressure.

B.4 Additional Sandia Models

Recognizing that the time scales predicted by the PSR code are several orders of magnitude too small, we attempted four other simulations using perfectly-stirred reactors and plug-flow reactors (PFR). These are delineated below:

1. PSR with full energy equation solution, i.e., not constant temperature
2. PSR with full energy solution and heat loss to constrain maximum temperature
3. PFR with full energy equation solution
4. PFR with specified temperature profile

Each of these simulations produced similar residence times for the production of ~46 ppm of NO, namely 1 to 30 μ s. We have concluded that the LDI burner cannot be simplistically modeled with either the PSR or PFR codes to produce realistic pollutant levels and time scales. We therefore have to approach the LDI burner from a more computationally demanding viewpoint.

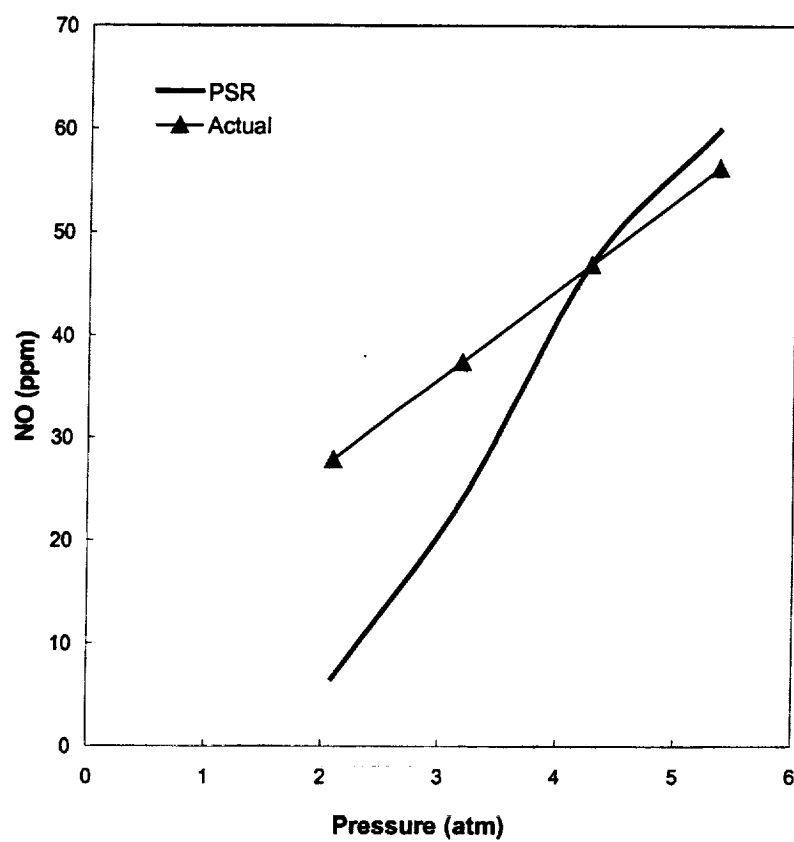


Figure B.5: Comparison of PSR predictions to measured pressure scaling in LDI flames.

B.5 REC Modeling

With the recognition that time-averaged, spatially-resolved NO concentration measurements yield limited information about the NO formation mechanism and its intricate dependence on the pressure, stoichiometry, and air preheat temperatures, we have worked with Dr. John Abraham to numerically model the spray combustion event. Using the REC code (Magi, 1987), we have simulated cold-flow air conditions to match the swirl geometry and are currently simulating combustng air plus gaseous fuel conditions. The time required to run the simulations prohibits complete analysis via the computational model. Nevertheless, the results obtained thus far are presented here.

The simulations were performed in a cylindrical volume matching the dimensions of the pressure vessel interior, with a constant pressure boundary at the exit and swirling air issuing into the chamber at an angle similar to the LDI burner exit. Several iterations were performed to simulate the 5-atm operating conditions, with the end result shown in Figure B.6 as a vector plot of the cold-flow velocity profiles. The combustng case is shown in figure B.7 at a time of 70 ms into the simulation. The cold-flow plot demonstrates the expected recirculation zone for swirl-stabilized flow. The combustng case, however, does not yield a recirculation zone at this time. Either the code has not reached a steady-state operating condition, or the addition of heat from combustion inhibits the formation of a recirculation zone.

The temperature and NO profiles for the 70-ms case are pictured in Figures B.8 and B.9, respectively. It is too early in the simulation to make conclusive statements regarding the utility of the REC code to predict the LDI characteristics, particularly with the absence of a recirculation zone in the combustng case. These simulations should be deferred to a full-time research project in order to yield a general insight into the combustion of swirl-stabilized spray flames. General simulated trends in the NO concentrations can be compared to the measured trends. The additional information provided by temperature, species, and velocity profiles should provide valuable insight into the actual NO formation mechanism and improve our understanding of the combustion of swirling sprays.

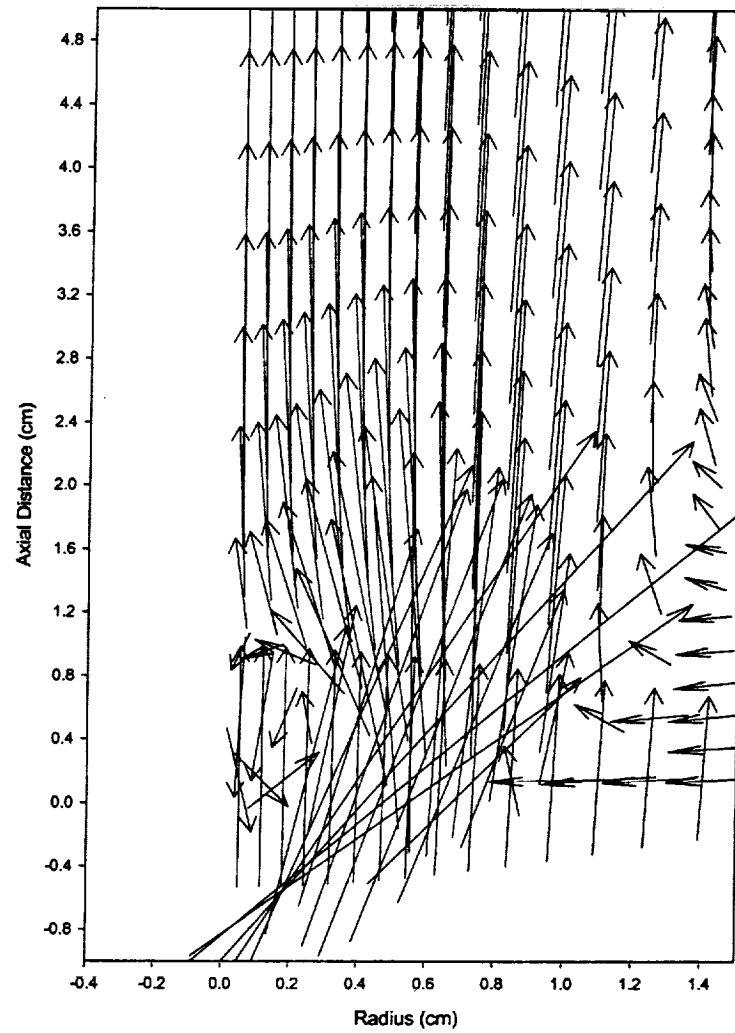


Figure B.6: Cold-flow velocity vector plot of REC simulation.

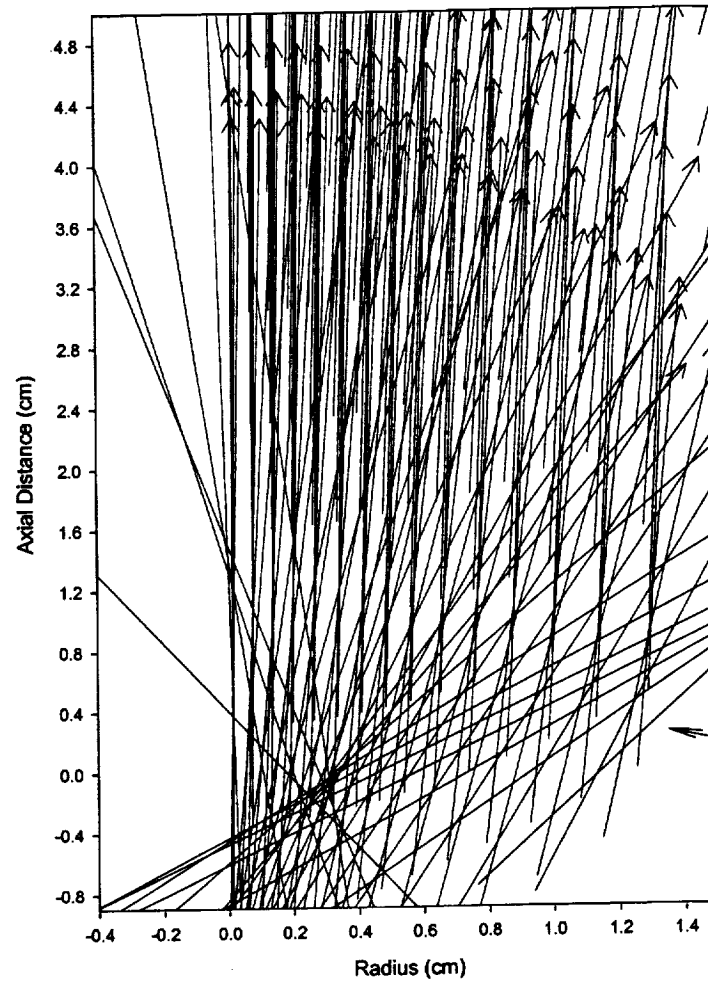


Figure B.7: Combusting-flow velocity vector plot of REC simulation.

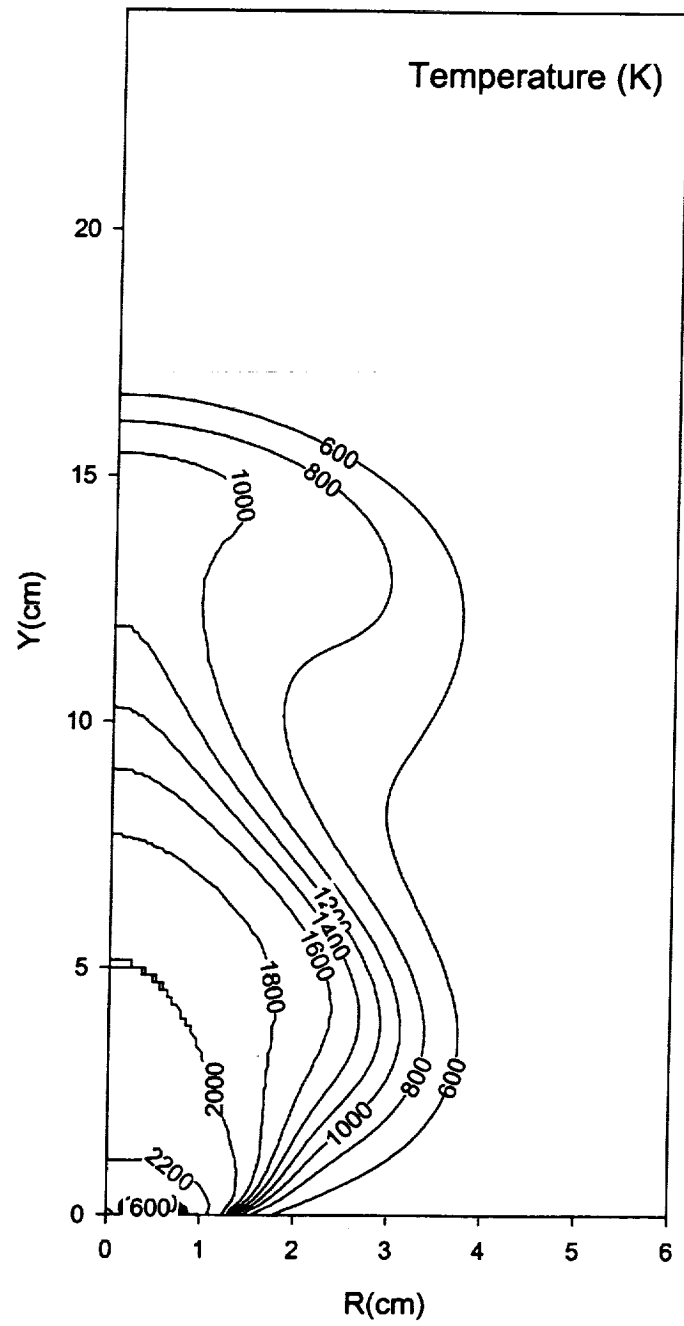


Figure B.8: Combusting-flow temperature contour plot of REC simulation.

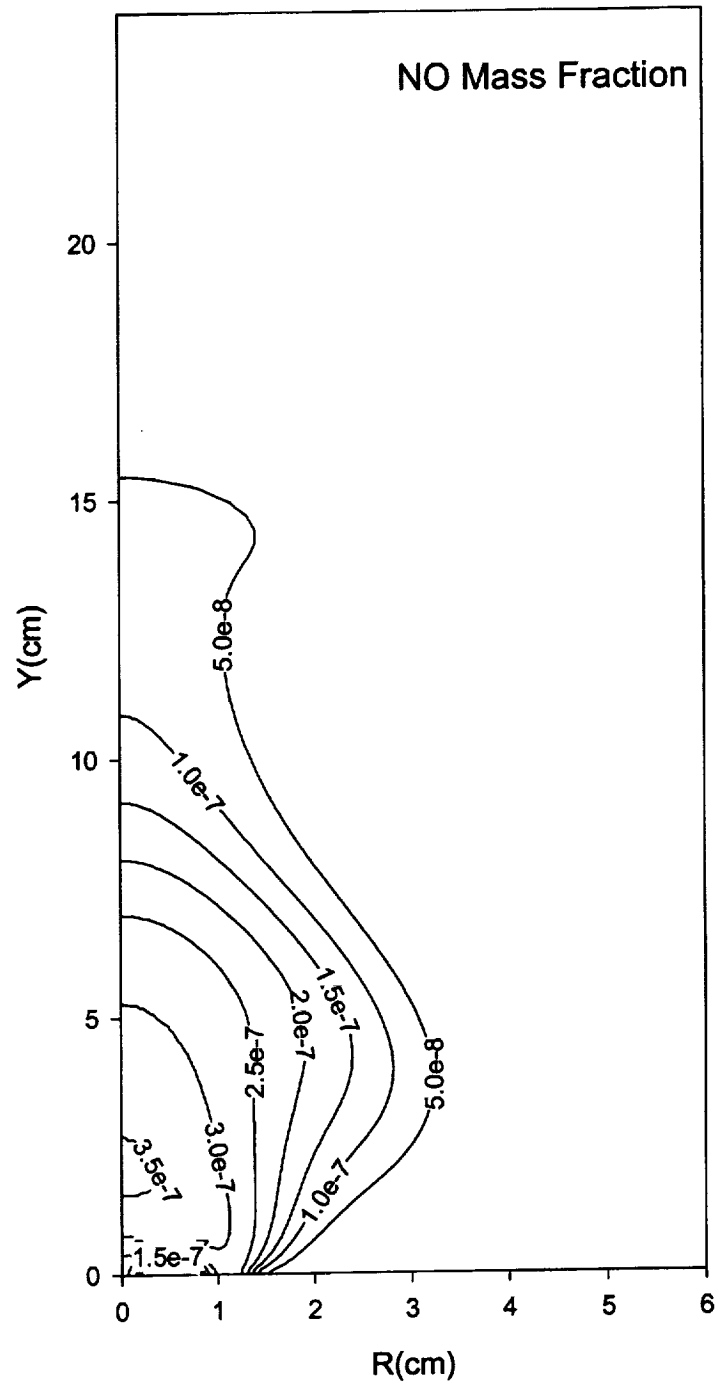


Figure B.9: Combusting-flow NO mass fraction contour plot of REC simulation.

REPORT DOCUMENTATION PAGE			Form Approved OMB No. 0704-0188	
Public reporting burden for this collection of information is estimated to average 1 hour per response, including the time for reviewing instructions, searching existing data sources, gathering and maintaining the data needed, and completing and reviewing the collection of information. Send comments regarding this burden estimate or any other aspect of this collection of information, including suggestions for reducing this burden, to Washington Headquarters Services, Directorate for Information Operations and Reports, 1215 Jefferson Davis Highway, Suite 1204, Arlington, VA 22202-4302, and to the Office of Management and Budget, Paperwork Reduction Project (0704-0188), Washington, DC 20503.				
1. AGENCY USE ONLY (Leave blank)		2. REPORT DATE August 2000		3. REPORT TYPE AND DATES COVERED Final Contractor Report
4. TITLE AND SUBTITLE Quantitative Measurements of Nitric Oxide Concentration in High-Pressure, Swirl-Stabilized Spray Flames			5. FUNDING NUMBERS WU-714-02-40-00 NAS3-27720	
6. AUTHOR(S) Clayton S. Cooper and Normand M. Laurendeau				
7. PERFORMING ORGANIZATION NAME(S) AND ADDRESS(ES) Purdue University West Lafayette, Indiana 47907			8. PERFORMING ORGANIZATION REPORT NUMBER E-12414	
9. SPONSORING/MONITORING AGENCY NAME(S) AND ADDRESS(ES) National Aeronautics and Space Administration Washington, DC 20546-0001			10. SPONSORING/MONITORING AGENCY REPORT NUMBER NASA CR-2000-210365	
11. SUPPLEMENTARY NOTES Project Manager, Yolanda R. Hicks, Turbomachinery and Propulsion Systems Division, NASA Glenn Research Center, organization code 5830, (216) 433-3410.				
12a. DISTRIBUTION/AVAILABILITY STATEMENT Unclassified - Unlimited Subject Categories: 07, 34, and 74 This publication is available from the NASA Center for AeroSpace Information, (301) 621-0390.			12b. DISTRIBUTION CODE Distribution: Nonstandard	
13. ABSTRACT (Maximum 200 words) Lean direct-injection (LDI) spray flames offer the possibility of reducing NO _x emissions from gas turbines by rapid mixing of the liquid fuel and air so as to drive the flame structure toward partially-premixed conditions. We consider the technical approaches required to utilize laser-induced fluorescence methods for quantitatively measuring NO concentrations in high-pressure LDI spray flames. In the progression from atmospheric to high-pressure measurements, the LIF method requires a shift from the saturated to the linear regime of fluorescence measurements. As such, we discuss quantitative, spatially resolved laser-saturated fluorescence (LSF), linear laser-induced fluorescence (LIF), and planar laser-induced fluorescence (PLIF) measurements of NO concentration in LDI spray flames. Spatially-resolved LIF measurements of NO concentration (ppm) are reported for preheated, LDI spray flames at pressures of 2-5 atm. The spray is produced by a hollowcone, pressure-atomized nozzle supplied with liquid heptane. NO is excited via the Q ₂ (26.5) transition of the γ(0,0) band. Detection is performed in a 2 nm region centered on the γ(0,1) band. A complete scheme is developed by which quantitative NO concentrations in high-pressure LDI spray flames can be measured by applying linear LIF. NO is doped into the reactants and convected through the flame with no apparent destruction, thus allowing a NO fluorescence calibration to be taken inside the flame environment. The in-situ calibration scheme is validated by comparisons to a reference flame. Quantitative NO profiles are presented and analyzed so as to better understand the operation of lean-direct injectors for gas turbine combustors. Moreover, parametric studies are provided for variations in pressure, air-preheat temperature, and equivalence ratio. Similar parametric studies are performed for lean, premixed-prevaporized flames to permit comparisons to those for LDI flames. Finally, PLIF is expanded to high pressure in an effort to quantify the detected fluorescence image for LDI flames. Success is achieved by correcting the PLIF calibration via a single-point LIF measurement. This procedure removes the influence of a preferential background that occurs in the PLIF detection window. In general, both the LIF and PLIF measurements verify that the LDI strategy could be used to reduce NO _x emissions in future gas turbine combustors.				
14. SUBJECT TERMS Combustion; Nitric oxide measurements; Laser-induced fluorescence			15. NUMBER OF PAGES 217	
			16. PRICE CODE A10	
17. SECURITY CLASSIFICATION OF REPORT Unclassified	18. SECURITY CLASSIFICATION OF THIS PAGE Unclassified	19. SECURITY CLASSIFICATION OF ABSTRACT Unclassified	20. LIMITATION OF ABSTRACT	